Eco-friendly biopolymer integrated three-dimensional hierachichal graphene materials for adsorptive removal of dyes and heavy metals

Kar Chiew Lai

Thesis submitted to the University of Nottingham for the degree of Doctor of Philosophy

February 2021

Abstract

The discharge of effluent containing heavy metals and dyes from various industries has led to severe water pollution threatening all forms of life and the environment. Adsorption of these pollutants onto graphene oxide (GO) nanosorbent has potrayed promising results, however, its application in industrial wastewater remediation is restricted by its nano-sized dimension, making the recovery steps costly. Lately, three-dimensional (3D) graphene materials have attracted great attention as an effective adsorbent for wastewater treatment. The intrinsic properties of 3D graphene structure such as ultra-large surface area and interconnected porous structure, can facilitate the transport of pollutants into the 3D network and provide abundant active sites for binding the pollutants.

Ice-templating was selected as the synthesis route for 3D graphene structures in this research due to its facile steps, cost effectiveness, high scalability potential and tuneable material porosity. A new 3D graphene structure, GO/chitosan aerogel (GOCA), was fabricated via this technique and employed for Metanil Yellow (MY) and Reactive Black 5 (RB5) dyes removal. The GOCA adsorption performance was evaluated by varying prominent adsorption factors. The combined effects of multiple parameters and optimum conditions for the dyes removal were determined by response surface methodology (RSM). GOCA exhibited adsorption capacities of 418.35 and 656.96 mg/g for MY and RB5 dyes, respectively. For both dyes, the adsorption kinetic obeyed the pseudo-first-order and pseudo-second-order models at low and high concentration regions, respectively. The adsorption equilibria for the dyes were best fitted to the Langmuir isotherm. The GOCA adsorbent was easily

separated after adsorption and regenerated for re-use in five adsorption-desorption cycles.

The GOCA was further assessed for continuous adsorption of MY and RB5 dyes using fixed-bed columns. The breakthrough characteristics were investigated as a function of bed height, inlet dye concentration and feed flowrate. The greatest bed adsorption capacities attained were 157.06 and 247.96 mg/g for MY and RB5 dyes, respectively. FTIR spectroscopy confirmed that electrostatic attraction and $\pi - \pi$ stacking were the prevailing mechanisms of interaction between the dye molecules and the adsorbent.

Another new 3D graphene structure, xanthan integrated GO functionalised by titanium dioxide (3D GXT composite), was successfully prepared for aqueous lead (Pb) and cadmium (Cd) removal. The 3D GXT composite exhibited maximum adsorption capacities of 204.76 and 67.33 mg/g for Pb and Cd, respectively, as optimised by RSM. The Pb and Cd adsorption onto 3D GXT was best described by the Langmuir and Freundlich isotherm, respectively. Meanwhile, the kinetic data were well fitted to the pseudo-second-order for both heavy metals. Moreover, the used 3D GXT was highly regenerable using 0.1 M hydrochloric acid at 30 ^{o}C.

The continuous adsorption of Pb and Cd onto 3D GXT composite was carried out in fixed-bed columns of varying bed heights, feed flowrates and inlet concentrations. The breakthrough curves were fitted to the Thomas, Yoon-Nelson and Adams-Bohart models. The highest bed adsorption capacities for Pb and Cd were 146.08 and 64.05 mg/g, respectively. FTIR spectroscopy and pH study verified that electrostatic interaction and complexation were the dominant adsorption mechanisms between the metal ions and the 3D GXT composite.

Acknowledgements

Firstly, I would like to give my immense thanks to God for giving me the strength, ability and good health to undertake and complete my PhD study in a timely manner. With much gratitude, I would like to convey my appreciation to my supervisor, Dr Lee Lai Yee, for her patience, continuous supervision and guidance. I would also like to express my deepest gratitude to Professor Gan Suyin and Dr Suchithra Thangalazhy Gopakumar for providing valuable advice and insightful discussion about my research.

Special acknowledgement goes to all technical support staff, especially, Ahmad Fareez Mohd Rawi, Noor Fatihah Suhaimi and Khairani Hasuna Jaapar for their assistance in the laboratory. I am also thankful to my senior, Billie Hiew Yan Zhang, who guided and supported me during my PhD journey.

To my parents and brother, I wish to extend my sincere thanks for instilling in me confidence and motivation to pursue my PhD. I could never have accomplished what I have now without their endless love and support. Finally, I would like to gratefully acknowledge the valuable support and encouragement provided by Dr Low Wei Hau.

Publication List

Selected publications:

[1] **K.C. Lai**, L.Y. Lee, B.Y.Z. Hiew, S. Thangalazhy-Gopakumar, S. Gan, Environmental application of three-dimensional graphene materials as adsorbents for dyes and heavy metals: Review on ice-templating method and adsorption mechanisms, Journal of Environmental Sciences 79 (2019) 174-199.

[2] **K.C. Lai**, L.Y. Lee, B.Y.Z. Hiew, S. Thangalazhy-Gopakumar, S. Gan, Facile synthesis of xanthan biopolymer integrated 3D hierarchical graphene oxide/titanium dioxide composite for adsorptive lead removal in wastewater, Bioresource Technology 309 (2020) 123296.

[3] **K.C. Lai**, B.Y.Z. Hiew, L.Y. Lee, S. Gan, S. Thangalazhy-Gopakumar, W.S. Chiu, P.S. Khiew, Ice-templated graphene oxide/chitosan aerogel as an effective adsorbent for sequestration of metanil yellow dye, Bioresource Technology 274 (2019) 134-144.

[4] **K.C. Lai**, L.Y. Lee, B.Y.Z. Hiew, T.C.K. Yang, G.T. Pan, S. Thangalazhy-Gopakumar, S. Gan, Utilisation of eco-friendly and low cost 3D graphene-based composite for treatment of aqueous Reactive Black 5 dye: Characterisation, adsorption mechanism and recyclability studies, Journal of the Taiwan Institute of Chemical Engineers (2020), https://doi.org/10.1016/j.jtice.2020.09.024.

Other publications:

[1] B.Y.Z. Hiew, L.Y. Lee, **K.C. Lai**, S. Gan, S. Thangalazhy-Gopakumar, G.-T. Pan, T.C.-K. Yang, Adsorptive decontamination of diclofenac by three-dimensional graphene-based adsorbent: Response surface methodology, adsorption

equilibrium, kinetic and thermodynamic studies, Environmental Research 168 (2019) 241-253.

[2] X.J. Lee, B.Y.Z. Hiew, **K.C. Lai**, L.Y. Lee, S. Gan, S. Thangalazhy-Gopakumar, S. Rigby, Review on graphene and its derivatives: Synthesis methods and potential industrial implementation, Journal of the Taiwan Institute of Chemical Engineers 98 (2019) 163-180.

Table of Contents

Abstract I

Acknowledgements III

Publication List IV

List of Figures X

List of Tables XIV

Nomenclatures XVI

Chapter 1. Introduction 1

1.1 Background 1

1.2 Problem statement 7

1.3 Aim and objectives 8

Chapter 2. Literature review 9

2.1 Ice-templating 9

2.1.1 Basics of ice-templating 9

2.1.2 Critical process parameters in ice-templating 11

2.1.3 Ice-templated 3D graphene-based materials 18

2.1.4 Physical properties of ice-templated 3D graphene materials 24

2.2 Adsorption properties and mechanisms of 3D graphene materials 29

2.2.1 Adsorption of dyes 29

2.2.2 Adsorption of heavy metals 46

Chapter 3. Materials and methodology 57

3.1 Materials 57

3.2 Preparation of GO, GOCA and 3D GXT composite 58

3.3 Characterisation tests 59

3.4 Batch adsorption studies 60

3.4.1 Adsorption kinetic and equilibrium models fitting 65

3.4.2 Thermodynamic study 67

3.5 Response surface methodology 67

3.6 Regeneration study 68

3.7 Fixed-bed column adsorption studies 69

3.7.1 Kinetic models for fixed-bed column adsorption 71

Chapter 4. Batch adsorption of Metanil Yellow and Reactive Black 5 dyes onto 3D GO/chitosan aerogel 73

4.1 Introduction 73

4.2 Results and discussion 76

4.2.1 Characterisation of GOCA 76

4.2.2 Adsorption performance of GOCA 82

4.2.3 RSM modelling and optimisation 101

4.2.4 Regeneration of GOCA 117

4.2.5 Comparison with literature data 119

4.3 Summary 121

Chapter 5. Fixed-bed column adsorption of Metanil Yellow and Reactive Black 5 dyes by 3D GO/chitosan aerogel 122

5.1 Introduction 122

5.2 Results and discussion 123

5.2.1 Effect of bed height on column adsorption 123

5.2.2 Effect of inlet concentration on column adsorption 125

5.2.3 Effect of feed flowrate on column adsorption 127

5.2.4 Kinetic modelling of column data 129

5.2.5 Proposed adsorption mechanisms 134

5.2.6 Comparison of MY and RB5 dyes adsorption onto GOCA 137

5.2.7 Comparison of bed adsorption capacity with other adsorbents 138

5.3 Summary 139

Chapter 6. Batch adsorption of lead and cadmium by 3D GO/xanthan/titanium dioxide composite 140

6.1 Introduction 140

6.2 Results and discussion 143

6.2.1 Characterisation of 3D GXT composite 143

6.2.2 Adsorptive Pb and Cd removal by 3D GXT composite 149

6.2.3 RSM modelling and optimisation 163

6.2.4 Reusability of 3D GXT composite 186

6.2.5 Comparison of 3D GXT composite with other adsorbents 187

6.3 Summary 189

Chapter 7. Fixed-bed column adsorption of lead and cadmium by 3D GO/xanthan /titanium dioxide composite 190

7.1 Introduction 190

7.2 Results and discussion 191

7.2.1 Effects of column parameters 191

7.2.2 Modelling of breakthrough curve 199

7.2.3 Proposed mechanisms for Pb and Cd adsorption onto 3D GXT composite .. 202

7.2.4 Comparison of bed adsorption capacity with other adsorbents 204

7.3 Summary..... 206

Chapter 8. Conclusions and Recommendations..... 207

8.1 Conclusions..... 207

8.2 Recommendations..... 208

References..... 210

List of Figures

	Page no.
Fig. 2.1 Schematic representation of the ice-templating process. Reprinted with permission from [59]. Copyright 2013 Materials Research Society.	10
Fig. 2.2 (a) Homogeneous freezing; (b) Unidirectional freezing. Reproduced with permission from [64]. Copyright 2017 Royal Society of Chemistry. (c) FESEM image of GO/CNT aerogel showing continuous and uniform macropores. Reprinted with permission from [62]. Copyright 2013 WILEY-VCH Verlag GmbH & Co. KGaA, Weinheim. (d) FESEM image of GO aerogel demonstrating unidirectional architecture. Adapted with permission from [63]. Copyright 2012 Elsevier.	13
Fig. 2.3 (a) Schematic illustrating the fabrication process for GO-chitosan beads; (b) photos of half-cut GO-chitosan bead showing core-shell structure; (c) schematic diagram showing the structural properties of GO-chitosan bead; (d) FESEM image of the surface morphology of GO-chitosan bead, and (e) FESEM image of the chitosan shell showing organised channels. Reprinted with permission from [89]. Copyright 2015 American Chemical Society.	23
Fig. 2.4 (a) Schematic illustrating the preparation of GO/chitosan aerogel microspheres; (b) schematic diagram of GO/chitosan aerogel microsphere10 with honeycomb-cobweb and radially oriented microchannel structures. Reprinted with permission from [49]. Copyright 2017 American Chemical Society. (c) Proposed mechanism for preparation of mimGO sponge. Adapted with permission from [102]. Copyright 2017 American Chemical Society.	24
Fig. 2.5 Proposed mechanism for the interaction of GO/polyethyleneimine aerogel with Methyl Orange and Methylene Blue dyes at different pH. Reprinted with permission from [105]. Copyright 2017 Elsevier.	38
Fig. 2.6 Schematic illustration of the adsorption mechanism of Malachite Green onto rGO. (a) Electrostatic interaction; (b) π-π stacking and π-cation interaction. Reproduced with permission from [128]. Copyright 2017 Elsevier	39
Fig. 2.7 Schematic illustrating the interactions between the surface of rGO and (a) cationic Methylene Blue dye, and (b) anionic Acid Red 1 dye. Adapted with permission from [127]. Copyright 2014 Elsevier.	40
Fig. 2.8 Schematic diagram of interactions between Direct Red 80 and mimGO sponge. Reproduced with permission from [102]. Copyright 2017 American Chemical Society.	41
Fig. 2.9 Molecular structures of (a) Malachite Green, (b) Methyl Violet and (c) Brilliant Green dyes.	42
Fig. 2.10 (a) Removal of Methylene Blue (left) and Eosin Y (right) dyes from water by filtration; (b) outlet concentration of dyes as a function of permeation volume; (c) adsorption capacity of the column	44

as a function of permeation volume. Reprinted with permission from [6]. Copyright 2013 Royal Society of Chemistry. (d) Images of the filtration set-up and the solution before and after filtration. The inset shows UV-vis absorption spectrum of the dye solution before and after filtration. Adapted with permission from [129]. Copyright 2016 Elsevier.	
Fig. 2.11 Schematic diagram for column adsorption of Methylene Blue dye onto GO/chitin nanofibril foam, the insets represent the solution (a) before and (b) after adsorption; GO/chitin nanofibril foam (c) before and (d) after adsorption. Reprinted with permission from [92]. Copyright 2016 Elsevier.	45
Fig. 2.12 Schematic illustrating the mechanisms for (a) Cr (VI) adsorption onto GO/polyethyleneimine aerogel. Reproduced with permission from [148]. Copyright 2018 Taylor & Francis, and (b) Pb (II), Cu (II), Cr (VI), Methylene Blue, Rhodamine B, Methyl Orange and Eosin Y dyes adsorption onto GO/chitosan aerogel microsphere. Adapted with permission from [49]. Copyright 2017 American Chemical Society.	52
Fig. 2.13 Breakthrough curves for column adsorption of (a) Sb (III) and (b) Sb (V). Reprinted with permission from [157]. Copyright 2016 American Chemical Society.	55
Fig 3.1 Schematic diagram of fixed-bed column set-up.	70
Fig. 4.1 FESEM images of (a) GOCA and (b) chitosan.	78
Fig. 4.2 FTIR spectra of chitosan, GO and GOCA.	79
Fig. 4.3 Thermogravimetric curves of chitosan and GOCA.	81
Fig. 4.4 XRD pattern of chitosan and GOCA.	82
Fig. 4.5 Effect of adsorbent mass on the removal of (a) MY and (b) RB5 dyes.	83
Fig 4.6 Effect of shaking speed on the removal of (a) MY dye and (b) RB5 dye.	85
Fig. 4.7 Effect of initial pH on the removal of (a) MY and (b) RB5 dyes by GOCA, and (c) PZC plot of GOCA.	88
Fig. 4.8 Comparison of experimental kinetic data with the PFO, PSO and Elovich models for (a) MY and (b) RB5 dyes removal.	90
Fig. 4.9 Intraparticle diffusion plots for (a) MY and (b) RB5 dyes removal.	92
Fig. 4.10 Effect of initial concentration on (a) MY and (b) RB5 dyes removal at different temperatures.	95
Fig. 4.11 Comparison of experimental equilibrium data with the Langmuir and Freundlich models at temperatures of (a) 30 ^{o}C, (b) 40 ^{o}C, (c) 50 ^{o}C, (d) 60 ^{o}C and (e) 70 ^{o}C for MY dye removal.	98
Fig. 4.12 Comparison of experimental equilibrium data with the Langmuir and Freundlich models at temperatures of (a) 30 ^{o}C, (b) 40 ^{o}C, (c) 50 ^{o}C, (d) 60 ^{o}C and (e) 70 ^{o}C for RB5 dye removal.	99
Fig. 4.13 Surface plots of MY dye adsorption onto GOCA with qe response: Effects of (a) initial concentration and adsorbent mass, (b) contact time and adsorbent mass, (c) shaking speed and adsorbent	107

mass, (d) contact time and initial concentration, (e) shaking speed and initial concentration and (f) shaking speed and contact time.	
Fig. 4.14. Diagnostic plots: (a) Normal probability plot, (b) predicted versus actual adsorption capacity plot and (c) internally studentised residuals versus run number plot.	113
Fig. 4.15 Response surface plots for adsorption of RB5 dye onto GOCA: Effects of (a) adsorbent mass and initial concentration, (b) adsorbent mass and contact time, (c) adsorbent mass and temperature, (d) initial concentration and contact time, (e) initial concentration and temperature and (f) contact time and temperature.	116
Fig. 4.16 Regeneration study for (a) MY and (b) RB5 dyes adsorption onto GOCA.	118
Fig. 5.1 Breakthrough curves obtained at different bed heights for (a) MY and (b) RB5 adsorption onto GOCA.	124
Fig. 5.2 Breakthrough curves obtained at different inlet concentrations for (a) MY and (b) RB5 adsorption onto GOCA.	127
Fig. 5.3 Breakthrough curves obtained at different feed flowrates for (a) MY and (b) RB5 adsorption onto GOCA.	129
Fig. 5.4 Non-linear fitting of (a – c) MY and (d – f) RB5 dyes column data with the Thomas, Yoon-Nelson and Adams-Bohart models.	132
Fig 5.5 FTIR spectra of MY and RB5 dyes, and GOCA before and after adsorption.	136
Fig. 5.6 Molecular structures of (a) MY and (b) RB5 dyes.	137
Fig. 6.1 TGA profiles of xanthan and 3D GXT composite.	144
Fig. 6.2 FTIR spectra of xanthan, GO and 3D GXT composite.	146
Fig. 6.3 FESEM images of (a) xanthan and (b) 3D GXT composite, and (c) EDX result of 3D GXT composite.	148
Fig. 6.4 Effect of adsorbent mass on (a) Pb and (b) Cd removal by 3D GXT composite.	150
Fig. 6.5 Effect of shaking speed on the (a) Pb and (b) Cd removal by 3D GXT composite.	151
Fig. 6.6 Effect of initial pH on (a) Pb and (b) Cd removal by 3D GXT composite.	153
Fig. 6.7 Comparison of experimental kinetic data with the PFO, PSO and Elovich models for (a) Pb and (b) Cd adsorption onto 3D GXT.	155
Fig. 6.8 Intraparticle diffusion plots for (a) Pb and (b) Cd removal by 3D GXT composite.	158
Fig. 6.9 Comparison of experimental equilibrium data with the Langmuir and Freundlich models at temperatures of (a) 30 ^{o}C, (b) 40 ^{o}C, (c) 50 ^{o}C, (d) 60 ^{o}C and (e) 70 ^{o}C for Pb uptake by 3D GXT composite.	161
Fig. 6.10 Comparison of experimental equilibrium data with the Langmuir and Freundlich models at temperatures of (a) 30 ^{o}C, (b) 40 ^{o}C, (c) 50 ^{o}C, (d) 60 ^{o}C and (e) 70 ^{o}C for Cd uptake by 3D GXT composite.	162

Fig. 6.11 Diagnostic plots: (a) Internally studentised residual plot, (b) internally studentised residuals vs run number plot, (c) predicted vs actual q plot and (d) Box-Cox plot.	168 - 169
Fig. 6.12 3D surface response plots for Pb adsorption onto 3D GXT: Effects of (a) adsorbent mass and concentration, (b) adsorbent mass and shaking speed, (c) adsorbent mass and temperature, (d) concentration and shaking speed, (e) concentration and temperature, and (f) shaking speed and temperature.	173
Fig. 6.13 Diagnostic plots: (a) Normal % probability plot, (b) residuals vs predicted q plot, (c) residuals vs run plot and (d) predicted vs actual q plot, and (e) perturbation plot.	180 - 181
Fig. 6.14 Response surface plots: Effects of (a) adsorbent mass and concentration, (b) adsorbent mass and pH, (c) adsorbent mass and shaking speed, (d) concentration and pH, (e) concentration and shaking speed and (f) pH and shaking speed on Cd adsorption capacity	185
Fig. 6.15 Adsorption capacity of 3D GXT composite versus regeneration cycle for (a) Pb and (b) Cd.	187
Fig. 7.1 Breakthrough curves obtained at different bed heights for (a) Pb and (b) Cd adsorption onto 3D GTX composite.	193
Fig. 7.2 Breakthrough curves obtained at different inlet concentrations for (a) Pb and (b) Cd adsorption onto 3D GTX composite.	196
Fig. 7.3 Breakthrough curves obtained at different feed flowrates for (a) Pb and (b) Cd adsorption onto 3D GTX composite.	198
Fig 7.4 (a) PZC plot of 3D GXT composite and (b) FTIR spectra of 3D GXT composite before and after Pb and Cd adsorption.	203

List of Tables

	Page no.
Table 1.1 Advantages and disadvantages of different synthesis methods for 3D graphene structures.	5 - 6
Table 2.1 Types of additives used in ice-templating and their respective influences on microstructure evolution.	14
Table 2.2 Physical properties of ice-templated 3D graphene-based materials.	27 - 28
Table 2.3 Adsorption properties and mechanisms of 3D graphene-based materials for dyes.	31 - 34
Table 2.4 Adsorption properties and mechanisms of 3D graphene-based materials for heavy metals.	48 - 50
Table 3.1 Experimental conditions for MY and RB5 dyes adsorption onto GOCA.	62
Table 3.2 Experimental conditions for Pb and Cd adsorption onto 3D GXT.	64
Table 3.3 Expressions for adsorption equilibrium and kinetic models, and error functions.	66
Table 4.1 Equilibrium, kinetic and thermodynamic parameters for MY dye adsorption onto GOCA.	96
Table 4.2 Equilibrium, kinetic and thermodynamic parameters for RB5 dye adsorption onto GOCA.	97
Table 4.3 CCD experimental design matrix for MY dye adsorption onto GOCA.	103
Table 4.4 ANOVA results of the quadratic model for MY dye adsorption onto GOCA.	104
Table 4.5 RSM design matrix with measured and predicted data, and residual errors for RB5 adsorption system.	110
Table 4.6 ANOVA results of the quadratic function for RB5 dye adsorption onto GOCA.	111
Table 4.7 Comparison of GOCA adsorption capacity with literature data.	120
Table 5.1 Data obtained for fixed-bed column adsorption of MY and RB5 dyes.	125
Table 5.2 Parameters of the Thomas, Yoon-Nelson and Adams-Bohart models for MY and RB5 dyes adsorption in GOCA fixed-bed column.	131
Table 5.3 Comparison of bed adsorption capacities for MY and RB5 dyes removal in fixed-bed column system.	138
Table 6.1 Equilibrium, kinetic and thermodynamic parameters for Pb adsorption onto 3D GXT composite.	156
Table 6.2 Equilibrium, kinetic and thermodynamic parameters for Cd adsorption onto 3D GXT composite.	157
Table 6.3 RSM-CCD experimental design matrix with measured and predicted responses, and residue for Pb adsorption system.	165

Table 6.4 ANOVA results on the optimisation of Pb adsorption onto 3D GXT composite.	170
Table 6.5 CCD design matrix for Cd adsorption onto 3D GXT composite with measured and predicted q, and residual error.	176
Table 6.6 ANOVA results for quadratic equation describing Cd adsorption onto 3D GXT composite.	177
Table 6.7 Comparison of Pb and Cd adsorption capacity of 3D GXT composite with other reported values.	188
Table 7.1 Column data for 3D GTX fixed-bed column adsorption of Pb and Cd.	194
Table 7.2 Parameters of the Thomas, Yoon-Nelson and Adams-Bohart models for Pb and Cd adsorption onto 3D GTX fixed-bed column.	201
Table 7.3 Chemical functional groups in 3D GXT composite before and, after Pb and Cd adsorption.	204
Table 7.4 Comparison of 3D GTX fixed-bed adsorption capacities for Pb and Cd with other fixed-beds.	205

Nomenclatures

Abbreviation	Description
2D	Two-dimensional
3D	Three-dimensional
3D GXT	Three-dimensional graphene oxide/xanthan/TiO_2
AAS	Atomic absorption spectroscope
ANOVA	Analysis of variance
APAM	Anionic polyacrylamide
ARE	Average relative error
CCD	Central composite design
CVD	Chemical vapour deposition
DI	Deionised
EDTA	Ethylenediaminetetraacetic acid
ERRSQ	Sum of the squares of errors
F-test	Fisher's test
FESEM	Field emission scanning electron microscope
FTIR	Fourier transform infrared spectroscopy
GO	Graphene oxide
GOCA	Graphene oxide/chitosan aerogel
ISISA	Ice-segregation-induced self-assembly
MPSD	Marquardt's percent standard deviation
MY	Metanil yellow
p-value	Probability value
PAA	Polyacrylic acid

PEG	Polyethylene glycol
PFO	Pseudo-first-order
PSO	Pseudo-second-order
PVA	Polyvinyl alcohol
PZC	Point of zero charge
RB5	Reactive black 5
rGO	Reduced graphene oxide
RSM	Response surface methodology
RMSE	Root mean square error
S_{RE}	Standard deviation of relative errors
SNE	Sum of normalised errors
TBA	Tert-butyl alcohol
TGA	Thermogravimetric analysis
TTIP	Titanium isopropoxide
XRD	X-ray diffraction

Symbol	**Description and Unit**
α	Elovich initial adsorption rate (mg/g.min)
β	Elovich constant (g/mg)
β_0	Intercept term
β_i	Linear term
β_{ii}	Quadratic term
β_{ij}	Interaction term

ε	Random error
τ	Time to reach 50% breakthrough (min)
v	Linear velocity (cm/min)
X^2	Chi-square
ΔG	Gibbs free energy change (kJ/mol)
ΔH	Enthalpy change (kJ/mol)
ΔS	Entropy change (kJ/mol.K)
A	Area under the breakthrough curve
C	Intercept of intraparticle diffusion plot (mg/g)
C_o	Initial concentration (mg/L)
C_e	Equilibrium concentration (mg/L)
C_{max}	Maximum initial concentration (mg/L)
k	Number of factors
k_1	PFO rate constant (1/min)
k_2	PSO rate constant (g/mg.min)
k_{AB}	Adams-bohart rate constant (L/mg.min)
K_c	Equilibrium constant
K_f	Freundlich isotherm constant ((mg/g)(L/mg)$^{1/n}$)
K_L	Langmuir isotherm constant (L/mg)
k_p	Intraparticle diffusion rate constant (mg/g.min$^{0.5}$)
k_{TH}	Thomas's constant (mL/min.mg)
k_{YN}	Yoon-Nelson reaction constant (1/min)
m_{ads}	Total amount of adsorbate adsorbed (mg)
n	Freundlich exponent

N_o	Volumetric adsorption capacity (mg/L)
Q	Flow rate (mL/min)
q	Adsorption capacity (mg/g)
q_m	Langmuir monolayer adsorption capacity (mg/g)
q_{exp}	Measured adsorption capacity (mg/g)
q_o	Theoretical adsorption capacity (mg/g)
q_{pred}	Predicted adsorption capacity (mg/g)
q_t	Adsorption capacity at time, t (mg/g)
R	Removal efficiency (%)
R_L	Separation factor
R^2	Correlation coefficient
S	Shaking speed (rpm)
t	Time (min)
t_b	Breakthrough time (min)
t_e	Exhaustion time (min)
T	Temperature (K)
V	Volume of solution (L)
V_t	Volume of effluent treated (mL)
W	Adsorbent mass (g)
X_i, X_j	Input factors
Y	Predicted response
Z	Bed height (cm)

Chapter 1. Introduction

1.1 Background

The rapid growth of industrial and agricultural activities has resulted in considerable amounts of pollutants being discharged into the environment, particularly dyes and heavy metals, causing major concern worldwide. Dyes are coloured chemical compounds which can impart mutagenic and carcinogenic effects on all living forms, whereas heavy metals are metallic chemical elements which can cause detrimental health effects on humans and other organisms [1]. For instance, the potential health hazards of metanil yellow (MY) and reactive black 5 (RB5) dyes include carcinogenicity and allergic dermatitis [2, 3]. Furthermore, exposure to lead (Pb) and cadmium (Cd) was reported to induce miscarriage and birth defects, respectively [4, 5]. The discharge limits for Pb and Cd imposed by the Malaysia Department of Environment are 0.10 and 0.01 mg/mL, respectively [4]. For these reasons, there is an urgent need to mitigate the discharge of such dangerous substances into the environment. Various remediation technologies have been developed and these include adsorption [6], chemical precipitation [7], ion exchange [8], coagulation [9], flotation [10] and membrane filtration [11]. Most of these methods suffer some drawbacks such as high operational cost, complicated and inefficient process, restricting their extensive applications. Adsorption is one of the most promising techniques as it is relatively low cost, easy to operate and has wide adaptability [6, 12, 13]. Till now, a variety of adsorbents such as activated carbons [14-16], zeolites [17, 18], polymeric materials [19, 20], agricultural wastes [21] and biological materials [22, 23] have been developed and employed to remove dyes and heavy metals. In addition to conventional carbon materials, some new

carbon nanomaterials such as graphene [24, 25], carbon nanotube [26-28] and carbon nanofiber [29] have been studied in recent years due to their high specific surface area and adsorption capabilities [6, 25].

In particular, graphene is widely investigated as the next generation of adsorbent for decontamination of water owing to its unique physicochemical properties such as large specific surface area (2630 m^2/g), mechanical flexibility, as well as thermal and chemical stabilities [25, 30]. The past research work demonstrated that adsorbate attachment occurred mostly at the sp^2 hybridised carbon atoms of pristine graphene sheets through van der Waals force. Hence, the application of graphene as a universal adsorbent is limited by this factor [6]. Graphene oxide (GO), a highly oxidised form of graphene, has plenty of oxygeneous groups such as epoxy and hydroxyl groups on the basal plane, and carboxylic group at the edge of graphene sheet [31]. The chemically reactive oxygen functionalities rendered GO as a useful adsorbent by endowing it with high affinity towards various pollutants such as dyes, heavy metals, oil and organic solvents [32]. Nevertheless, GO has several limitations which hinder its use in large scale wastewater treatment. The strong inter-planar interaction causes graphene to agglomerate and restack, consequently reducing greatly its surface area [6, 33, 34]. Moreover, the utilisation of nanosorbent (adsorbent in nanometer size) suffers from retrieving difficulties, additional cost for disposal of exhausted nanosorbent and secondary water pollution arising from incomplete recovery of the nanosorbent [35].

In order to facilitate separation of nanosorbent from the liquid phase after adsorption, intensive research work has been carried out recently to incorporate magnetic nanoparticles into graphene or GO as the paramagnetism property allows

the graphene material to be withdrawn under an external magnetic field [36-38]. However, many constraints still remain unresolved, for instance, the use of expensive and toxic reagents, complicated fabrication process, low removal efficiency and incomplete solid-liquid separation [39]. In addition, the distribution of magnetic nanoparticles is usually not uniform and they are easily detached from the surface of adsorbent. The pores of the adsorbent can also be blocked easily by the magnetic nanoparticles which substantially impede the application of magnetised graphene as an effective adsorbent [39].

Assembly of GO sheets into highly porous 3D hierarchical architectures is perceived as one of the most promising approaches to overcome the aforementioned issues, particularly, easy retrieval of the 3D assembled graphene after adsorption and elimination of environmental threat caused by graphene discharge. It is worth noting that the 3D assembled graphene offers not only new collective properties, but also retains the intrinsic properties of graphene which further enhances the practical application of graphene [32, 35]. Furthermore, the 3D assembled graphene may exhibit an architecture with multi-level pores, such as micro-, meso- and macropores. The micro- and mesoporosity render the graphene structure with high surface area, while the macroporosity offers easy access to the sorption surface [40]. Moreover, the 3D network prevents the restacking and agglomeration of graphene, thus facilitating mass transfer and eventually improving the adsorption performance [32]. The 3D assembled graphene can also be decorated with different materials such as polymers, organic molecules and inorganic/metal nanoparticles to impart new functional properties to the final adsorbent [41].

The synthesis of 3D graphene structures using GO as the precursor can be classified into solution based and chemical vapour deposition (CVD) techniques [4, 40-43]. The solution based approach can be further divided into template-directed and template-free synthesis. Among the template-directed methods, ice-templating is relatively straightforward and able to produce hierarchically porous 3D graphene structures. The template-free methods such as hydrothermal reduction, chemical reduction and cross-linking induced-assemblies are commonly used owing to their simplicity and effectiveness in preparing 3D graphene materials. Despite the ability of CVD technique in producing 3D graphene structures with superior physicochemical properties, the difficulty in scaling up and economic infeasibility have made it less favourable. The advantages and disadvantages of different synthesis techniques are summarised in **Table 1.1**. In summary, ice-templating is a facile approach for preparing high quality 3D graphene materials.

Zamani and Tabrizi [44] reported that the adsorption capacity of GO aerogel (416.67 mg/g) prepared by ice-templating for Methylene Blue dye is comparable to other nanomaterials such as carbon nanotube (188.68 mg/g), GO (243.90 mg/g) [45] and highly oxidised GO (598.80 mg/g) [46]. Furthermore, the versatility of the ice-templating process allowed the 3D structure to be decorated easily with a variety of materials which introduce additional functional groups and consolidate the resulting materials [47, 48]. Furthermore, the ice-templating process can be integrated with other fabrication techniques such as electro-spraying to create a 3D graphene assembly with inimitable microstructures which are beneficial for adsorption application [49].

Table 1.1 Advantages and disadvantages of different synthesis methods for 3D graphene structures.

Synthesis method	Advantages	Disadvantages	References
Solution based, template-directed			
Colloidal-sphere based	• Better control over pore structure • Facile and scalable process	• Required to remove template by acid etching/burning	[41]
Ice-templating	• Green and sustainable process (water ice crystals as porogen) • Straight forward method and scalable • Control over pore structure • Cost effective • High purity product	• Less uniform morphology	[4, 41, 49]
Hydrothermal template	• Facile and scalable process • Versatile cost (expensive with the use of metal template and *vice versa* with the use of polymer template)	• Required to remove template by acid etching/burning • Difficult to control final morphology • Requires expensive reactor that can withstand high temperature and pressure	[4, 41]
Carbonisation of polymer frameworks	• Facile and scalable process • High quality product	• High temperature operation • Cost ineffective	[41]
Solution based, template-free			
Hydrothermal reduction induced assembly	• Allows simultaneous elemental doping/decoration • No post thermal treatment for reduction of GO • Facile (one-pot) and scalable process	• Requires expensive reactor that can withstand high temperature and pressure	[41]

	• Control over the morphology		
Chemical reduction induced assembly	• Facile and scalable process • Low temperature process	• Use of strong reducing agents (such as hydrazine) • Use of high pressure equipment • Products may contain residual chemical	[42]
Cross-linking induced assembly	• Imparts new functionalities to the final product • Process versatility (availability of various efficient cross-linkers)	• Cross linker may engulf the GO and hinder accessibility to the surface of GO	[4, 41, 47]
Filtration assisted assembly	• Facile process • Cost effectiveness • Homogeneous film with control over thickness	• Post treatment/expensive ionic liquids needed to prevent the restacking of graphene sheets	[41]
Centrifugal vacuum evaporation	• No substrate requirement and no further drying steps • Facile and green process	• Difficult to scale up • Energy intensive process (high speed centrifugation is required)	[41, 50]
Sugar blowing	• Facile process • Product with high chemical and mechanical stabilities	• High temperature operation • Cost ineffective	[41, 50]
Chemical vapour deposition (CVD)	• High quality product	• High temperature operation • Cost ineffective • Difficult to scale up • Sacrificial template requirement	[41, 42]

This new class of adsorbing 3D graphene materials have demonstrated outstanding adsorption capabilities for a variety of pollutants such as gas pollutant [51], dyes [52], heavy metals [53] and oil [54]. Hence, the main focus of the research was on development of 3D graphene structures by ice-templating method for adsorptive removal of dyes and heavy metals. The positive outcomes of this research can be applied in the remediation of water pollution to safeguard the environment and human health.

1.2 Problem statement

The rapid industrialisation has led to the increase in disposal of dyes and heavy metals into the aquatic environment causing serious environmental and health problems. The removal of these pollutants by adsorption using graphene oxide (GO) has potrayed promising results, however, the application of GO in wastewater remediation is restricted by several limitations. Firstly, the inherent inter-planar interactions resulted in the restacking of GO which enormously minimise the surface area available for adsorption. Besides, the collection of GO from the liquid phase after adsorption requires the use of energy intensive separators, such as centrifugation and membrane separation, which complicates the post-adsorption process. The partial recovery of GO from water may also cause undesirable secondary water pollution. It is believed that these restraints could be rectified by assembling GO into porous 3D hierarchical architecture which offers several advantages. The assembled 3D GO manifests porous structure and the 3D network prevents the restacking of GO, thus promoting the diffusion process and enhanced the adsorption performance. Moreover, the 3D GO could be decorated with a

variety of functional materials. Therefore, this research focused on the synthesis of new 3D GO composites for the adsorptive removal of dyes and heavy metals.

1.3 Aim and objectives

The ultimate aim of this research was to develop novel 3D graphene architectures for the adsorption of dyes and heavy metals. The adsorption performance of the as-prepared graphene structures was evaluated via batch and continuous adsorption modes.

The specific objectives for the research project are:

- To configure GO into novel 3D architectures which are structurally stable in the aqueous environment and allow efficient solid-liquid separation.
- To establish the physicochemical properties of the prepared 3D graphene structures by analyses: X-ray diffraction, field emission scanning electron microscope, Fourier transform infrared and thermogravimetric analysis.
- To determine the effects of batch adsorption parameters such as dosage, shaking speed, initial pH, initial concentration, contact time and temperature on the removal of dyes (MY and RB5 dyes) and heavy metals (Pb and Cd).
- To evaluate the equilibrium, kinetic and mechanism of batch adsorption of dyes (MY and RB5 dyes) and heavy metals (Pb and Cd) onto the 3D graphene structures.
- To determine the continuous adsorption performance of the 3D graphene structures by fixed-bed column studies.
- To investigate the regeneration ability of the 3D graphene architectures by chemical elution technique.

Chapter 2. Literature review

Three dimensional (3D) graphene derived composites can be presented in several forms such as aerogel, monolith, hydrogel, sponge, bead and foam depending on the synthesis method. There are several solution based methods for preparing 3D graphene structures such as hydrothermal reduction, chemical reduction, cross-linking and ice-templating. Owing to the versatility of the ice-templating technique to form porous 3D graphene structures with certain properties, this review focuses on its basic principles, critical process parameters and properties of resulting materials. The literature study also covers the application of 3D graphene materials as effective adsorbents to remove dyes and heavy metals. The adsorption mechanisms for the uptake of both adsorbate groups by the 3D graphene adsorbents were also discussed along with their regeneration efficiency.

2.1 Ice-templating

2.1.1 Basics of ice-templating

The ice-templating process is associated with different terms which include freeze-casting [55], ice-segregation-induced self-assembly (ISISA) [41], unidirectional freeze-drying [53] or simply just freeze-drying [56]. The basic principle of the process involves segregation-induced templating of a second phase by a solidifying solvent [57]. Since the process is material-agnostic in nature, the second phase can be literally any kind of materials, from ceramic to metal, polymer, carbon nanomaterial such as graphene, GO or carbon nanotube, which is soluble in the solvent or forms a stable dispersion, and is expelled from the growing crystals of the solvent [58]. The solidified solvent is eliminated by ice sublimation at very low

temperature and vacuum, producing a porous material where the pores are replica of the solidified solvent structure. The resulting product can be used as derived or further sintered to consolidate and densify the material, depending on its final application [59]. The main steps of the ice-templating process are represented in **Fig. 2.1**.

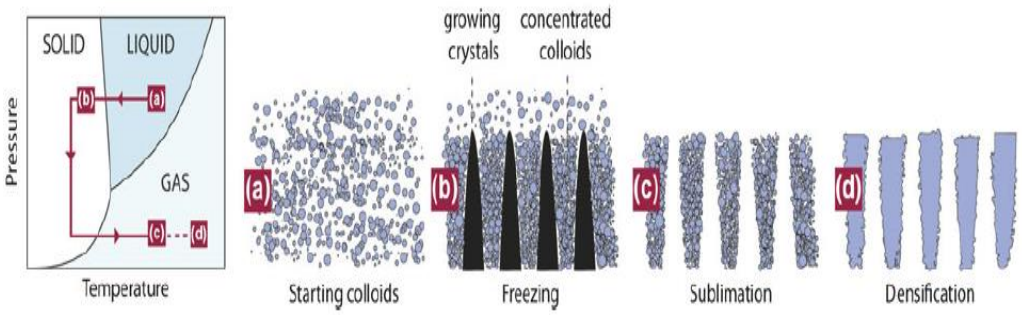


Fig. 2.1 Schematic representation of the ice-templating process. Reprinted with permission from [59]. Copyright 2013 Materials Research Society.

Generally, the process depends on the low solubility of the second phase in the solidifying solvent which in turn favours the segregation of particles during solidification. As a consequence, the choice of solvent is of great importance as it influences not only the solubility of the solute, but also the solidification condition, crystal morphology, sublimation condition and eventually the final structure of product [60]. There are three commonly used solvents in ice-templating including water, camphene and tert-butyl alcohol. Among these solvents, water is the most desirable dispersing medium for the ice-templating method as it is environmentally friendly, abundantly available, low cost and non-toxic. However, the use of water is less popular in ice-templating of polymers due to their poor solubility in water.

Camphene, the second most used solvent, has a freezing point above room temperature (44 – 48 ^{o}C). This peculiar attribute allows camphene to sublime at room temperature and atmospheric pressure, eliminating the need of a freeze-dryer or specific equipment to achieve low temperature. Furthermore, evaporation/sublimation is another distinct feature of the camphene system since it has a vapour pressure of 2 kPa at 55 ^{o}C. Typically, the evaporation and sublimation locations can affect the density and porosity of the prepared material. The upper layer camphene exposed to ambient condition can evaporate before being frozen, causing a great impact on the porous structure of the final product [61]. Hence, the handling of the camphene system is more challenging and complicated compared to the water system. In addition, camphene is relatively expensive (RM473/kg) and highly flammable, restricting its practical application [57]. Tert-butyl alcohol (TBA) is a co-solvent with water and is usually employed in the field of pharmaceutical, specifically in freeze-drying of drugs [60]. Likewise, TBA is expensive (RM 1420/kg), highly flammable and harmful [57], and hence, it is less popular.

From the standpoint of green synthesis and sustainable technology, water is the most suitable solvent for ice-templating method. Consequently, the following section covers the ice-templating process using water as the dispersing medium.

2.1.2 Critical process parameters in ice-templating

There are a number of critical factors which influence the microstructure, morphology and properties of the ice-templated materials, in particular, freezing mode, additive effect, solid loading and freezing conditions (freezing temperature,

rate and time). The studies on these parameters enabled prediction of the behaviour of porous microstructures at different conditions. Albeit the effects of the processing parameters were mainly investigated for materials such as metals and ceramics, the resulting trends could be applied on graphene based systems since the ice-templating process is material agnostic.

2.1.2.1 Freezing mode

There are two different freezing modes, namely homogeneous and directional freezing, and each has significant effect on the formation of pore morphologies. For homogeneous freezing, the uniform distribution of temperature throughout the sample hinders the anisotropic growth of ice crystals. Hence, homogeneous (cellular) microstructures with interconnected pores can be shaped after freeze-drying [61]. The freezing step involves placing the aqueous suspension/gel in a freezer or dipping it in a liquid nitrogen bath (**Fig. 2.2(a)**). Sun et al. [62] fabricated a GO/CNT ultra-flyweight aerogel using the homogeneous freeze-drying method which manifested microstructures with high uniformity, as presented in **Fig. 2.2(c)**. Conversely, for unidirectional freezing, the existence of temperature gradient or expulsion of particles in a certain direction favours the anisotropy growth of ice crystals which eventually results in well-defined directional (lamellar) microstructures [61]. Typically, only the bottom part of the suspension/gel is in contact with the cold finger in a directional freezing process (**Fig. 2.2(b)**). Mi et al. [63] reported the synthesis of a GO aerogel through unidirectional freeze-drying which demonstrated an ordered porous structure with unidirectional channel (**Fig. 2.2(d)**).

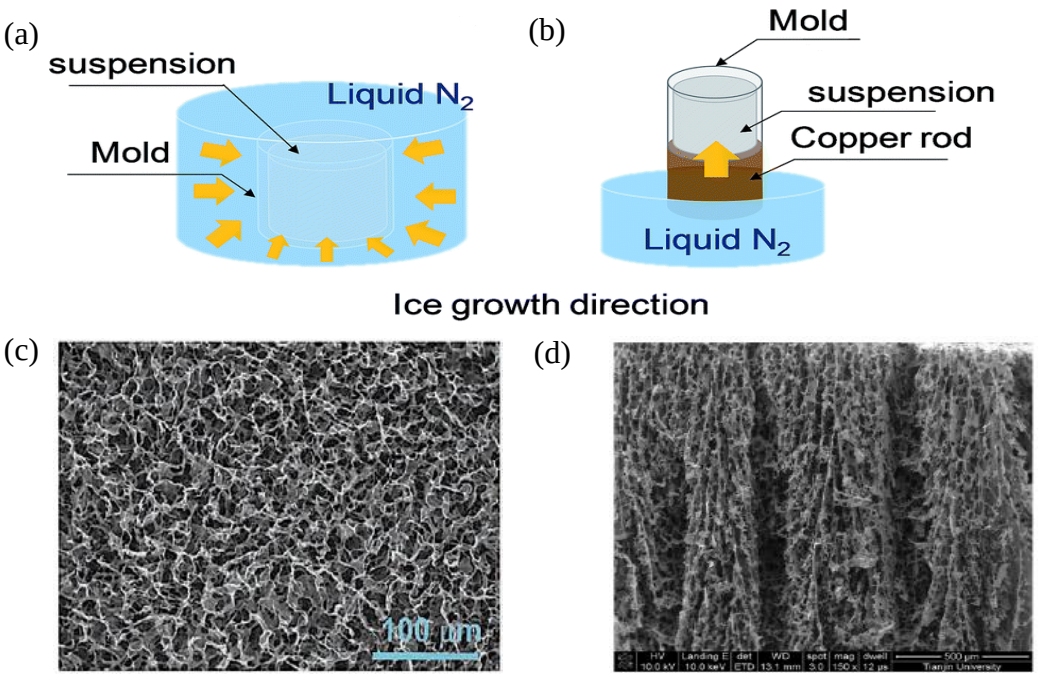


Fig. 2.2 (a) Homogeneous freezing; (b) Unidirectional freezing. Reproduced with permission from [64]. Copyright 2017 Royal Society of Chemistry. (c) FESEM image of GO/CNT aerogel showing continuous and uniform macropores. Reprinted with permission from [62]. Copyright 2013 WILEY-VCH Verlag GmbH & Co. KGaA, Weinheim. (d) FESEM image of GO aerogel demonstrating unidirectional architecture. Adapted with permission from [63]. Copyright 2012 Elsevier.

2.1.2.2 Additive effect

The additives are usually incorporated into the system to alter the freezing point, suspension viscosity, ice expansion effect, particle expulsion or particle hindrance on the ice crystal growth and eventually microstructure. Moreover, some additives are able to form bonds with solvent molecule or induce a gelation effect [61]. Many additives have been tested such as glycerol, gelatin, polyvinyl alcohol (PVA), polyethylene glycol (PEG), sodium chloride, sucrose, clay and dioxane, and their effects on the microstructure evolution are summarised in **Table 2.1**.

Table 2.1 Types of additives used in ice-templating and their respective influences on microstructure evolution.

Additives	Effects	References
Glycerol	Improves microstructure homogeneity and reduces ice crystal size and hence pore size	[65, 66]
Gelatin	Improves microstructure uniformity and suppresses anisotropy growth of ice crystal	[67, 68]
Poly(vinyl alcohol)	Increases the suspension viscosity and reduces the ice crystal size and hence pore size	[69]
Polyethylene glycol	Promotes the growth of pore	[70]
Sodium chloride	Alters the morphology of ice crystal	[71]
Sucrose	Suppresses the dendritic growth of ice crystal	[71]
Silica and clay	Improves microstructure homogeneity and increases pore size	[72]
Dioxane	Supresses directional ice crystal growth and reduces the pore size	[73]

Overall, the introduction of additives to the ice-templating system influences the pore structure by changing the ice solidification behaviour (modifying the freezing temperature and ice expansion), limiting the diffusion of water molecules and particle expulsion. Albeit only a few additives were reviewed, other additives capable of refining the microstructure with similar behaviour can also be introduced to control the final pore structure [61].

2.1.2.3 Solid loading

Solid loading is the concentration of particles in the initial suspension which affects the freezing stage and features of the ice-templated product. In addition to the

additives being added into the suspension, solid loading will also influence the viscosity of the suspension. In the ice-templating process, the suspension viscosity must be regulated appropriately as it governs the expulsion and encapsulation of particles by the ice crystals. In general, an increase in viscosity will favour the encapsulation of particles as this will enhance the drag force that acts on the particles. Furthermore, the solid loading of the suspension partially controls the freezing point and thus influences the first freezing stage. Nevertheless, the steady-state regime is not governed by the freezing point [60].

Owing to the conservation of mass, the porosity content is inversely related to the solid loading of suspension. A suspension with a high load of solid particles which suppress the volume of water available for the ice crystal growth, produces ice-templated material with a higher density and lower porosity. Moreover, the lower water content reduces the ice expansion effect and thus, enhances the density of the resulting materials [61]. Contrasting results are expected for a suspension with low solid loading. Furthermore, a suspension with low solid loading renders the final material with varying porosity and density as it is less stable and thus, segregation phenomenon occurs in the second stage [57].

The suspension solid loading can also impact the homogeneity of the final microstructure. A study on alumina system by Sofie and Dogan [65] showed that spherical pores were formed at a low solid loading as a result of effective particle expulsion while at a very high solid loading, the formation of pores was inhibited as the rejection of solid particles was hindered by the crowded particles. Despite the microstructure homogeneity being affected by solid loading, the basic

mechanisms of the microstructure evolution are still dependent on the particle rejection and hindrance effect [61].

The versatility of the ice-templating process allows the fabrication of materials with a wide range of porosity content, from highly dense (0 % porosity) to ultralight materials, normally known as aerogel (99.9 % porosity). According to Deville [60], the solid loading used in the ice-templating studies typically ranged from 10 – 30 vol.% as porous materials for practical applications, such as environmental pollution control, energy storage, biomedical applications and catalyst support, should have adequate strength and structure stability. Within this solid loading range, materials with porosity content ranging from 40 to 70 % were produced.

2.1.2.4 Freezing conditions

Solidification is the most critical stage in defining the final characteristics of the synthesised material as the pores are the duplicates of ice crystals. The freezing temperature, rate and time are pivotal elements influencing the ice nucleation and crystal growth rate, and eventually the morphology and arrangement of the pore structures. Despite different systems may react differently to these factors, the overall trend in the microstructure evolution is shared by most materials [60, 61].

The freezing temperature dictates the relative dominance of the ice nucleation and crystal growth rate. Typically, the freezing temperatures for aqueous system range from -18 to -196 ^{o}C. Under high supercooling (very low temperature) condition, the nucleation rate is much faster than the crystal growth rate and this favours the ice nucleation rather than the ice crystal growth. The low temperature encourages the formation of many miniature ice crystals. In addition, small pores

are evenly distributed within the porous architecture [61]. Contrarily, the ice crystal growth dominates the freezing process when low supercooling is applied. This will yield final materials with larger pores as a small number of large ice crystal is formed during solidification [61]. Liu et al. [74] investigated the effect of freezing temperature (-40 and -10 ^{o}C) on the morphology of xanthan-GO hybrid aerogel. It was reported that an ordered hierarchical thin sheet structure was obtained for the hybrid aerogel frozen at -40 ^{o}C while the thickness of the sheets was increased when the freezing temperature was raised to -10 ^{o}C. Moreover, materials with higher porosity were fabricated at lower solidifying temperature due to inadequate rearrangement of the particles under high supercooling condition [75].

The freezing rate is another governing factor in the final morphology of the 3D porous structure. At a high freezing rate, the ice nucleation rate is higher than the crystal growth rate thereby favouring fine pore formation. Besides, the disperse state of suspension is better maintained at a higher freezing rate as little time is available for the particles to redistribute. Contrasting results are expected at a low freezing rate since more time is available for the particles to redistribute and hence, results in a denser particle packing. For instance, Zhang et al. [76] investigated the effect of freezing rate on the pore morphology of graphene sponge assembled with soap, by employing liquid nitrogen and refrigerator as rapid and slow freezing medium, respectively. The graphene sponge frozen in liquid nitrogen had ordered quasi-round pores with slot pores on the wall while that frozen in the refrigerator manifested disordered pores without any pores on the wall. Furthermore, the heat transfer within the sample has a significant influence on the freezing rate [77]. When the temperature gradient is small, the heat transfer efficiency is low and

diffusion of water molecules and growth of ice crystals are greatly hampered, thus resulting in pores with an oval shape. Meanwhile, a high heat transfer efficiency allows the continuous growth of ice crystals which may result in an interconnected or dendritic porous architecture.

The growth of ice crystal is also dependent on the freezing time albeit to a lesser extent. When a sample is kept in an environment with a constant freezing temperature, the ice crystals grow continuously and hence, favour the development of larger crystals. The particles expelled by the solidifying crystals are shaped into a wall while the ice crystals will grow into a dendritic structure. As a consequence, columnar and lamellar microstructures are more likely formed after a long freezing time [61].

In summary, samples with homogeneous microstructures can be realised by freezing for a shorter time and at a low temperature gradient. Besides, the sample can be tailored to possess numerous fine pores by employing a low freezing temperature but a high freezing rate.. Thus, the evolution of porous microstructure can be anticipated with all the factors regulated appropriately.

2.1.3 Ice-templated 3D graphene materials

As aforementioned, GO is an oxidised form of graphene with numerous reactive oxygen functionalities which render it a high solubility and dispersibility in water to form a stable GO suspension. As a result, GO foam can be easily fabricated by freezing the bare GO suspension, followed by freeze-drying. A number of studies have successfully developed pure GO foam/aerogel by ice-templating method which was subsequently applied in air purification, oil spill clean-up, and heavy

metal and dye contaminated water remediation [44, 51, 63, 78-81]. Despite being assembled into a 3D structure, the GO foam can be re-suspended in water effortlessly as its intrinsic properties, in particular, its high solubility in water, is not altered during the assembly process. As a result, the application of GO foam in water remediation is not realisable as the problem associated with retrieving the adsorbent after adsorption still remains.

Various approaches have been investigated to resolve the above-mentioned issue and these include post-thermal reduction to produce reduced GO (rGO) foam which is highly hydrophobic [80] and incorporation of additives/modifiers into the GO suspension to strengthen its structural stability in aqueous system, which may also impart new functionalities to the as-synthesised foam [47, 53, 82]. The latter approach is preferred as the resulting foam has more oxygeneous functional groups compared to rGO foam, where these groups can serve as the active sites for binding pollutants. Additionally, the rGO foam is usually employed in the removal of oil and organic solvent due to its excellent hydrophobic property, where the hydrophobic surface plays a major role in the adsorption mechanism. Hence, a number of rGO foams have been successfully produced through ice-templating method, followed by thermal treatment for adsorption of oil and organic pollutants [76, 80, 83, 84].

As mentioned earlier, the use of pure GO foam in water decontamination is not feasible and to resolve this matter, it is necessary to add chemical additives into the GO suspension during the assembly of 3D graphene adsorbent. The addition of chemical additives could assist in the formation of stable foam which did not disintegrate easily in the aqueous system. A number of chemical additives were

examined and these include cellulose nanofibril [85], chitosan [48, 49, 53, 86-90], sodium alginate [52, 82, 91], chitin/chitosan nanofibril [92], polyvinyl alcohol (PVA) [47, 93], microcrystalline cellulose [94], xanthan [74, 95], polyacrylic acid (PAA) [96], carboxymethyl cellulose [97, 98], anionic polyacrylamide (APAM) [99] and carbon nanotube [62].

It is worth noting that several studies have been accomplished to fabricate 3D GO/chitosan aerogel for environmental pollution remediation. Chitosan is a popular chemical additive for assembly of 3D graphene architecture as it is readily available, biocompatible, biodegradable and non-toxic. Furthermore, it has abundant hydroxyl groups and reactive amino groups which can be effective chelating groups for heavy metals [100, 101].

Zhang et al. [53] successfully developed a chitosan-gelatin/GO monolith cross-linked with glutaraldehyde through unidirectional freeze-drying method. The monolith was employed in treating water contaminated with Cu (II) and Pb (II). Their findings suggested that the unidirectional porous structure of the monolith facilitated diffusion of the heavy metals to the sorption sites rendering them high adsorption capacities (approximately 100 mg/g). The authors also revealed that the addition of ethylenediaminetetraacetic acid (EDTA) to Cu (II) solution enhanced the adsorption capability of the adsorbent even at low pH as the EDTA formed complexes with Cu (II). The complexes were anionic and easily removed by the adsorbent through electrostatic interaction.

A spongy chitosan/GO monolith with GO content less than 1 wt.% was synthesised by Wang et al. [90] through cross-linking with methyl aldehyde. The adsorption ability of the monolith was examined for both anionic and cationic

pollutants, which were modelled by Methyl Orange dye and Cu (II), respectively. This composite monolith manifested high adsorption capacities for the dye (567.07 mg/g) and heavy metal (53.69 mg/g). The formation mechanism of the composite monolith was elucidated by Fourier transform infrared (FTIR) analysis and substantiated by X-ray photoelectron spectroscopy (XPS). The results indicated that hydrogen bonding and reaction between the amino groups of chitosan and the epoxy groups of GO were the plausible interactions.

Within a year, the same research group, Wang et al. [48], reported the synthesis of chitosan/GO aerogel with smaller dimension and minor modification in the preparation steps. This composite aerogel demonstrated enhanced adsorption capacity for Methyl Orange dye (686.89 mg/g) and a comparatively high adsorption capacity for Amido Black 10B dye (573.47 mg/g). The improvement in the removal of Methyl Orange dye could be related to the relatively high water absorption ability (5848 – 8917 %) of this aerogel [90]. The high water absorption ability assisted the pollutant molecules to reach the adsorbent surface.

It is unambiguous that the 3D GO/chitosan adsorbents possess excellent adsorption capabilities for different pollutants, however they are associated with long equilibrium time. For instance, the aerogel synthesised by Wang et al. [48] attained adsorption equilibrium only after 60 h. A long equilibrium time is usually inevitable due to the tortuous internal diffusion path within the disorganised network of 3D GO adsorbents. In order to accelerate the adsorption process, Ouyang et al. [89] constructed millimetre-sized core-shell structured graphene-chitosan beads through a two-step freeze-drying process for adsorption of Methyl Orange dye. The GO beads, formed initially by injecting GO solution into liquid

nitrogen, were placed in chitosan solution and then freeze-dried to produce the composite beads, as shown in **Fig. 2.3**. A significant improvement in the adsorption rate was attained by the composite beads with an equilibrium time of around 4 h, albeit with a lower dye adsorption capacity of 353 mg/g. The small beads with parallel and uniform channels provided shorter diffusion pathway for the dye molecules and thus enhanced the adsorption rate.

Recently, a GO/chitosan aerogel microsphere was produced by Yu et al. [49] and used as a universal adsorbent for rapid adsorption of pollutants such as Pb (II), Cu (II), Cr (VI), phenol and various dyes (Methylene Blue, Rhodamine B, Methyl Orange and Eosin Y). In their work, the GO composite microspheres with inimitable configurations were developed by integrating electro-spraying with freeze casting (**Fig. 2.4(a)**). As delineated in **Fig. 2.4(b)**, the microspheres possessed a honeycomb-cobweb structure which enlarged the surface area and hence improved the adsorption capacity. Furthermore, the adsorption of pollutants on these microspheres achieved equilibrium in less than an hour as the diffusion process was facilitated by a shorter internal diffusion pathway.

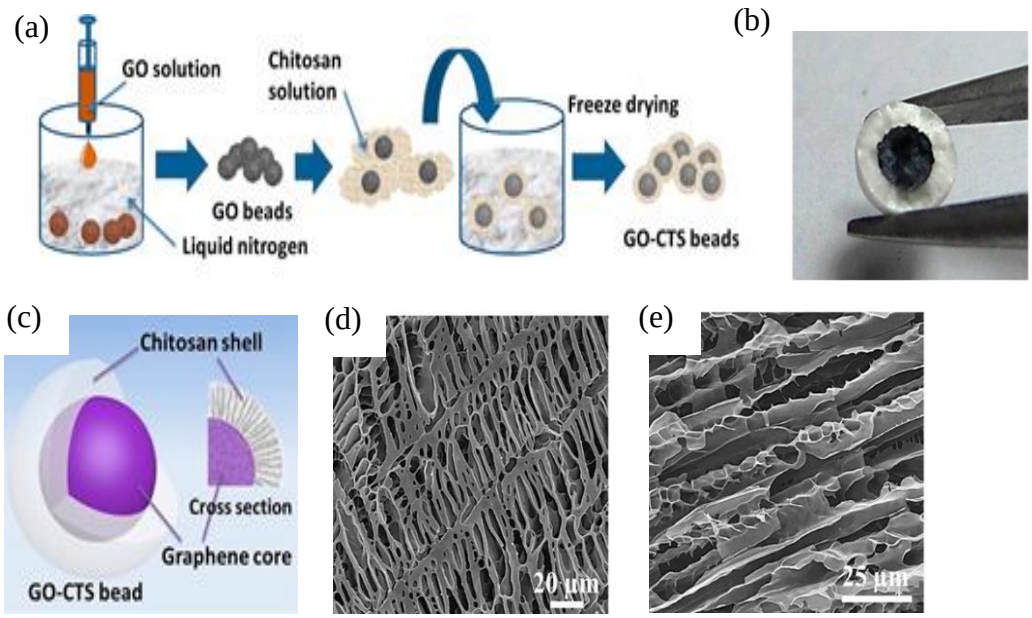


Fig. 2.3 (a) Schematic illustrating the fabrication process for GO-chitosan beads; (b) photos of half-cut GO-chitosan bead showing core-shell structure; (c) schematic diagram showing the structural properties of GO-chitosan bead; (d) FESEM image of the surface morphology of GO-chitosan bead, and (e) FESEM image of the chitosan shell showing organised channels. Reprinted with permission from [89]. Copyright 2015 American Chemical Society.

Apart from the commonly used additives, some studies involved the employment of environmentally friendly ionic liquids to functionalise the GO before assembling it into a 3D structure. For instance, Zambare et al. [102] prepared a methylimidazolium ionic-liquid-functionalised GO sponge (mimGO) for the removal of anionic Direct Red 80 dye. As shown in **Fig. 2.4(c)**, the imidazolium ionic liquid was anchored on the GO surface through interaction between its amine groups and the carboxylic groups of GO, endowing the resulting material with abundant cationic imidazole ring and amine groups which served as the binding sites for the dye. The mimGO sponge manifested an ultrafast adsorption rate of 588.2 mg/(g.min) and an adsorption capacity of 501.3 mg/g for Direct Red 80 dye where the exceptional performance could be explained by the strong interaction

between anionic sulphonic acid on dye molecules and the cationic sorption sites of the adsorbent at low pH value.

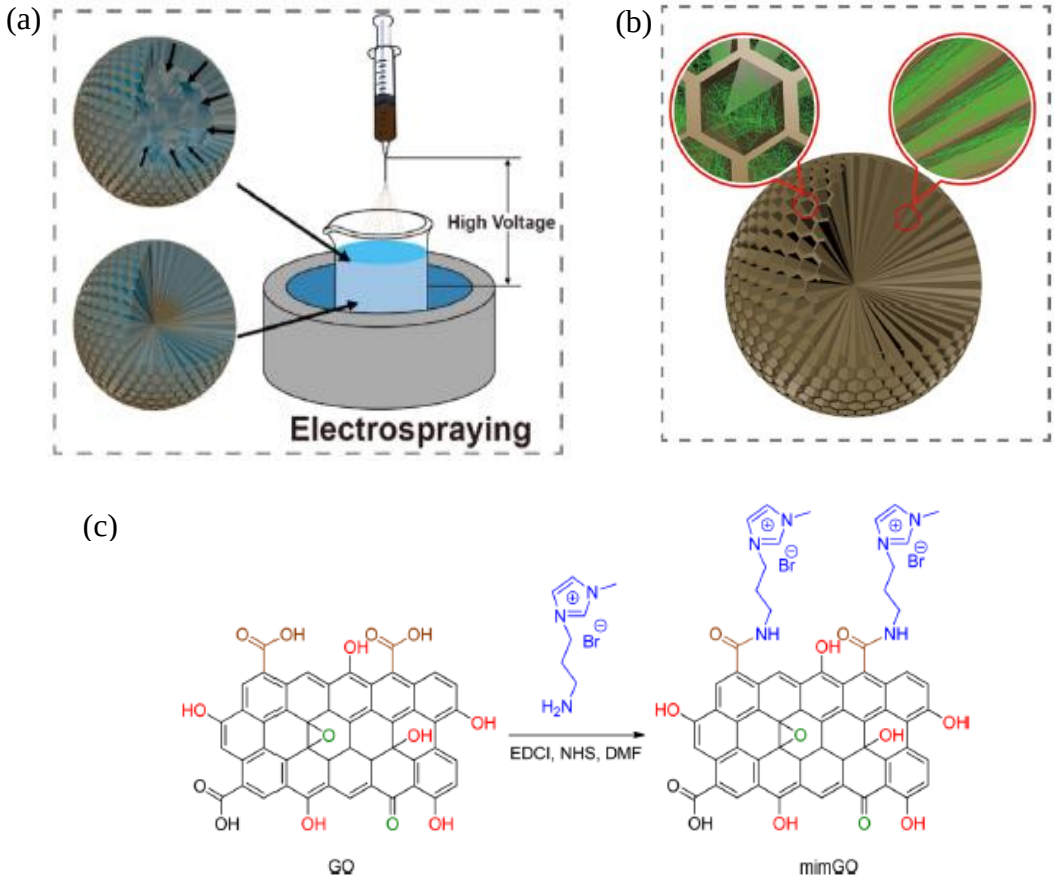


Fig. 2.4 (a) Schematic illustrating the preparation of GO/chitosan aerogel microspheres; (b) schematic diagram of GO/chitosan aerogel microsphere10 with honeycomb-cobweb and radially oriented microchannel structures. Reprinted with permission from [49]. Copyright 2017 American Chemical Society. (c) Proposed mechanism for preparation of mimGO sponge. Adapted with permission from [102]. Copyright 2017 American Chemical Society.

2.1.4 Physical properties of ice-templated 3D graphene materials

Table 2.2 depicts the prominent physical properties of ice-templated 3D graphene materials such as specific surface area, pore structure, density and mechanical properties. In general, the density of a material correlates with its porosity content whereby highly porous materials possess low density and *vice versa*. It is noticeable

that all the ice-templated 3D graphene materials presented in **Table 2.2** are highly porous and light in weight. These are desirable attributes of an adsorbent applied in wastewater treatment as high porosity can facilitate the transfer of heavy metals and dyes from the bulk solution to the surface and internal pores of the adsorbent, contributing to high adsorption rate and remarkable removal efficiencies of these pollutants [90, 91]. It is also favourable to have low density adsorbents for certain application such as oil spill clean-up since the oil is less dense than water.

The surface area of adsorbent is a critical indicator of its adsorption efficiency for specific pollutant. Generally, a high specific surface area indicates abundant sorption sites available for contacting with the pollutants. The ice-templated 3D materials exhibited specific surface areas varying within the range of 0.014 - 272 m^2/g. The GO aerogel prepared by Liao et al. [80] showed relatively low specific surface area. This might be due to the miniature and extremely light microspheres which complicated the surface area analysis. In order to obtain sufficient mass for the surface area measurement, the microspheres were compressed which resulted in the low specific surface area.

The mechanical strength of 3D graphene structures plays a vital role in column adsorption where the adsorbents must be sufficiently sturdy to be packed into the column and structurally stable during the adsorption process. Furthermore, mechanical strength is one of the factors governing the regenerability of the graphene adsorbent for reutilisation. Ma et al. [92] compared the packed column performance of GO/chitin nanofibril foam with a neat GO foam. They reported that the nanofibril foam maintained its shape and macroscopical morphology even after 3 cycles of column adsorption due to its high compressive strength. Meanwhile, the

neat GO foam collapsed and dispersed during the column adsorption process. The incorporation of chitin nanofibril reinforced the mechanical strength of the composite foam through electrostatic interaction and hydrogen bonding with GO. Dai et al. [47] compared the mechanical stability of pristine GO aerogel and GO/polyvinyl alcohol aerogel in water. The GO aerogel could not be removed from the water as its 3D structure collapsed severely in the water. The formation of secondary water pollution by the disintegrated GO aerogel made it unsuitable for use in wastewater treatment. Contrarily, the GO/polyvinyl alcohol aerogel with appropriate PVA content showed excellent stability in water and was employed in the removal of dyes. These reported findings suggested that it is imperative to introduce an appropriate additive during the preparation process in order to synthesise 3D graphene materials with high structural stability.

Table 2.2 Physical properties of ice-templated 3D graphene materials.

3D graphene sample	Specific surface area (m^2/g)	Pore volume, size and type	Density (g/cm^3)	Mechanical properties	Reference
Cellulose nanofibril/GO aerogel	97.5	Pore volume: 0.4 cm^3/g; mesopores	0.00184	-	[85]
Porous GO/chitosan	-	Pore sizes: 50 – 200 μm	-	-	[86]
rGO foams	-	Pore sizes: 5 – 50 μm	0.008	Compressive strength 2.5 – 5 kPa	[84]
Chitosan-gelatin/GO monoliths	-	Pore sizes: about 200 μm; Porosity: 97.1 – 97.5 %	-	Compressive strength 2.5 – 10 kPa	[53]
GO/alginate bead	9 - 39	Pore volume: 0.007 – 0.2 cm^3/g; micropores, mesopores	-	Young's modulus 192 kPa	[82]
GO/chitin nanofibril foam	-	Macropores	-	Compressive strength 10.5 – 24.3 kPa	[92]
GO/chitosan aerogel microsphere	-	Pore sizes: about 10 μm	-	-	[49]
GO/polyvinyl alcohol hydrogel	-	Micropores, mesopores	-	Tensile strength 3.3 MPa	[93]
GO/microcrystalline cellulose aerogel	30.4 – 43.7	-	-	-	[94]
GO/xanthan aerogel	-	-	0.016 – 0.019	-	[74]
GO/polyvinyl alcohol aerogel	-	Porosity: >95 %; Pore sizes: 71 – 75 μm	0.009 – 0.034	Flexible and compressible	[47]
Spongy graphene	-	Pore sizes: 10 – 50 μm	< 0.001	-	[83]

Graphene-chitosan bead	26.7	Porosity: 94 – 96 %; Mesopores volume: 0.246 cm^3/g	-	-	[89]
Spongy graphene aerogel	-	Pore sizes: 5 – 10 μm	0.024	Compressive strength 63 kPa	[54]
Reduced GO/polyacrylic acid aerogel	-	Porosity: > 99.6 %	0.004 – 0.006	Compressive strength 25 kPa	[96]
Spongy GO/chitosan monolith	-	Porosity: 96 – 98 %	0.044 – 0.061	Flexible and compressible	[90]
GO foams	-	Pore sizes: About 20 μm	0.002 – 0.02	-	[81]
GO/chitosan aerogels	-	Porosity: 97.96 – 98.78 %	0.021 – 0.035	Storage modulus 3.3 – 4 MPa	[48]
GO/carboxymethyl cellulose monolith	-	Porosity: 80 – 96 %	-	Compressive strength 35 – 70 kPa	[97]
GO aerogel	-	Porosity: > 97 %	0.002	-	[63]
GO aerogel	42	Pore volume: 4.38 cm^3/g	-	-	[44]
GO/sodium alginate aerogel	-	Pore sizes: 50 – 100 μm; Porosity: 90.7 – 91.8 %	-	Compressive strength 249 – 324 kPa	[91]
GO/chitosan nanocomposite	54.64	-	-	-	[88]
Graphene sponge	51 - 105	Micro, meso and macropores	0.002 – 0.008	Flexible and compressible	[76]
Graphene based nanocomposite aerogel	270	Pore sizes: Several micrometers	0.028	Compressive strength 0.27 MPa	[103]
mimGO sponge	31.72	Pore volume: 0.22 cm^3/g	-	-	[102]

2.2 Adsorption properties and mechanisms of 3D graphene materials

Due to unique properties such as enormous surface area, interconnected porous structure and high structural integrity, 3D graphene materials offer an alternative solution for the eradication of pollutants from water bodies [92, 104]. A few studies have demonstrated the excellent stability of 3D graphene derived adsorbents in various environment, varying from severe conditions such as strong acidic, alkaline and salty polar solvents [104, 105] to even organic solvents such as cyclohexane [47], methanol, acetone and methylbenzene [105]. These mechanically stable 3D graphene adsorbents facilitated not only the separation process after adsorption, but also the subsequent regeneration process, further improving the economic feasibility of the adsorbents in water purification. The role of 3D graphene materials as adsorbent for two major types of pollutant, namely dyes and heavy metals, is discussed in the following section.

2.2.1 Adsorption of dyes

Contamination of water bodies caused by dyes discharged from printing, textile, leather, electroplating and cosmetic industries is an on-going environmental concern. Dyes which are toxic and non-biodegradable are known to impart negative effects on humans and the environment [92, 100]. Generally, most dyes are soluble in water and only few are non-ionic/dispersive. The water-soluble dyes are generally cationic (basic dyes) or anionic (acidic dyes) in nature. Methylene Blue, Rhodamine B, Neutral Red, Malachite Green and Basic Fuchsin dyes are the cationic dyes which have been adsorbed onto 3D graphene materials developed by ice-templating and ice-templating assisted by other methods, meanwhile, Methyl

Orange, Amido Black 10B, Congo Red, Eosin Y, Acid Chrome Blue K, Metanil Yellow and Direct Red 80 dyes are the anionic dyes treated (**Table 2.3**). The reported literature indicated that only a limited number of dyes were tested using ice-templated graphene adsorbents till recently.

The 3D graphene derived adsorbents demonstrated very promising adsorption performance which is higher than those of conventional and other innovative adsorbents. For instance, an anionic polyacrylamide/GO aerogel adsorbed as much as 1034.3 mg/g of Basic Fuchsin dye [99]. Its removal capability outperformed many other adsorbents such as mussel shell biomass waste – 186.67 mg/g [106], leather activated carbon – 182.48 mg/g [107], eggshell membrane – 47.86 mg/g [108] and Al-MCM-41 – 54.44 mg/g [109]. The excellent performance of the aerogel was due to the interconnected porous structure and abundant functional groups of the aerogel [99]. The porous structure enlarged the specific surface area and exposed the active sites as well as facilitated the diffusion of the dyes into the internal network of the adsorbent. The abundant functional groups provided large quantities of sorption site for anchoring the dyes.

Table 2.3 Adsorption properties and mechanisms of 3D graphene materials for dyes.

Dyes	Adsorbents	Synthesis method	Adsorption capacity (mg/g)	Isotherms	Kinetics	Adsorption mechanism	Regeneration	References
Methylene blue	GO-sodium alginate gel	(C) + (I)	833.3*	Langmuir	PSO	Electrostatic interaction, π- π stacking	×	[52]
	GO/chitin nanofibril foam	(E) + (I)	173.3*	Langmuir	-	Electrostatic interaction, π- π stacking	√	[92]
	GO/chitosan aerogel microspheres	(ES) + (I)	584.6	Langmuir	PSO	Electrostatic interaction, π- π stacking	√	[49]
	Xanthan/GO aerogel	(I)	290.57	-	PFO	-	√	[74]
	PVA-supported GO aerogel	(C) + (I)	~25	-	-	Electrostatic interaction, π- π stacking, hydrogen bonding	×	[47]
	GO aerogel	(I)U	416.67*	Langmuir	PSO	Electrostatic interaction, π- π stacking	×	[44]
	Chitosan/GO nanocomposite	(C) + (I)	662.25*	Langmuir	PSO	Electrostatic interaction	×	[88]

	Polydopamine coated GO aerogel	(C) + (I)	633*	Langmuir	-	Electrostatic interaction, π- π stacking, hydrogen bonding	×	[110]
	PVA/PCMC/GO bentonite hydrogel	(I)	172.14*	Langmuir	PSO	Electrostatic interaction	√	[98]
	3D GO/lignosulfonate aerogel	(C) + (I)	1023.90*	Langmuir	PSO	Electrostatic interaction, π- π stacking, hydrogen bonnding	√	[111]
Rhodamine B	GO/chitosan aerogel microspheres	(ES) + (I)	492.8	Langmuir	PSO	Electrostatic interaction, π- π stacking	√	[49]
	Xanthan/GO aerogel	(I)	244.36	-	PFO	-	√	[74]
	TiO_2-rGO aerogel	(H) + (I)	~80%	-	-	π- π stacking	×	[112]
Neutral red	PVA-supported GO aerogel	(C) + (I)	> 96%	-	-	π- π stacking, hydrogen bonding	×	[47]
	Polydopamine coated GO aerogel	(C) + (I)	~94.6%	-	-	hydrogen bonding, π- π stacking	×	[110]
Malachite green	PVA-supported GO aerogel	(C) + (I)	> 96%	-	-	Electrostatic interaction, π- π stacking, hydrogen bonding	×	[47]

	Amphiphilic graphene aerogel	(H) + (I)	352	Langmuir	PSO	Electrostatic interaction	√	[113]
Basic fuchsin	Anionic polyacrylamide/GO aerogel	(C) + (I)	1034.3*	Langmuir	PSO	π- π stacking, hydrogen bonding, intermolecular force	×	[99]
Methyl orange	GO/chitin nanofibril foam	(E) + (I)	39.7 %	-	-	-	×	[92]
	GO/chitosan aerogel microspheres	(ES) + (I)	189.4	Langmuir (low conc.) and Freundlich (high conc.)	PFO + PSO	Electrostatic interaction, π- π stacking	√	[49]
	GO-chitosan beads	2 steps (I)	353	Langmuir	PSO	-	×	[89]
	Chitosan/GO monolith	(C) + (I)	567.07	-	PSO	Electrostatic interaction	×	[90]
	Chitosan/GO aerogel	(C) + (I)	686.89	-	PSO	Electrostatic interaction	×	[48]
	GO aerogel	(I)	55.56	Langmuir	PSO	Electrostatic interaction, π- π stacking	×	[78]
Amido black 10B	Chitosan/GO aerogel	(C) + (I)	573.47	-	PSO	Electrostatic interaction	×	[48]

Congo red	PVA-supported GO aerogel	(C) + (I)	~55	-	-	π- π stacking, hydrogen bonding	×	[47]
Eosin Y	GO/chitosan aerogel microspheres	(ES) + (I)	124.8	Freundlich	PSO	Electrostatic interaction, π- π stacking	√	[49]
	PVA-supported GO aerogel	(C) + (I)	81.6%	-	-	π- π stacking, hydrogen bonding	×	[47]
Acid chrome blue K	PVA-supported GO aerogel	(C) + (I)	8.1%	-	-	π- π stacking, hydrogen bonding	×	[47]
	Polydopamine coated GO aerogel	(C) + (I)	~51.4%	-	-	π- π stacking	×	[110]
Metanil y**ellow**	Graphene oxide-chitosan aerogel	(I)	558.18*	Langmuir	PFO + PSO	Electrostatic interaction	√	[114]
Direct red 80	mimGO sponge	(I)	501.3	Langmuir	PSO	Electrostatic interaction, π- π stacking, hydrogen bonnding	√	[102]

Note: (C) – cross-linking induced assembly, (I) – ice-templating, (I)U – unidirectional ice-templating, (H) – hydrothermal reduction induced assembly, (E) – evaporation, (ES) – electrospraying, PFO – pseudo-first-order kinetic model, PSO – pseudo-second-order kinetic model. '*' denotes maximum adsorption capacity based on Langmuir isotherm model. The values expressed in % represent removal efficiency.

2.2.1.1 Mechanisms of dyes adsorption

The 3D graphene materials exhibit different adsorption mechanisms for different dyes which are related to the charge property of the dye. Methylene Blue, a cationic dye, was adsorbed easily onto the graphene materials, as illustrated in **Table 2.3**. In general, the high adsorption capability of the adsorbent was partially attributed to the strong electrostatic force between the negatively charged GO and the positively charged Methylene Blue dye. It is a widely held view that the deprotonation of oxygenated functional groups (hydroxyl, carboxyl and carbonyl) on GO sheets contributes to the high negative surface charge density of 3D graphene adsorbent. Hence, the quantity of oxygen-containing groups determines the surface charge properties of the adsorbent and consequently, its adsorption capability for the cationic dye. The 3D graphene materials have been proved to be effective adsorbents for eliminating cationic dyes and electrostatic interaction was determined in the past studies to be the dominating mechanism [49, 94, 115, 116].

The inherent negatively charged GO endows the 3D networks with good removal capability for cationic dyes but unsatisfactory adsorption performance for anionic dyes which can be ascribed to the electrostatic repulsion between the functional groups of acidic dyes and the oxygenated functional groups of GO [47]. In order to counteract the problem faced by 3D GO adsorbents in removing anionic dyes, it is desirable to tune their surface charge by grafting positively charged functional groups to the GO sheets. Chitosan, a cationic multifunctional polysaccharide possessing abundant reactive amino groups, is frequently cross-linked with GO sheets to modify the surface charge of the resulting composite materials [6, 48, 90]. For example, the chitosan/GO aerogel fabricated by Wang et al. [48] manifested a

high adsorption capacity (>500 mg/g) towards anionic dyes (Methyl Orange and Amido Black 10B dyes). The amino group on the chitosan chains served as the positively charged sorption site and thus, adsorption of the anionic dyes was mainly due to the electrostatic interaction between the amino group of chitosan and acidic groups of the dyes. In addition, the synthesis of a universal adsorbent for sequestrating both cationic and anionic dyes could be realised with appropriate GO to chitosan ratio [6, 49, 117]. Yu et al. [49] examined the dye adsorption capacity of the as-synthesised GO/chitosan aerogel microspheres for both cationic dyes (Methylene Blue (MB) and Rhodamine B (Rh B)) and anionic dyes (Methyl Orange (MO) and Eosin Y). This composite aerogel demonstrated equilibrium adsorption capacities of 584.6, 492.8, 189.4 and 124.8 mg/g for MB, Rh B, MO and Eosin Y, respectively, proving its capability as a broad-spectrum adsorbent.

The pH of solution is regarded as one of the most crucial factors in affecting the adsorption of organic dyes on 3D graphene materials. Typically, the adsorption of anionic dyes increases with decreasing pH and *vice versa* for cationic dyes [32, 99, 117, 118]. At high pH condition, there is an intense competition between OH^- and anionic dyes. Besides, the deprotonation of carboxyl and hydroxyl groups of 3D graphene materials to $–COO^-$ and $–O^-$ intensifies the electrostatic repulsion between the sorption sites and anionic dyes, and hence, hampers the dyes from approaching the adsorbent surface. When the pH decreases, the competition between OH^- and anionic dyes becomes negligible. Contrastingly, the hydroxyl and carboxyl groups would be protonated to form $–OH_2^+$ groups, which strengthens the electrostatic attraction between adsorbent surface and anionic dyes, resulting in high adsorption capacity.

It is noteworthy that electrostatic interaction is not the only governing mechanism for adsorption of dyes onto 3D graphene materials. Other predominant interaction includes π-π stacking. Generally, 3D graphene adsorbents exhibit higher adsorption performance for dyes with enriched aromatic moieties (benzene ring-containing structure) by virtue of π-π stacking [105, 119, 120]. For instance, the graphene aerogel fabricated by Wang et al. [119] could remove Calcein, Rose Bengal sodium salt and Amido Black 10B dyes (~700 – 1200 mg/g) better than other dyes tested in their research (~100 – 500 mg/g), owing to their polybenzene structures which had stronger interactions with the adsorbent surfaces. In addition, π-π stacking was the major interactive force between a neutral dye, such as Acridine Orange dye [121], and the π-conjugated structure of graphene. Consequently, π-π stacking allows efficacious adsorption of dyes onto the 3D graphene materials in spite of their surface charges.

Owing to the benzene ring structure and surface charge properties of most dyes, the adsorption of dyes onto 3D graphene materials is usually the result of synergistic effects between electrostatic interaction and π-π stacking. The adsorption mechanism of anionic Methyl Orange dye and cationic Methylene Blue dye onto GO/polyethyleneimine aerogel at different pH is illustrated in **Fig. 2.5**. This aerogel possesses two different active sites for adsorption of ionic dyes, including the sp^2 structure of the GO nanosheets and the surface functional groups with tunable charge via variation of solution pH. The zeta potential curve of GO/polyethyleneimine aerogel demonstrated a positive surface charge at pH <10 and a negative charge at pH >10. The authors reported that at pH 10.5, the negatively charged aerogel could still adsorb a significant amount of MO (59.8

mg/g) which was due to the π-π stacking between the anionic dyes and the GO sheets.

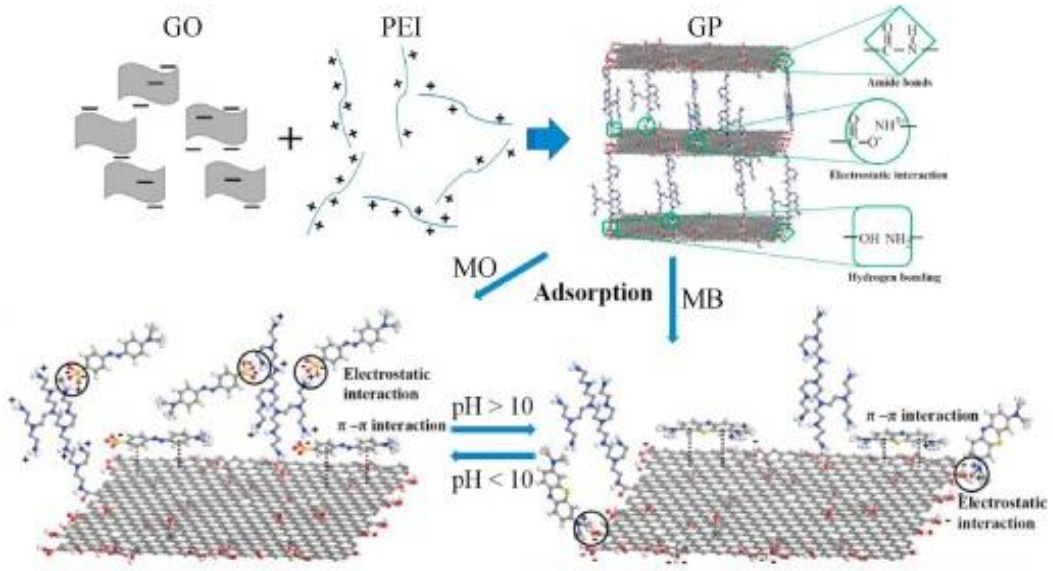


Fig. 2.5 Proposed mechanism for the interaction of GO/polyethyleneimine aerogel with Methyl Orange and Methylene Blue dyes at different pH. Reprinted with permission from [105]. Copyright 2017 Elsevier.

Although the rGO obtained from chemical/hydrothermal reduction of GO has lesser oxygeneous functional groups, it was demonstrated to be able to adsorb dyes through π-π stacking and electrostatic interaction [122-124]. Taking Malachite Green dye as the representative dye, the possible mechanisms for the dye adsorption onto rGO are illustrated in **Fig. 2.6**. In addition to the prominent π-π stacking and electrostatic interaction, the π-cation interaction could also occur with the positively charged centre of the dye. Besides, hydrogen bonding and van der Waals interaction could also contribute to the adsorption of the dye onto 3D graphene materials [47, 125, 126]. Kim et al. [127] exemplified the different interactions of cationic dye (Methylene Blue) and anionic dye (Acid Red 1) with the sorption sites of rGO

macrostructure using a schematic diagram (**Fig. 2.7**). Apart from the π-π stacking between the localised π electrons in the aromatic rings of rGO macrostructure and dye molecules, hydrogen bonding was found to play a significant role in the adsorption of Acid Red 1 dye in lieu of the electrostatic interaction. This was mainly attributed to the anionic sulphonate (SO_3^-) groups of Acid Red 1 dye which hindered the dye molecules from coming into close proximity with the moderately negative charged surface of rGO. In their research, the adsorption isotherm of Methylene Blue and Acid Red 1 dyes obeyed Langmuir and Freundlich models, respectively. The authors speculated that the intermolecular hydrogen bonding between the oxygenated functional groups of rGO and dye molecules promoted the multilayer stacking of the Acid Red 1 dye molecules on the adsorbent surface.

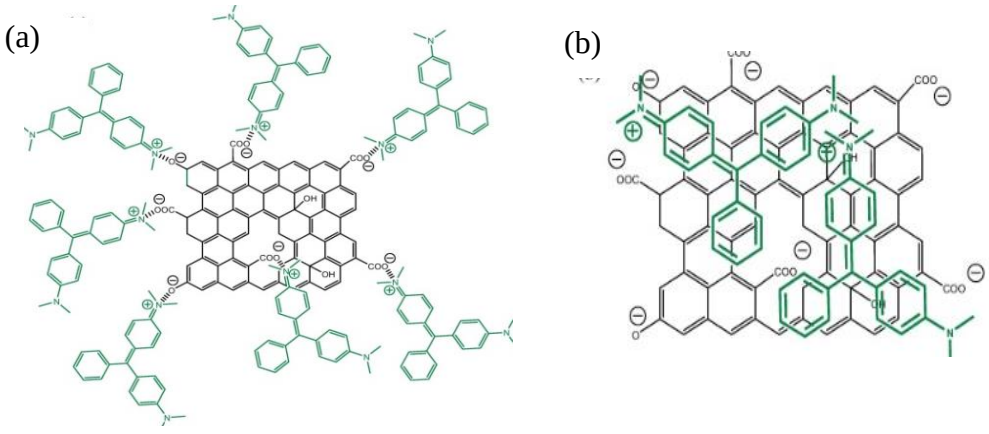


Fig. 2.6 Schematic illustration of the adsorption mechanism of Malachite Green onto rGO. (a) Electrostatic interaction; (b) π-π stacking and π-cation interaction. Reproduced with permission from [128]. Copyright 2017 Elsevier

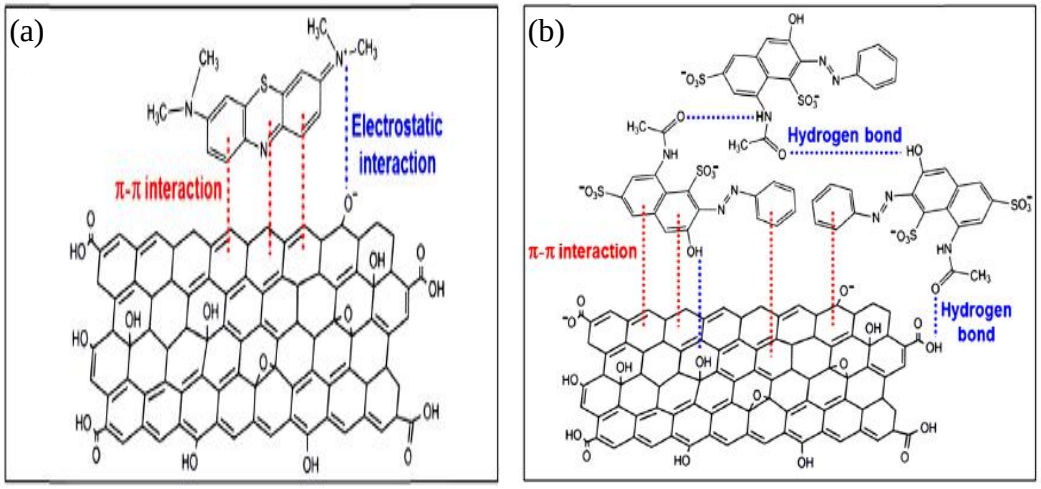


Fig. 2.7 Schematic illustrating the interactions between the surface of rGO and (a) cationic Methylene Blue dye, and (b) anionic Acid Red 1 dye. Adapted with permission from [127]. Copyright 2014 Elsevier.

Likewise, the removal mechanisms of Direct Red 80 dye by mimGO sponge are shown in **Fig. 2.8**. The molecular structure of Direct Red 80 dye contained anionic sulphonic acid group and rich aromatic rings, which could form strong electrostatic interaction and π-π stacking with the cationic functionalities and the conjugated structure of mimGO sponge, respectively. The adsorption performance was further enhanced by the hydrogen bonding between the hydroxyl group of mimGO sponge and the nitrogen containing groups of Direct Red 80 dye. Hence, the prominent electrostatic interaction together with π-π stacking and hydrogen bonding promoted the superior adsorption performance of mimGO sponge.

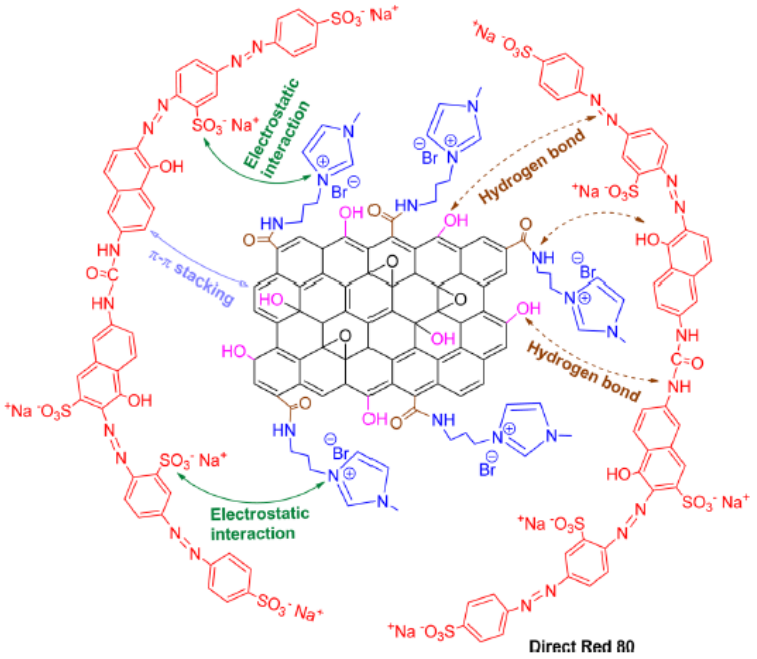


Fig. 2.8 Schematic diagram of interactions between Direct Red 80 and mimGO sponge. Reproduced with permission from [102]. Copyright 2017 American Chemical Society.

Other than the surface charge properties, the structure of dyes also plays a vital role in their adsorption. Wang et al. [121] compared the adsorption of Malachite Green dye onto a GO-agarose hydrogel/rGO-agarose hydrogel with other cationic dyes of similar structure such as Methyl Violet and Brilliant Green dyes. Malachite Green dye is a cationic triphenylmethane dye with a central carbon attached with numerous carbon-carbon bonds and three phenyls that can rotate readily in solution. The interaction of Malachite Green dye with graphene restricted the rotation of the carbon-carbon bonds, causing the dye molecules to become stiff and flat on the surfaces of graphene, thereby further intensifying the π-π stacking between the graphene and the dye molecules. The authors reported that the adsorption capabilities were in the order of Malachite Green > Methyl Violet > Brilliant Green, which was ascribed to the slight disparity in their molecular structures. As depicted

in **Fig. 2.9**, Malachite Green dye has four –CH_3 groups at the end of phenyls, while Methyl Violet and Brilliant Green dyes contain five –CH_3 groups and four –CH_2CH_3 groups in their chemical structure, respectively. It is a well acknowledged fact that the conjugated property of the dye molecules deteriorates with the quantity of flexible alkanes contained within a molecule. Owing to this, the adsorbent demonstrated the strongest affinity towards Malachite Green dye among the three tested dyes.

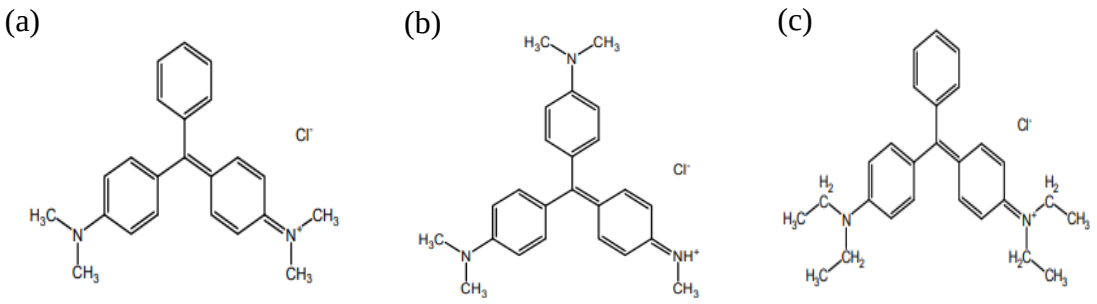


Fig. 2.9 Molecular structures of (a) Malachite Green, (b) Methyl Violet and (c) Brilliant Green dyes.

2.2.1.2 Column adsorption of dyes

In addition to batch adsorption, several research studies have demonstrated the practicability of continuous adsorption of dyes onto 3D graphene materials packed in columns [6, 105, 121, 129, 130]. A typical set-up is portrayed in **Fig. 2.10**, where the loaded column eliminated dyes through filtration by gravitational force, consequently a visually clear filtrate was obtained. The absence of the characteristic peak of dye in the UV-vis spectrum suggested that a complete removal of the dye was achieved (**Fig. 2.10(d)**). According to Chen et al. [6], the adsorption capacity and permeation volume were linearly proportional to each other during the whole filtration process, suggesting that the column was stable and capable of maintaining

its high affinity towards the dye. It is noteworthy that the operational capacity of the column was based on the permeation volume (**Fig. 2.10(b))** for adsorption of Methylene Blue dye which was about 80 mL. An increase in volume greater than the permeation volume would result in the residual dye leaving the column.

Apart from the column filtration set-up using a syringe, a more sophisticated arrangement for column adsorption with the aid of peristaltic pump was demonstrated by Ma et al. [92] in **Fig. 2.11**. In their investigation, Methylene Blue dye solution flowed through the GO/chitin nanofibril foam where the dye molecules were attracted to GO by means of electrostatic interaction and captured in the macropores of foam. A clear filtrate was collected while the adsorbent transformed from brown to black.

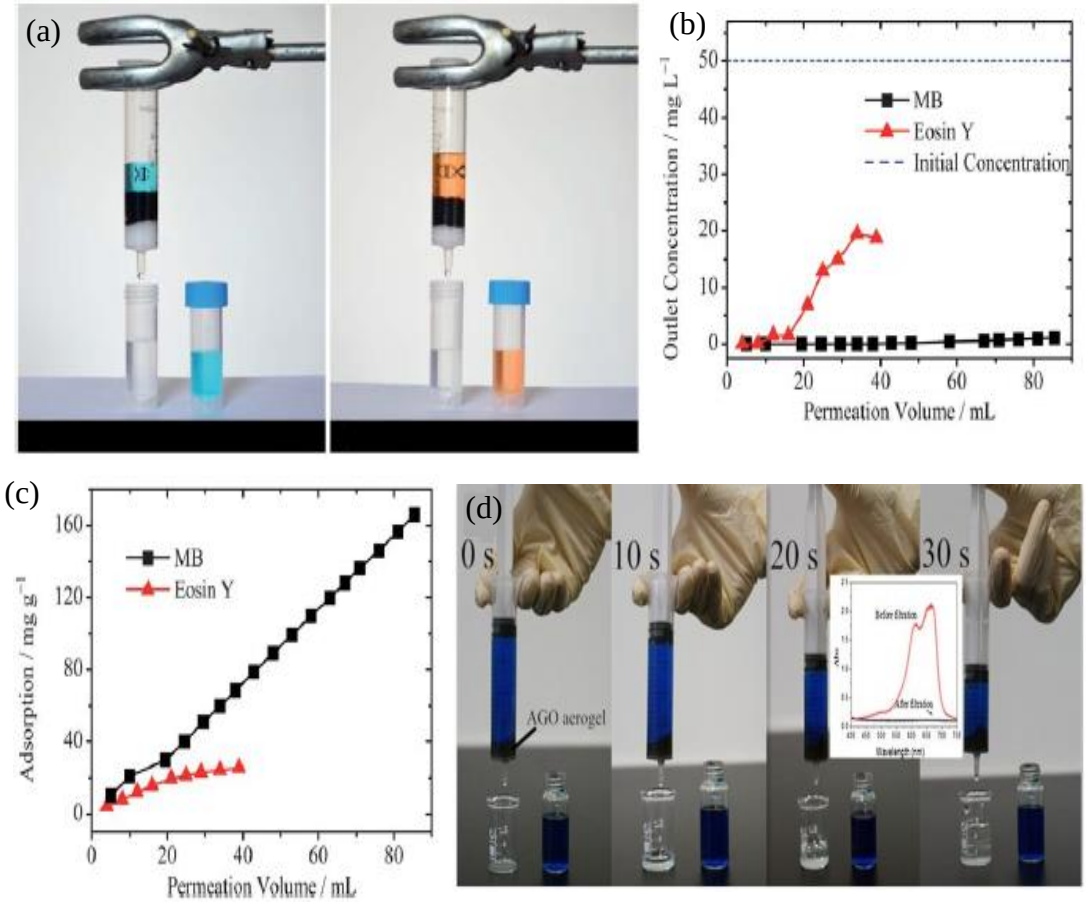


Fig. 2.10 (a) Removal of Methylene Blue (left) and Eosin Y (right) dyes from water by filtration; (b) outlet concentration of dyes as a function of permeation volume; (c) adsorption capacity of the column as a function of permeation volume. Reprinted with permission from [6]. Copyright 2013 Royal Society of Chemistry. (d) Images of the filtration set-up and the solution before and after filtration. The inset shows UV-vis absorption spectrum of the dye solution before and after filtration. Adapted with permission from [129]. Copyright 2016 Elsevier.

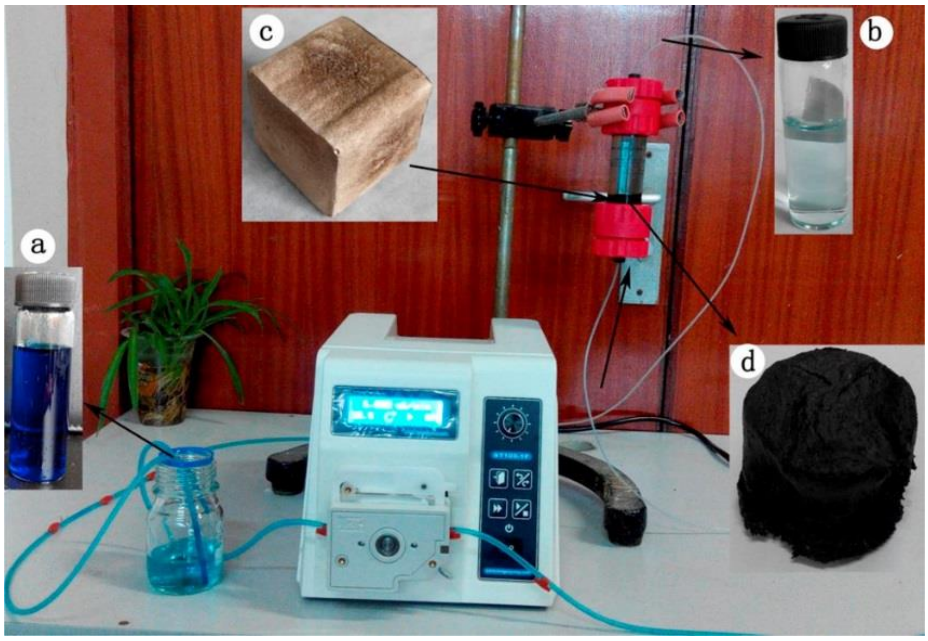


Fig. 2.11 Schematic diagram for column adsorption of Methylene Blue dye onto GO/chitin nanofibril foam, the insets represent the solution (a) before and (b) after adsorption; GO/chitin nanofibril foam (c) before and (d) after adsorption. Reprinted with permission from [92]. Copyright 2016 Elsevier.

2.2.1.3 Regeneration of dye-loaded 3D graphene adsorbents

Regeneration of exhausted 3D graphene adsorbent is an essential step to recover the material for re-use in subsequent adsorption cycles. This practice is imperative to prevent secondary waste generation and to ensure that the adsorbent is economically viable for commercial wastewater treatment. The regeneration of exhausted adsorbents can be attained by washing with acids [49, 117], alkalis [49, 117], solvent [74, 131-133] or mixture of these chemicals [92, 93]. For instance, Ma et al. [92] employed a mixture of ethanol and NaOH solution to elute Methylene Blue dye from the spent adsorbent. After three successive adsorption-desorption cycles, the adsorbent was capable of maintaining its removal efficiency at about 90%. In the work of Yu et al. [49], acid (HCl) and alkali (NaOH) were used to elute the cationic and anionic dyes, respectively, from the spent GO/chitosan aerogel

microsphere. When the adsorbent was immersed in acidic solution, the amino groups of chitosan were protonated to produce $–NH_3^+$ which formed strong electrostatic repulsion with the cationic dyes, resulting in the liberation of cationic dyes from the adsorbent. Undoubtedly, the 3D graphene materials are promising adsorbents for dyes with possible high removal capability and recyclability.

2.2.2 Adsorption of heavy metals

The disposal of heavy metals contaminated wastewater is a serious environmental problem encountered in mining, metallurgical, electroplating, chemical manufacturing and electronic industries [53, 90, 134]. Heavy metals are highly poisonous even at very low concentrations [63]. They tend to accumulate in the living organisms or the food chain as they are biologically not degradable [135, 136]. 3D graphene materials developed by ice-templating and ice-templating assisted by other methods have been shown to be able to remove heavy metals in the water environment. As presented in **Table 2.4**, the treated heavy metals include lead-Pb (II), copper-Cu (II), chromium-Cr (VI), nickel-Ni (II), cobalt-Co (II) and cadmium-Cd (II). In general, the new class of adsorbent exhibited relatively high removal capabilities for the heavy metals.

For instance, GO/chitosan aerogel microspheres exhibited outstanding adsorption capacities for Pb (II) (747.5 mg/g) [49] and Cu (II) (457.5 mg/g) [49], and these were much higher than those of cucumber peel adsorbent (133.6 mg/g) [137], biochar-supported rGO composite (26.1 mg/g) [138] and almond shell activated carbon (112 mg/g) [139] for Pb (II), and those of pomegranate peel (30.12 mg/g) [140] and grape bagasse activated carbon (43.47 mg/g) [141] for Cu (II). In

addition, Jiao et al. [91] prepared a sodium alginate/GO aerogel which demonstrated a high adsorption capacity (267.4 mg/g) for Pb (II). The enhanced adsorption capacity was primarily due to the presence of reactive functional groups and the unique 3D structure with large specific surface area.

Table 2.4 Adsorption properties and mechanisms of 3D graphene materials for heavy metals.

Adsorbates	Adsorbents	Synthesis method	Adsorption capacity (mg/g)	Isotherms	Kinetics	Adsorption mechanism	Regeneration	References
Pb (II)	Chitosan-gelatin/GO monoliths	(C) + (I)U	~100	-	-	Chelation	×	[53]
	GO/chitin nanofibril foam	(E) + (I)	92.2 %	-	-	-	×	[92]
	GO/chitosan aerogel microspheres	(ES) + (I)	747.5	Langmuir (low conc.) and Freundlich (high conc.)	PSO	Electrostatic interaction, chelation	√	[49]
	GO/carboxymethyl cellulose monolith	(I)U	76.7	-	-	Electrostatic interaction	×	[97]
	Sodium alginate/GO aerogel	(C) + (I)	267.4*	Langmuir	PSO	-	×	[91]
	Glycol-GO aerogel	(C) + (I)	101.1*	Freundlich	Elovich	Electrostatic interaction	√	[142]
	Lactic acid-GO aerogel	(C) + (I)	86.81*	Freundlich	Elovich	Electrostatic interaction	√	[142]
	Succinic acid-GO aerogel	(C) + (I)	42*	Freundlich	PFO	Electrostatic interaction	×	[142]
	3D GO/xanthan/TiO_2 composite	(I)	199.22*	Langmuir	PSO	Electrostatic interaction, complexation	√	[95]

	GO/carboxymethyl chitosan aerogel	(V) + (I)	249.38	Langmuir	PSO	Complexation	×	[143]
	Magnetic polysaccharide//GO@Fe_3O_4 gel beads	(C) + (I)	189.04*	Langmuir	PSO	Chelation	√	[144]
Cu (II)	Chitosan-gelatin/GO monoliths	(C) + (I)U	~115	-	-	Chelation	√	[53]
	GO/chitosan aerogel microspheres	(ES) + (I)	457.5	Freundlich	PFO + PSO	Electrostatic interaction, chelation	√	[49]
	Xanthan/GO aerogel	(I)	53.2	-	-	-	×	[74]
	Chitosan/GO monolith	(C) + (I)	53.69	Langmuir	PSO	-	×	[90]
	GO/carboxymethyl cellulose monolith	(I)U	82.93	-	-	Electrostatic interaction	×	[97]
	GO aerogel	(I)U	29.59*	Langmuir	PSO	Ion exchange, electrostatic interaction	×	[63]
	Sodium alginate/GO aerogel	(C) + (I)	98*	Langmuir	PSO	-	×	[91]
	GO-chitosan aerogel	(C) + (I)	25.4*	Langmuir	PSO	-	×	[145]
	GO/carboxymethyl chitosan aerogel	(V) + (I)	95.37	Langmuir	PSO	Complexation	×	[143]
	Magnetic polysaccharide//GO@Fe_3O_4 gel beads	(C) + (I)	55.96*	Langmuir	PSO	Chelation	√	[144]

Cr (VI)	GO/chitosan aerogel microspheres	(ES) + (I)	292.8	Freundlich	PSO	Electrostatic interaction, complexation coordination	√	[49]
Ni (II)	GO/carboxymethyl cellulose monolith	(I)U	72.04	-	-	Electrostatic interaction	×	[97]
Co (II)	GO/carboxymethyl cellulose monolith	(I)U	59.99	-	-	Electrostatic interaction	×	[97]
Cd (II)	GO/carboxymethyl cellulose monolith	(I)U	46.13	-	-	Electrostatic interaction	×	[97]
	Magnetic polysaccharide//GO@Fe_3O_4 gel beads	(C) + (I)	86.28*	Langmuir	PSO	Chelation	√	[144]
	CNT-graphene aerogel	(CR)	64	-	-	Electrostatic interaction	×	[146]

Note: (C) – cross-linking induced assembly, (I) – ice-templating, (I)U – unidirectional ice-templating, (V) – vacuum assisted self-assembly, (CR) – chemical reduction induced assembly, (E) – evaporation, (ES) – electrospraying, PFO – pseudo-first-order kinetic model, PSO – pseudo-second-order kinetic model. '*' denotes maximum adsorption capacity based on Langmuir isotherm model. The values expressed in % represent removal efficiency.

2.2.2.1 Mechanisms of heavy metals adsorption

The adsorption mechanisms of heavy metals onto the 3D graphene materials are the most intriguing aspect to be studied among researchers. Initially, ion exchange was proposed as the pre-eminent mechanism for the adsorption of heavy metals. As reported by Mi et al. [63], the H_3O^+ ions which initially covered the surface of GO aerogel were liberated at higher pH, making the active sites accessible for Cu (II). Later, electrostatic interaction was suggested as the principal adsorption mechanism in lieu of ion exchange [131, 147]. The oxygenated functional groups on GO sheets such as carboxyl and hydroxyl groups, served as the negatively charged active sites which attracted the cationic heavy metals. It was also determined that pristine 3D GO macrostructure was less conducive for the adsorption of anionic Cr (VI) owing to its intrinsic negatively charged surface. Modification approaches were attempted to change the surface charge properties of the 3D graphene materials by incorporating positive functional groups into the GO sheets [49, 148-151]. Feng et al. [148] cross-linked polyethyleneimine, a cationic polymer containing numerous amine groups, with GO to form an aerogel. This aerogel exhibited a maximum adsorption capacity of 370.37 mg for Cr (VI). The main adsorption mechanism was revealed to be electrostatic interaction between the anionic Cr (VI) and the positively charged amine groups, as illustrated in **Fig. 2.12(a)**. The authors also suggested that the Cr (VI) was reduced to Cr (III) under the action of π electrons from the six-member ring of GO/polyethyleneimine aerogel during the adsorption process. Consequently, the cationic Cr (III) was attracted to the negatively charged groups ($-COO^-$) via electrostatic attraction. Cong et al. [152] developed graphene/α-FeOOH adsorbent for the removal of Cr (VI) via surface complexation in addition

to electrostatic interaction and ion exchange. Generally, surface complexation took place between the heavy metal and the metal oxyhydroxides derived from the incorporated Fe ions. Yu et al. [49] demonstrated that the adsorption mechanism of GO/chitosan aerogel microspheres for Cr (VI) was mainly attributed to the complexation and coordination of the carboxyl group of GO sheets and the electrostatic attraction between the amino group of chitosan and metal ions, as shown in **Fig. 2.12(b)**.

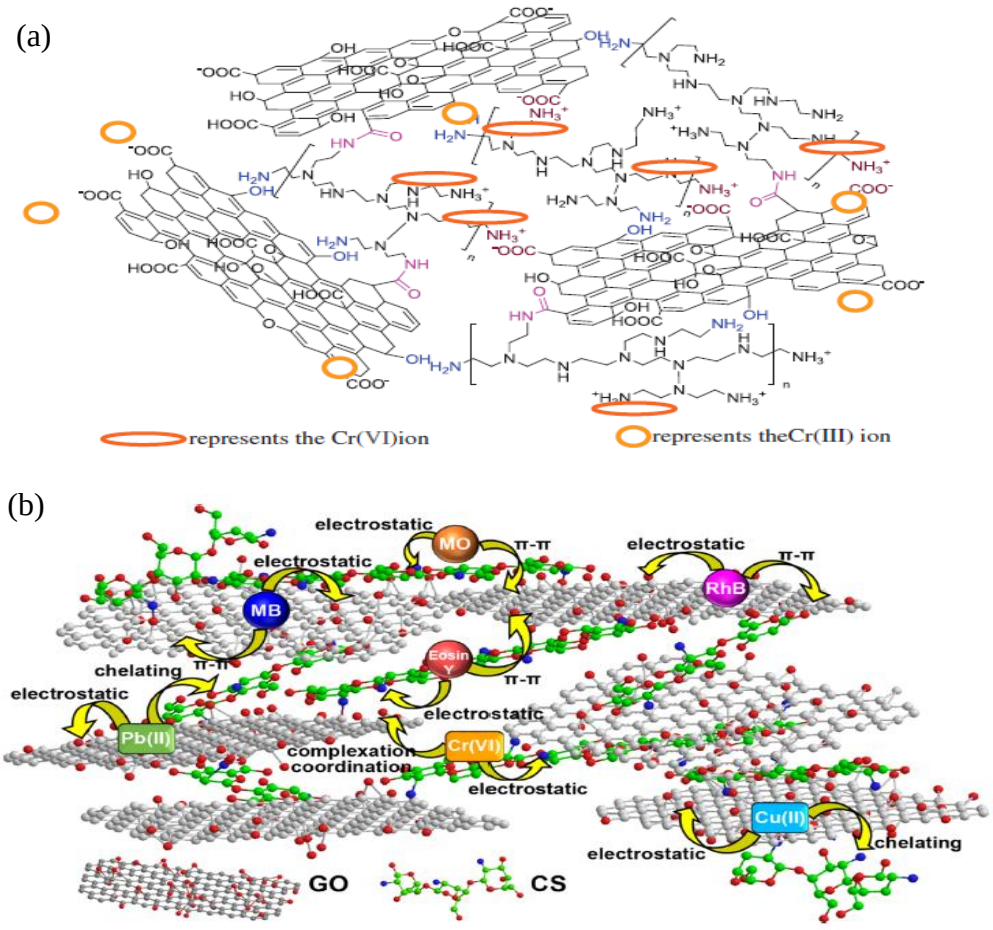


Fig. 2.12 Schematic illustrating the mechanisms for (a) Cr (VI) adsorption onto GO/polyethyleneimine aerogel. Reproduced with permission from [148]. Copyright 2018 Taylor & Francis, and (b) Pb (II), Cu (II), Cr (VI), Methylene Blue, Rhodamine B, Methyl Orange and Eosin Y dyes adsorption onto GO/chitosan aerogel microsphere. Adapted with permission from [49]. Copyright 2017 American Chemical Society.

From **Fig. 2.12(b)**, it is noticeable that the incorporation of chitosan with positive amino groups was not only beneficial for the anionic pollutants adsorption, but it also resulted in the enhancement of Pb (II) and Cu (II) adsorption due to their chelation with the amino groups of chitosan.

The solution pH influences the adsorption of heavy metals to a great extent whereby the adsorption of most heavy metals is favourable at high pH condition, except for the anionic metals such as Cr (VI). At low pH condition, protonation of the surface functional groups of 3D graphene adsorbent results in electrostatic repulsion. Furthermore, the relatively high concentration of H^+ competes with the heavy metal ions for the sorption sites, reducing further the adsorption capacity. An improvement in adsorption capacity is usually observed at higher pH owing to the stronger electrostatic attraction between the heavy metal and deprotonated surface functional groups of 3D graphene adsorbent. Nonetheless, too high pH (>7) should be avoided to circumvent the formation of metal hydroxide as a result of the hydrolysis of metal ions [13, 63, 131].

Furthermore, the ionic strength or coexisting cations can impose significant influences on the adsorption capacity [145, 153]. Generally, the positively charged coexisting ions can compete with the heavy metal for sorption sites according to the adsorption affinity between the metal and the adsorbent. A high ionic strength impedes the ionisation of the oxygenated functional groups in the 3D graphene adsorbent, weakening their electrostatic interaction with the heavy metal and consequently, lowering the adsorption capacity. Meanwhile, the diffusion of metal ions from the solution to the adsorbent surface is hampered as the ionic strength can alter the activity coefficient of the metal [154].

Generally, GO sheets possess strong affinity for various heavy metals, but it changes with the type of heavy metal. It was reported that among Cu (II), Zn (II), Cd (II) and Pb (II), the GO sheets had higher tendency to adsorb Pb (II), followed by Cu (II), Cd (II) and Zn (II) [155]. This order was in accordance with both the metal electronegativity and standard reduction potential, where stronger electrostatic interaction occurred for heavy metals with higher electronegativity and more positive standard reduction potential. The standard reduction potential for Pb (II), Cu (II), Cd (II) and Zn (II) were reported as -0.1262, -0.3419, -0.4030 and -0.7618 V, respectively [156], indicating that Pb (II) was more likely to be reduced. Nonetheless, this affinity order may only be true for pristine GO and change when additional chemical functional groups are incorporated within the GO sheets. For instance, the GO-DNA gel fabricated by Cheng et al. [115] showed a higher affinity for Cu (II) instead of Pb (II) which was mainly due to the presence of additional amino groups. The authors proposed that there was surface complexation between the heavy metal and the amino groups, where Cu (II) has a higher constant of complexing stability as compared to Pb (II). Hence, the affinity order for heavy metals should be investigated for different systems.

2.2.2.2 Column adsorption of heavy metals

Several studies have demonstrated the feasibility of 3D graphene materials as column packing for the adsorption of heavy metals [92, 157]. Zou et al. [157] evaluated the applicability of 3D rGO/Mn_3O_4 composite in column adsorption of Sb (III) and Sb (V) at initial metal concentration of 225 ppb. The breakthrough curves of their studies are presented in **Fig. 2.13**. A typical "S" shape profile was

observed for the experiments and the breakthrough volumes for Sb (III) and Sb (V) were 859 mL and 633 mL, respectively, suggesting the as-prepared graphene composite as an effective adsorbent for both Sb (III) and Sb (V).

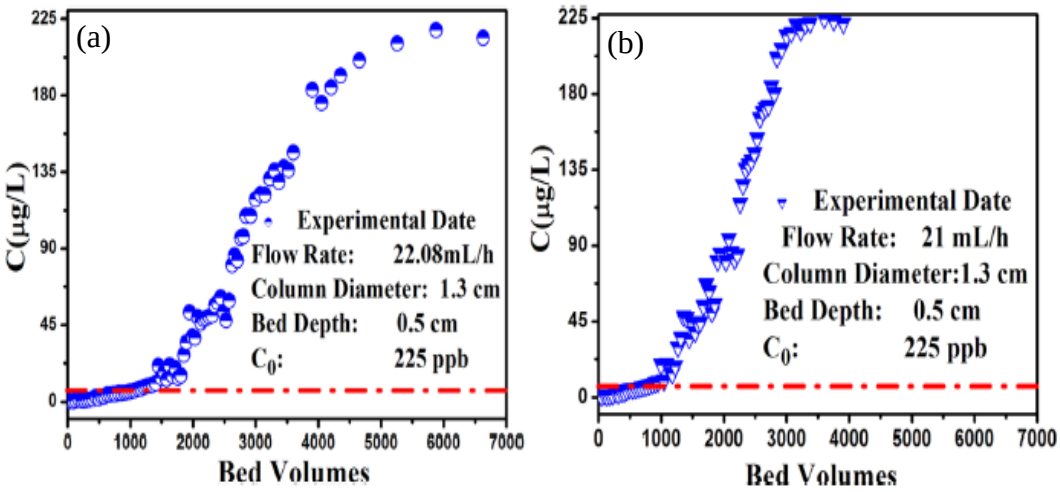


Fig. 2.13 Breakthrough curves for column adsorption of (a) Sb (III) and (b) Sb (V). Reprinted with permission from [157]. Copyright 2016 American Chemical Society.

2.2.2.3 Regeneration of heavy metal-loaded 3D graphene adsorbents

A promising adsorbent should possess both high adsorption capability and recyclability. Regeneration of spent adsorbents offers two major advantages which include minimising the overall operating cost and preventing the formation of secondary solid waste. The regeneration of heavy metal loaded adsorbents is commonly performed by contacting with acids [13, 53, 158-160], alkalis [13, 151, 158] or solvents [149, 161]. As an illustration, the GO/cellulose hydrogel prepared by Chen et al. [158] was regenerated using 0.1 M HCl solution followed by 0.1 M NaOH after the adsorption of Cu (II). The immersion of the exhausted adsorbent in acidic solution facilitated desorption of the heavy metal as the protons competed

vigorously with the metal ions for the active sites. After treating with basic solution, the carboxyl group of the adsorbent was transformed to $–COO^-$ groups which adsorbed Cu (II) via electrostatic interaction. The adsorbent was able to maintain its adsorption capacity even after five adsorption-desorption cycles. Liang et al. [149] studied the reutilisation ability of tetraethylenetetramine/polypyrrole/GO aerogel by adopting a variety of eluting agents including water, acid, alkali and thiourea. Among these desorption agents, acidic thiourea solution was reported to be the most effective as the adsorbent was able to retain 93% of its initial adsorption capacity after five adsorption-desorption cycles. Therefore, the choice of appropriate eluting agent is very crucial for efficient regeneration and thus, minimising the substitution cost for the exhausted adsorbent.

Chapter 3. Materials and methods

The present chapter covers the materials and methods of the research work. Initially, the preparation methods for graphene oxide (GO) and new 3D graphene materials, such as graphene oxide/chitosan (GOCA) and 3D graphene oxide/xanthan/titanium dioxide (3D GXT) composites, were described, followed by methods on characterisation of the materials using several analytical tools. The descriptions on the procedures for batch adsorption study and optimisation evaluation by response surface methodology are provided in this chapter. Finally, a detailed methodology on fixed-bed adsorption test and data analysis are provided.

3.1 Materials

Graphite, chitosan (high molecular weight), titanium isopropoxide (TTIP), potassium permanganate ($KMnO_4$), sodium nitrate ($NaNO_3$), Metanil Yellow (MY) dye ($C_{18}H_{14}N_3NaO_3S$, 375.38 g/mol, 70 % dye content) and Reactive Black 5 (RB5) dye ($C_{26}H_{21}N_5Na_4O_{19}S_6$, 991.82 g/mol, 50 % dye content) were obtained from Sigma Aldrich, Germany. Sulphuric acid (H_2SO_4, 98 %), hydrogen peroxide (H_2O_2, 30 %) and hydrochloric acid (HCl, 37 %), acetic acid (CH_3COOH), potassium nitrate (KNO_3) and sodium hydroxide (NaOH) were supplied by Fischer Scientific, USA. Xanthan, cadmium nitrate tetrahydrate ($Cd(NO_3)_2{\cdot}4H_2O$, 308.482 g/mol) and lead nitrate ($Pb(NO_3)_2$, 331.2 g/mol) were purchased from R&M Chemicals, Acros Organics and Merck, respectively. All the chemicals were used as received without any purification and deionised (DI) water was used for all experiments.

3.2 Preparation of GO and 3D graphene composites

Firstly, GO was prepared according to the modified Hummers method [162]. 1 g of graphite powder and 0.5 g of $NaNO_3$ were added into a 250 mL conical flask, followed by the addition of 23 mL of concentrated H_2SO_4. The mixture was stirred for 2.5 h and kept well below 20 ^oC in an ice-bath. 3 g of $KMnO_4$ was then added gradually into the mixture and stirred for another 1 h. Thereafter, the temperature was raised to 35 ^oC and maintained for 0.5 h. 46 mL of DI water was added into the mixture and heated to 98 ^oC for 1 h. Next, 140 mL of DI water was added and stirred for 0.5 h. In order to terminate the chemical reaction, 10 mL of H_2O_2 was added and stirred for 0.5 h. The obtained yellowish brown mixture was filtered and washed alternately with DI water and 0.1 M HCl to remove impurities. Finally, the solid particles were rinsed several times with DI water until a neutral pH was recorded. Dark brown GO flakes were obtained after drying the wet filter cake at 60 ^oC for 3 days.

For the synthesis of GOCA, a GO suspension of 2 mg/mL was initially prepared by ultrasonication for 0.5 h. A chitosan solution of 20 mg/mL was then obtained by dissolving chitosan powder in 0.2 M acetic acid solution. Equal volumes of GO suspension and chitosan solution were mixed and stirred for 24 h to obtain a homogeneous mixture. Next, the mixture was transferred to a mould and frozen at -20 ^oC for 24 h. The freezing process was necessary for the formation of ice crystals within the GO/chitosan matrix to provide structural support for the composite material. Upon lyophilisation at -55 ℃ and under vacuum condition for 24 h, the ice crystals inside the structure sublimated, forming a porous interconnected

structure between the GO and chitosan. The final product was labelled as GOCA and stored in a desiccator.

The 3D GXT composite was prepared as follows: GO suspension of concentration 2 mg/mL was prepared by exfoliating 200 mg of graphite oxide in 0.1 L of deionised water for 0.5 h. Then, 1 mL of TTIP was pipetted into the GO solution and the mixture was sonicated for 0.5 h. Upon sonication, 2 g of xanthan biomass was added into the mixture. The mixture was stirred for another 8 h and then frozen at -20 ^{o}C overnight. The solidified mixture was lyophilised at -55 ^{o}C for 24 h and lastly, heated at 100 ^{o}C for 24 h to form the 3D GXT composite.

3.3 Characterisation tests

The scanning electron microscopy image and elemental composition of adsorbents were analysed using field emissions scanning electron microscope (FESEM) and energy dispersive X-ray spectroscopy (EDX) (FEI Quanta 400F, USA), respectively. The sample was mounted on a conductive carbon tape to create a clean background for better visualisation prior to analysis in the instrument under a vacuum condition.

Fourier transform infrared spectroscopy (FTIR, Spectrum RXI Perkin-Elmer, USA) analysis was carried out to identify the chemical functional groups in the adsorbents. 10 mg of sample was gently pressed against a high refractive index diamond prism by a stainless steel tip. The sample was scanned through infrared wavelength ranging from 400 to 4000 cm^{-1} at 2 cm^{-1} spectral resolution.

Thermogravimetric analysis (TGA, Mettler Toledo, USA) was performed to examine the thermal properties of the graphene composites under a nitrogen flow

of 50 mL/min. The heating rate was set at 5 °C/min while the TGA temperature was increased from 25 to 800 °C. After keeping the sample at 800 °C for 10 min, the nitrogen gas was switched to oxygen gas (50 mL/min) and the temperature was increased to 900 °C and maintained for 15 min.

The crystallinity of sample was determined by powder X-ray diffraction (XRD, Panalytical X'Pert-Pro diffractometer, USA) operated at a scan rate of 2 °/min from 10 to 90 ° with Cu-Kα radiation source (λ = 1.5406 Å) generated at 45 kV and 40 mA.

The point of zero charge (PZC) of the adsorbents was conducted to examine its surface charge properties. Firstly, a fixed mass of adsorbent was added to a series of 0.1 M KNO_3 solutions of constant volume but different initial pH (2-11). The pH of solutions was altered using either 0.1 M HCl or 0.1 M NaOH. The mixtures were then agitated in a waterbath shaker (Protech, Malaysia) at 200 rpm and 30 °C for 24 h. The final pH of the solutions was recorded.

3.4 Batch adsorption studies

The efficiencies of the as-synthesised adsorbents in eliminating the representative dyes (MY and RB5) and heavy metals (Cd and Pb) were expressed in terms of removal efficiency, R (%), and adsorption capacity, q_e (mg/g), as given by **Eqs. (3.1)** and **(3.2)**, respectively.

$$R = \frac{(C_0 - C_e)}{C_o} \times 100\% \quad \textbf{(3.1)}$$

$$q_e = \frac{(C_0 - C_e)V}{W} \quad \textbf{(3.2)}$$

where C_0 (mg/L) and C_e (mg/L) are the adsorbate concentration at the beginning and equilibrium, respectively, V (L) is the volume of solution and W (g) is the mass

of adsorbent. The effects of process parameters on the dyes and heavy metals removal were examined, such as adsorbent mass, shaking speed, initial pH, initial concentration and temperature. The control experiments which were carried out under similar conditions but without adsorbent, confirmed that the removal of the adsorbates by sorption on the glass wall, volatilisation or degradation was not significant.

For the dyes removal, 1000 mg/L of MY and RB5 dyes stock solutions were prepared by dissolving 1.429 and 2 g of the respective dye in 1 L of DI water. The dye solutions of desired concentrations were attained by diluting the stock solution with appropriate amount of DI water.

For both dyes removal, the adsorption experiments were conducted in 100 mL conical flasks containing a fixed mass of GOCA and 30 mL of dye solution of known concentration. The mixtures were agitated for 2 h in the waterbath shaker with the temperature controlled. The preliminary test indicated that adsorption equilibrium could be achieved within this contact time. The experimental conditions used for the dyes adsorption studies are summarised in **Table 3.1**. After adsorption, approximately 4 mL of dye solution was withdrawn for dye concentration measurement by UV-vis spectrophotometer (Perkin-Elmer Lamda 35, USA) at maximum absorbance values of 440 and 598 nm for MY and RB5 dyes, respectively.

Table 3.1 Experimental conditions for MY and RB5 dyes adsorption onto GOCA.

MY dye

Variables	**pH**	***W*** **(mg)**	***C*$_o$** **(mg/L)**	***t*** **(min)**	***T*** **(ºC)**	***S*** **(rpm)**
Adsorbent mass	5.8	1 - 50	50	120	30	200
Shaking speed	5.8	5	50	90 (1, 2, 3, 5, 7, 10, 15, 20, 30, 40, 60, 90)	30	50 - 250
Initial pH	2 - 11	5	50	120	30	200
Kinetic study	5.8	5	10 – 90	90 (1, 2, 3, 5, 7, 10, 15, 20, 30, 40, 60, 90)	30	200
Isotherm study	5.8	5	20 - 600	120	30 - 70	200

RB5 dye

Variables	**pH**	***W*** **(mg)**	***C*$_o$** **(mg/L)**	***t*** **(min)**	***T*** **(ºC)**	***S*** **(rpm)**
Adsorbent mass	5.3	1 - 50	100	120	30	150
Shaking speed	5.3	10	100	90 (1, 2, 3, 5, 7, 10, 15, 20, 30, 40, 60, 90)	30	50 - 250
Initial pH	2 - 11	10	100	120	30	150
Kinetic study	5.3	10	50 – 150	90 (1, 2, 3, 5, 7, 10, 15, 20, 30, 40, 60, 90)	30	150
Isotherm study	5.3	10	100 - 600	120	30 - 70	150

Note: *W* (mg) – adsorbent mass, C_o (mg/L) – initial concentration, *t* (min) – contact time, *T* (ºC) – temperature and *S* (rpm) – shaking speed.

For the heavy metals removal, the Pb stock solution of concentration 1000 mg/L was made by dissolving 1.598 g of $Pb(NO_3)_2$ in 1 L of DI water. Meanwhile, 1000 mg/L of Cd stock solution was prepared by dissolving 2.744 g of $Cd(NO_3)_2 \cdot 4H_2O$ into 1 L of DI water. Then Pb and Cd solutions of specific concentrations for different experiments were prepared from the stock solutions by adding in known quantity of DI water.

For the adsorption experiments, a certain mass of 3D GXT composite was placed in several conical flasks filled with 50 mL Pb/ 30 mL Cd solutions of fixed concentration. The flasks were shaken in the waterbath at 200 rpm and 30 ^{o}C for 4 h. The experimental conditions for each heavy metal removal are summarised in **Table 3.2**. After adsorption, a certain amount of sample was collected for the heavy metal concentration detection using atomic absorption spectroscope (AAS, Perkin Elmer, USA).

Table 3.2 Experimental conditions for Pb and Cd adsorption onto 3D GXT.

Pb						
Variables	**pH**	***W*** **(mg)**	***C*$_o$** **(mg/L)**	***t*** **(min)**	***T*** **(ºC)**	***S*** **(rpm)**
Adsorbent mass	5.2	5 - 50	50	180	30	200
Shaking speed	5.2	25	50	180 (3, 5, 7, 10, 15, 20, 30, 40, 60, 90, 120, 180)	30	50 - 200
Initial pH	2 - 6	25	50	180	30	200
Kinetic study	5.2	25	20 – 60	240 (3, 5, 7, 10, 20, 30, 40, 60, 90, 120, 180, 240)	30	200
Isotherm study	5.2	25	10 - 300	240	30 - 70	200
Cd						
Variables	**pH**	***W*** **(mg)**	***C*$_o$** **(mg/L)**	***t*** **(min)**	***T*** **(ºC)**	***S*** **(rpm)**
Adsorbent mass	5.2	5 - 50	30	240	30	200
Shaking speed	5.2	25	30	240 (3, 5, 7, 10, 20, 30, 40, 60, 90, 120, 180, 240)	30	50 - 200
Initial pH	2 - 7	25	30	180	30	200
Kinetic study	5.2	25	20 – 100	240 (3, 5, 7, 10, 20, 30, 40, 60, 90, 120, 180, 240)	30	200
Isotherm study	5.2	25	10 - 300	240	30 - 70	200

Note: *W* (mg) – adsorbent mass, C_o (mg/L) – initial concentration, *t* (min) – contact time, *T* (ºC) – temperature and *S* (rpm) – shaking speed.

3.4.1 Adsorption kinetic and equilibrium models fitting

In order to identify the best equilibrium isotherm for the adsorption system, the experimental data were fitted to two isotherm models such as the Langmuir and Freundlich models. Kinetic models such as the pseudo-first-order (PFO), pseudo-second-order (PSO) and Elovich models were fitted to the time-dependent experimental data for evaluating the adsorption rate and mechanism. The kinetic data were also fitted to the intraparticle diffusion model for the determination of rate-limiting step for the process. Microsoft Excel Solver was employed to predict the model parameters by non-linear regression. The goodness-of-fit of different models was evaluated using several error functions such as coefficient of determination (R^2), chi-square (X^2), root mean square error ($RMSE$), average relative error (ARE), standard deviation of relative errors (S_{RE}), Marquardt's percent standard deviation ($MPSD$) and sum of the squares of errors ($ERRSQ$). Since each error function would result in a different set of model parameters, the sum of normalised errors (SNE) approach was used to identify the best equilibrium and kinetic models by normalising across the error functions [163]. The expressions for the adsorption equilibrium and kinetic models, as well as the error functions are provided in **Table 3.3**.

Table 3.3 Expressions for adsorption equilibrium and kinetic models, and error functions.

Model	Equation	Reference
Equilibrium		
Langmuir	$q_e = \frac{q_m K_L C_e}{1 + K_L C_e}$	[164]
Freundlich	$q_e = K_f C_e^{\frac{1}{n}}$	[165]
Kinetic		
Pseudo-first-order (PFO)	$q_t = q_e(1 - e^{-k_1 t})$	[166]
Pseudo-second-order (PSO)	$q_t = \frac{k_2 t q_e^2}{1 + k_2 t q_e}$	[167]
Elovich	$q_t = \frac{1}{\beta} ln\alpha\beta + \frac{1}{\beta} lnt$	[168]
Intraparticle diffusion	$q_t = k_p\sqrt{t} + C$	[169]
Error function		
Correlation coefficient (R^2)	$R^2 = \frac{\sum(q_{e,exp} - \bar{q}_{e,cal})^2}{\sum(q_{e,exp} - \bar{q}_{e,cal})^2 + \sum(q_{e,exp} - q_{e,cal})^2}$	[170]
Chi-square (X^2)	$X^2 = \sum \frac{(q_{e,exp} - q_{e,cal})^2}{q_{e,cal}}$	[171]
Root mean square error (*RMSE*)	$RMSE = \sqrt{\frac{1}{n-2}\sum(q_{e,exp} - q_{e,cal})^2}$	[172]
Average relative error (*ARE*)	$ARE = \frac{100}{n}\sum\left\|\frac{q_{e,exp} - q_{e,cal}}{q_{e,exp}}\right\|$	[173]
Standard deviation of relative error (S_{RE})	$S_{RE} = \sqrt{\frac{\sum[(q_{e,exp} - q_{e,cal}) - ARE]^2}{n-1}}$	[170]
Marquardt's percent standard deviation (*MPSD*)	$MPSD = 100\sqrt{\frac{1}{n-p}\sum\left(\frac{q_{e,exp} - q_{e,cal}}{q_{e,exp}}\right)^2}$	[174]
Sum square errors (*ERRSQ*)	$ERRSQ = \sum(q_{e,exp} - q_{e,cal})^2$	[172]

Nomenclature: q_m (mg/g) – Langmuir monolayer adsorption capacity, K_L (L/mg) – Langmuir isotherm constant, K_f ((mg/g)(L/mg)$^{1/n}$) – Freundlich isotherm constant, n (dimensionless) – Freundlich exponent, k_1 (1/min) – PFO rate constant, k_2 (g/mg.min) – PSO rate constant, α (mg/g.min) – Elovich initial adsorption rate, β (g/mg) – Elovich constant, k_p (mg/g.min$^{0.5}$) – intraparticle diffusion rate constant, C (mg/g) – intercept of intraparticle diffusion plot, $q_{e,exp}$ (mg/g) – equilibrium adsorption capacity obtained from experiment, $q_{e,cal}$ (mg/g) – equilibrium adsorption capacity calculated from model, n – number of experimental data and p – number of isotherm parameters.

3.4.2 Thermodynamic study

The thermodynamic parameters for the adsorption process including the Gibbs free energy change, ΔG (kJ/mol), enthalpy change, ΔH (kJ/mol), and entropy change, ΔS (kJ/mol.K), were determined using **Eq. (3.3)** and **Eq. (3.4)**:

$$\Delta G = -RTlnK_C \quad \textbf{(3.3)}$$

$$\Delta G = \Delta H - T\Delta S \quad \textbf{(3.4)}$$

where R (J/mol.K) is the universal gas constant, T (K) is the absolute temperature and K_C ($= q_e/C_e$) is the equilibrium constant. The plot of ΔG versus T gives the values of ΔS and ΔH from the slope and intercept, respectively.

3.5 Response surface methodology

Response surface methodology (RSM) is the most preferred statistical technique for designing experimental runs as it is easy to use and provides greater accuracy for the testing data [175]. For optimisation study, RSM is usually applied in combination with Box-Behnken design (BBD) and central composite design (CCD). BBD varies the experimental points over 3 levels only. Nevertheless, CCD is always preferred as it randomises and changes the experimental points over 5 levels (-α, -1, 0, +1, +α) [163] which can define the interactions between 4 pivotal adsorption parameters and provide a more comprehensive study. The adsorption capacity was assigned as the response in the design of experiments. In addition, the highest adsorption capacity was attained by optimising the process parameters using the Derringer's desirability method [176].

A quadratic mathematical model as expressed in **Eq. (3.5)** was employed to elucidate the behaviour of the adsorption system:

$$Y = \beta_0 + \sum_{i=1}^{k} \beta_i X_i + \sum_{i=1}^{k} \beta_{ii} X_i^2 + \sum \sum_{i<j} \beta_{ij} X_i X_j + \varepsilon \quad \textbf{(3.5)}$$

where Y is the predicted response, X_i and X_j are the input factors which influence the response, β_0 represents the intercept term, β_i, β_{ii} and β_{ij} are the linear, quadratic and interaction terms, respectively, k is the number of factors and ε denotes the random error. Analysis of variance (ANOVA) was used to determine the best model and significance of each model term using the F-test (Fisher's test), p-value (probability-value), lack-of-fit test and other adequacy measures.

For MY dye removal, the interactive effects between the four adsorption factors, namely adsorbent mass (A: 2 – 10 mg), initial MY dye concentration (B: 100 – 500 mg/L), contact time (C: 20 – 60 min) and shaking speed (D: 100 – 200 rpm) were investigated using RSM-CCD. Meanwhile, the studied factors for RB5 dye adsorption were adsorbent mass (A: 4 – 12 mg), initial RB5 dye concentration (B: 100 – 500 mg/L), contact time (C: 30 – 90 min) and temperature (D: 30 – 70 ℃).

For the Pb removal, 4 important parameters were varied: adsorbent weight (A: 10 – 30 mg), initial Pb concentration (B: 100 – 300 mg/L), shaking speed (C: 100 – 200 rpm) and temperature (D: 30 – 70 ^{o}C), while the response was Pb adsorption capacity (q, mg/g). The influences of four variables, namely adsorbent mass (A: 15 – 35 mg), initial Cd concentration (B: 100 – 300 mg/L), initial pH (C: 3 - 7) and shaking speed (D: 100 – 200 rpm)) were studied for the Cd-3D GXT adsorption system.

3.6 Regeneration study

The reusability of GOCA was assessed by conducting 5 successive cycles of adsorption-desorption tests. The MY dye-loaded GOCA contacted initially with 50

mg/L of the dye solution for 1.5 h, was washed several times with DI water to remove any unadsorbed MY dye. Thereafter, the dye-loaded GOCA was desorbed with 30 mL of 0.1 M NaOH for 1.5 h and then regenerated with 0.1 M HCl for 0.25 h. The regenerated GOCA was rinsed with DI water and reutilised in subsequent adsorption experiment. Similar procedures were repeated using RB5 dye solution of 100 mg/L concentration at a contact time of 1 h.

Similarly, the reusability of the 3D GXT composite was evaluated by performing 5 continuous cycles of adsorption-regeneration tests. Initially, the composite was contacted with 50 mL Pb solution of concentration 50 mg/L for 4 h, at 200 rpm and 30 ^{o}C. The Pb-loaded composite was eluted with 0.1 M HCl for 1 h. The recycled adsorbent was washed thoroughly with DI water before the next cycle of adsorption. Similar procedures were repeated for Cd removal using 30 mL Cd solution of concentration 30 mg/L.

3.7 Fixed-bed column adsorption studies

The continuous dye and heavy metal adsorption studies were carried out in borosilicate glass columns with an internal diameter of 10 mm and total length of 30 cm. All the experiments were performed without pH modification and at room temperature. Glass beads were placed at both ends of the fixed-bed to support the graphene bed and ensure uniform liquid distribution (**Fig. 3.1**). The adsorbate solution was pumped in a down-flow manner through the column at a controlled flowrate using a syringe pump (Kd Scientific – 200). The solution samples were collected at the bottom of the column at specific time intervals.

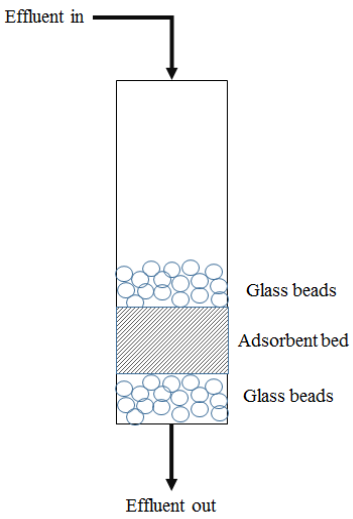


Fig 3.1 Schematic diagram of fixed-bed column set-up.

For the dyes removal, several parameters affecting the column performance were investigated such as bed height (3, 4 and 5 cm corresponding to 0.1, 0.15 and 0.2 g of GOCA, respectively), inlet concentration (100, 150 and 200 mg/L for MY dye and 100, 200 and 300 mg/L for RB5 dye) and feed flowrate (2, 3 and 4 mL/min). The concentration of the samples was examined using UV-vis spectrophotometer (Perkin-Elmer Lamda 35, USA) at maximum absorbance values of 598 and 440 nm for RB5 and MY dyes, respectively.

For the heavy metals removal, the effect of bed height on the column performance was investigated using 2, 3 and 4 cm beds, which corresponded to 0.1, 0.15 and 0.2 g of 3D GXT composite, respectively. The influence of inlet concentration was studied at 100, 150 and 200 mg/L for Pb, and 50, 75 and 100 mg/L for Cd. The impact of feed flowrate was examined at three different levels: 1, 2 and 3 mL/min. The heavy metal concentrations were determined using atomic absorption spectroscope (AAS, Perkin Elmer, USA).

The breakthrough curve which determines the adsorbent affinity and pathways, is generally plotted as C_t/C_o against time, *t*, where C_t ad C_o are the concentration at time, *t*, and beginning, respectively. The breakthrough time (t_b, min) refers to the time at which 5 % of initial concentration was detected in the effluent. The exhaustion time (t_e, min) of the column was determined at the time when the concentration of the effluent reaches 90 % of the inlet concentration. Several parameters could be obtained from the breakthrough curve which include total volume of effluent treated (V_t, mL), total amount of adsorbate adsorbed (m_{ads}, mg) and bed adsorption capacity (q, mg/g), as represented by **Eq. (3.6)**, **Eq. (3.7)** and **Eq. (3.8)**.

$$V_t = Q \times t_e \quad \textbf{(3.6)}$$

$$m_{ads} = \frac{Q \times A}{1000} = \frac{Q}{1000} \int_{t=0}^{t=t_e} C \ dt \quad \textbf{(3.7)}$$

$$q = \frac{m_{ads}}{W} \quad \textbf{(3.8)}$$

where Q represents the flowrate (mL/min), A is the area under the breakthrough curve and W is the mass of adsorbent (mg).

3.7.1 Kinetic models for fixed-bed column adsorption

In order to understand the dynamic behaviour of column adsorption, several mathematical models were employed such as the Thomas, Yoon-Nelson and Adams-Bohart models.

The Thomas model developed based on the Langmuir isotherm and second-order reversible kinetics [177], is expressed by **Eq. (3.9)**.

$$\frac{C_t}{C_o} = \frac{1}{1+exp\left[\left(\frac{k_{TH}q_oW}{Q}\right)-k_{TH}C_ot\right]} \quad \textbf{(3.9)}$$

where k_{TH} and q_o are the Thomas's constant (mL/min.mg) and theoretical adsorption capacity (mg/g), respectively.

The Yoon-Nelson model is less complicated as it requires no information regarding the adsorbate characteristics, adsorbent nature and physical properties of the adsorption bed [178]. This model also predicted the time for 50% breakthrough. The Yoon-Nelson model in non-linear form is shown by **Eq. (3.10)**.

$$\frac{C_t}{C_o} = \frac{1}{1+exp[k_{YN}\times(\tau-t)]} \quad \textbf{(3.10)}$$

where k_{YN} refers to the reaction constant (min^{-1}) and τ is the time (min) to reach 50% breakthrough.

The Adams-Bohart model assumes that the adsorption rate is proportional to the adsorbent adsorption capacity and adsorbate concentration. Generally, this model which is represented by **Eq. (3.11)**, is used to describe the initial part (<50%) of the breakthrough curve [179]:

$$\frac{C_t}{C_o} = exp(k_{AB}C_ot - k_{AB}N_oZ/v) \quad \textbf{(3.11)}$$

where k_{AB} is the rate constant (L/mg.min), N_o is volumetric adsorption capacity (mg/L), v is the linear velocity (cm/min) and Z is the bed height (cm).

The parameters for all these models were determined by non-linear regression using Microsoft Excel Solver. Correlation coefficient (R^2) was employed to determine the fit of different models to the experimental data, whereby R^2 closest to one indicates the most appropriate model for describing the adsorption system.

Chapter 4. Batch adsorption of Metanil Yellow and Reactive Black 5 dyes onto 3D GO/chitosan aerogel

4.1 Introduction

The discharge of large quantity of organic dyes by diverse industries which include textile, paper and pulp, pharmaceutical and cosmetic, plastic and food manufacturing has resulted in major water pollution [180]. The presence of dyes in water bodies not only causes unpleasant aesthetic view to the environment, but also reduces transmission of sunlight into the water body required by aquatic plants for photosynthesis [181]. Metanil Yellow (MY, 3-(4-anilinophenylazo) benzene sulphonic acid sodium salt) dye which is an azo dye, is widely applied in leather and textile dyeing, paper staining and soap colouring. Despite being non-permitted in the food and drink industries, MY dye is still used as a colourant in sweet meat, ice creams, beverages and turmeric coating [181]. The potential health hazards of MY dye include infertility and carcinogenicity [2]. It has also been reported to be responsible for toxic methemoglobinemia [182] and cyanosis [183] in humans upon oral ingestion and allergic dermatitis upon skin contact [184]. Moreover, Reactive Black 5 (RB5) dye, a recalcitrant dye, is employed extensively in the textile industry [185]. During the dyeing stage, the vinyl sulphone moieties of RB5 dye were hydrolysed to 2-hydroxy ethyl sulphone groups which could no longer be attached to the fabrics, and thus were released to the water body. An earlier study indicated that long term exposure to reactive dyes leads to health issues such as asthma, rhinitis, allergic conjunctivitis, dermatitis and other allergic reactions [3]. Furthermore, RB5 dye comprises aromatic moieties which induce carcinogenic and

mutagenic effects [186]. The aromatic amines are readily adsorbed through the skin as they can be mobilised by water or sweat, thereby leading to an increased risk of cancer [187]. Therefore, this has prompted extensive investigations on the dye decontamination methods.

Both MY and RB5 dyes are non-biodegradable, highly stable and resistant against heat, light and oxidising agents, making them very hard to be treated in existing wastewater treatment facilities [188]. Recently, adsorption has been considered as a promising technology for dye treatment due to its simple operation, low cost and high effectiveness in azo dye removal [189].

Chitosan, the second most abundant natural biopolymer, is a relatively low cost polyaminosaccharide [190]. It can be derived from biowastes such as the exoskeletons of crustaceans (prawns and crabs) via deacetylation process [191]. The use of chitosan adsorbent in wastewater remediation has met with considerable success due to the abundant amine and hydroxyl functional groups in this material, as well as its low toxicity, good biocompatibility and biodegradability [192]. However, raw chitosan has poor mechanical strength and readily dissolves in acidic condition. These properties have hindered its application in large scale operation. Hence, researchers have focused their efforts in overcoming these limitations through modification or cross-linking of the raw chitosan.

Graphene oxide (GO) is a two-dimensional (2D) sp^2 hybridised single carbon atom decorated with oxygeneous functional groups such as hydroxyl, epoxide, carbonyl and carboxylic groups. It has been used as a cost effective carbon precursor for the improvement of mechanical, chemical, thermal and electrical properties of composite materials in various applications [193, 194]. Though GO

has exhibited remarkable adsorption performance in dyes decontamination, the high colloidal stability and tendency to aggregate through strong π-π interaction have restricted its application as a practical adsorbent in wastewater treatment [195].

Based on the advantages of both chitosan and GO, studies have been conducted to develop chitosan/GO composites for dyes decontamination [20, 196, 197]. GO generally can bind with chitosan through coordination, electrostatic interaction and covalent bonding between the amine group of chitosan and the oxygen group of GO to form chitosan/GO composites [192]. For instance, a magnetic chitosan/GO composite developed by Fan et al. [198] exhibited an adsorption capacity of 180.83 mg/g for Methylene Blue dye, while Zhang et al. [197] fabricated a chitosan/graphene nanoplate composite with adsorption capacities of 230.91 and 132.94 mg/g for Methyl Orange and Acid Red 1 dyes, respectively. Moreover, a porous β-cyclodextrin/chitosan functionalised GO was reported to have a high adsorption capacity (1134 mg/g) for Methylene Blue dye [196]. These literature data indicated the possibility of configuring various forms of chitosan/GO composites and their potential use in various dyes removal.

Response surface methodology (RSM) is commonly used to design experiments as it minimises the number of experiments and optimises the process. Many researchers have employed RSM for optimisation of dye removal. For instance, Kafshgari et al. [199] optimised the adsorption of Direct Red 16 dye onto multiwalled carbon nanotube using RSM and yielded a maximum adsorption capacity of 285.56 mg/g. Zaman et al. [200] reported that Methylene Blue dye adsorption capacity of GO-cellulose nanocomposite to be 334.19 mg/g under the RSM optimised conditions.

In this research, GO/chitosan aerogel (GOCA) was fabricated through facile ice-templating without the use of any cross-linking agents. The developed aerogel was used to sequester MY and RB5 dyes in aqueous solutions. The combination of GO and chitosan into three dimensional (3D) macrostructures offers several advantages which include: (1) an enhanced structural stability of the 3D graphene in water system, (2) elimination of cross-linking agent use for chitosan, (3) tuning of the surface charge of adsorbent to favour dye adsorption, and (4) facile separation of 3D graphene after adsorption. This is the first reported work which demonstrated the effective adsorption of MY and RB5 dyes onto GOCA through a series of experimental and modelling studies. Firstly, the effects of batch adsorption conditions such as adsorbent mass, shaking speed, initial pH, contact time, initial concentration and temperature, were investigated. Then, RSM was applied in the design of experiments to establish the interactive effects of adsorption factors and to optimise the process parameters. In order to gain more insights into the MY and RB5 dyes adsorption, the experimental data were fitted to different adsorption equilibrium, kinetic and thermodynamic models. Finally, regeneration study was carried out to determine the reusability of GOCA, an important aspect in the development of practical adsorbents.

4.2 Results and discussion

4.2.1 Characterisation of GOCA

The surface morphological structures of GOCA and chitosan were observed by FESEM. Chitosan exhibited irregular shaped particles with rough surface (**Fig. 4.1 (b)**) while the porous GOCA structure was interconnected by smooth fluffy sheets

(**Fig. 4.1 (a)**). Furthermore, several irregular wrapped zones were observed in GOCA which could be attributed to the presence of GO in the chitosan matrix. This indicated that the interaction between GO and chitosan has resulted in a loosely packed 3D structure of GOCA which is in accordance with others' findings [48, 90]. The results also suggested the homogeneous dispersion of chitosan on GO sheets and confirmed the successful incorporation of chitosan between the GO sheets probably via electrostatic interaction and hydrogen bonding.

A number of "micro-ribbons" emerged from the pore walls can also be seen in **Fig. 4.1 (a)** (as delineated in the red circles), which can be explained by the viscosity of solution. Owing to the strong electrostatic interactions between GO and chitosan, the mixture solution was viscous [6]. During the ice-templating process, ice crystals were formed where the viscous solution greatly retarded the growth of ice crystals and hence led to the formation of "micro-ribbons" [53, 86]. It was presumed that these "micro-ribbons" might enhance the adsorption performance by enlarging the surface area of 3D structure, thus enabling access to more functional groups for binding with the dye molecules [86]. Since these "micro-ribbons" were strong and not easily broken by ice [53], the structural stability of the 3D network structure was greatly improved which consequently allows the facile retrieval of adsorbent after adsorption. Besides, the 3D structure had interconnected pores which facilitated the diffusion of MY and RB5 dye molecules into the aerogel and this might enhance the adsorption capability of GOCA.

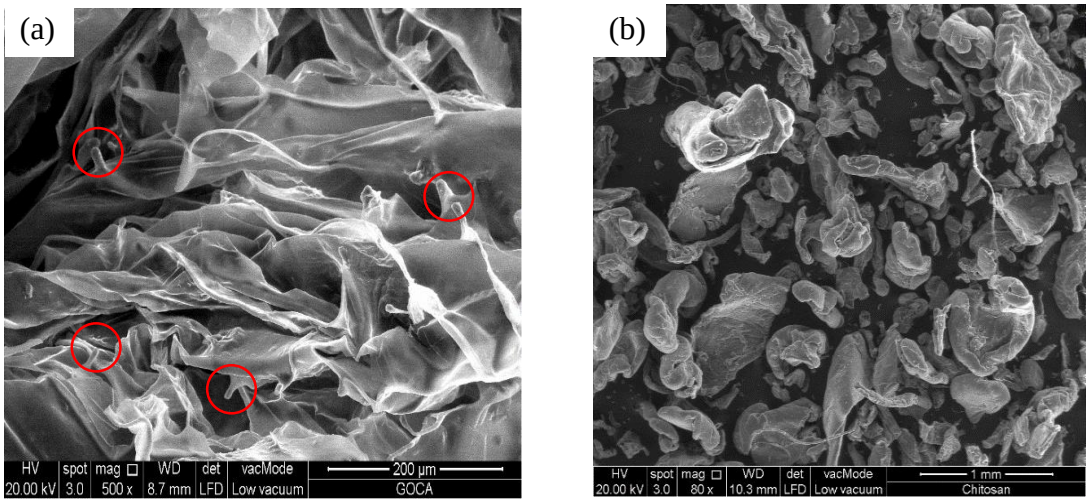


Fig. 4.1 FESEM images of (a) GOCA and (b) chitosan.

Apart from identifying the functional groups present in GOCA, FTIR analysis was also performed to determine the plausible interactions between GO and chitosan. As observed in **Fig. 4.2**, the precursors (GO and chitosan) and GOCA possessed similar absorption bands at around 1020 to 1040 cm^{-1} owing to the stretching vibration of C–O in –C–OH and also at around 3100 to 3300 cm^{-1} as a result of the stretching vibrations of –OH and $–NH_2$ [117]. The FTIR spectrum of GO manifested absorption peaks of GO located at 1226, 1617 and 1712 cm^{-1}. The peaks at 1226 and 1617 cm^{-1} corresponded to the stretching vibration of C–O in the epoxide group and C=C stretching mode of the sp^2 hybridised carbon skeletal network, respectively [48, 49, 90]. Meanwhile, the peak at 1712 cm^{-1} was assigned to the stretching vibration of C=O which could either be the carboxyl group on the edge of GO or the conjugated carbonyl group [48, 90]. The FTIR spectrum of chitosan and its characteristic peaks could be recognised at 1065 cm^{-1} (C–O stretching vibration), 1408 cm^{-1} (C–N axial deformation), 1546 cm^{-1} (N–H bending

of amine), 1636 cm^{-1} (N–H deformation of amide) and 2924 cm^{-1} (C–H stretching vibration) [89, 201, 202].

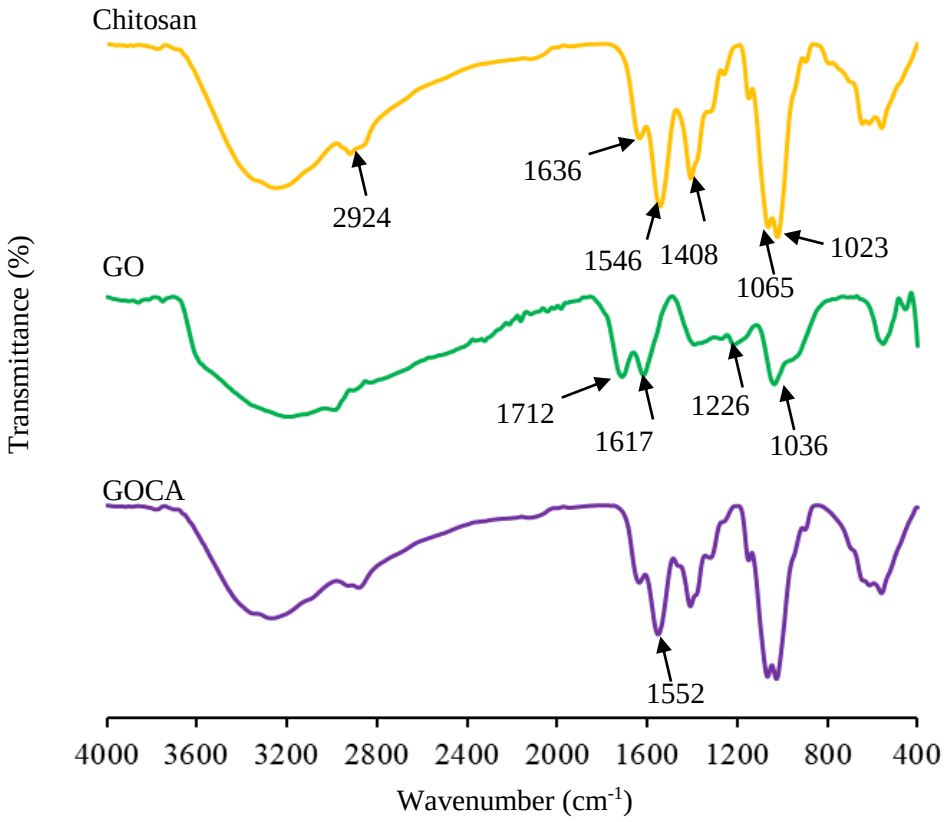


Fig. 4.2 FTIR spectra of chitosan, GO and GOCA.

From **Fig. 4.2**, it is noticeable that the absorption peak at 1712 cm^{-1} has disappeared, indicating the carboxyl groups of GO interacted with chitosan via hydrogen bonding [161, 202]. Moreover, the distinctive peak of chitosan at 1546 cm^{-1} representing the bending vibration of N–H shifted to 1552 cm^{-1} in GOCA. Meanwhile, the peak of GO at 1226 cm^{-1} was also absent in the FTIR spectrum of GOCA. This may be due to the chemical reaction between the epoxide group of GO and the amino group of chitosan [49]. Hence, the interactions between GO and chitosan provided the structural stability of GOCA [117]. Furthermore, the

resemblance between the spectra of chitosan and GOCA suggested that GOCA could eliminate both MY and RB5 dyes as the inherent cationic nature of chitosan which was beneficial for anionic dye adsorption has been embedded into the 3D graphene structure [203].

TGA provides information on the proximate analysis (moisture, volatile matter, fixed carbon and ash contents) of GOCA and chitosan samples [204]. The thermograms for GOCA and chitosan are presented in **Fig. 4.3**. Approximately 9.30 and 7.53 % weight losses were observed in GOCA and chitosan, respectively, from 30 to 110 ℃. The weight losses were attributed to the removal of physically adsorbed water and moisture content. Furthermore, the volatile organic matter for GOCA (52.95 %) and chitosan (57.18 %) were determined from the gradual weight loss from 110 to 800 ℃, resulting from the decomposition of chitosan chain [205]. An additional weight loss step was found in GOCA between 110 and 240 ℃ as compared to chitosan. This implied that about 6.88 % of GO functional groups experienced thermal decomposition, confirming the successful interaction between GO and chitosan [48, 90]. After complete oxidation of the organic compounds in GOCA, the aerogel exhibited relatively lesser final mass loss due to the presence of GO, further proving the successful development of GOCA. Additionally, the near vertical line at 800 ℃ and the horizontal line between 800 and 900 ℃ corresponded to the fixed carbon content and ash content of GOCA and chitosan, respectively [189, 206]. In comparison, GOCA possessed a lower fixed carbon content (23.05 %) and a higher ash content (14.7 %) than chitosan (30.59 % fixed carbon content and 4.7 % ash content). This study revealed that the incorporation of GO in chitosan

improved the thermal stability of chitosan, but yielded a relatively higher ash content and lower fixed carbon content than raw chitosan.

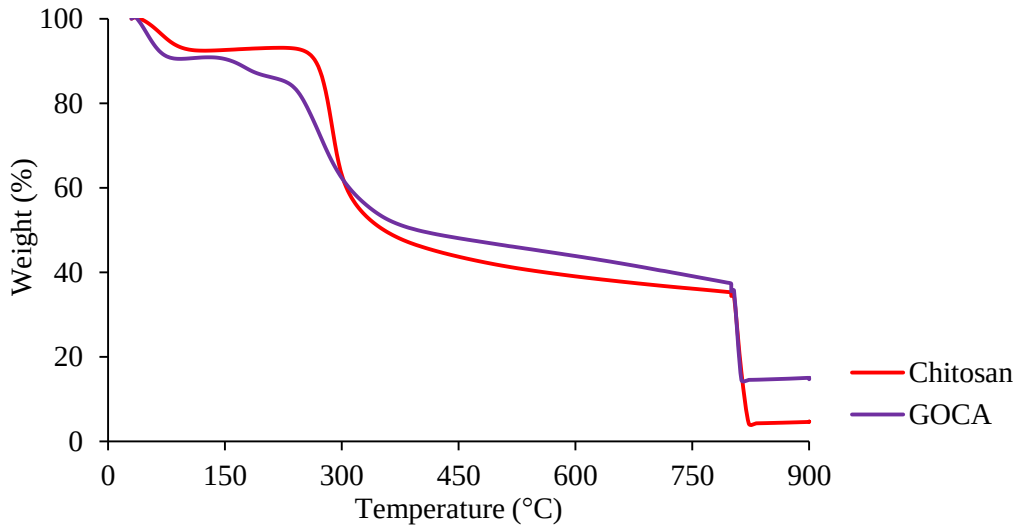


Fig. 4.3 Thermogravimetric curves of chitosan and GOCA.

Fig. 4.4 delineates the XRD spectra of chitosan and GOCA. Both the chitosan and GOCA portrayed a prominent broad peak of chitosan at 2θ about 21° indicating the amorphous nature of the materials. The absence of the distinctive peak of GO at 2θ approximately 11-12 ° could be due to the low content of GO within the GOCA. The similarity between the XRD patterns of both chitosan and GOCA implied that GO had negligible influence on the crystalline properties of chitosan [53].

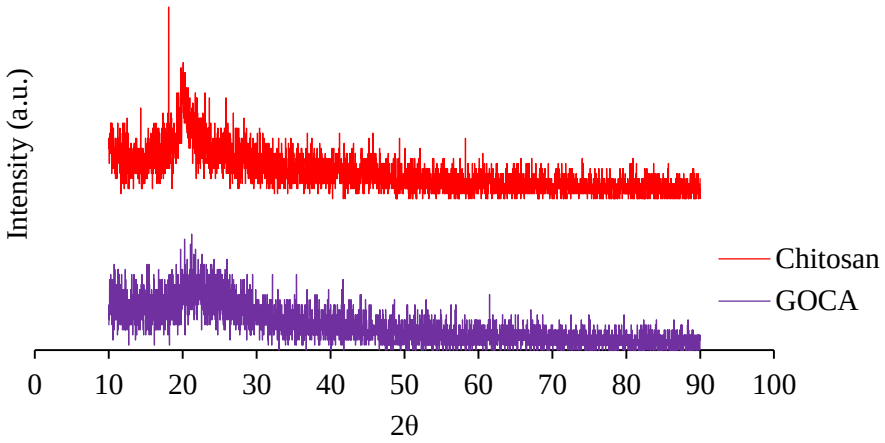


Fig. 4.4 XRD pattern of chitosan and GOCA.

4.2.2 Adsorption performance of GOCA

4.2.2.1 Effects of dosage, shaking speed and pH

From the economy standpoint, the identification of optimum adsorbent mass is crucial to ensure low cost and effective adsorption operation at the least amount of adsorbent. The influence of adsorbent mass on the removal efficiency of MY and RB5 dyes is illustrated in **Fig. 4.5 (a)** and **(b)**, respectively. The removal efficiency of MY dye increased from 34 to 94 % as the mass of GOCA was increased from 1 to 5 mg. A plateau trend for the removal of the dye was observed as more than 5 mg of GOCA was used. The initial sharp increase in MY dye removal was attributed to the increase in surface area and active sites for the dye adsorption [189]. For the RB5 dye, the removal percentage increased from 20.14 to 99.73 % with the increase in GOCA mass from 1 to 10 mg, but it deteriorated with further increase in adsorbent mass. At too high dosage, the adsorbent particles tended to aggregate which diminished the total surface area and consequently reduced the adsorption performance [189]. Unlike the positive trend observed for removal efficiency, the

adsorption capacity declined from 506 to 28 mg/g for MY dye, and from 689.83 to 55.81 mg/g for RB5 dye, with increasing adsorbent mass from 1 to 50 mg. These observations indicated that abundant active sites remained unsaturated as a result of increased mass at fixed dye concentration and solution volume [207]. As clearly evident from **Fig. 4.5 (a)** and **(b)**, the optimum adsorbent masses which yielded relatively high MY and RB5 dyes removal were 5 and 10 mg, respectively, and these masses were applied in subsequent experiments.

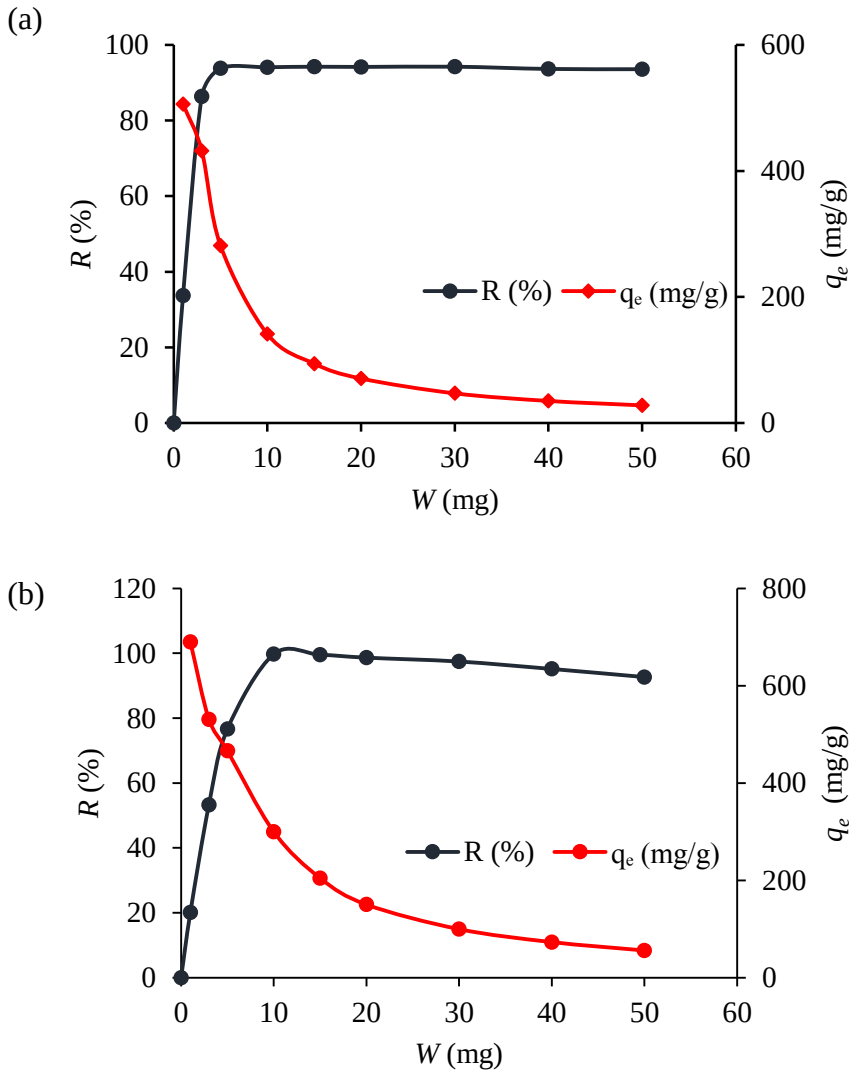


Fig. 4.5 Effect of adsorbent mass on the removal of (a) MY and (b) RB5 dyes.

The shaking speed defines the frequency of collision between the adsorbent and dye molecules. The influence of shaking speed on the removal of MY and RB5 dyes is delineated in **Fig. 4.6 (a)** and **(b)**, respectively. It can be seen that the removal efficiency of both dyes increases with increasing shaking speed. The increased speed enhanced the bulk diffusion of the dye molecules by reducing the thickness of the boundary layer surrounding the adsorbent. The improved removal was also attributed to the continuous interactions between the active sites and the dye molecules at a higher shaking rate [208]. It was also observed that a shorter equilibrium time was attained at the higher agitation speed and this was due to the enhanced mass transfer of dye molecules which subsequently accelerated the adsorption process. Since there was no significant increase in the MY removal at 250 rpm, the shaking speed selected for use in further experiments was 200 rpm. For the RB5 removal, the subsequent experiments were performed at an agitation speed of 150 rpm as no further enhancement in adsorption capacity was observed at shaking speeds higher than 150 rpm.

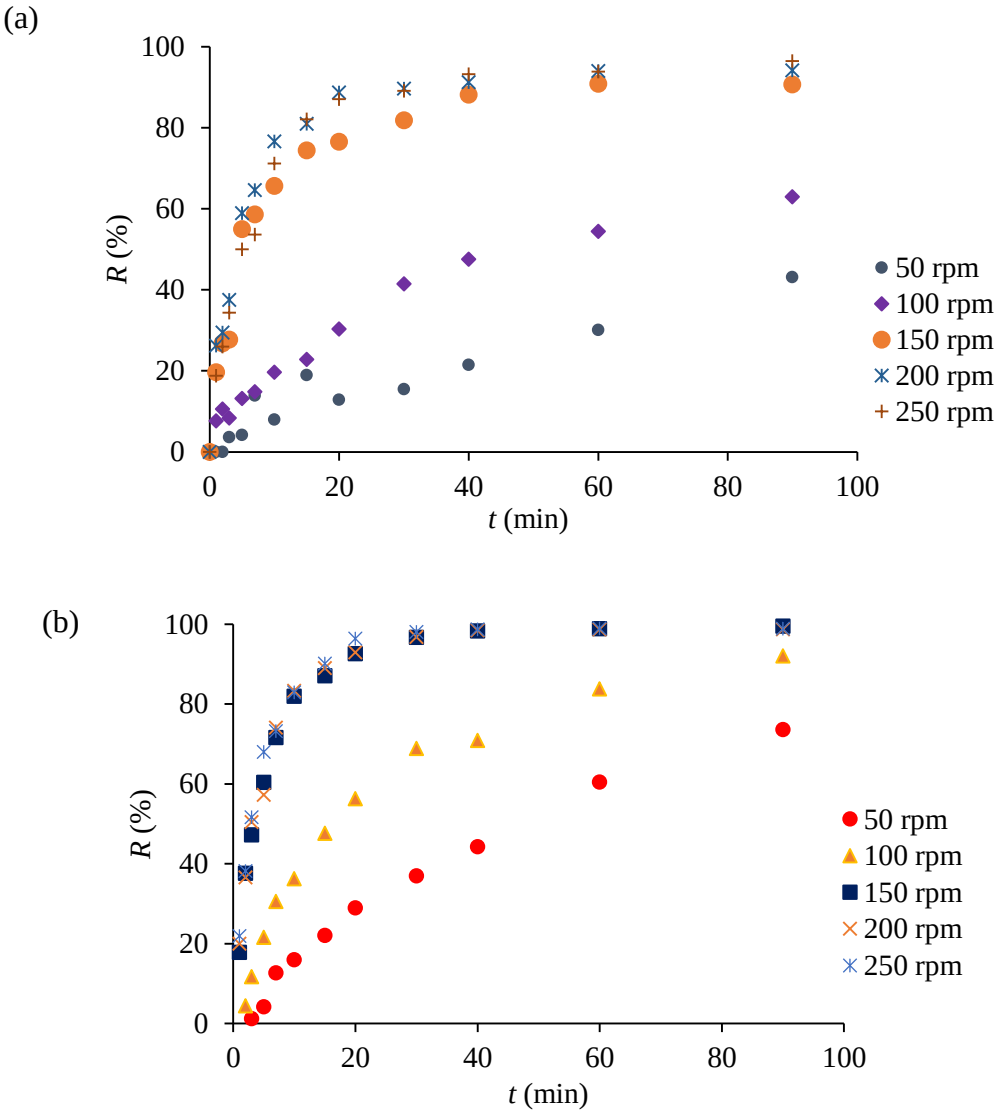


Fig 4.6 Effect of shaking speed on the removal of (a) MY dye and (b) RB5 dye.

The pH of solution plays a crucial role in adsorption process as it can alter the surface charge of the adsorbent as well as modify the structure and chemistry of the dye molecules. **Fig. 4.7 (a)** illustrates the influence of initial pH on MY dye removal by GOCA where relatively high removal efficiencies (85.12 – 96.44 %) could be observed between pH 2 – 8. As pH was increased to above 8, the removal of MY dye was greatly decreased, reaching zero at pH 11. The results were in agreement

with those of other anionic dyes such as Methyl Orange and Amido Black 10B dyes [48, 90]. Meanwhile, **Fig. 4.7 (b)** demonstrates the impact of initial pH on the percentage removal of RB5 dye by GOCA. The high removal efficiencies (93.92-98.66 %) observed over a wide pH range (pH 2-10) indicated that the dye removal was nearly independent of pH. Nonetheless, the dye uptake was reduced to 55.39 % at pH 11. Generally, RB5 dye dissociates into anionic sulphonate in aqueous media as indicated by **Eq. (4.1)** whereby its anionic nature originates from the sulphonate and sulphatoethylsulphone reactive groups [209].

$$\text{RB5-SO}_3\text{Na} \xrightarrow{\text{water}} \text{RB5-SO}_3^- + \text{Na}^+ \qquad \textbf{(4.1)}$$

Generally, at low pH, protonation of GOCA contributed to its positively charged surface which acted as the sorption site for the anionic dye molecules via electrostatic attraction. At high pH, the surface of GOCA became negatively charged due to deprotonation which impeded the adsorption of the dyes through electrostatic repulsion. Moreover, the deterioration in adsorption performance at high pH could be ascribed to the competition between the anionic dyes and hydroxyl ions for the binding sites. It is noteworthy that a significant amount of MY and RB5 dyes were removed at pH > 6, implying that there might be other interactions between GOCA and the dyes in addition to coulombic interaction, such as π–π stacking and hydrogen bonding.

The impact of pH on the MY and RB5 dyes removal can be substantiated by the PZC for GOCA (**Fig. 4.7 (c)**), which was determined to be 6. This indicated that the surface of GOCA was positively charged at pH < 6 and negatively charged at

pH > 6. These findings further confirmed that electrostatic interaction was not the only adsorption mechanism in both dyes removal. The pH control study, without adsorbent usage, is presented in **Fig. 4.7 (a)** where an appreciable amount of MY dye was sequestered at pH 2 and 3. This phenomenon might be due to the structural changes or chemical reactions of the dye molecules under the extremely acidic condition [21]. Furthermore, **Fig. 4.7 (b)** demonstrates that RB5 dye could not be removed simply by altering the solution pH. As illustrated in **Fig. 4.7 (a)** and **(b)**, a precise pH control was not necessary for the sequestration of MY and RB5 dyes in this graphene aerogel system as relatively high removal efficiencies of the MY dye (91.5 – 96.4 %) and RB5 dye (96.48 – 98.66 %) could be achieved within a wide pH range. Since the natural pH of the MY (~pH 5.8) and RB5 dye (~pH 5.3) solutions were within this pH range, further adsorption tests were performed without any pH adjustment. The wide pH range tolerance of GOCA has rendered it a promising adsorbent for MY and RB5 dyes removal as it allows operation without additional chemicals requirement which in turn reduces the operating cost.

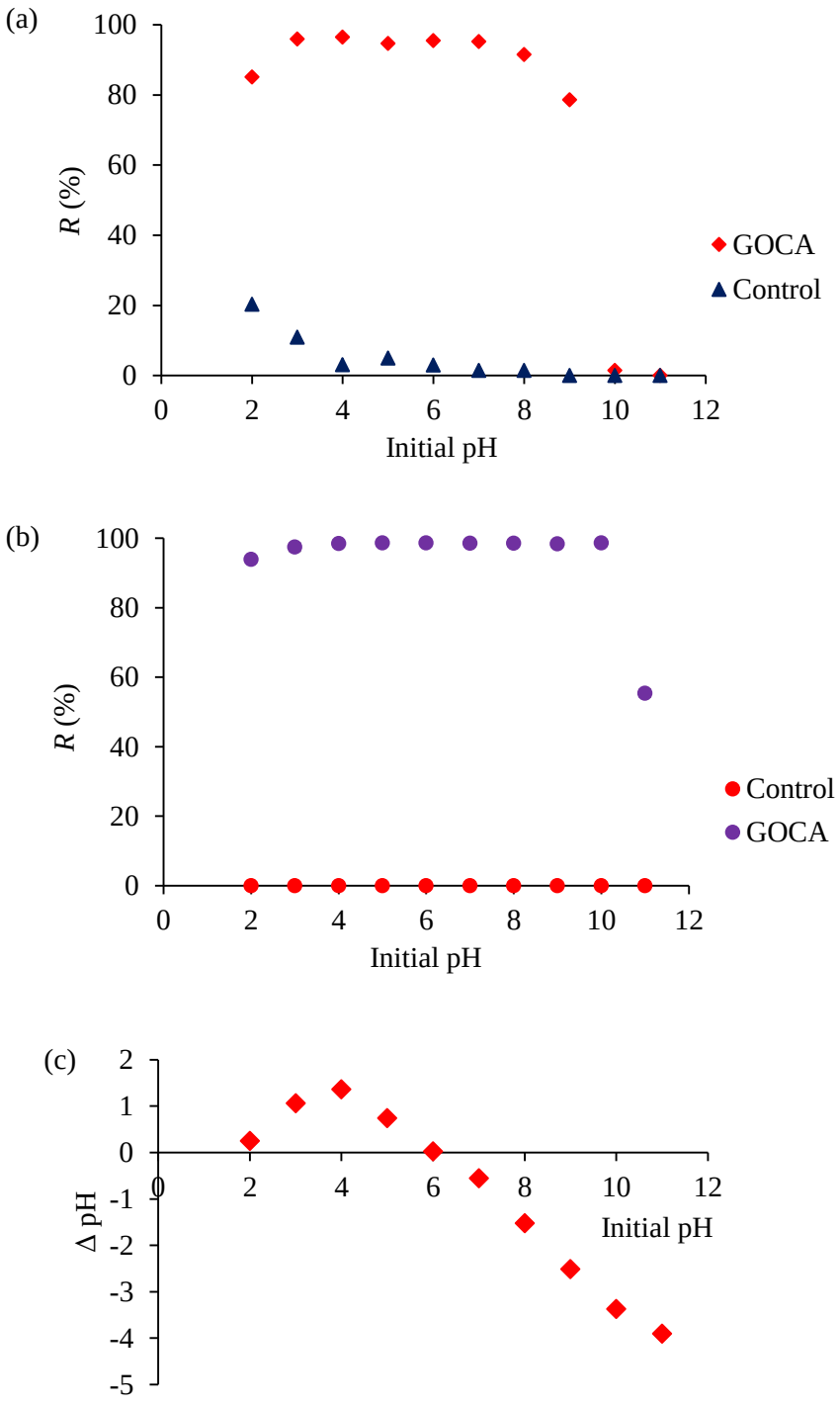


Fig. 4.7 Effect of initial pH on the removal of (a) MY and (b) RB5 dyes by GOCA, and (c) PZC plot of GOCA.

4.2.2.2 Effect of contact time and adsorption kinetic modelling

Fig. 4.8 (a) and **(b)** depict the influence of contact time on the adsorption of MY and RB5 dyes onto GOCA at different initial concentrations (10 – 90 mg/L for MY dye and 50 – 150 mg/L for RB5 dye). It can be observed that the uptake of dye increased with initial dye concentration and contact time, and was constant upon attaining adsorption equilibrium. Nonetheless, at higher initial concentration, a longer time was required to reach equilibrium as there were more dye molecules to be adsorbed. Generally, the adsorption of MY and RB5 dyes onto GOCA could be represented by three distinct stages: (1) very fast dye removal at the initial stage, (2) gradual dye removal at the second stage, and (3) nearly steady state at the final stage. The quick dye removal at the beginning could be attributed to the presence of abundant active sites for adsorption. As the adsorption proceeded, more active sites were exhausted and the remaining sites were more resistant towards dye molecules adsorption as a result of repulsive forces between the dye molecules of the bulk and solid phases, which prolonged the time to reach equilibrium [90]. The relatively short equilibrium time (20 – 60 min, varied with initial concentration) indicated that GOCA is an effective adsorbent for the removal of MY and RB5 dyes.

The kinetic modelling of the adsorption system defines the rate and determining step of the adsorption process. The non-linear kinetic models of the PFO, PSO and Elovich were fitted to the experimental data (**Fig. 4.8 (a)** and **(b)**). The best parameters for each kinetic model were determined according to the sum of normalised errors (SNE). **Tables 4.1** and **4.2** present the kinetic parameters of each model together with the corresponding SNE for MY and RB5 dyes, respectively.

The SNE denotes the errors normalised across the kinetics in lieu of error functions. It is noticeable that the adsorption kinetic followed the PFO kinetic model at low concentration region (10 – 30 mg/L for MY dye and 50 – 75 mg/L for RB5 dye) as the SNE values were the lowest among the three models (3.51 – 5.49 for MY dye and 2.24 – 2.42 for RB5 dye). Additionally, the adsorption capacities computed using the PFO model were in good agreement with the experimental adsorption capacities. The kinetics at high concentration range (50 – 90 mg/L for MY dye and 100 – 150 mg/L for RB5 dye) were best fitted to the PSO kinetic model exhibiting the smallest SNE (3.81 – 4.85 for MY dye and 2.03 – 3.35 for RB5 dye).

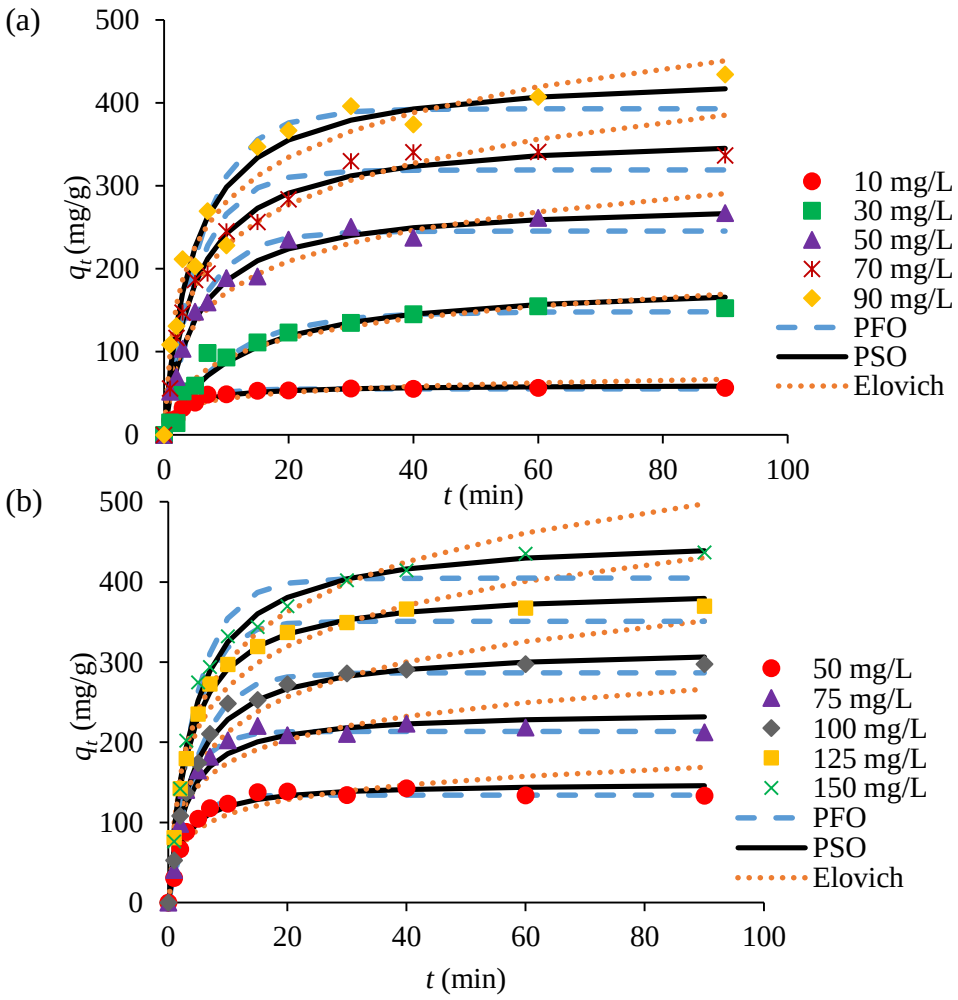


Fig. 4.8 Comparison of experimental kinetic data with the PFO, PSO and Elovich models for (a) MY and (b) RB5 dyes removal.

Hence, the kinetic model fitting unveiled that the adsorption of MY and RB5 dyes onto GOCA was governed by both physisorption and chemisorption depending on the initial concentration [163]. The rate constant, k_2, decreased with an increase in the initial concentration supporting that a longer time was needed to achieve equilibrium at higher initial concentration. The decline in rate constant could be due to the high dye concentrations slowing down the uptake of dye molecules. Since a constant amount of adsorbent was used for all the tested initial concentrations, the adsorption sites might not be adequate for quick adsorption of the dye when the initial concentration was high [210].

The uptake of MY and RB5 dyes from bulk solution by GOCA comprises three steps: boundary layer (film) diffusion, pore (intraparticle) diffusion and surface attachment of the dye molecules. Under vigorous shaking, there is negligible resistance on the surface adsorption and hence it is a rapid process as compared to the first and second steps. The rate-determining step was identified based on the intraparticle diffusion model, by plotting the MY and RB5 dyes uptake against the square root of time (**Fig. 4.9 (a)** and **(b)**). The multi-linearity of the plots indicated that the adsorption rate was not solely restricted by pore diffusion. Furthermore, the absence of a straight line passing through the origin also implied that the rate was controlled by two or more steps [169]. The first linear segment could be ascribed to the transport of dye molecules through the boundary layer encompassing the external surface of GOCA while the second stage described the movement of the dye molecules through the internal pores of GOCA. Therefore, it can be inferred that the adsorption processes were controlled by both external film and intraparticle diffusion.

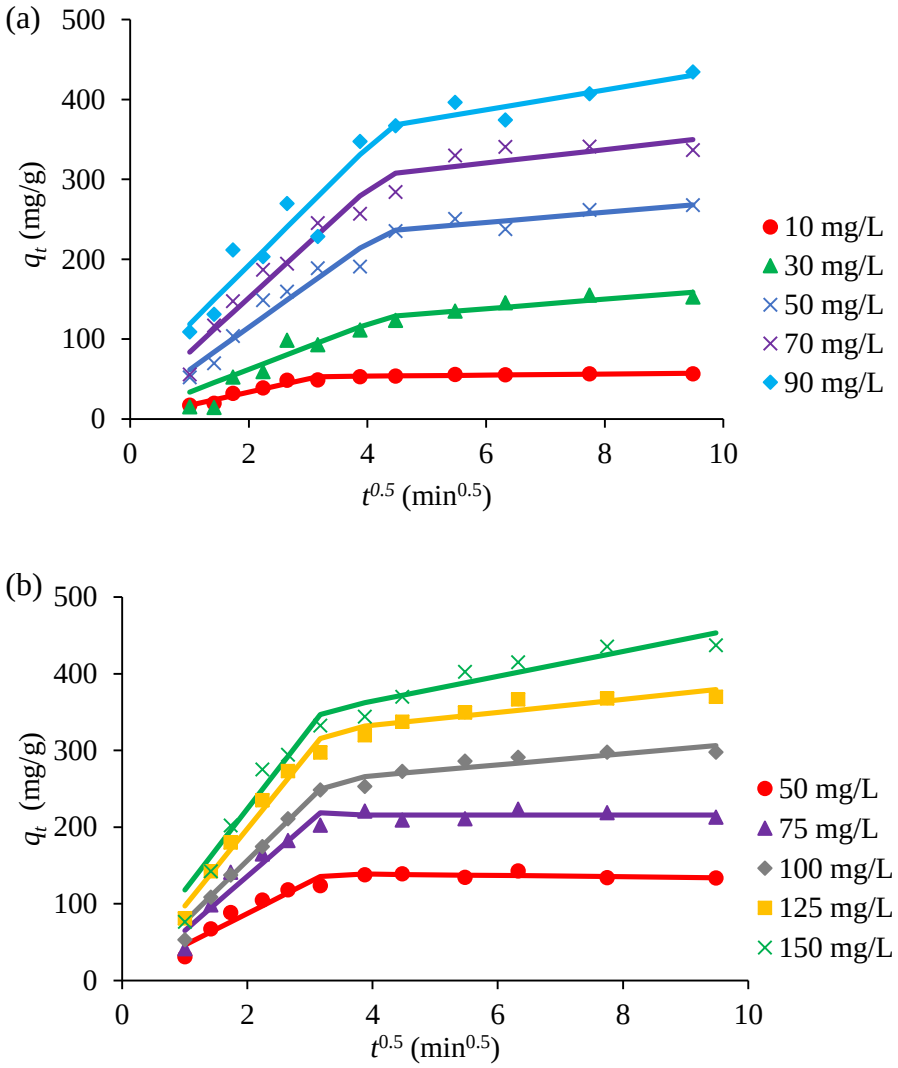


Fig. 4.9 Intraparticle diffusion plots for (a) MY and (b) RB5 dyes removal.

4.2.2.3 Effect of initial concentration and adsorption isotherm modelling

Adsorption of MY and RB5 dyes onto GOCA as a function of initial dye concentration at different temperatures is shown in **Fig. 4.10 (a)** and **(b)**, respectively. It can be observed that the adsorption capacity increased with the initial concentration and became constant after reaching the saturated adsorption capacity of GOCA. The increment in adsorption capacity could be ascribed to the enhanced mass transfer driving force at higher initial concentration which resulted in better adsorption of the dyes. **Fig. 4.10 (a)** highlights the exothermic nature of

the adsorption of MY dye onto GOCA whereby a decrease in adsorption capacity could be seen when the temperature was increased from 30 to 70 ℃. At higher temperatures, the weak bonding forces between MY dye and GOCA, for instance Van der Waals forces and hydrogen bonding, could easily break down releasing the dye molecules from the adsorbent surface [189]. Contrarily, an increment in the saturated adsorption capacity could be observed for RB5 dye removal (**Fig. 4.10 (b)**) as temperature was raised from 30 to 70 ℃ which signified that the system was endothermic. As the temperature was elevated, the mobility of the dye molecules was enhanced as they possessed higher kinetic energy. This transport phenomena assisted the penetration of RB5 dye molecules into the adsorbent. The larger adsorption capacity at higher temperatures could be further explained by the weakening or breaking of structural bonds near the edge of the 3D graphene composite, leading to the formation of more sorption sites for trapping the dye molecules [202].

The study of the equilibrium relationship between MY and RB5 dyes, and GOCA is imperative for the estimation of the maximum adsorption capacity of the adsorbent. Two isotherm models which include the Langmuir and Freundlich models, were fitted to the experimental data. The best-fit isotherm model for the adsorption of MY and RB5 dyes onto GOCA was selected from among the models with the smallest SNE. The regressed model parameters together with the SNE values are given in **Tables 4.1** and **4.2** while the comparisons between the measured and predicted data are plotted in **Fig. 4.11** and **4.12**. For both dyes removal, the adsorption system was best described by the Langmuir isotherm based on the lowest SNE values (3.06 – 5.80 for MY dye and 2.27 – 3.92 for RB5 dye). The good fit of

data by the Langmuir isotherm suggested that a monolayer of dye molecules were adsorbed onto uniformly distributed sorption sites in GOCA with zero interaction between the adsorbed molecules on neighbouring sites [164]. The exothermic nature of the MY dye adsorption process was further validated by the declining trends in both q_m and k_L. Meanwhile, the maximum adsorption capacity estimated by the Langmuir model varied from 555.28 to 638.93 mg/g within the temperature range of 30 - 70 ℃, thus further proving that the RB5 dye removal process was endothermic. The adsorption process was favourable as indicated by the values of the separation factor, R_L (**Eq. (4.2)**), which lied between 0 and 1.

$$R_L = \frac{1}{1+K_L C_{max}} \quad \textbf{(4.2)}$$

where K_L (L/mg) and C_{max} (mg/L) denote the Langmuir isotherm constant and maximum initial dye concentration, respectively.

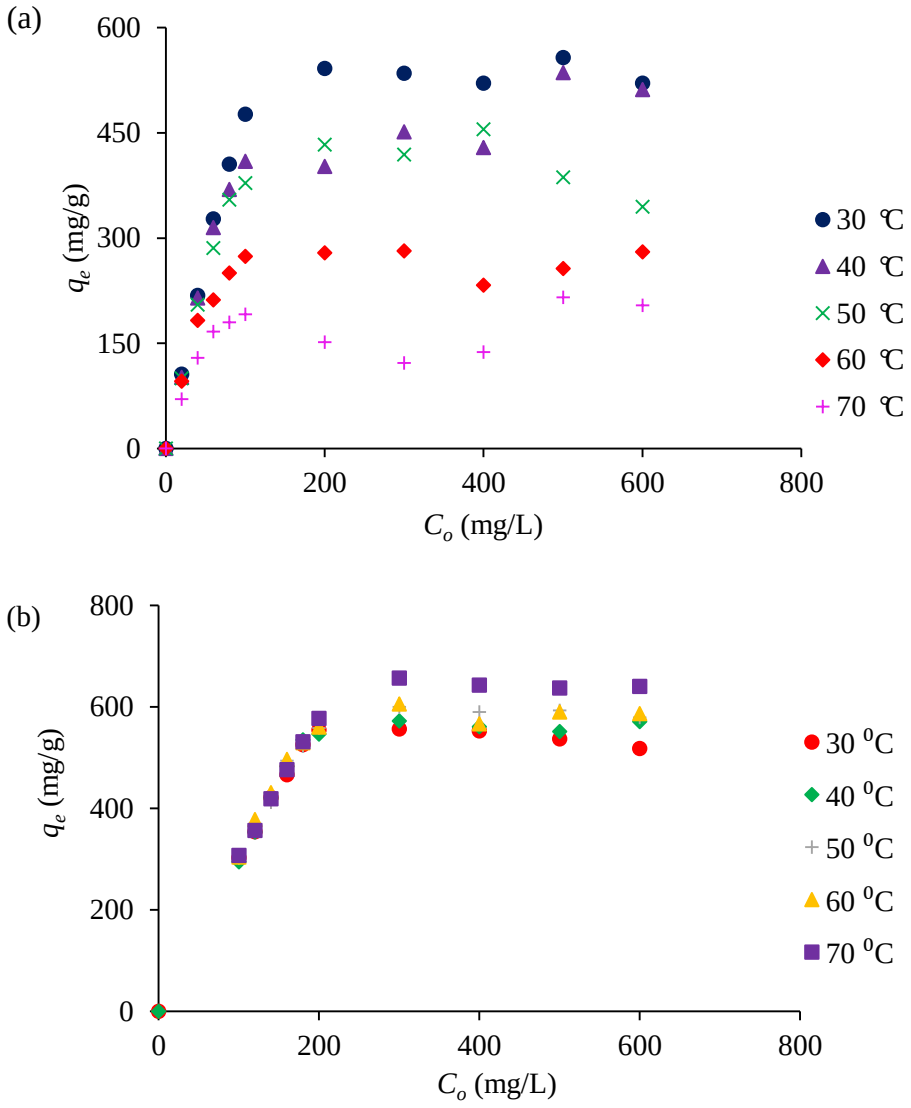


Fig. 4.10 Effect of initial concentration on (a) MY and (b) RB5 dyes removal at different temperatures.

Table 4.1 Equilibrium, kinetic and thermodynamic parameters for MY dye adsorption onto GOCA.

Equilibrium	**Temperature (℃)**				
model	**30**	**40**	**50**	**60**	**70**
Langmuir					
q_m (mg/g)	558.18	485.31	429.81	278.15	180.40
K_L	0.184	0.162	0.142	0.161	0.135
R_L	0.009	0.010	0.012	0.010	0.012
SNE	3.06	4.55	3.38	3.35	5.80
Freundlich					
K_F	209.39	164.13	170.94	144.15	96.93
n	6.31	5.46	7.09	9.50	9.72
SNE	6.88	6.94	6.86	6.90	6.95
Kinetic	**C_o (mg/L)**				
model	**10**	**30**	**50**	**70**	**90**
Pseudo- first -order (PFO)					
$q_{e,\,exp}$	56.45	152.71	267.44	336.69	434.40
$q_{e,\,calc}$	55.11	148.09	245.32	319.18	392.80
k_1	0.266	0.099	0.174	0.179	0.158
SNE	3.51	5.49	6.97	6.97	6.97
Pseudo- second –order (PSO)					
$q_{e,\,calc}$	60.28	186.55	281.59	364.46	438.66
k_2	0.006	4.72E-04	6.90E-04	5.46E-04	4.86E-04
SNE	3.58	6.11	4.22	3.81	4.85
Elovich					
α	68.43	48.11	129.09	175.24	291.14
β	0.096	0.028	0.018	0.014	0.013
SNE	6.94	6.85	6.54	5.03	4.52

Thermodynamics	**Δ*G* (kJ/mol)**					**Δ*H***	**Δ*S* (kJ/mol K)**
						(kJ/mol)	
C_o (mg/L)	**30 ℃**	**40 ℃**	**50 ℃**	**60 ℃**	**70 ℃**		
80	-26.18	-25.79	-26.17	-24.33	-23.36	-48.11	-0.071
100	-25.33	-24.64	-24.81	-23.61	-22.65	-44.82	-0.064
200	-21.44	-20.87	-21.84	-20.79	-19.30	-34.89	-0.043
300	-19.76	-19.80	-20.17	-19.43	-17.34	-36.13	-0.052
400	-18.69	-18.68	-19.47	-17.91	-16.83	-32.84	-0.045
500	-18.20	-18.68	-18.24	-17.53	-17.52	-26.16	-0.025
600	-17.45	-17.97	-17.34	-17.25	-16.79	-23.92	-0.020

Table 4.2 Equilibrium, kinetic and thermodynamic parameters for RB5 dye adsorption onto GOCA.

Equilibrium	**Temperature (℃)**				
model	**30**	**40**	**50**	**60**	**70**
Langmuir					
q_m (mg/g)	555.28	569.21	592.18	581.78	638.93
K_L	1.720	2.231	1.666	4.151	2.589
R_L	0.001	0.001	0.001	0.0004	0.001
SNE	3.18	3.38	3.15	3.92	2.27
Freundlich					
K_F	405.97	412.02	416.58	427.63	422.93
n	17.77	16.33	15.01	17.08	12.37
SNE	6.92	6.93	6.93	6.95	6.93
Kinetic	**C_o (mg/L)**				
model	**50**	**75**	**100**	**125**	**150**
Pseudo- first -order (PFO)					
$q_{e,\,exp}$	133.32	212.64	297.68	369.93	436.86
$q_{e,\,calc}$	134.21	213.53	286.49	351.08	404.63
k_1	0.303	0.296	0.203	0.236	0.209
SNE	2.24	2.42	3.09	3.71	5.28
Pseudo- second –order (PSO)					
$q_{e,\,calc}$	149.88	238.84	320.01	394.14	459.24
k_2	0.003	1.47E-03	7.82E-04	7.22E-04	5.28E-04
SNE	3.51	3.69	2.99	2.03	3.35
Elovich					
α	162.92	267.33	183.21	285.23	258.89
β	0.037	0.024	0.016	0.014	0.011
SNE	6.89	6.90	6.96	6.96	6.97

Thermodynamics	**ΔG (kJ/mol)**					**ΔH (kJ/mol)**	**ΔS (kJ/mol K)**
C_o (mg/L)	**30 ℃**	**40 ℃**	**50 ℃**	**60 ℃**	**70 ℃**		
160	-31.26	-33.18	-33.52	-36.00	-36.24	7.28	0.128
180	-28.50	-29.24	-33.01	-34.00	-35.99	31.64	0.197
200	-25.68	-27.30	-28.61	-29.40	-33.62	29.15	0.180
300	-21.39	-22.36	-23.43	-24.07	-25.71	10.07	0.104
400	-19.83	-20.52	-21.43	-21.84	-23.35	5.60	0.084
500	-18.70	-19.45	-20.35	-20.98	-22.05	6.25	0.082
600	-17.90	-18.87	-19.51	-20.17	-21.22	6.13	0.079

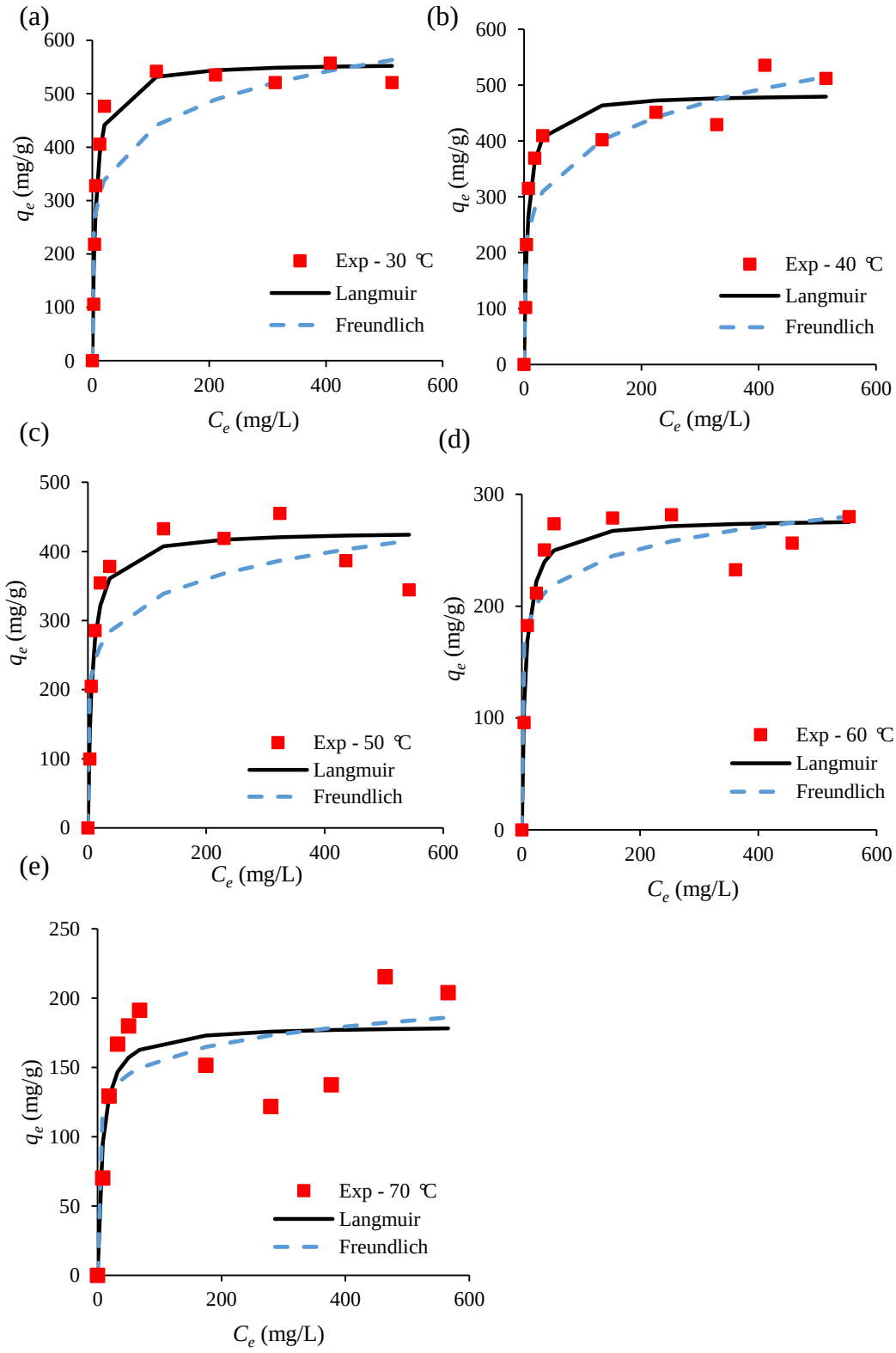


Fig. 4.11 Comparison of experimental equilibrium data with the Langmuir and Freundlich models at temperatures of (a) 30 ^{o}C, (b) 40 ^{o}C, (c) 50 ^{o}C, (d) 60 ^{o}C and (e) 70 ^{o}C for MY dye removal.

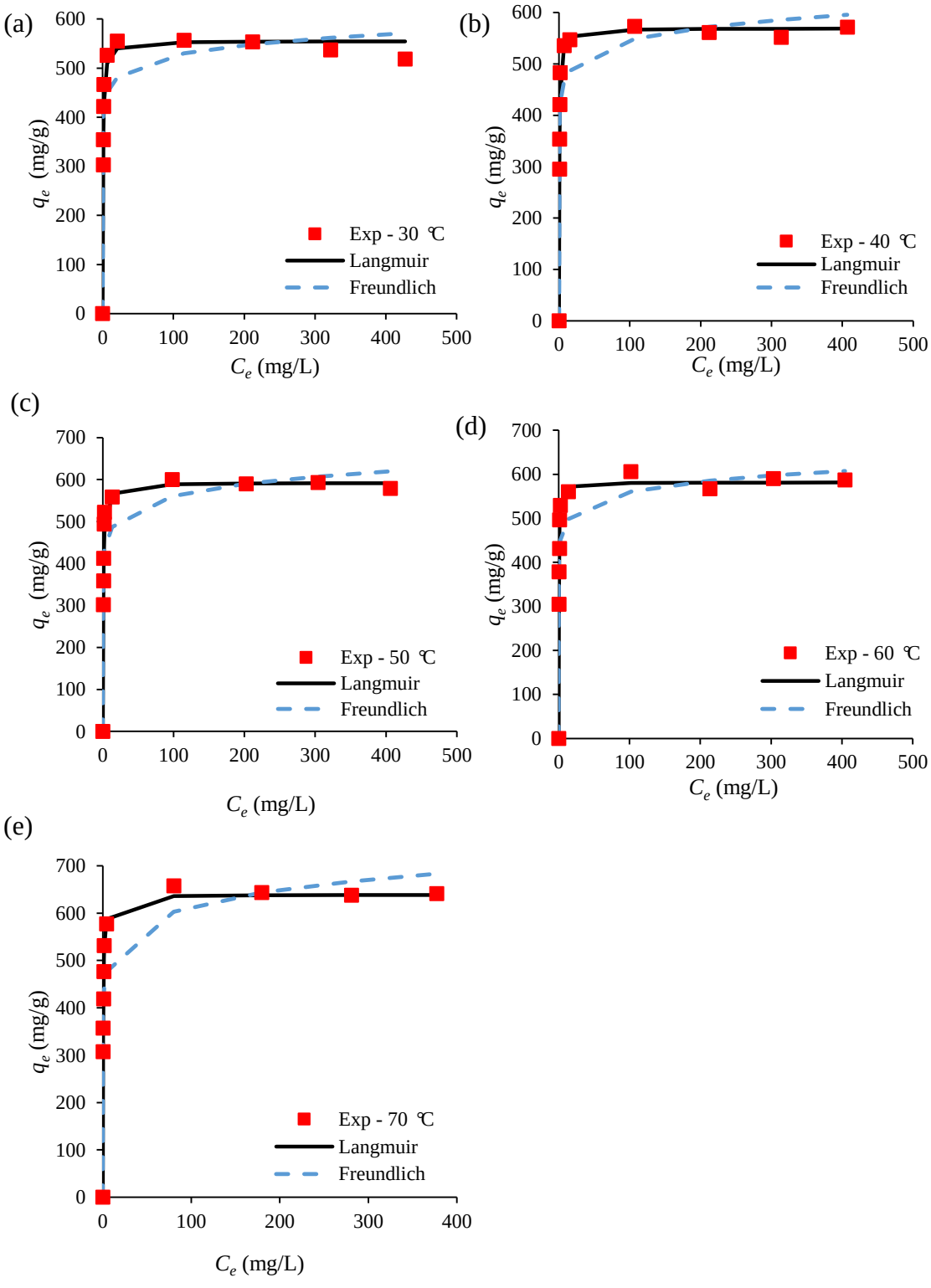


Fig. 4.12 Comparison of experimental equilibrium data with the Langmuir and Freundlich models at temperatures of (a) 30 ºC, (b) 40 ºC, (c) 50 ºC, (d) 60 ºC and (e) 70 ºC for RB5 dye removal.

4.2.2.4 Adsorption thermodynamics

The results of thermodynamic analysis on the uptake of MY and RB5 dyes by GOCA are presented in **Tables 4.1** and **4.2**, respectively. For the removal of MY dye, the negative Δ*G* values indicated that the adsorption process was spontaneous and feasible. The Δ*G* values increased as the initial concentration and temperatures were increased, suggesting that the adsorption process was more spontaneous at low concentration and temperature conditions. The negative Δ*H* values confirmed the exothermic nature of the adsorption process and further advocated the increased feasibility of MY dye adsorption at lower temperature. The decreased randomness at the solid-liquid interface during the adsorption of MY dye onto GOCA was reflected by the negative Δ*S* values.

The RB5 dye removal process was confirmed to be spontaneous with high feasibility for the dye attachment as denoted by the negative Δ*G* values. For each concentration investigated, the Δ*G* values decreased with increased temperature implying that RB5 dye removal was more spontaneous and favourable at higher temperatures. Furthermore, the positive Δ*H* (5.60 - 31.64 kJ/mol) values revealed the endothermic nature of the process, explaining the increased adsorption capacity at higher temperatures. The increase in randomness at the solid-liquid interface and high affinity of the GOCA adsorbent for RB5 dye are supported by the positive ΔS (0.079 - 0.197 kJ/mol K). The dye molecules displaced the water molecules adsorbed on the adsorbent surface in which the translational entropy lost by the dye molecules was less than that gained by the water molecules resulting in the increased randomness [211].

4.2.3 RSM modelling and optimisation

4.2.3.1 Optimisation of MY dye adsorption onto GOCA

In the RSM study, the interactive effects of several critical adsorption factors were investigated, and these include adsorbent mass (A), initial dye concentration (B), contact time (C) and shaking speed (D). The complete CCD matrix is delineated in **Table 4.3** and the corresponding experimental results were analysed using Design Expert Software 7.0. The quadratic model correlating the MY dye adsorption capacity to the four adsorption factors in terms of coded factors, was obtained from the RSM modelling and is represented by **Eq. (4.3)**:

$$q = 427.03 + 53.29A - 5.00B - 1.02C + 28.03D - 10.19AB - 23.87AC + 5.80AD - 12.55BC - 21.19BD + 11.97CD - 30.51A^2 - 2.17B^2 - 27.72C^2 - 19.95D^2 \quad \textbf{(4.3)}$$

The validity of the quadratic model was evaluated based on the ANOVA results (**Table 4.4**) where the model was shown to be significant with sufficiently high F-value (22.91), $p < 0.0001$ and non-significant "lack of fit" ($p = 0.5357$). The adequacy of the model was further substantiated by the relatively high R^2 (0.8071 – 0.9553) and adequate precision (17.367), as well as low C.V.% (6.11). On the whole, this quadratic function could be utilised in anticipating the response for given values of the studied factors. As presented in **Table 4.4**, the significance of the regression coefficients of each factor and their interactive terms in **Eq. (4.3)** was also investigated by ANOVA. The high F-value and small p-value ($p < 0.05$) signify the importance of the corresponding coefficient. Hence, the variables and

interactions that had the greatest influences on the adsorption of MY dye were A, D, AC, BC, BD, CD, A^2, C^2 and D^2. It is worth mentioning that the magnitude of the regression coefficient in **Eq. (4.3)** represents the intensity, whereas the sign denotes the type of influence (positive or negative) of an individual factor on the response. Taking the factor D with a coefficient of 28.03 as an illustration, an increase in shaking speed would have a significant and positive effect on the MY dye adsorption capacity.

Table 4.3 CCD experimental design matrix for MY dye adsorption onto GOCA.

Run No.	A	B	C	D	Measured q_e (mg/g)	Predicted q_e (mg/g)	Residual error (%)
1	4	200	30	125	224.89	221.35	1.60
2	8	200	30	125	381.71	384.44	0.71
3	4	400	30	125	335.25	299.21	12.04
4	8	400	30	125	414.86	421.55	1.59
5	4	200	50	125	260.55	268.22	2.86
6	8	200	50	125	351.03	335.83	4.52
7	4	400	50	125	302.55	295.91	2.24
8	8	400	50	125	332.40	322.76	2.99
9	4	200	30	175	284.48	284.26	0.08
10	8	200	30	175	467.34	470.57	0.69
11	4	400	30	175	265.58	277.36	4.25
12	8	400	30	175	440.44	422.91	4.15
13	4	200	50	175	389.10	379.00	2.66
14	8	200	50	175	443.64	469.83	5.57
15	4	400	50	175	334.50	321.92	3.91
16	8	400	50	175	371.85	371.98	0.04
17	2	300	40	150	180.15	198.41	9.20
18	10	300	40	150	416.46	411.56	1.19
19	6	100	40	150	440.35	428.37	2.80
20	6	500	40	150	383.05	408.39	6.20
21	6	300	20	150	308.35	318.18	3.09
22	6	300	60	150	310.60	314.13	1.12
23	6	300	40	100	270.80	291.19	7.00
24	6	300	40	200	410.35	403.32	1.74
25	6	300	40	150	432.00	427.04	1.16
26	6	300	40	150	395.75	427.04	7.33
27	6	300	40	150	431.15	427.04	0.96
28	6	300	40	150	440.60	427.04	3.18
29	6	300	40	150	456.00	427.04	6.78
30	6	300	40	150	406.65	427.04	4.77

Table 4.4 ANOVA results of the quadratic model for MY dye adsorption onto GOCA.

Source	Sum of squares	DF	Mean Square	F value	p-value Prob >F
Model	157566	14	11255	22.91	< 0.0001
A	68160	1	68160	138.75	< 0.0001
B	598.91	1	598.91	1.22	0.2869
C	24.82	1	24.82	0.05	0.8252
D	18860	1	18860	38.39	< 0.0001
AB	1661	1	1661	3.38	0.0858
AC	9117	1	9117	18.56	0.0006
AD	538.93	1	538.93	1.10	0.3115
BC	2519	1	2519	5.13	0.0388
BD	7186	1	7186	14.63	0.0017
CD	2291	1	22901	4.66	0.0474
A^2	25539	1	25539	51.99	< 0.0001
B^2	128.66	1	128.66	0.26	0.6163
C^2	21078	1	21078	42.91	< 0.0001
D^2	10913	1	10913	22.22	0.0003
Residual	7368	15	491.23		
Lack of Fit	4910	10	490.95	0.9983	0.5357
Pure Error	2459	5	491.77		
Others	R^2	0.9553		Std. dev.	22.16
	R^2_{adj}	0.9136		Mean	362.75
	R^2_{pred}	0.8071		C.V.%	6.11
	Adeq. precision	17.37		PRESS	31820

The simultaneous interactions between two independent factors on the process response (q_e) were studied using 3D response surface plots (**Fig. 4.13**) to determine the optimum range for the adsorption process. The interactive influences of GOCA mass (A, mg) with initial concentration (B: mg/L), time (C, min) and shaking speed (D, rpm) are illustrated in **Fig. 4.13 (a)**, **(b)** and **(c)**, respectively. In general, the

adsorbent dosage demonstrated a synergistic effect onto q_e which could be attributed to the increase in binding sites availability for higher MY dye molecules uptake. The highest possible q could be achieved when A > 6 mg, 200 < B < 300 mg/L, C < 40 min and D > 150 rpm.

Fig. 4.13 (a), **(d)** and **(e)** present the interactions of B and A, B and C, and B and D, respectively. Overall, the effect of initial concentration showed a flatter increment in q_e as the initial concentration increased. The potential maximum q_e could be attained when A > 6 mg, B > 300 mg/L, C < 40 min and D > 150 rpm. At higher initial concentration, there was a large driving force which sufficiently overcame the mass transfer resistance at the solid-liquid interface thus increasing the adsorption capacity [189].

The effects of C with A, B and D also demonstrated a positive effect onto q_e as portrayed in **Fig. 4.13 (b)**, **(d)** and **(f)**, respectively. In general, the adsorption attained the highest possible q_e when C was kept between 30 – 40 min while A > 6 mg, 200 < B < 300 mg/L and D > 150 rpm. The q_e was observed to be increased rapidly when C < 30 min due to large availability of binding sites, followed by the gradual adsorption uptake between 30 – 40 min and saturation when C > 40 min. The increase in contact time after the saturation of GOCA would not promote the removal of MY.

The respective surface plots for the interactions of D and A, D and B and D and C are illustrated in **Fig. 4.13 (c)**, **(e)** and **(f)**. At higher shaking speed, the kinetic energies of MY dye and GOCA were sufficiently high for collisions between the two species, thereby eliminating the external diffusional layer to improve the MY

dye uptake. Therefore, the desirable conditions to achieve highest q_e were A > 6 mg, B > 300 mg/L, C < 40 min and D > 150 rpm.

The optimum adsorption conditions for maximum adsorption capacity of MY dye in this system were determined by the Derringer's desirability method. The highest desirability (0.956) was achieved when A = 8 mg, B = 400 mg/L, C = 35.19 min and D = 175 rpm which yielded a predicted maximum adsorption capacity of 430.99 mg/g. The predicted outcomes were authenticated by reproducing the experiments at the optimum conditions at least three times. The measured adsorption capacity was 418.35 mg/g with a residual error of only 2.93 %, which further proved the adequacy of the model to predict the response together with the optimisation of process parameters.

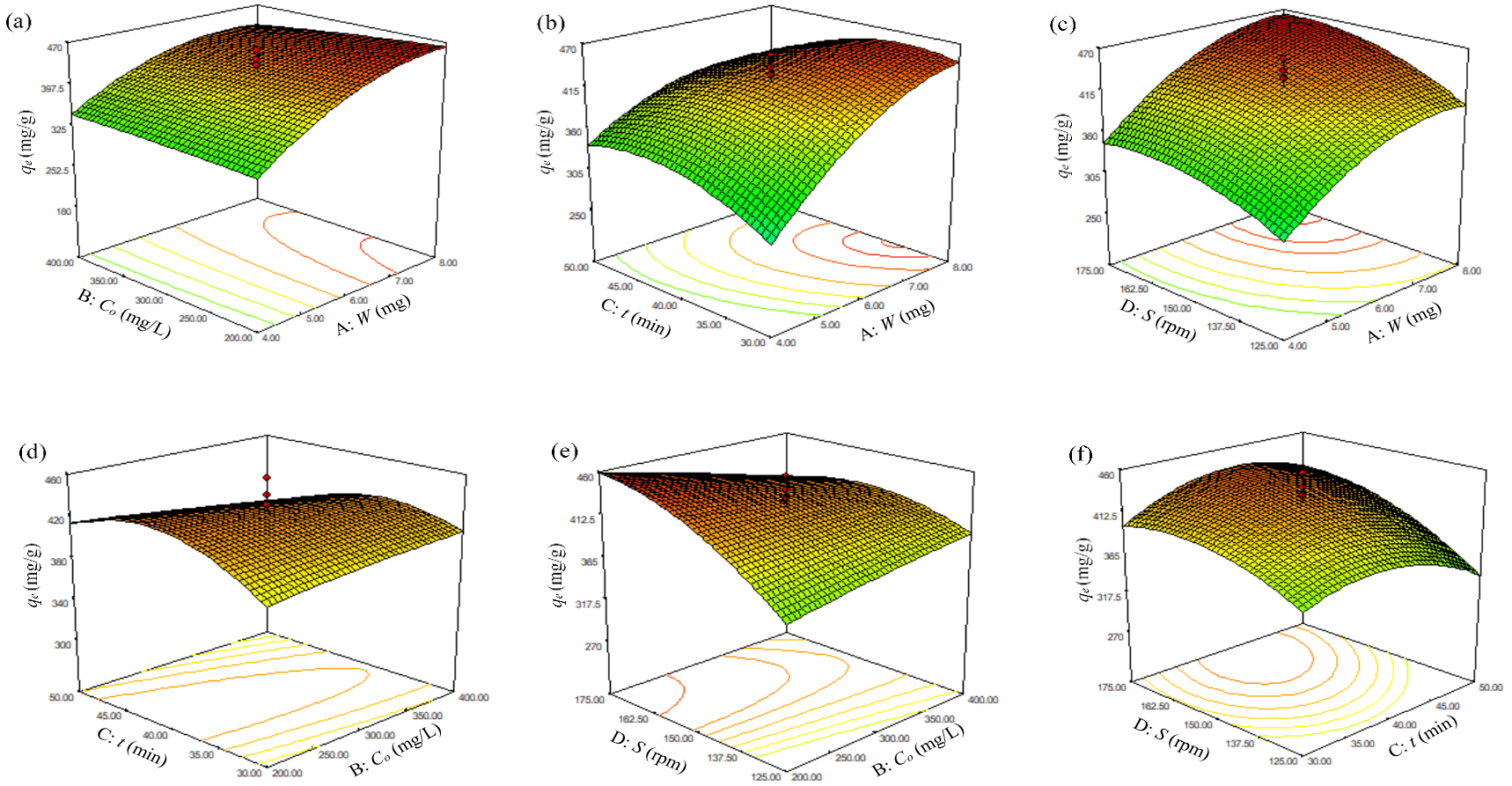


Fig. 4.13 Surface plots of MY dye adsorption onto GOCA with q_e response: Effects of (a) initial concentration and adsorbent mass, (b) contact time and adsorbent mass, (c) shaking speed and adsorbent mass, (d) contact time and initial concentration, (e) shaking speed and initial concentration and (f) shaking speed and contact time.

4.2.3.2 Optimisation of RB5 dye adsorption onto GOCA

The influences of pivotal operating variables which encompass the adsorbent mass (A: *W*, mg), initial RB5 dye concentration (B: C_o, mg/L), contact time (C: *t*, min) and temperature (D: *T*, ℃) were studied using RSM according to CCD. A quadratic polynomial model correlating the responding adsorption capacity (q) to the operating variables (A, B, C and D) in coded form was obtained upon substitution of experimental results in **Table 4.5** into **Eq. (3.5)**. The model is given by **Eq. (4.4)**.

$$q = 612.14 - 7.34A + 36.50B + 10.33C + 8.71D - 3.49AB + 0.054AC - 0.48AD - 2.10BC + 8.59BD + 1.22CD + 10.41A^2 - 31.38B^2 + 3.07C^2 + 2.55D^2 \quad \textbf{(4.4)}$$

For each experimental run in **Table 4.5**, the predicted adsorption capacity (q_{pred}) was computed using **Eq. (4.4)**. The computed data agreed very well with the experimental results (q_{exp}) portraying residual errors within the range of 0.04-3.80 %, thereby providing the initial validation of the model. The validity and significance of the regression model were further examined using the ANOVA results (**Table 4.6**) and diagnostic plots (**Fig. 4.14 (a)-(c)**). As shown in **Table 4.6**, the developed model is statistically significant as indicated by the adequately high *F*-value (81.65), $p<0.0001$ and insignificant 'lack-of-fit' ($p=0.1993$). Additionally, the coefficient of determination (R^2), adjusted R^2 and predicted R^2 for the model are 0.9870, 0.9750 and 0.9358, respectively. Conventionally, the R^2 increases when more variables are included in the polynomial expression while the adjusted R^2 will only increase when the added term is significant, and *vice versa*. The R^2 and

adjusted R^2 revealed that the terms included in the quadratic equation are significant. Additionally, the relatively high predicted R^2 also demonstrated that this function could be used to predict the adsorption capacity for the given factors. Meanwhile, the reproducibility of the model is confirmed by the low coefficient of variation (C.V.) % (1.34<10) [212].

Table 4.5 RSM design matrix with measured and predicted data, and residual errors for RB5 adsorption system.

Run	A: W, mg	B: C_o, mg/L	C: t, min	D: T, ºC	q_{exp}, mg/g	q_{pred}, mg/g	Residual error, %
1	6	400	75	40	630.75	635.46	0.74
2	4	300	60	50	667.63	670.07	0.36
3	10	200	45	40	551.00	546.59	0.81
4	10	400	75	40	614.55	614.86	0.05
5	6	400	45	40	617.74	621.54	0.61
6	10	200	45	60	548.22	543.44	0.88
7	10	400	45	40	590.16	600.72	1.76
8	8	300	60	50	614.67	613.75	0.15
9	6	200	45	40	558.12	553.46	0.84
10	12	300	60	50	636.88	640.70	0.60
11	8	300	60	50	615.48	613.75	0.28
12	8	300	60	70	638.18	641.38	0.50
13	6	200	45	60	549.00	552.21	0.58
14	8	300	60	30	603.48	606.54	0.50
15	8	300	60	50	617.47	613.75	0.61
16	8	300	30	50	604.00	605.37	0.23
17	8	500	60	50	571.81	562.32	1.69
18	10	400	75	60	646.35	650.95	0.71
19	6	400	45	60	651.11	654.67	0.54
20	8	100	60	50	398.40	414.14	3.80
21	10	200	75	40	572.77	569.14	0.64
22	8	300	90	50	641.81	646.70	0.76
23	10	400	45	60	628.79	631.95	0.50
24	8	300	60	50	613.54	613.75	0.04
25	8	300	60	50	610.93	613.75	0.46
26	6	400	75	60	665.53	673.45	1.18
27	8	300	60	50	600.72	613.75	2.12
28	6	200	75	60	590.03	579.40	1.83
29	10	200	75	60	571.13	570.85	0.05
30	6	200	75	40	575.42	575.79	0.06

Table 4.6 ANOVA results of the quadratic function for RB5 dye adsorption onto GOCA.

Source	Sum of Squares	DF	Mean Square	F Value	p-value Prob > F
Model	73867.59	14	5276.26	81.65	< 0.0001
A	1294.11	1	1294.11	20.03	0.0004
B	31981.65	1	31981.65	494.90	< 0.0001
C	2562.91	1	2562.91	39.66	< 0.0001
D	1820.88	1	1820.88	28.18	< 0.0001
AB	194.61	1	194.61	3.01	0.1032
AC	0.047	1	0.047	7.216E-4	0.9789
AD	3.62	1	3.62	0.056	0.8160
BC	70.69	1	70.69	1.09	0.3122
BD	1181.79	1	1181.79	18.29	0.0007
CD	23.63	1	23.63	0.37	0.5544
A^2	2971.24	1	2971.24	45.98	< 0.0001
B^2	27009.62	1	27009.62	417.96	< 0.0001
C^2	258.66	1	258.66	4.00	0.0639
D^2	178.49	1	178.49	2.76	0.1173
Residual	969.34	15	64.62		
Lack-of-Fit	789.60	10	78.96	2.20	0.1993
Pure Error	179.74	5	35.95		
Others	R^2	0.9870		Std. dev.	8.04
	Adjusted R^2	0.9750		Mean	599.86
	Predicted R^2	0.9358		C.V.%	1.34
	Adequate precision	45.33		PRESS	4806.95

Fig. 4.14 (a) delineates the normal probability plot and it portrays a linear profile indicating that the residuals are normally distributed. This finding further implies the good adequacy of the regression model for RB5 dye attachment to GOCA. This plot also suggests that neither response transformation was required nor was there any refusal in the assumptions underlying the model [213]. The actual

(experimentally measured) and predicted adsorption capacities of GOCA are presented in **Fig. 4.14 (b)**. The cluster of points along the diagonal line highlights the high correlation between the measured and model predicted responses, validating further the appropriateness of this model for predictive application. **Fig. 4.14 (c)** illustrates the outlier plot for the 30 batch runs of RB5 dye adsorption onto GOCA, whereby the potential outlier can be identified based on the magnitude of the residuals. Typically, a residual with magnitude beyond the interval of ±3 is regarded as an outlier. From **Fig. 4.14 (c)**, the random distribution of all the internally studentised residuals across the batch runs along with the magnitudes of residuals within the limits confirm the absence of any outlier. This finding demonstrates the compatibility of the developed model with the actual data. On the whole, the ANOVA results together with the diagnostic plots proved that the model is appropriate for characterising the adsorptive removal of RB5 dye by GOCA.

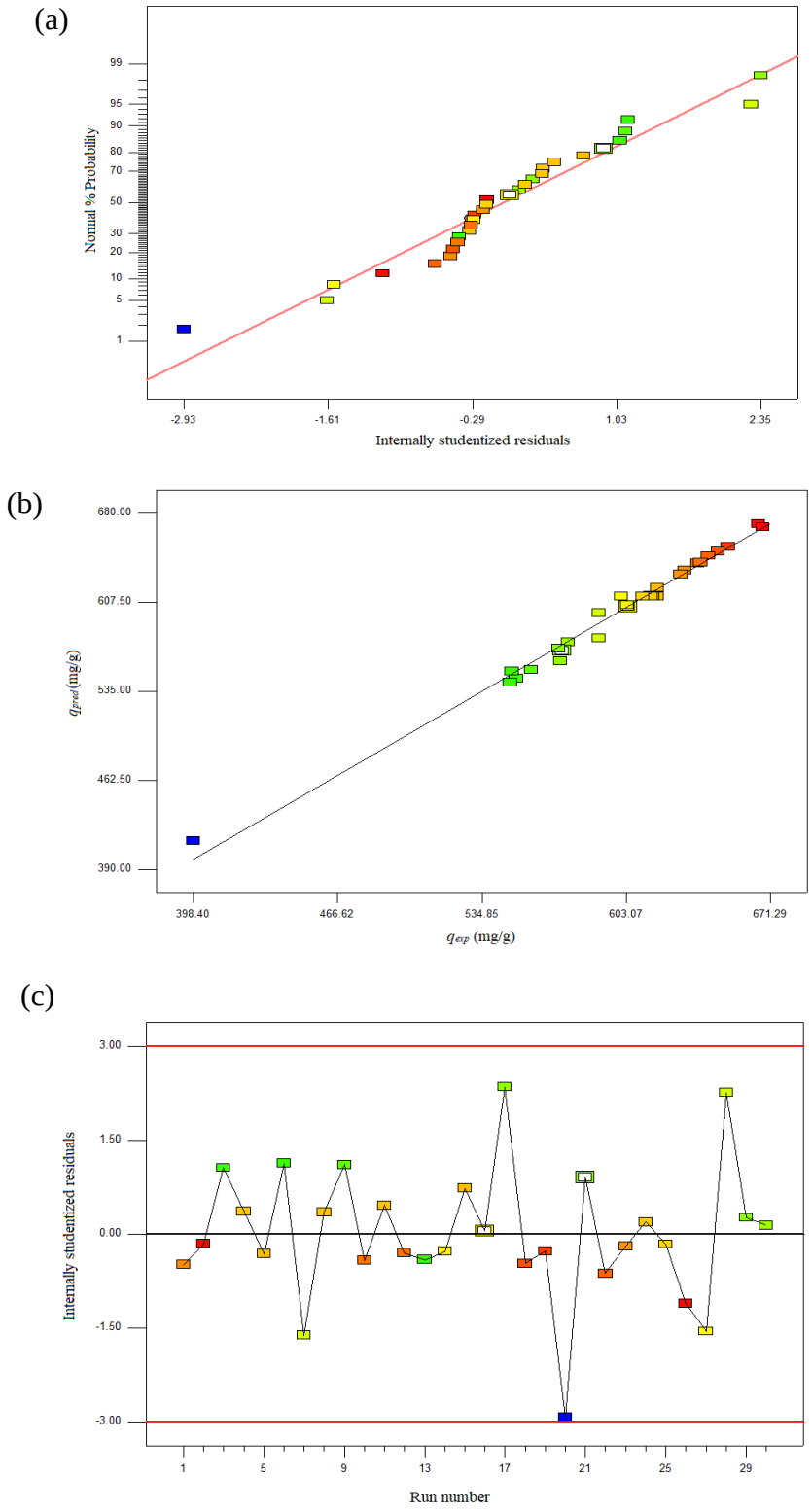


Fig. 4.14. Diagnostic plots: (a) Normal probability plot, (b) predicted versus actual adsorption capacity plot and (c) internally studentised residuals versus run number plot.

As shown in **Table 4.6**, ANOVA was also employed in determining the importance of each independent variable together with their respective interactive and quadratic terms in **Eq. (4.4)**. The *p*-value (typically $p < 0.05$) is usually applied to decide whether the term is statistically significant at 95 % confidence level. The term becomes more significant when its corresponding *p*-value becomes smaller. Accordingly, the adsorption factors and interactions which could substantially influence the adsorption of RB5 dye are A, B, C, D, BD, A^2 and B^2. Both the magnitude and sign of the regression coefficients are indicators of the extent of effect of each term towards the response. The negative sign of A indicates that higher adsorbent mass would have an antagonistic effect on the adsorption capacity. Meanwhile, the influences of B and C are more prominent as denoted by their higher numerical values.

The interactive effects of two variables on the response (q) were examined using 3D response surface plots with the remaining factors held at their central point (A: W at 8 mg, B: C_o at 300 mg/L, C: t at 60 min and D: T at 50 ℃). **Fig. 4.15 (a)**, **(b)** and **(c)** depict the simultaneous interactions between W and C_o, W and t, and W and T, respectively. Generally, a higher adsorbent mass has a negative effect on the response. The agglomeration of particles at higher concentration of GOCA adsorbent contributed to a smaller surface area and longer diffusional pathway for RB5 dye molecules to arrive at the sorption sites, thereby reducing the adsorption capacity [214]. The lower adsorption capacity could also be caused by a high amount of sorption sites remain unoccupied. As seen from **Fig. 4.15 (a)**, **(b)** and **(c)**, maximum q could be attained at the following conditions: $W < 8$ mg, $C_o > 300$ mg/L, $t > 60$ min and $T > 50$ ℃.

The response surface plots for the interactions of C_o and W, C_o and t plus C_o and T are demonstrated in **Fig. 4.15 (a)**, **(d)** and **(e)**, respectively. As revealed by the interactive plots and **Eq. (4.4)**, the adsorption capacity was enhanced at higher RB5 dye concentrations. This could be explained by the larger driving force at higher C_o which eased the transport of the dye molecules between the liquid and solid GOCA [215]. Hence, a higher adsorption capacity of RB5 dye could be achieved when C_o > 300 mg/L, W < 8 mg, t > 60 min and T > 50 ℃.

The interactive effects of contact time, t, with W, C_o and T are presented in **Fig. 4.15 (b)**, **(d)** and **(f)**, respectively. It was observed that the adsorption capacity increased with time. Nonetheless, as adsorption progressed, the adsorption capacity did not increase significantly as most of the sorption sites were taken up by the dye molecules. According to **Fig. 4.15 (b)**, **(d)** and **(f)**, the greatest adsorption capacity could be obtained by keeping t > 60 min with W < 8 mg, C_o > 300 mg/L and T > 50 ℃.

Fig. 4.15 (c), **(e)** and **(f)** demonstrate the endothermic nature of RB5 dye adsorption onto GOCA where the adsorption capacity was further enhanced at higher temperatures, T > 50 ℃. At high temperatures, the decrease in the solution viscosity accelerated the transport of the dye molecules from the bulk solution to GOCA which in turn augmented its adsorption capacity. Furthermore, the higher RB5 dye removal could be ascribed to the availability of more active sites at higher temperatures.

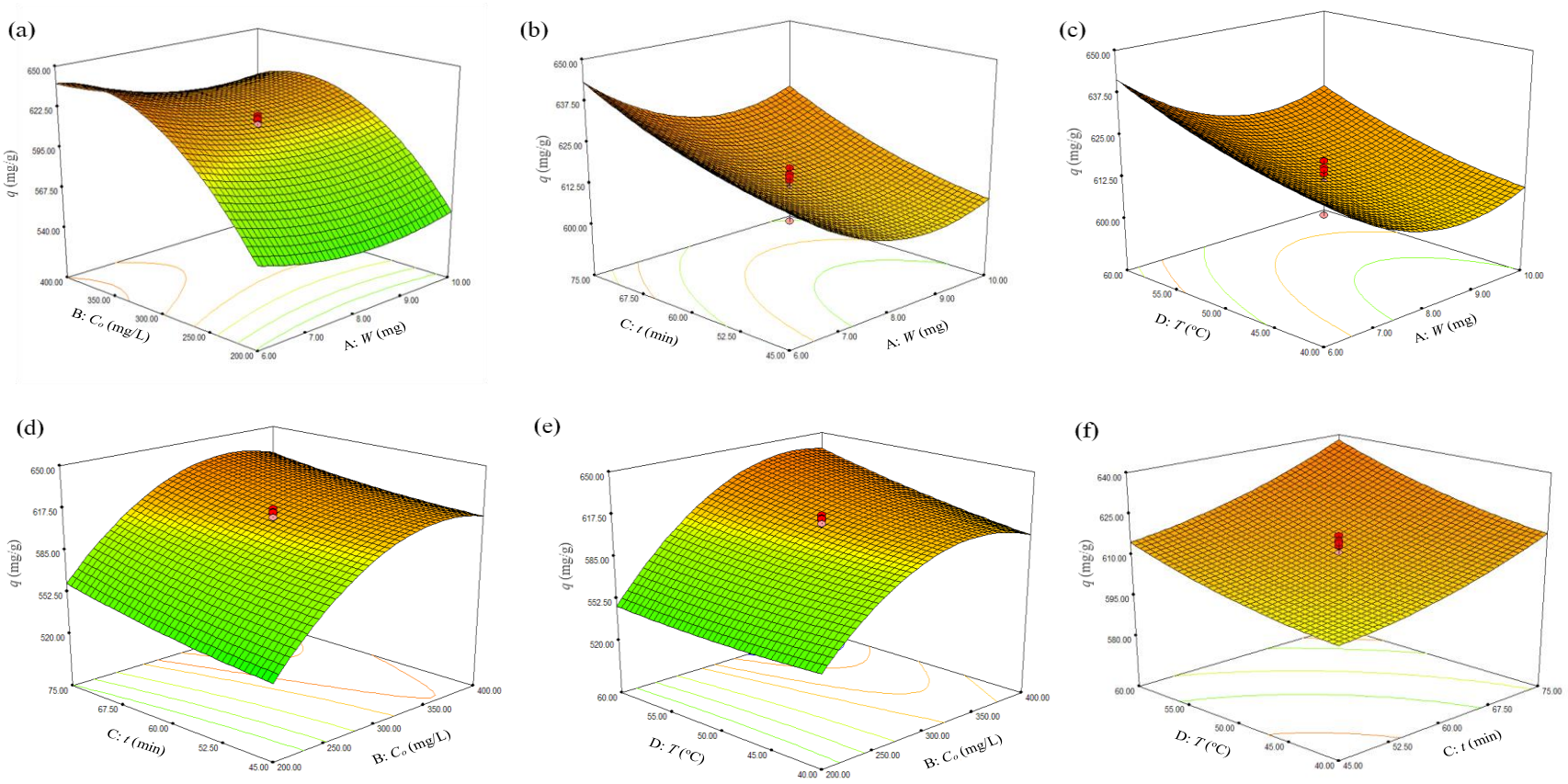


Fig. 4.15 Response surface plots for adsorption of RB5 dye onto GOCA: Effects of (a) adsorbent mass and initial concentration, (b) adsorbent mass and contact time, (c) adsorbent mass and temperature, (d) initial concentration and contact time, (e) initial concentration and temperature and (f) contact time and temperature.

In order to achieve the highest removal of RB5 dye by GOCA, optimisation of process parameters was accomplished by the Derringer's desirability method. The responding q was set to be maximum while the ultimate goals for each process variable were designed as follows: minimum W, maximum C_o and within the investigation range for t and T. The proposed optimisation outcome was that a maximum q of 668.09 mg/g could be attained along with the greatest desirability of 1 at the following conditions: W = 6 mg, C_o = 400 mg/L, t = 75 min and T = 59 ℃. The results predicted by the model were confirmed by triplicate adsorption tests at the aforementioned conditions. The measured q was determined to be 656.96 mg/g with a negligible residual error of 1.67 %, thereby, further authenticating the adequacy of the developed quadratic function in modelling the adsorption of RB5 dye onto the synthesised GOCA.

4.2.4 Regeneration of GOCA

Regeneration of the spent GOCA adsorbent is essential in large scale wastewater treatment to minimise material substitution cost and prevent secondary solid waste generation. The regeneration of exhausted GOCA was investigated with the use of 0.1 M NaOH and 0.1 M HCl solutions. Through preliminary tests, these two chemicals were found to be effective for the regeneration of GOCA. The results of regeneration study for MY and RB5 dyes removal are shown in **Fig. 4.16 (a)** and **(b)**, respectively. It can be seen from **Fig. 4.16 (a)** that GOCA manifested satisfactory reusability with the adsorption capacity of MY dye remaining above 80 % even after 5 cycles of adsorption-desorption. As for RB5 dye (**Fig. 4.16 (b))**, the GOCA adsorbent could retain approximately 90 % of its adsorption capacity

(296.77 to 270.11 mg/g) after 5 successive adsorption-desorption cycles. In 0.1 M NaOH solution, the intensive competition between OH^- and the anionic dye was responsible for the elution of the adsorbed dye. Thereafter, the regeneration process with HCl solution enabled the GOCA surface to be protonated which later showed a high affinity for MY and RB5 dyes [158]. Furthermore, the 3D GOCA adsorbent was easily recovered from the solution by forceps thus simplifying the solid-liquid separation post adsorption. The small decrease in the adsorption capacity could be due to the partial collapse of internal 3D network of GOCA [49]. Furthermore, some loss of GOCA in the form of tiny fragments was observed during the regeneration study. The present study revealed that GOCA could be reused with promising adsorption performance and hence its practical application could be envisaged.

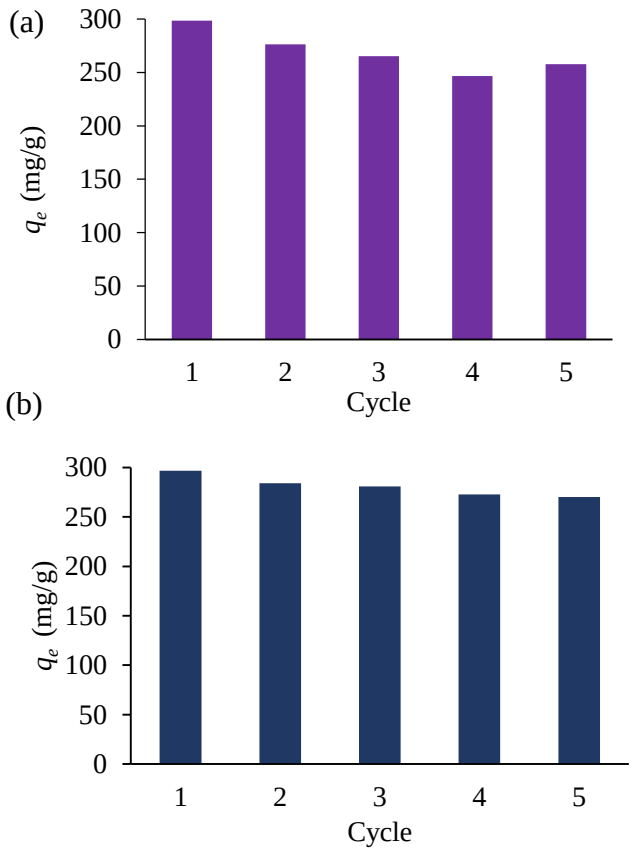


Fig. 4.16 Regeneration study for (a) MY and (b) RB5 dyes adsorption onto GOCA.

4.2.5 Comparison with literature data

The adsorption performance of GOCA was compared with other adsorbents reported in the literature, and the results are summarised in **Table 4.7**. It is noteworthy from **Table 4.7** that activated carbons synthesised from a variety of agricultural products were frequently employed for the adsorptive removal of MY dye. Notably, the adsorption performance of GOCA (418.35 mg/g) is comparable with that of grape waste activated carbon (386 mg/g) and outperforms most of the adsorbents reported. In addition to GO and chitosan, a number of adsorbents have been developed and applied for decontamination of aqueous RB5 dye such as modified dolomite, polyethyleneimine modified spent tea leaves, polyaniline nanofibers, etc. Referring to **Table 4.7**, GOCA has a relatively high adsorption capacity (656.96 mg/g) for RB5 dye which is comparable to the adsorption capacities for chitosan film (589.50 mg/g) and polyethyleneimine grafted chitosan beads (709.27 mg/g). Therefore, GOCA is an effective adsorbent for the removal of MY and RB5 dyes in aqueous media.

Table 4.7 Comparison of GOCA adsorption capacity with literature data.

MY dye		
Adsorbent	q_e (mg/g)	Reference
Grape waste activated carbon	386	[216]
Sepiolite – (3-aminopropyl)triethoxysilane	59.78	[217]
Tomato waste activated carbon	385	[218]
Peanut shell activated carbon	66.7	[219]
Ceratonia silique L. activated carbon	568	[220]
GOCA	**418.35**	***Present study***
RB5 dye		
Adsorbent	q_e (mg/g)	Reference
Modified dolomite	80.90	[221]
Polyethyleneimine modified spent tea leaves	71.94	[222]
Chitosan film	589.50	[223]
Polyaniline nanofibers	434.70	[224]
Polyethyleneimine grafted chitosan beads	709.27	[225]
GOCA	**656.96**	***Present study***

4.3 Summary

The as-fabricated GOCA exhibited promising results in the decontamination of water stained by MY and RB5 dyes. The formation of 'micro-ribbons' on the pore walls might promote the adsorption capabilities of GOCA by increasing its surface area and hence exposing more surface functional groups for interaction with the dyes. For both dyes, the adsorption kinetic obeyed the pseudo-first-order and pseudo-second-order kinetic models at low and high concentration regions, respectively. Similarly, the adsorption equilibria were best described by the Langmuir model for both systems. The negative ΔG values indicated that adsorption of both dyes onto GOCA was spontaneous. The negative ΔH values for MY dye removal implied exothermic process while the positive ΔH values for RB5 dye removal suggested endothermic nature of the process. Process optimisation by RSM yielded a MY dye adsorption capacity of 418.35 mg/g under these optimum conditions: adsorbent mass of 8 mg, concentration of 400 mg/L, contact time of 35.19 min and shaking speed of 175 rpm. Likewise, the results of response surface methodology revealed that the GOCA adsorbed the most RB5 dye (656.96 mg/g) at 75 min and 59 ℃ with 6 mg adsorbent mass and 400 mg/L initial dye concentration. GOCA was successfully regenerated using NaOH and HCl. This study concluded that GOCA is a high performance adsorbent for MY and RB5 dyes removal.

Chapter 5. Fixed-bed column adsorption of Metanil Yellow and Reactive Black 5 dyes by 3D GO/chitosan aerogel

5.1 Introduction

The efficiency of adsorbent in removing different adsorbates is usually examined by batch adsorption mode. However, for practical wastewater treatment, fixed-bed column adsorption is preferred as it can treat the polluted effluent on a continuous mode. The fixed-bed system allows large volume of wastewater to be treated at minimum contact time between the adsorbent and adsorbate. Several studies have demonstrated the successful application of 3D graphene materials in fixed-bed column adsorption. For instance, Jang and Lee [226] employed polyvinyl alcohol (PVA)-alginate encapsulated Prussian Blue-GO hydrogel beads in fixed-bed column system to remove cesium and a maximum adsorption capacity of 164.5 mg/g was achieved. Chen et al. [227] utilised PVA-GO macroporous hydrogel beads as column adsorbent to sequester various pollutants such as p-nitrophenol, Methylene Blue dye and uranium ion. Moreover, Singh et al. [228] performed the hexavalent chromium removal in a continuous adsorption process using graphene/polylysine aerogel and the highest adsorption capacity recorded was 133.18 mg/g.

In this work, GO was integrated with chitosan biopolymer through ice-templating process to produce GOCA which was applied as the fixed-bed column adsorbent to remove MY and RB5 dyes for the first time. The influences of column parameters such as bed height, inlet concentration and feed flowrate on the column performance were evaluated. The experimental data were then analysed with

several kinetic models such as the Thomas, Yoon-Nelson and Adams-Bohart models to predict the dynamic adsorption behaviour.

5.2 Results and discussion

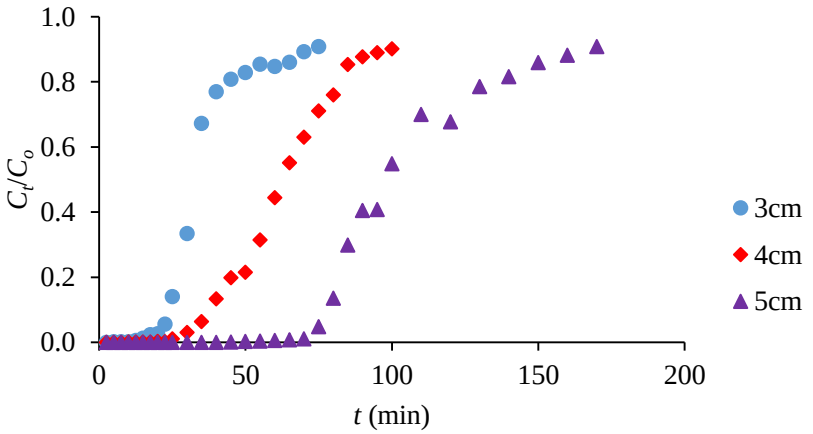
5.2.1 Effect of bed height on column adsorption

Bed height is a crucial operating parameter in the fixed-bed column adsorption as it determines the quantity of adsorbent used in the process and hence affecting the quality of effluent produced. The quantity of active sites available is related to the adsorbent mass. The dynamic adsorption of both MY and RB5 dyes was carried out at different bed heights (3, 4 and 5 cm). Meanwhile, the feed flowrate and inlet concentration were maintained at 2 mL/min and 150 mg/L for MY dye, and 200 mg/L for RB5 dye. The results are delineated in **Fig. 5.1** and **Table 5.1**. The results demonstrated that taller bed could treat larger volume of effluent. It is also discernible that the increase in bed height had extended the breakthrough time (t_b) and saturation time (t_e), and hence led to slower exhaustion of the GOCA bed. For instance, the t_b and t_e increased from 22.5 to 75 min and 75 to 170 min, respectively, for MY dye, while for RB5 dye, the t_b and t_e were extended from 20 to 50 min and 130 to 300 min, respectively.

In addition, the slope of the breakthrough curve became less steep at taller bed, resulting in the broadening of mass transfer zone. As shown in **Table 5.1**, when the bed height was increased from 3 to 5 cm, the amount of dye adsorbed escalated from 10.63 to 31.30 mg for MY dye, while it increased from 19.09 to 49.32 mg for RB5 dye. Moreover, the bed adsorption capacity was improved from 106.75 to 157.06 mg/g for MY dye, and from 190.48 to 247.96 mg/g for RB5 dye. This

suggested that the total amount of dyes adsorbed was highly dependent on the bed height. A taller bed has a larger adsorbent loading in the column and thus more binding sites were available for adsorption. Furthermore, the larger bed height also provided more contact time for the dye molecules to interact with the adsorbent leading to greater uptake of the dyes. The amount of RB5 dye adsorbed in the GOCA column was higher in comparison to MY dye, and this result suggested that the GOCA bed has a lower affinity for MY dye. Similar findings were reported by other researchers [229-231].

(a)



(b)

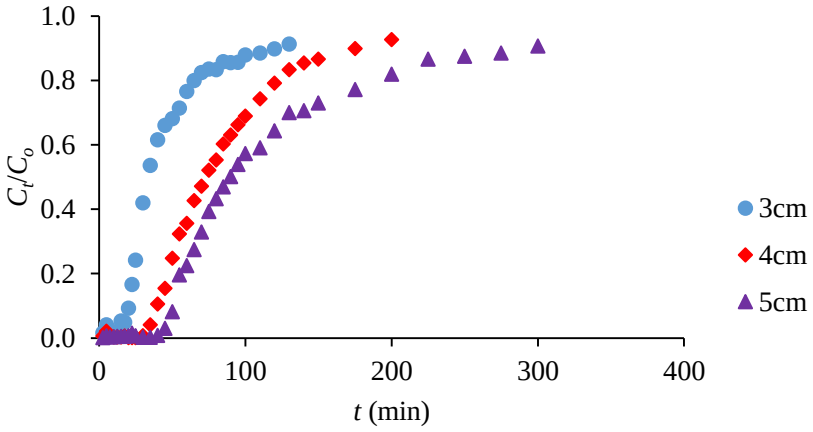


Fig. 5.1 Breakthrough curves obtained at different bed heights for (a) MY and (b) RB5 adsorption onto GOCA.

Table 5.1 Data obtained for fixed-bed column adsorption of MY and RB5 dyes.

MY dye							
***Z* (cm)**	***C*$_o$ (mg/L)**	***Q* (mL/min)**	***t*$_b$ (min)**	***t*$_e$ (min)**	***V*$_t$ (mL)**	***m*$_{ads}$ (mg)**	***q* (mg/g)**
3	150	2	22.5	75	150	10.63	106.75
4	150	2	35	100	200	18.62	124.65
5	150	2	75	170	340	31.30	157.06
4	100	2	50	110	220	14.20	94.99
4	200	2	30	90	180	20.89	139.00
4	150	3	26.67	73.33	220	18.50	122.56
4	150	4	20	40	160	16.23	107.60
RB5 dye							
***Z* (cm)**	***C*$_o$ (mg/L)**	***Q* (mL/min)**	***t*$_b$ (min)**	***t*$_e$ (min)**	***V*$_t$ (mL)**	***m*$_{ads}$ (mg)**	***q* (mg/g)**
3	200	2	20	130	260	19.09	190.48
4	200	2	40	200	400	35.33	234.74
5	200	2	50	300	600	49.32	247.96
4	100	2	55	400	800	32.90	220.04
4	300	2	22.5	175	350	36.59	245.22
4	200	3	23.33	133.33	400	33.01	220.80
4	200	4	15	100	400	32.30	215.03

5.2.2 Effect of inlet concentration on column adsorption

Inlet concentration is another critical variable influencing fixed-bed column adsorption as concentration gradient serves as the driving force for mass transfer. **Fig. 5.2 (a)** and **(b)** present the effects of inlet MY dye concentration (100, 150 and 200 mg/L) and inlet RB5 dye concentration (100, 200 and 300 mg/L), respectively, on the breakthrough curves for a GOCA bed of 4 cm and feed flowrate of 2 mL/min. The variation in the inlet concentration had a considerable impact on the column performance and shape of breakthrough curve. At higher inlet concentration, the GOCA bed was quickly occupied by the dye molecules. Hence, both the

breakthrough and exhaustion times were greatly reduced, suggesting less volume of dye solution was treated. Moreover, the breakthrough curve became steeper and shifted towards the origin at higher inlet concentration. On the contrary, the breakthrough curve was dispersed at lower inlet concentration. The column data obtained at different inlet concentrations are summarised in **Table 5.1**.

Diffusion of the dyes in fixed-bed column is a concentration-dependent process as the change in concentration gradient altered the breakthrough and saturation times to a great extent. The larger concentration gradient at higher inlet concentrations contributed to a greater mass transfer driving force and rapid adsorption rate, thus leading to the quicker exhaustion of the column. Contrarily, the extension of exhaustion time at lower inlet concentration was caused by the slower mass transfer of the dye molecules as a result of weaker driving force. Despite the shortened breakthrough time, the bed adsorption capacity was augmented with increasing inlet concentrations (94.99 - 139 mg/g for MY dye and 220.04 - 245.22 mg/g for RB5 dye). At higher inlet concentration, more dye molecules could diffuse into the adsorbent bed with lower overall mass transfer resistance and hence boosted the dye uptake capacity. The direct relationship between bed adsorption capacity and inlet concentration was also reported in other studies [232, 233].

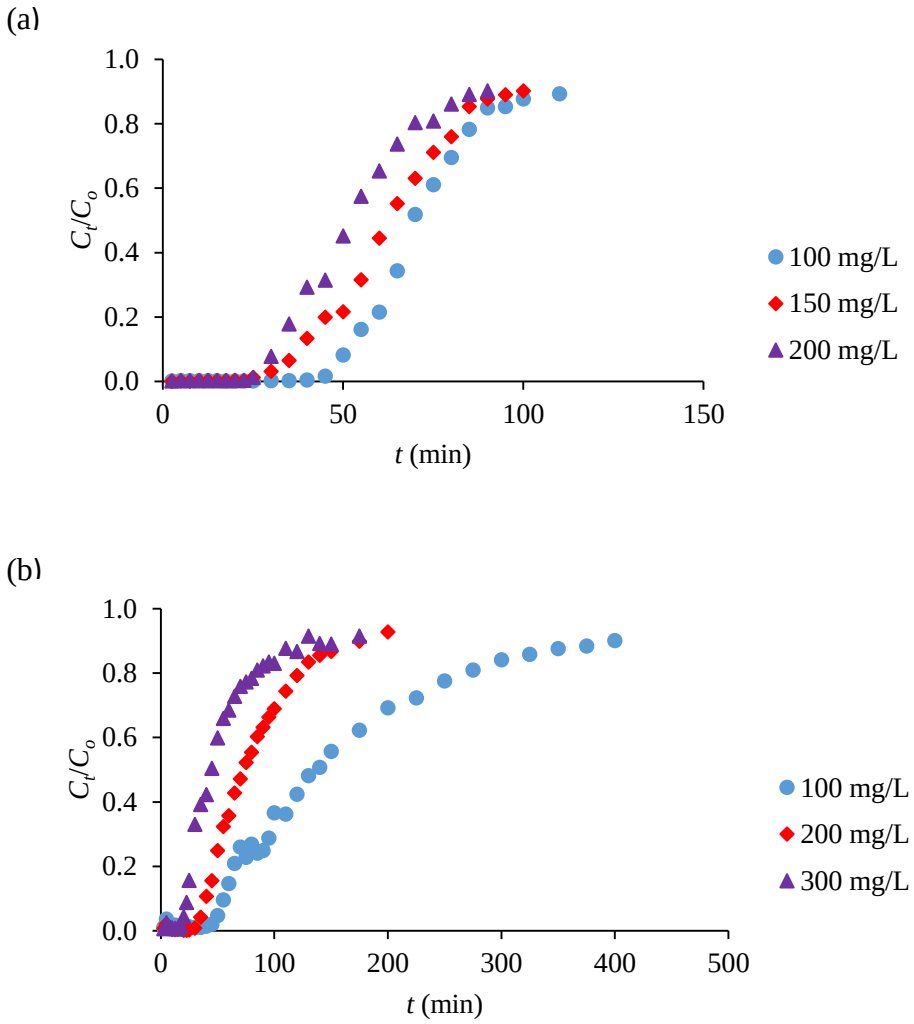


Fig. 5.2 Breakthrough curves obtained at different inlet concentrations for (a) MY and (b) RB5 adsorption onto GOCA.

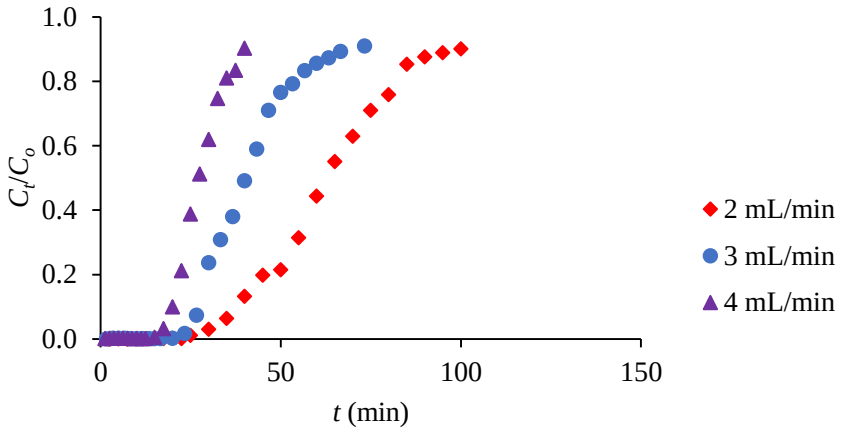
5.2.3 Effect of feed flowrate on column adsorption

The feed flowrate determines the period of interaction between the dye molecules and adsorbent. As depicted in **Fig. 5.3 (a)** and **(b)**, the effects of feed flowrate (2, 3 and 4 mL/min) on the dynamic adsorption of MY and RB5 dyes were determined at an inlet concentration of 150 mg/L for MY dye and 200 mg/L for RB5 dye, and GOCA bed length of 4 cm. The column parameters obtained for the studies are demonstrated in **Table 5.1**. The time required to achieve the breakthrough point at

different flowrates of 2, 3 and 4 mL/min were 35, 26.67 and 20 min for MY dye, and 40, 23.33 and 15 min for RB5 dye, respectively. The results indicated that the adsorption process was accelerated at higher feed flowrate to attain the breakthrough point earlier. Similar trend was observed for the exhaustion time. The shifting of the breakthrough curve towards the origin at higher flowrate also demonstrated a shortened breakthrough time.

The early breakthrough and exhaustion was due to the inadequate contact time between the dye molecules and GOCA bed. The residence time of the dye molecules in the column was not sufficient for achieving the adsorption equilibrium at the high flowrate. Likewise, a negative trend was noticed on the bed adsorption capacity with increasing flowrate. The bed adsorption capacity for MY dye declined from 124.65 to 107.60 mg/g while that for RB5 dye decreased from 234.74 to 215.03 mg/g. At higher flowrates, the dye molecules had inadequate time to diffuse into the adsorbent bed and attach onto it, leading to the deteriorated column performance. Therefore, low feed flowrate is important for effective adsorption which was also reported in other studies [234-236].

(a)



(b)

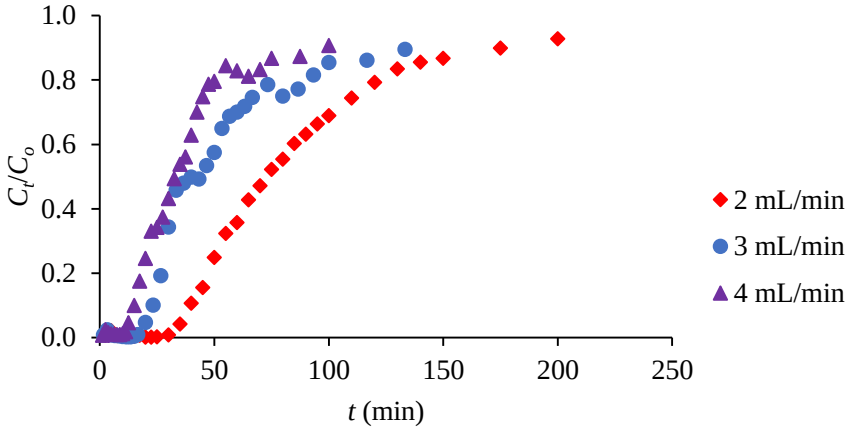


Fig. 5.3 Breakthrough curves obtained at different feed flowrates for (a) MY and (b) RB5 adsorption onto GOCA.

5.2.4 Kinetic modelling of column data

The Thomas model was used to describe the column adsorption with 100 % breakthrough, especially when the external and internal diffusion resistances are negligible. This model delivered indicative results such as bed adsorption capacity (q_o) and Thomas model constant (k_{TH}) for better interpreting the process. Column data analysis using the Thomas model was performed at different bed heights, inlet dye concentrations and feed flowrates, as portrayed in **Table 5.2** and **Fig. 5.4**. The

adequacy of the model for describing both dyes adsorption is substantiated by the high R^2 values (0.964 – 0.996 for MY dye and 0.932 – 0.970 for RB5 dye) acquired under different experimental conditions.

It is noticeable from **Table 5.2** that the k_{TH} increased as the feed flowrate increased, while the q_o depreciated. However, with an increase in the inlet concentration, the q_o improved, conversely, the k_{TH} depleted. The decrease in k_{TH} implied a decline in the dye adsorption rate. The Thomas model considers the adsorption to be driven by interface mass transfer but not limited by chemical reaction [234]. Furthermore, at higher inlet concentrations, the immense driving force as a result of large contrast in the dye concentrations in liquid and solid phases eventually intensified the bed adsorption capacity. An identical trend was observed for the variation in bed height. Accordingly, lower feed flowrate, greater inlet concentration and bed height were favourable for enhancing the bed adsorption capacity and thus attaining better column performance.

Table 5.2 Parameters of the Thomas, Yoon-Nelson and Adams-Bohart models for MY and RB5 dyes adsorption in GOCA fixed-bed column.

MY dye										
***Z* (cm)**	***C_o* (mg/L)**	***Q* (mL/min)**	**Thomas**			**Yoon-Nelson**			**Adams-Bohart**		
			k_{TH}	***q_o***	***R^2***	***k_{YN}***	***τ***	***R^2***	***k_{AB}***	***N_o***	***R^2***
3	150	2	1.153	102.18	0.964	0.173	33.92	0.964	0.730	5.272	0.936
4	150	2	0.545	128.72	0.996	0.082	64.10	0.996	0.444	6.981	0.981
5	150	2	0.416	154.84	0.971	0.062	102.86	0.971	0.454	8.227	0.948
4	100	2	0.977	96.03	0.992	0.098	71.78	0.992	0.937	4.889	0.990
4	200	2	0.437	142.64	0.988	0.087	53.60	0.988	0.370	7.835	0.956
4	150	3	0.837	122.72	0.987	0.126	41.18	0.987	0.671	6.824	0.952
4	150	4	1.535	111.24	0.992	0.230	27.96	0.992	1.393	5.804	0.975
RB5 dye										
***Z* (cm)**	***C_o* (mg/L)**	***Q* (mL/min)**	**Thomas**			**Yoon-Nelson**			**Adams-Bohart**		
			k_{TH}	***q_o***	***R^2***	***k_{YN}***	***τ***	***R^2***	***k_{AB}***	***N_o***	***R^2***
3	200	2	0.341	170.33	0.943	0.071	40.71	0.943	0.495	7.170	0.958
4	200	2	0.213	218.87	0.970	0.045	78.57	0.970	0.221	11.485	0.938
5	200	2	0.158	209.12	0.945	0.033	100.09	0.945	0.190	11.040	0.934
4	100	2	0.185	202.38	0.954	0.019	151.28	0.954	0.190	10.640	0.898
4	300	2	0.185	212.59	0.948	0.059	49.56	0.948	0.217	10.791	0.894
4	200	3	0.313	192.13	0.932	0.065	46.44	0.932	0.356	9.799	0.879
4	200	4	0.446	192.09	0.965	0.093	34.45	0.965	0.434	10.396	0.920

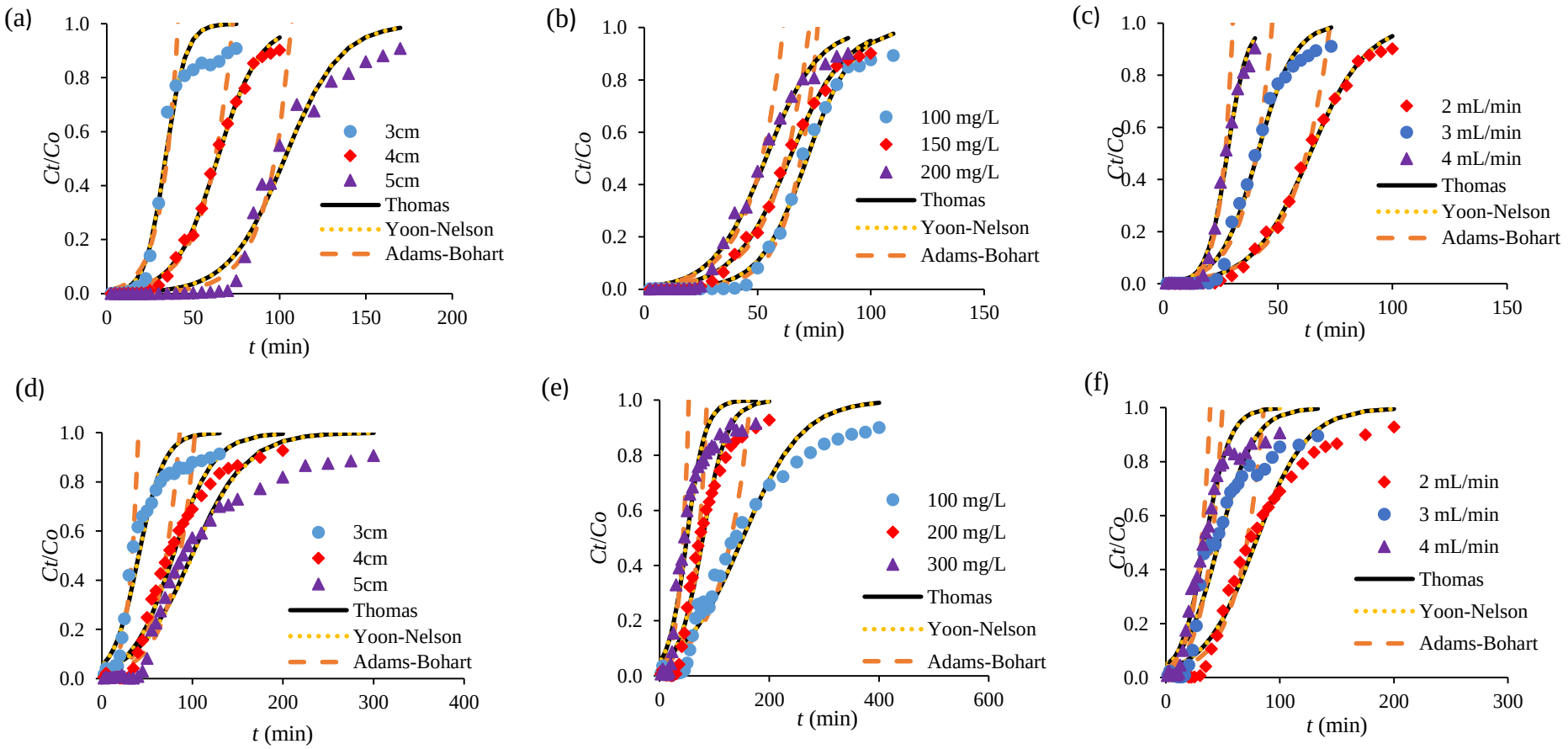


Fig. 5.4 Non-linear fitting of (a – c) MY and (d – f) RB5 dyes column data with the Thomas, Yoon-Nelson and Adams-Bohart models.

The experimental column data of MY and RB5 dyes adsorption under different conditions were fitted to the Yoon-Nelson model and the corresponding results are presented in **Fig. 5.4** and **Table 5.2**. The rate constant (k_{YN}) and time for attaining 50 % breakthrough (τ) are the important parameters determined from this model. The column data were adequately expressed by the Yoon-Nelson model with the R^2 values ranging from 0.964 – 0.996 and 0.932 – 0.970 for MY and RB5 dyes, respectively. In general, the k_{YN} and τ are inversely correlated.

For the increment in both inlet concentration and feed flowrate, the τ decreased and *vice versa* for k_{YN}. At higher inlet concentration, more dye molecules are available for adsorption thus leading to rapid uptake of MY and RB5 dyes. The rapid dye uptake rate caused the dyes to breakthrough earlier and the GOCA bed to be exhausted faster. Contrarily, the τ increased while the rate constant decreased for longer bed. This is due to the fact that more time is required for the dye molecules to travel though a longer bed. By comparing the R^2 values, both the Thomas and Yoon-Nelson models could be used to express the adsorption of MY and RB5 dyes onto GOCA in a fixed-bed column.

The Adams-Bohart model is usually applied to study the initial behaviour of the breakthrough curve. As shown in **Table 5.2** and **Fig. 5.4**, this model could represent satisfactorily the column data, up to 50 % of inlet concentration, with R^2 varying from 0.936 – 0.990 and 0.879 – 0.958 for MY and RB5 dyes, respectively. Notably, the k_{AB} increased at higher flowrates but decreased at larger bed height. The greater kinetic constants implied lesser mass transfer resistance, which were also illustrated by the steeper breakthrough curves. Furthermore, the N_o increased at larger bed heights and inlet concentrations, but decreased at higher feed flowrates. The taller

bed indicated more sorption sites and thus higher surface area for effective dye attachment onto the adsorbent. The appropriate fitting of the column data with the Adams-Bohart model suggested that the initial part of the column adsorption was dominated by the external mass transfer [237].

5.2.5 Proposed adsorption mechanisms

In order to gain more insights into the adsorption mechanism, the FTIR spectra for MY and RB5 dyes, as well as GOCA before and after adsorption were determined. As observed in **Fig. 5.5**, the indicative peaks of MY dye could be found at 3020 (aliphatic –CH), 1597 (C=C aromatic vibration), 1431-1490 (azo-bond –N=N– vibrations), 1336 and 1043 (–SO_3 stretching), 993 (–NH and =C–H) and 650-800 cm^{-1} (aromatic rings) [238]. Meanwhile, the characteristic peaks for the RB5 dye are located at 3407 (stretching vibration of –OH and –NH_2), 2854-2925 (aliphatic –CH_2), 1574-1616 (C=C aromatic skeletal vibrations), 1414-1489 (representative azo-bond –N=N– vibrations), 1042-1340 (–SO_3 stretching), 990 (–NH and =C–H) and 650-800 cm^{-1} (aromatic rings) [239, 240]. The FTIR peaks of the adsorbent before adsorption such as 3267 (stretching vibration of –OH and –NH_2), 2881 (stretching vibration of –CH_2), 1636 (–C=O stretching vibration of amide), 1552 (N–H bending of amine), 1409 (C–N axial deformation) and 1020-1065 cm^{-1} (stretching vibration of C–O) demonstrated the presence of various functional groups which were possibly the sorption sites for MY and RB5 dyes attachment.

The new peaks in the GOCA after the adsorption of MY dye are located at 1495 (azo-bond –N=N–), 1378 and 1031 (sulfonate group –SO_3), and 650-800 cm^{-1} (aromatic rings). The FTIR spectrum of the adsorbent after the RB5 dye adsorption

presents new peaks at 1492, 1042-1378, and 734-890 cm^{-1} which could be linked to the vibration of azo-bond –N=N–, sulphonate groups $–SO_3$ and aromatic ring of RB5 dye, respectively. This observation indicated the successful deposition of the dye onto the adsorbent. The weakening of the amino peak at 1552 cm^{-1} after adsorption was probably due to the interaction of RB5 dye with the amino groups of the GOCA adsorbent [202]. The easily protonated amino groups of the adsorbent and the dissociation of RB5 dye into anionic sulphonate facilitated the removal of the dye through electrostatic attraction as depicted by **Eq. (5.1)** [202].

$$\text{R-NH}_3^+ + \text{RB5-SO}_3^- \longleftrightarrow \left(\text{R-NH}_3^+\right)\left(\text{RB5-SO}_3^-\right) \qquad \textbf{(5.1)}$$

The identification of nitrogen atoms in GOCA adsorbent as the primary sites for MY and RB5 dyes binding were further substantiated by the disappearance of the C–N axial deformation and the shift of amide-carbonyl peak. For instance, the peak corresponding to the stretching vibration of –NHCO– was shifted from 1636 to 1633 cm^{-1} for MY dye, and to 1631 cm^{-1} for RB5 dye. The peak attributed to the carboxyl groups of GO (at around 1712 cm^{-1}) is absent from the FTIR spectrum of the adsorbent. Hence, $\pi - \pi$ stacking interaction between the aromatic rings of the dye molecules and the basal planes of GO was deduced to be stronger as the electrostatic repulsion was shielded by the binding of GO's carboxyl groups to chitosan [202]. Apart from that, the peaks of RB5 dye ascribed to the aromatic rings at 732, 843 and 899 cm^{-1} shifted to 734, 845 and 890 cm^{-1}, thus further confirming the presence of $\pi - \pi$ stacking interaction. In summary, MY and RB5 dyes were adsorbed onto the GOCA by electrostatic attraction and $\pi - \pi$ stacking interactions.

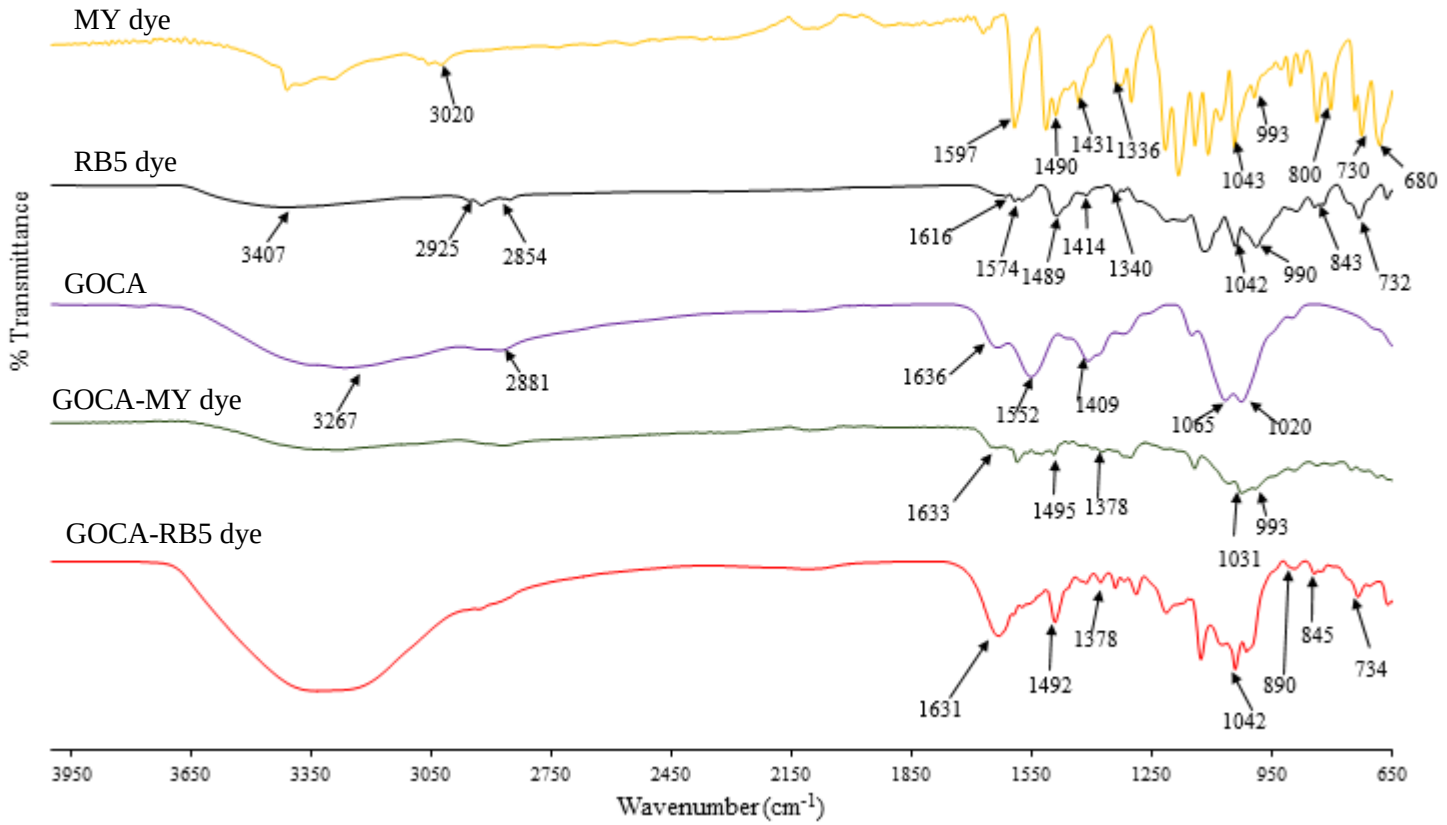


Fig 5.5 FTIR spectra of MY and RB5 dyes, and GOCA before and after adsorption.

5.2.6 Comparison of MY and RB5 dyes adsorption onto GOCA

The point of zero charge (PZC) of GOCA was determined as 6. The natural pH of the MY and RB5 dye solutions were approximately 5.8 and 5.3, respectively. The GOCA surface was protonated when in contact with the dye solutions, making it favourable for attracting the anionic dyes through electrostatic interaction.

Under similar experimental conditions, the GOCA adsorbed more RB5 dye than MY dye. This discrepancy was ascribed to the different ionic strengths of the dye molecules and electrostatic interaction between the negatively charged dye molecules and the positively charged amine groups of GOCA [241]. The higher affinity of the GOCA adsorbent for RB5 dye molecules is related to its higher charge density. As shown in **Fig. 5.6**, the RB5 dye molecule contains 4 sulphonate groups which could interact with the amine groups via electrostatic attraction while the MY dye molecule possesses only 1 sulphonate group. As a result, it is plausible for the RB5 dye molecules to bind more strongly to the adsorbent, contributing to the higher adsorption capacity.

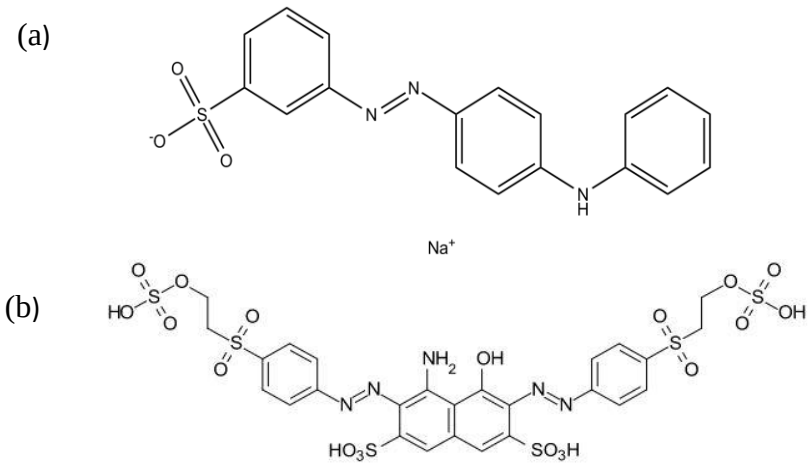


Fig. 5.6 Molecular structures of (a) MY and (b) RB5 dyes.

5.2.7 Comparison of bed adsorption capacity with other adsorbents

As shown in **Table 5.3**, some researchers have employed activated carbon and other materials such as waste and biopolymer for dynamic adsorption of MY and RB5 dyes. A comparison between result of present study and other published data suggested that the fixed-bed column performance of GOCA has outperformed some studies. This finding indicates that GOCA is a promising adsorbent for fixed-bed column adsorption of MY and RB5 dyes.

Table 5.3 Comparison of bed adsorption capacities for MY and RB5 dyes removal in fixed-bed column system.

Adsorbent	Bed adsorption capacity, q (mg/g)		Reference
	MY dye	RB5 dye	
GOCA	**157.06**	**247.96**	***Present study***
Activated carbon (oil palm fruit mesocarpfibre)	15.982	-	[242]
Fertiliser plant waste carbon slurry	248	-	[243]
Activated carbon (Gmelina bark)	19.93	-	[244]
Bamboo waste activated carbon	-	39.02	[245]
Polyethylenimine-crosslinked chitin	-	295.5	[246]
Commercial activated carbon Filtrasorb 400	-	0.107	[247]

5.3 Summary

In the present study, GOCA exhibited promising performance for fixed-bed column adsorption of MY and RB5 dyes. The findings indicated that the adsorption of these dyes was highly dependent on bed length, inlet concentration and feed flowrate. For both dyes, higher bed adsorption capacities were obtained at larger bed height, higher inlet concentration and lower feed flowrate. The maximum bed adsorption capacities obtained were 157.06 and 247.96 mg/g for MY and RB5 dyes, respectively. Furthermore, the column data of both dyes were well correlated to the Thomas and Yoon-Nelson models. The Adams-Bohart model could also describe the initial 50 % of breakthrough curve satisfactorily. The results of pH test and FTIR analysis supported that the adsorption mechanisms were contributed by electrostatic interaction and $\pi - \pi$ stacking. This work manifested that GOCA is more effective in RB5 dye adsorption than MY dye. The existence of four negatively charged sulphonate groups in the RB5 dye molecule enabled stronger electrostatic attraction with the GOCA bed. Summarily, GOCA has a great potential in practical sequestration of both MY and RB5 dyes.

Chapter 6. Batch adsorption of lead and cadmium by 3D GO/xanthan/TiO_2 composite

6.1 Introduction

Aquatic pollution as a consequence of indiscriminate disposal of heavy metal laden effluents is one of the major environmental concerns to be addressed. Anthropogenic activities such as production of semiconductor and energy storage systems, utilisation of pesticides and fertilisers, and mining, usually release a vast amount of heavy metals such as lead, mercury, cadmium and nickel into natural water resources, where these cationic metals cannot be biologically degraded and may accumulate at a high concentration [248]. In particular, lead (Pb) is a highly stable pollutant discharged from manufacturing firms of paints, batteries, ceramics and metal plating to the nearby water sources. The ubiquitous presence of Pb due to its high solubility and mobility further enhances its detrimental impacts on living beings [249]. Specifically, children are more vulnerable to Pb poisoning and may face irreversible mental retardation when exposed to severe Pb poisoning. Cadmium (Cd), generally known for its acute toxicity and carcinogenicity even at a relatively low concentration, is one of the most harmful heavy metal contaminants [250]. Cd can cause bone disease (Ouch-Ouch disease), high blood pressure, lung cancer and kidney failure [250-253]. Thus, effective removal of Pb and Cd contaminants from water sources is necessary for the protection of the environment and human life.

On the basis of cost effectiveness and efficacy, adsorption presents an attractive alternative for the remediation of heavy metal polluted water [254]. In recent years,

graphene nanomaterials configured into a three-dimensional (3D) hierarchical structure have acquired much attention from the research community for two main reasons: (1) enormous specific surface area and interconnected porous network for sorption of pollutants; (2) 3D macrostructure enabling easy recovery and regeneration [32]. Graphene oxide (GO) is popularly explored in this area owing to its abundant reactive surface functional groups and facile assembly into 3D hierarchical graphene architects [85]. Among the various 3D graphene assembly techniques, ice-templating has emerged as a relatively simple, cost effective and green approach in fabricating 3D graphene structures with excellent adsorption capabilities [255].

A series of 3D GO based adsorbing materials prepared by ice-templating have been employed for the removal of a diverse toxic pollutants. However, the pristine GO nanosheets are held together by weak interactions such as π-π stacking producing a fragile adsorbent which disintegrates in water during adsorption. To increase the robustness of the 3D GO networks, chemical integration agents can be applied to improve both the mechanical and adsorption performance. For example, Yousefi et al. [256] assembled an ultra-strong reduced GO-cellulose nanocrystal sponge which could remove Cd with an adsorption capacity of 76.3 mg/g. Wu et al. [144] fabricated magnetic polysaccharide/GO@Fe_3O_4 gel beads which could efficiently remove Pb (189.04 mg/g) and Cd (86.28 mg/g), and retained 80 % of its adsorption performance after 5 successive adsorption-desorption cycles. Another work by Zhang et al. [97] demonstrated that the as-synthesised GO/carboxymethyl cellulose monolith could remove Pb with an adsorption capacity of 76.70 mg/g. The

literature data indicated that the incorporation of cellulose-based biomass into 3D GO network offered promising application in wastewater purification.

Xanthan is a low cost bacterial polysaccharide of glucose, mannose and glucuronic acid monomers. It can be derived through aerobic fermentation of a bacterium species known as *Xanthamonas campestris*. Its chemical structure which is anionic in nature, resembles that of cellulose. The use of xanthan biomass for wastewater remediation is of great potential owing to the existence of abundant hydrophilic groups as well as its non-toxicity and good biodegradability [257]. Furthermore, its unique rheological properties such as high viscosity at slow stirring and *vice versa*, enables it to be a friendly backbone matrix for facile fabrication of graphene composites [74].

The incorporation of active materials such as ferric oxide [258], titanium dioxide (TiO_2) [112] and manganese dioxide [13] into graphene structures has evoked a broad interest in the field of adsorption as the metallic compounds may enhance the adsorption performance by providing additional active sites. Significantly, TiO_2 is receiving more attention in the field of environmental protection as it is readily available, low cost, non-toxic and chemically stable [112]. Zhao et al. [259] compared the adsorption performance of pristine multi-walled carbon nanotubes (MWCNTs) and TiO_2/MWCNTs nanocomposite on Pb removal. Their results indicated that TiO_2 had augmented the adsorption of Pb. Sharififard et al. [260] reported that Cd adsorption capacity of nano-clay enhanced from 8.92 to 16.20 mg/g following modification with TiO_2. Hence, the incorporation of TiO_2 into 3D graphene network could be beneficial for application in toxic water clean-up.

Response surface methodology (RSM) is used for process modelling and optimisation. A number of works have reported the use of RSM for developing empirical models to describe and predict heavy metals adsorption. Murugesan et al. [261] modelled the Pb adsorption onto chelating resin by varying the solution pH, initial concentration and temperature using RSM. Lee et al. [163] optimised the Pb adsorption onto palm oil sludge-biochar using RSM and obtained a maximum adsorption capacity of 20.87 mg/g.

In this research, a new 3D graphene oxide/xanthan/TiO_2 (GXT) composite was designed and prepared via the ice-templating method. This is the first work which investigated on the adsorptive Pb and Cd removal by 3D GXT composite. The as-synthesised 3D GXT was characterised using different analytical techniques and the effects of various adsorption parameters on its adsorption for the heavy metals were evaluated. Besides, the interactive effects of selected adsorption parameters were studied through RSM. The experimental adsorption data were finally correlated to different kinetic and equilibrium models.

6.2 Results and discussion

6.2.1 Characterisation of 3D GXT composite

TGA is an effective technique for studying the thermal decomposition behaviour and approximating the chemical compositions of the 3D GXT composite and xanthan. As shown in **Fig 6.1**, approximately 14 and 10 % loss in weight were exhibited by the 3D composite and xanthan, respectively, as temperature was increased from 30 to 130 ^{o}C. These early minor weight losses were due to the elimination of moisture content in the samples. Degradation of the polymer chain

started from 230 to 800 ^{o}C and hence the volatile organic matters for 3D GXT and xanthan were determined to be 57 and 68 %, respectively [262]. It is noteworthy that the graphene composite experienced a greater weight loss up to 250 ^{o}C when compared with the xanthan biomass which could be due to the presence of GO. GO contains abundant oxygenated groups such as carboxyl and hydroxyl groups which decompose at temperatures between 100 to 300 ^{o}C [263]. The TGA results suggested the successful integration of GO and xanthan within the 3D composite. The fixed carbon and ash contents of 3D GXT composite were determined to be 10.80 and 18.20 %, respectively. Meanwhile, the xanthan biomass possessed a higher fixed carbon content of 14.70 %, but lower ash content of 7.30 %. The increment in the ash amount from 7.30 to 18.20 % indicated that the successful integration of GO and TiO_2 with xanthan biopolymer might enhance the thermal stability of the composite.

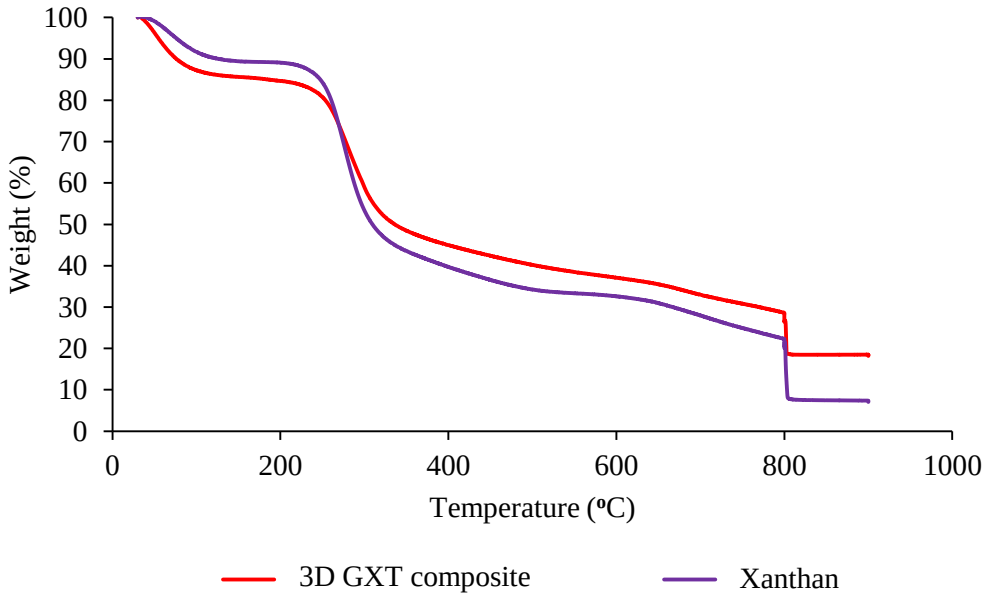


Fig. 6.1 TGA profiles of xanthan and 3D GXT composite.

The precursors (GO and xanthan) and 3D GXT composite were analysed by FTIR to identify the chemical functionalities in their structures and the results are depicted in **Fig. 6.2**. The FTIR indicative peaks for xanthan were detected at 3264, 2894, 1710, 1600, 1406 and 1023 cm^{-1}. A broad band detected at 3264 cm^{-1} was ascribed to the stretching vibration of hydroxyl (–OH) group while the peak at 2894 cm^{-1} corresponded to the stretching vibration of C–H in methylene groups. The peaks at 1710 and 1406 cm^{-1}, respectively, indicated the symmetrical and asymmetrical stretching vibration of $–COO^-$ in the carboxylate salt groups. The FTIR absorption peak at 1600 cm^{-1} was related to the axial deformation of C=O of enols (β-diketones) whereas the stretching vibration of C–O–C groups was represented by the peak at 1023 cm^{-1} [74, 264].

The FTIR spectrum of GO demonstrated the C–O stretching mode in C–OH at 1036 cm^{-1}, C–O stretching mode in epoxide group at 1216 cm^{-1}, O–H deforming vibration in C–OH at 1391 cm^{-1}, C=C vibration of the sp^2 hybridised carbon skeletal network at 1617 cm^{-1} and C=O stretching vibration in carboxylic and/or carbonyl groups at 1712 cm^{-1} [265]. Notably, the resemblance between the spectra of the xanthan and 3D GXT composite could be due to the high content of xanthan within the composite. The presence of an additional peak at 1048 cm^{-1} supported the successful incorporation of GO in the 3D composite. In addition, the peak at 1400 cm^{-1} could be assigned to the Ti-O-Ti vibration. A new peak at 1273 cm^{-1} was identified in the composite which might be assigned to the Ti–O–C vibrations. The generation of Ti–O–C bond could be explicated based on the reaction between the OH groups in both TiO_2 and GO [265-267].

During the 3D GXT composite synthesis, GO and TiO_2 were mixed with xanthan under mechanical stirring to form a stable suspension. The xanthan biopolymer becomes less viscous at high shear rate and *vice versa* at low shear rate. Hence, continuous stirring during the preparation process is imperative as it enabled the GO and TiO_2 to be distributed uniformly within the xanthan matrix. At the end of the blending process, the solution became viscous and allowed the GO and TiO_2 to be suspended throughout the matrix without settling down at the bottom [74].

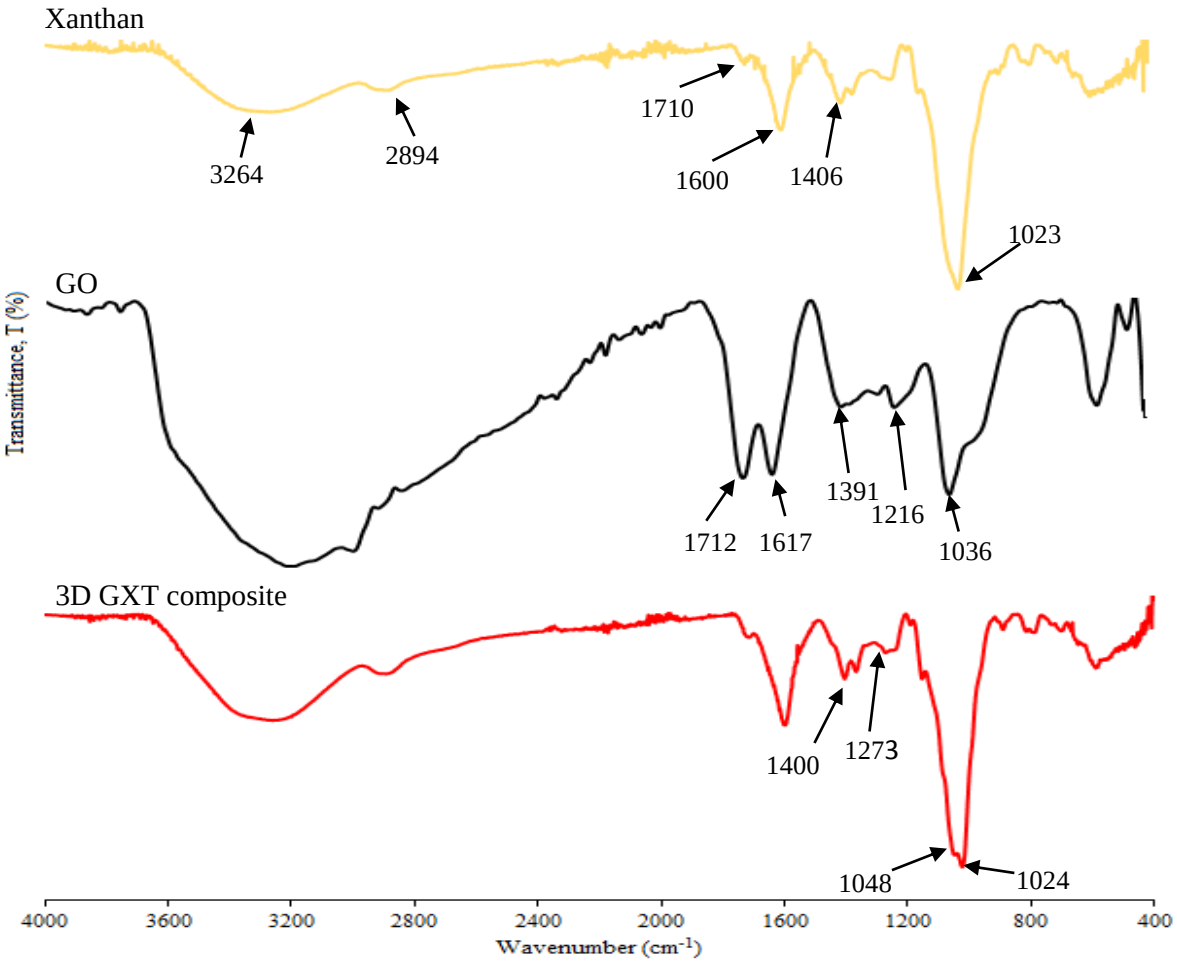


Fig. 6.2 FTIR spectra of xanthan, GO and 3D GXT composite.

The morphological structures of the 3D GXT composite and xanthan were characterised by FESEM (**Fig. 6.3 (a)** and **(b)**). The aggregates of particles with rough surface and impermeable structure were observed in the FESEM images of xanthan. The non-porous structure of xanthan was a disadvantage for adsorption as limited surface area would be available for contact with the adsorbate. Conversely, the 3D GXT composite manifested porous network-like architecture with the biopolymer connecting the pores. This result indicated that the incorporation of GO had modified the morphology of xanthan into a desirable porous structure for adsorption. The development of sponge-like structure could be attributed to the solution viscosity and growth of the ice crystals. During freezing of GO/xanthan/TiO_2 solution, ice crystals were formed and grew with time. Nonetheless, the highly viscous attribute of the mixture had substantially impeded the growth of ice crystals and thus resulted in the morphology of microstructures with interconnected pores. In general, the 3D GXT composite prepared by ice-templating appeared as an open channel sponge with the pores formed by sublimation of ice crystals.

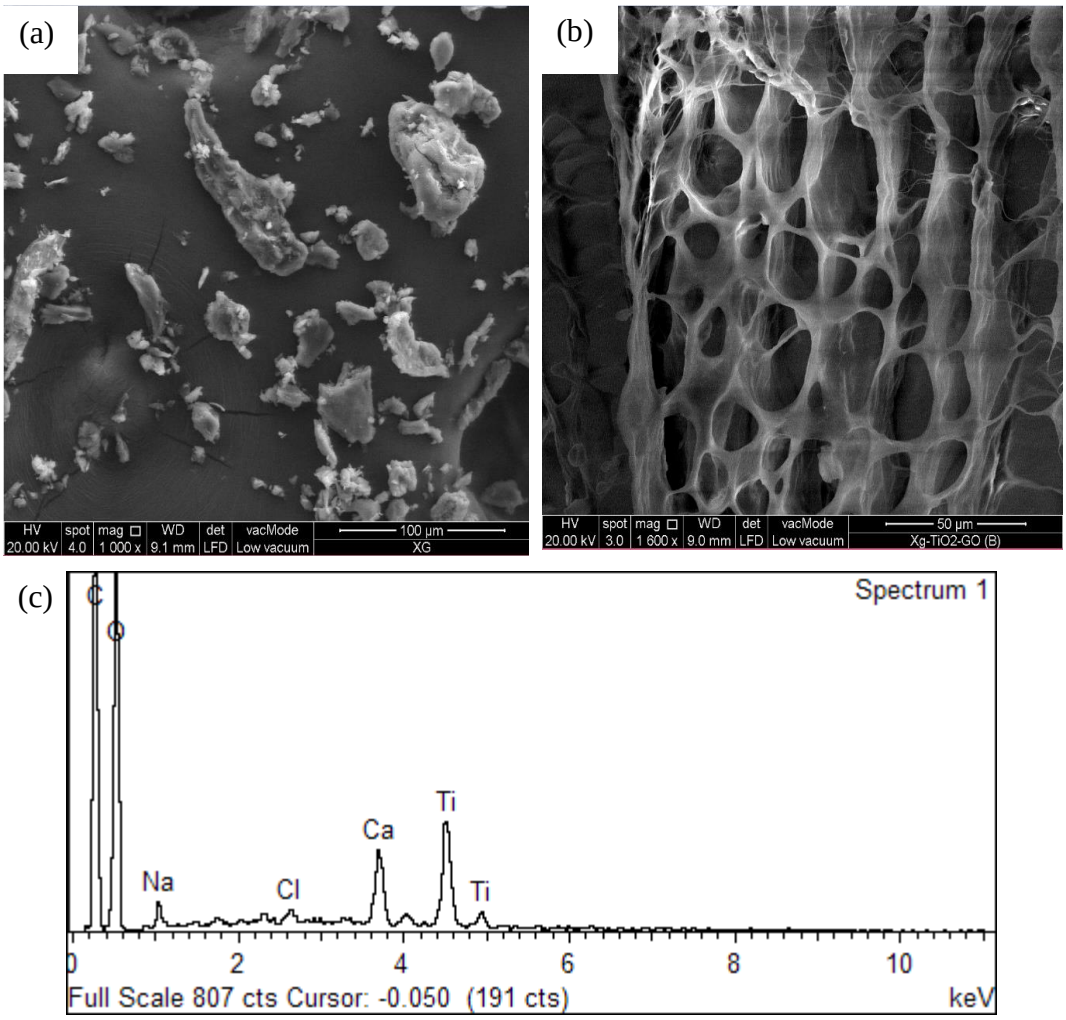


Fig. 6.3 FESEM images of (a) xanthan and (b) 3D GXT composite, and (c) EDX result of 3D GXT composite.

The presence of carbon (C), oxygen (O) and titanium (Ti) in the 3D GXT composite was confirmed by EDX analysis (**Fig.6.3 (c)**). The results implied that the as-synthesised adsorbent had high purity and Ti was successfully integrated with GO and xanthan biomass.

6.2.2 Adsorptive Pb and Cd removal by 3D GXT composite

6.2.2.1 Effects of different adsorption parameters

The effect of 3D GXT mass on the adsorption capacity (q_e) and removal efficiency (R) of Pb and Cd was examined by varying the mass from 5 to 50 mg and the results are delineated in **Fig. 6.4 (a)** and **(b)**, respectively. As shown in **Fig. 6.4**, significant improvement in the removal efficiency of Pb (28.62 to 80.81 %) and Cd (23.15 – 75 %) was observed when the adsorbent mass was increased from 5 to 25 mg. This was attributed to a larger amount of sorption sites available for the heavy metals adsorption at a higher mass of 3D GXT composite. Contrarily, the adsorption capacities were reduced from 149.06 to 45.26 mg/g and 42.52 to 15.32 mg/g for Pb and Cd, respectively, as the adsorbent mass increased from 5 to 50 mg. The negative impact of adsorbent mass on the adsorption capacity could be linked to the diminished total surface area resulting from clumping of sorption sites at higher adsorbent masses. Furthermore, an increased mass at constant liquid volume and initial concentration caused the unsaturation of sorption sites as the availability of heavy metal in the liquid phase was limited, hence leading to the decline in adsorption capacity [268]. Summarily, an adsorbent mass of 25 mg was used in subsequent batch experiments as this mass yielded relatively high removal and adsorption capacity for Pb and Cd.

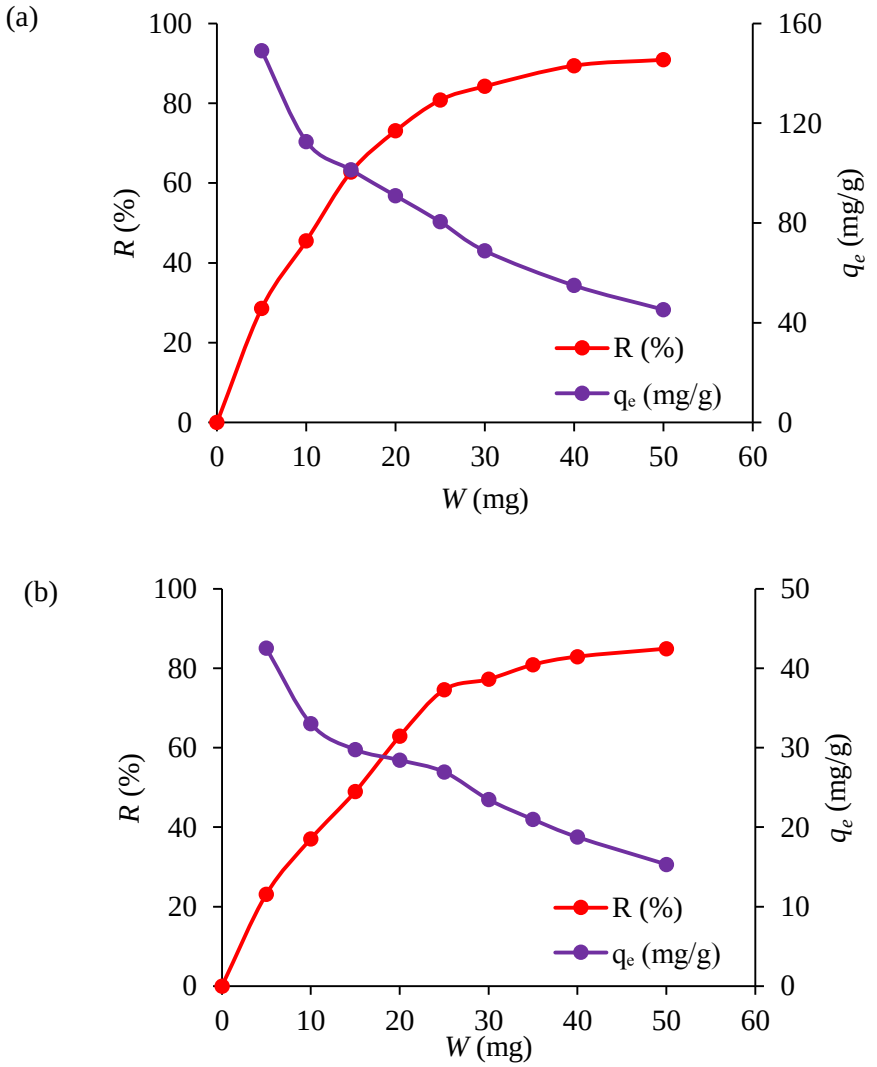


Fig. 6.4 Effect of adsorbent mass on (a) Pb and (b) Cd removal by 3D GXT composite.

Fig. 6.5 (a) and **(b)** portray the influence of shaking speed (50 – 200 rpm) on the adsorption capacity of Pb and Cd, respectively. In general, the adsorption process achieved equilibrium at a shorter time and higher adsorption capacity as the shaking speed was increased. The increase in shaking speed enhanced the mobility of Pb and Cd ions towards the adsorbent and thus promoted the collision between the adsorbate and adsorbent [269]. The shaking speed selected for the following

experiments was 200 rpm as this speed gave the highest Pb and Cd adsorption capacity.

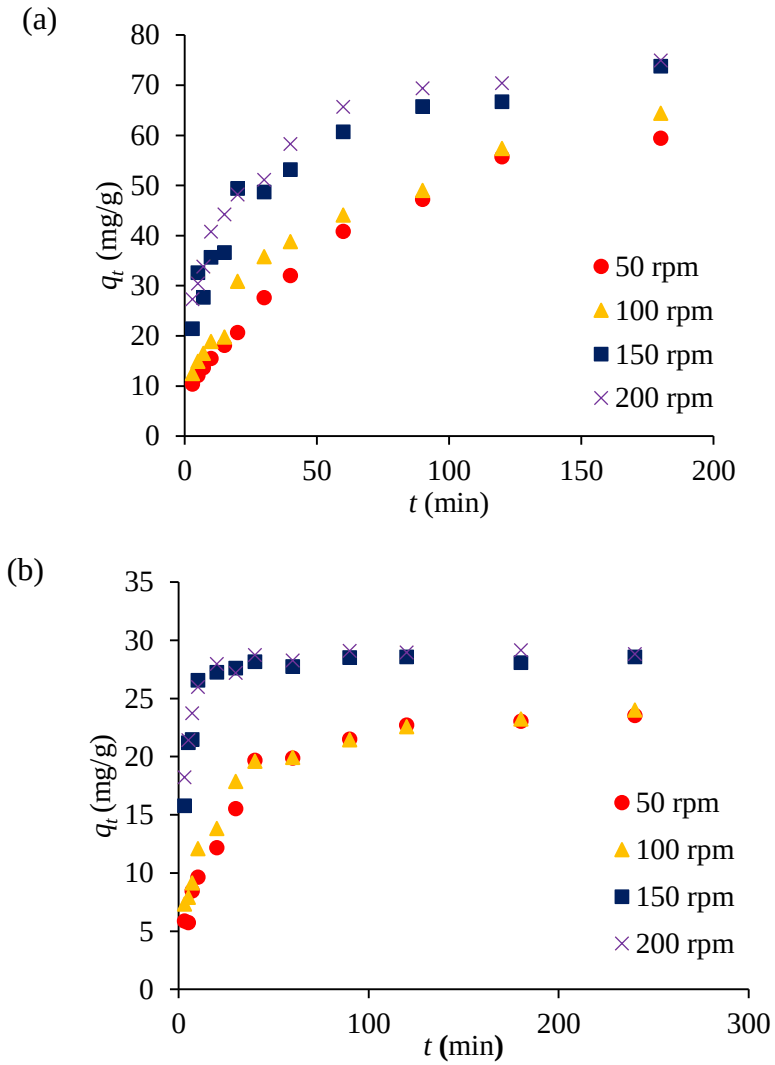


Fig. 6.5 Effect of shaking speed on the (a) Pb and (b) Cd removal by 3D GXT composite.

Solution pH is one of the controlling variables which affect the heavy metal removal process as it determines the speciation of the metal in aquatic system. The effect of initial pH on the Pb and Cd removal by 3D GXT composite is shown in **Fig. 6.6 (a)** and **(b)**, respectively. For the removal of Pb, the pH effect was investigated between pH 2 to 6 as Pb can exist in the forms of Pb^{2+}, $Pb(OH)^{+1}$ and

their combination. The effect of pH study was not performed at pH > 6 as Pb ions can form polymerised complexes as a result of hydrolysis. Hence, the removal of Pb due to precipitation was excluded in this study [270]. The plot for control test carried out without any 3D GXT adsorbent usage, confirmed that Pb would not be removed simply by modifying the solution pH.

For the Cd adsorption, the effect of initial pH was studied within the pH range of 2 – 7 as $Cd(OH)_2$ precipitates can be formed at pH > 8. At pH < 8, Cd mainly exists in the form of Cd^{2+} and only minority exists as $Cd(OH)^+$ [271]. As shown in **Fig. 6.6 (b)**, there was a positive correlation between the Cd removal and initial pH. Under very acidic condition, the surface of 3D GXT composite was covered with abundant hydrogen ions which hindered the metal ions from approaching the sorption sites. Meanwhile, the low pH condition also altered the activity of the surface functional groups of 3D GXT composite. The increased positive charge density on the adsorbent surface at low pH induced an electrostatic repulsion between the sorption sites and metal ions. As the pH was increased, lesser hydrogen ions were available for competing with the metal ions. Furthermore, more surface functional groups in the 3D GXT composite became negatively charged as a result of deprotonation, which in turn attracted more metal ions and thus enhanced the adsorption performance. The natural pH of the solutions was 5.2 which is within the range for high Pb and Cd removal. Thus, further experiments were conducted without any modification of the solution pH.

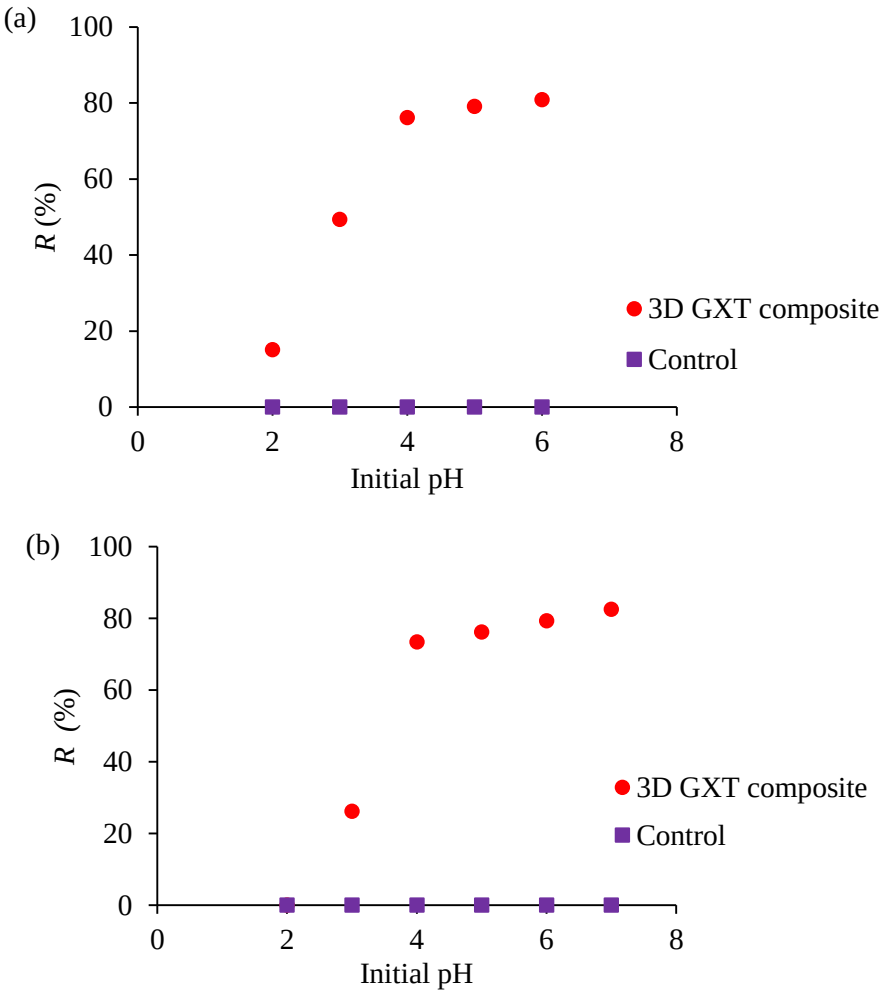


Fig. 6.6 Effect of initial pH on (a) Pb and (b) Cd removal by 3D GXT composite.

6.2.2.2 Adsorption kinetic modelling

Adsorption kinetic study is imperative for determining the efficacy of adsorbent and also adsorption mechanism type [272]. The kinetic behaviour of 3D GXT composite was examined by performing time-dependent studies at concentrations varying from 20 to 60 mg/L (**Fig. 6.7 (a)**) for Pb, and 20 to 100 mg/L for Cd (**Fig. 6.7 (b)**). It is noticeable from the plots that initial concentration exhibited a positive influence on the adsorption capacity. The increase of Pb and Cd uptake by the 3D GXT composite at higher initial concentration was a result of the stronger

concentration driving force. At higher concentration, the sorption sites of the adsorbent would be surrounded by more metal ions, thus minimising the mass transfer resistance and allowing for larger adsorption [273].

Generally, Pb and Cd adsorption onto the 3D GXT composite could be divided into 3 main phases which included a rapid metal ions uptake during the first 20 min, gradual metal ions removal from 20 – 90 min and near equilibrium after 90 min of contact. The plentiful sorption sites at the start of adsorption contributed to the swift metal ions adsorption [274]. The declined adsorption rate after 20 min was attributed to a decrease in the concentration driving force and insufficient vacant sites. It could also be inferred from the kinetic results that the 3D GXT composite was effective in removing Pb and Cd at a relatively short equilibrium time.

The kinetic data were further analysed using the pseudo-first-order (PFO), pseudo-second-order (PSO) and Elovich rate equations to obtain detailed adsorption kinetic information. The kinetic parameters are reported in **Tables 6.1** and **6.2** along with their corresponding SNE values. For the concentration range studied, the PSO model showed the lowest SNE (2.70 – 4.73 for Pb and 2.52 – 5.00 for Cd), followed by the PFO (3.00 – 6.96 for Pb and 3.24 – 6.97 for Cd) and Elovich (3.59 – 6.96 for Pb and 3.57 – 6.98 for Cd) models. In addition, the measured adsorption capacities were congruent with those predicted by the PSO model. The best fit of the PSO model with kinetic data indicated that chemisorption was the governing mechanism for Pb and Cd adsorption onto 3D GXT composite. This might involve electron sharing/exchange between the metal ions and chemical functional groups of the adsorbent [206].

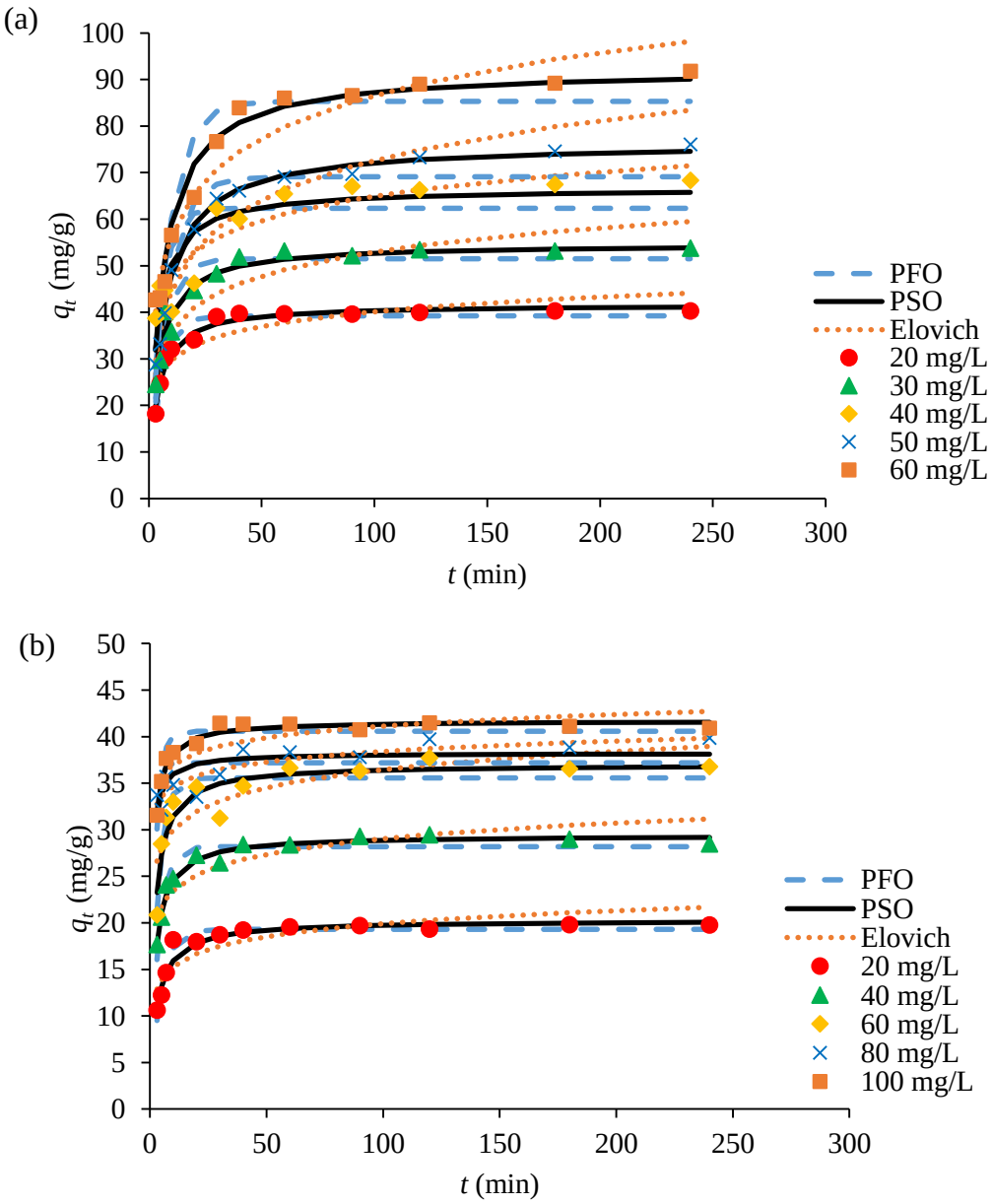


Fig. 6.7 Comparison of experimental kinetic data with the PFO, PSO and Elovich models for (a) Pb and (b) Cd adsorption onto 3D GXT.

Table 6.1 Equilibrium, kinetic and thermodynamic parameters for Pb adsorption onto 3D GXT composite.

Equilibrium	**Temperature (℃)**				
model	**30**	**40**	**50**	**60**	**70**
Langmuir					
$q_{e,\,exp}$	132.09	155.26	162.86	177.09	191.71
q_m (mg/g)	132.18	156.93	150.34	174.67	199.22
K_L	0.271	0.147	0.226	0.168	0.101
R_L	0.012	0.022	0.015	0.020	0.032
SNE	2.41	6.18	2.89	3.12	3.87
Freundlich					
K_F	44.94	48.10	42.24	44.55	43.81
n	4.31	4.13	3.92	3.53	3.26
SNE	6.93	6.19	6.91	6.96	6.97
Kinetic model	**C_o (mg/L)**				
	20	**30**	**40**	**50**	**60**
Pseudo- first -order (PFO)					
$q_{e,\,exp}$	40.27	53.76	68.30	76.07	91.77
$q_{e,\,calc}$	39.20	51.47	62.36	69.12	85.34
k_1	0.198	0.172	0.201	0.124	0.122
SNE	3.00	6.00	6.91	6.70	6.96
Pseudo- second –order (PSO)					
$q_{e,\,calc}$	41.71	54.73	66.66	76.40	92.23
k_2	0.007	4.75E-03	4.60E-03	2.20E-03	1.91E-03
SNE	2.70	3.61	4.73	2.93	4.06
Elovich					
α	325.86	91.24	440.33	45.84	92.66
β	0.221	0.134	0.134	0.082	0.076
SNE	6.95	6.96	3.59	6.50	4.18

Thermodynamics	**Δ*G* (kJ/mol)**					**Δ*H***	**Δ*S***
C_o (mg/L)	30 ℃	40 ℃	50 ℃	60 ℃	70 ℃	**(kJ/mol)**	**(kJ/mol K)**
30	-25.29	-26.36	-27.73	-28.07	-28.91	1.70	0.090
90	-20.67	-21.65	-23.18	-23.78	-24.10	6.38	0.090
100	-20.14	-21.13	-22.40	-23.14	-24.21	10.62	0.102
150	-18.38	-19.57	-19.73	-21.46	-22.46	12.14	0.100
200	-17.48	-18.72	-18.94	-20.14	-21.22	9.49	0.089
250	-16.62	-17.67	-17.96	-19.60	-20.58	13.34	0.098
300	-16.04	-17.06	-17.78	-18.66	-19.55	10.02	0.086

Table 6.2 Equilibrium, kinetic and thermodynamic parameters for Cd adsorption onto 3D GXT composite.

Equilibrium	**Temperature (℃)**				
model	**30**	**40**	**50**	**60**	**70**
Langmuir					
q_m (mg/g)	62.20	53.18	53.66	49.81	48.04
K_L	0.070	0.119	0.084	0.129	0.131
R_L	0.045	0.027	0.038	0.025	0.025
SNE	6.97	6.91	6.96	6.95	3.71
Freundlich					
K_F	10.42	11.45	10.63	12.24	12.09
n	2.884	3.263	3.173	3.640	3.688
SNE	4.60	2.32	3.91	5.64	6.96
Kinetic	***C*$_o$ (mg/L)**				
model	**20**	**40**	**60**	**80**	**100**
Pseudo- first -order (PFO)					
$q_{e,\,exp}$	19.75	28.47	36.76	39.85	40.92
$q_{e,\,calc}$	19.31	28.18	35.58	37.18	40.59
k_1	0.226	0.281	0.301	0.646	0.450
SNE	3.24	4.46	4.09	6.97	4.60
Pseudo- second –order (PSO)					
$q_{e,\,calc}$	20.29	29.43	37.05	38.24	41.71
k_2	0.018	1.73E-02	1.51E-02	4.16E-02	2.60E-02
SNE	2.95	2.65	4.28	5.00	2.52
Elovich					
α	408.70	4004.78	12305.14	3.24E08	1.53E08
β	0.498	0.414	0.356	0.617	0.556
SNE	6.95	6.97	6.97	3.57	6.98

Thermodynamics	**Δ*G* (kJ/mol)**					**Δ*H***	**Δ*S* (kJ/mol K)**
***C*$_o$ (mg/L)**	**30 ℃**	**40 ℃**	**50 ℃**	**60 ℃**	**70 ℃**	**(kJ/mol)**	
80	-17.29	-17.17	-17.87	-18.03	-19.31	-2.10	0.049
100	-16.71	-16.70	-17.26	-17.92	-18.47	-2.08	0.047
150	-15.43	-15.82	-16.25	-16.32	-16.50	-7.53	0.026
200	-15.02	-15.19	-15.67	-16.08	-16.51	-3.19	0.039
250	-14.38	-14.62	-14.89	-15.37	-15.63	-4.49	0.032
300	-14.28	-14.50	-14.71	-14.88	-15.14	-7.93	0.021

The mass transfer of the adsorption systems could be determined using the intraparticle diffusion model proposed by Weber and Morris [169]. The typical processes involved in the transport of metal ions from the bulk solution to the 3D GXT composite include diffusion across the boundary layer encircling the adsorbent, diffusion within the pores of adsorbent and surface adsorption. Surface adsorption was considered as an expeditious process since the adsorption studies were conducted under vigorous agitation. The intraparticle diffusion plot which represents the adsorption capacity as a function of square root of time is delineated in **Fig. 6.8 (a)** and **(b)** for Pb and Cd, respectively. The plots manifest multiple linear lines which did not pass through the origin, suggesting that the Pb and Cd adsorption onto the 3D GXT composite involved more than one rate-limiting step such as boundary layer and intraparticle diffusion.

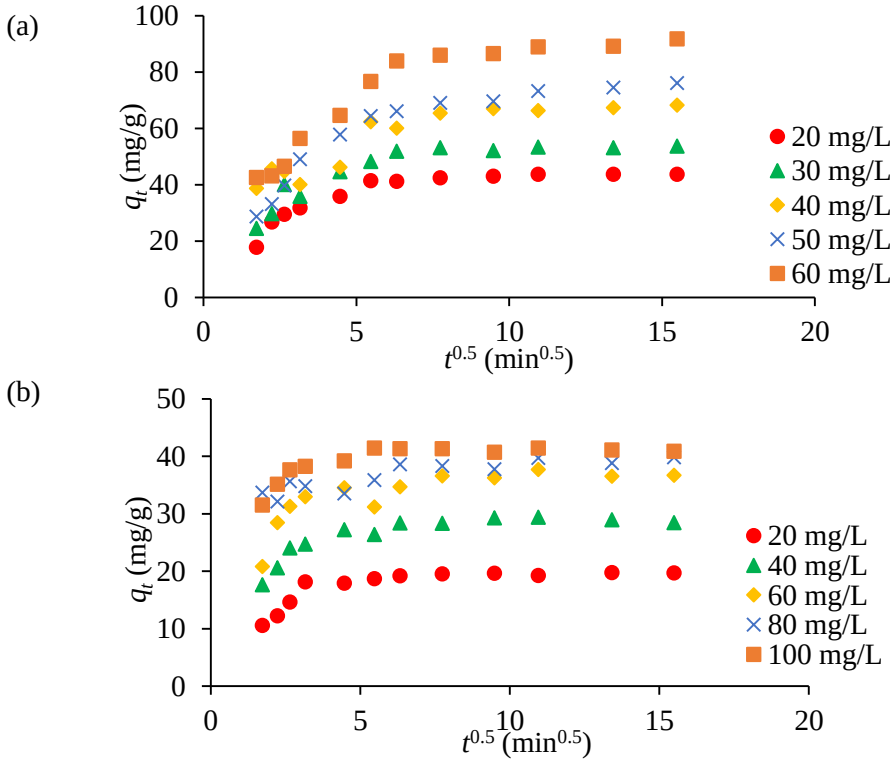


Fig. 6.8 Intraparticle diffusion plots for (a) Pb and (b) Cd removal by 3D GXT composite.

6.2.2.3 Adsorption isotherm modelling and thermodynamics

The isotherm modelling of Pb adsorption onto 3D GXT composite is depicted in **Fig. 6.9** for temperatures varying from 30 to 70 ^{o}C. Notably, the adsorption capacity intensified at larger concentrations and temperatures. The higher adsorption capacities obtained at higher temperatures indicated that the adsorption was endothermic. The high Pb removal suggested that more active sites were available for adsorption at higher temperatures. Moreover, the solution became less viscous at high temperature and thus facilitated the transfer of Pb to the adsorbent surface [274].

Fig. 6.10 demonstrates the isotherm modelling of Cd uptake by 3D GXT composite at temperatures varying from 30 to 70 ^{o}C. Similarly, the Cd adsorption capacity increased with the initial concentration. The increase in initial concentration caused higher driving force for mass transfer which eventually resulted in the saturation of sorption sites [275]. Furthermore, **Fig. 6.10** also unveils that the adsorption process of Cd onto the 3D graphene composite was exothermic as the adsorption capacity was reduced at higher temperature.

The equilibrium between the metal ions immobilised on the adsorbent and those remained in the solution was studied by employing two isotherm models which include the Langmuir and Freundlich models. The Langmuir model describes the adsorption process as a monolayer of adsorbates reside on the adsorbent surface with uniform sorption sites of identical energy and no interactions between the adsorbates [164]. In the Freundlich model, multilayer and reversible adsorption occurs on a heterogeneous surface with interactions between the adsorbates.

Moreover, it assumes that the adsorption capacity increases infinitely with the metal ion concentration [165].

Table 6.1 contains the predicted isotherm parameters and their corresponding SNE values for Pb removal by 3D GXT composite. Notably, the Langmuir model defined the adsorption system precisely with the SNE values between 2.41 and 6.18, suggesting a single layer sorption of Pb on the homogeneous surface with identical sorption sites [164]. Additionally, the maximum adsorption capacities were close to those estimated by the Langmuir model (132.18-199.22 mg/g), proving the adequacy of this model. The equilibrium separation factor, R_L, a dimensionless constant and crucial characteristic of the Langmuir model, was employed to determine the affinity between Pb and 3D GXT composite. Accordingly, the adsorption process is irreversible, favourable, linear and unfavourable when R_L = 0, $0 < R_L < 1$, $R_L = 1$ and $R_L > 1$, respectively. Hence, the adsorption of Pb onto 3D GXT composite was favourable as indicated by the R_L values which lie within the range of 0.012 – 0.032 (**Table 6.1**).

Table 6.2 presents the predicted isotherm parameters for Cd removal by the 3D GXT composite. Accordingly, the measured equilibrium data was best described by the Freundlich model. Hence, there was a multilayer attachment of Cd ions on the heterogeneous surface of the 3D graphene composite. The n_F values of the Freunlich model (2.884 – 3.688) also suggested that Cd adsorption onto 3D GXT composite was a favourable process. Additionally, the separation factor, R_L, was analysed to determine the favourability of the process. Since the R_L lies between 0 and 1 (**Table 6.2**), the 3D GXT composite is a suitable material for removing Cd and the adsorption process is favourable.

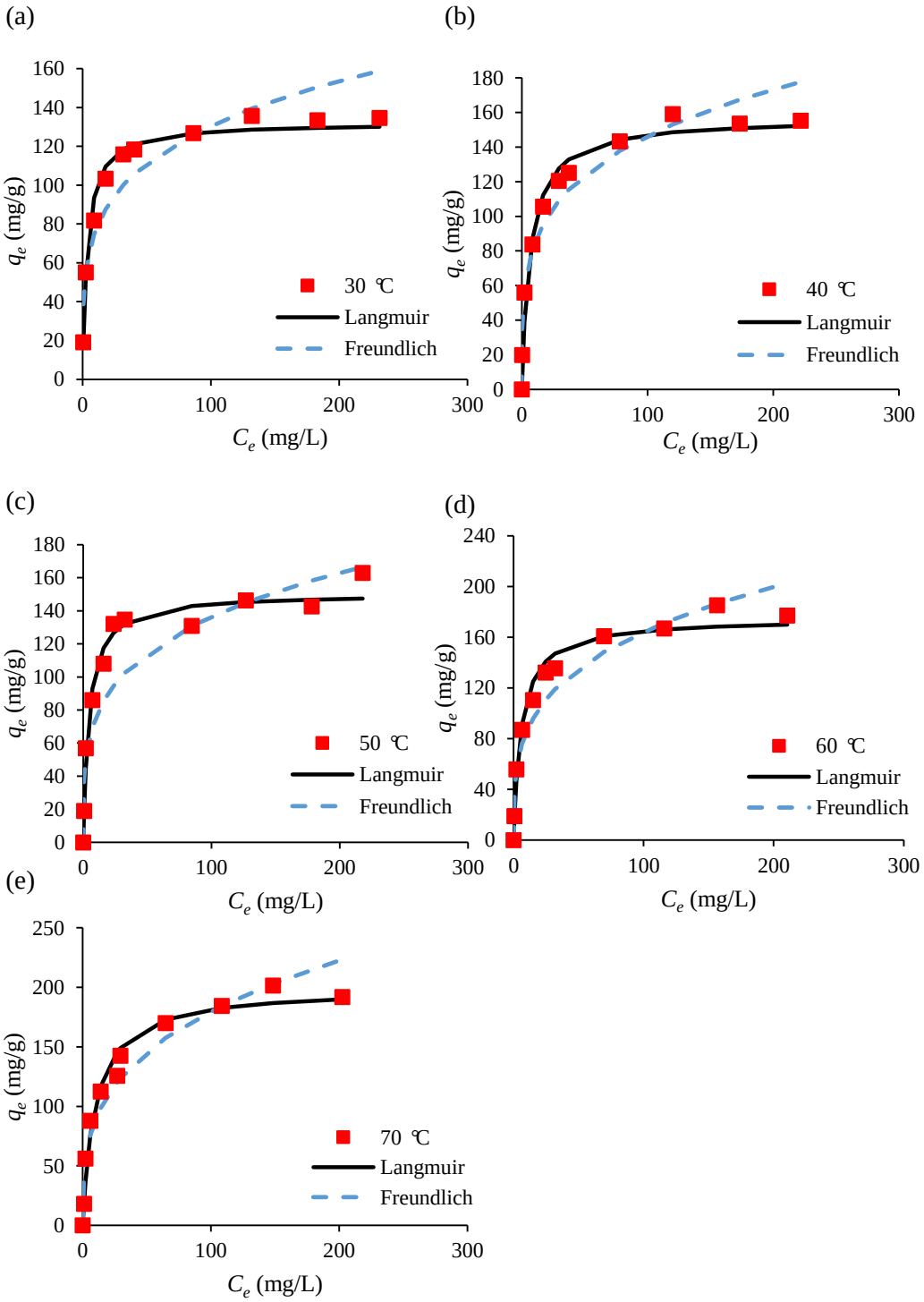


Fig. 6.9 Comparison of experimental equilibrium data with the Langmuir and Freundlich models at temperatures of (a) 30 ºC, (b) 40 ºC, (c) 50 ºC, (d) 60 ºC and (e) 70 ºC for Pb uptake by 3D GXT composite.

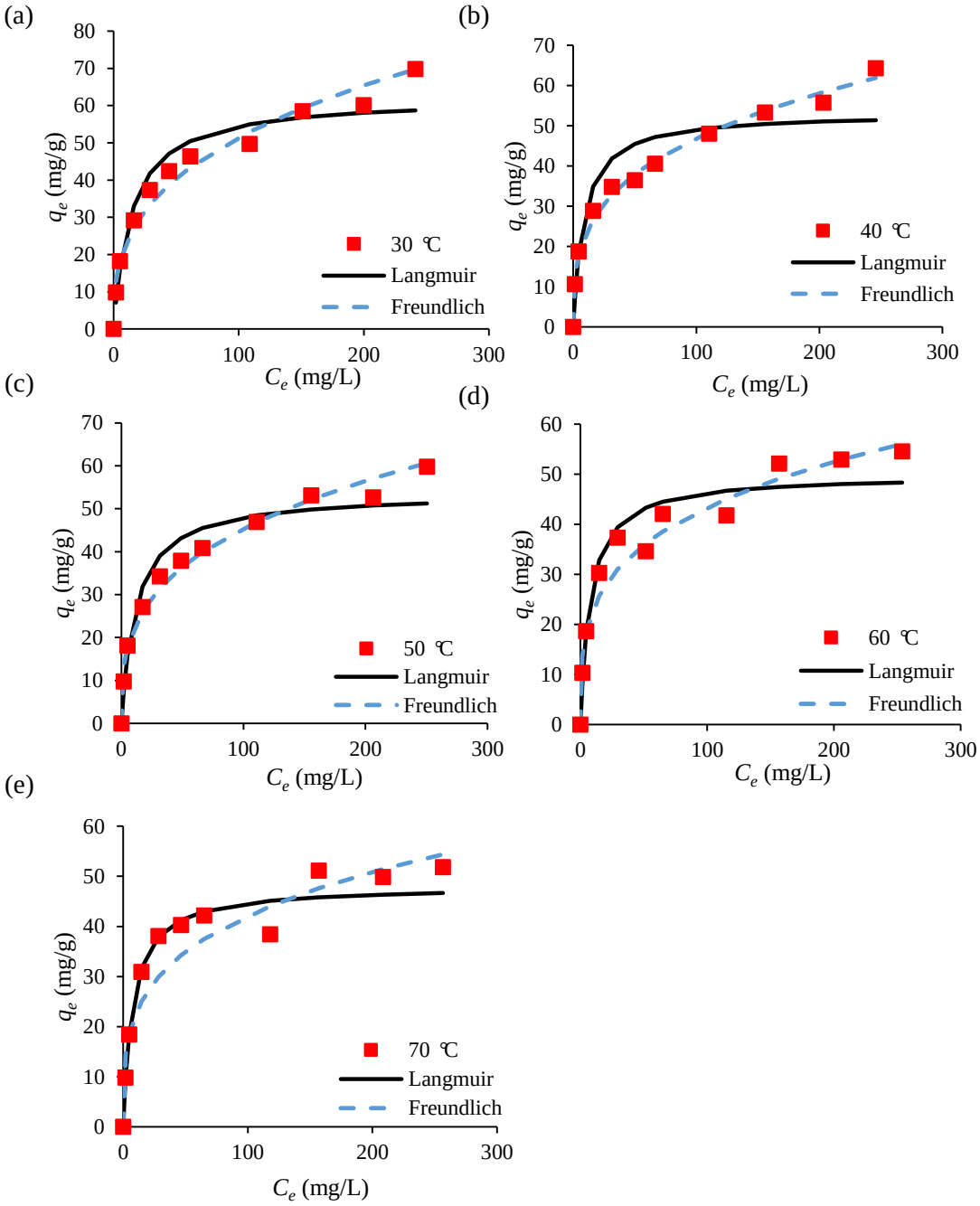


Fig. 6.10 Comparison of experimental equilibrium data with the Langmuir and Freundlich models at temperatures of (a) 30 ^{o}C, (b) 40 ^{o}C, (c) 50 ^{o}C, (d) 60 ^{o}C and (e) 70 ^{o}C for Cd uptake by 3D GXT composite.

The thermodynamic parameters of ΔG, ΔH and ΔS were adopted to evaluate the thermodynamic behaviour of Pb and Cd adsorption by the 3D GXT composite. These parameters at certain concentrations and temperatures are listed in **Tables 6.1** and **6.2**. As demonstrated in **Tables 6.1** and **6.2**, the adsorption of Pb and Cd onto the 3D GXT composite was spontaneous and feasible processes as advocated by negative ΔG. For both Pb and Cd removal, it is noteworthy that the ΔG values increased with the initial concentration, signifying that the adsorption process was more efficient at lower initial concentration. For the Pb removal, the smaller ΔG values observed at higher temperatures indicated that at higher temperatures, the adsorption process would be more spontaneous. Furthermore, the positive ΔH values ranging from 1.70 to 13.34 kJ/mol revealed that the Pb removal was endothermic. Thus, the adsorption capacities were enhanced at higher temperatures. The negative values of ΔH supported that the Cd adsorption process was exothermic in nature. Moreover, the positive values of ΔS reflected an increased randomness at the interface between the metal ions and 3D GXT composite.

6.2.3 RSM modelling and optimisation

6.2.3.1 Optimisation of Pb adsorption onto 3D GXT composite

The adsorption of Pb onto 3D GXT composite was investigated based on the RSM-CCD experimental design matrix shown in **Table 6.3**. In the first step of the study, the interactive effects of 4 operating variables were examined, followed by optimisation of the variables to attain the highest adsorption capacity of Pb. A total run of 30 randomised experiments were carried out and the results were used to generate the empirical relationship between the input variables and process

response. The quadratic function describing the correlation between the 4 variables and the response is expressed by **Eq. (6.1)** in terms of coded factors.

$$q = 151.24 - 6.56A + 11.48B + 8.83C + 9.52D - 3.21AB - 3.00AC - 2.62AD - 1.49BC + 2.87BD + 4.49CD - 3.59A^2 - 2.92B^2 - 2.24C^2 - 3.36D^2 \quad \textbf{(6.1)}$$

Eq. (6.1) was used to predict the adsorption capacity for the given 4 factors in **Table 6.3**. The predicted adsorption capacity (q_{pred}) are similar to the measured data (q_{exp}) with the absolute residue lied in the range of 0.06 to 4.59 mg/g only, thus, the equation is adequate in predicting the response. The quadratic equation was further analysed for the model adequacy using the diagnostic plots (**Fig. 6.11**) and ANOVA results (**Table 6.4**).

Table 6.3 RSM-CCD experimental design matrix with measured and predicted responses, and residue for Pb adsorption system.

Run	A (mg)	B (mg/L)	C (rpm)	D (°C)	q_{exp} (mg/g)	q_{pred} (mg/g)	Residue
1	15	150	125	40	113.73	112.90	-0.83
2	25	150	125	40	114.82	117.45	2.63
3	15	250	125	40	141.05	139.53	-1.51
4	25	250	125	40	130.52	131.23	0.71
5	15	150	175	40	129.16	130.57	1.41
6	25	150	175	40	120.42	123.13	2.71
7	15	250	175	40	150.83	151.22	0.40
8	25	250	175	40	132.61	130.93	-1.68
9	15	150	125	60	118.10	122.47	4.37
10	25	150	125	60	118.45	116.54	-1.91
11	15	250	125	60	164.80	160.58	-4.22
12	25	250	125	60	140.53	141.80	1.27
13	15	150	175	60	160.31	158.09	-2.22
14	25	150	175	60	135.97	140.17	4.20
15	15	250	175	60	190.17	190.23	0.06
16	25	250	175	60	160.14	159.46	-0.68
17	10	200	150	50	148.15	150.01	1.86
18	30	200	150	50	126.82	123.79	-3.04
19	20	100	150	50	121.19	116.60	-4.59
20	20	300	150	50	159.09	162.51	3.42
21	20	200	100	50	124.30	124.64	0.34
22	20	200	200	50	161.47	159.96	-1.51
23	20	200	150	30	120.10	118.77	-1.32
24	20	200	150	70	156.72	156.87	0.15
25	20	200	150	50	153.22	151.24	-1.98
26	20	200	150	50	153.40	151.24	-2.16
27	20	200	150	50	149.91	151.24	1.33
28	20	200	150	50	148.79	151.24	2.45
29	20	200	150	50	149.95	151.24	1.29
30	20	200	150	50	148.22	151.24	3.02

The normal % probability against internally studentised residual plot is portrayed in **Fig. 6.11 (a)** which measures the ability of the model in satisfying the

assumptions of ANOVA and determines whether the data is normally distributed. As observed, the experimental data are normally distributed as all the points are reasonably aligned along the straight line. Additionally, transformation of response is not required [276]. **Fig. 6.11 (b)** shows the residuals in 30 batch runs which help to identify the outlier. In general, most of the residuals should lie within the range of ±3 while any point sits beyond this range is considered an outlier. All the residuals seem to be randomly scattered around the zero centre point and fall within the limits, proving that the model is fairly good with the absence of outlier. There is only a slight deviation from the diagonal line in the plot of predicted q against measured q (**Fig. 6.11 (c)**), illustrating that the model is appropriate for prediction. The normal distribution of the data was verified again using the Box-Cox plot as shown in **Fig. 6.11 (d)**. For the data which are not normally distributed, the plot could also be used to determine the order for power transformation of the model [277]. The current lambda, λ, value for the Pb adsorption onto 3D GXT composite is 1, which lies between the lambda values at low (-2.14) and high (2.07) confidence limits. This implies a normal distribution of the data and no power transformation is needed for **Eq. (6.1)**.

In addition to diagnostic plots, the following ANOVA results (**Table 6.4**) justified the suitability of the developed model in navigating the design space and describing the adsorption process. The statistical significance of the model was examined based on the F-value and p-value. The p-values < 0.05 and > 0.1 indicate the statistical significance and insignificance, respectively. Hence, the quadratic model was significant as advocated by its high F-value (53.62), $p < 0.0001$ and insignificant lack-of-fit (F-value = 1.14 and p-value = 0.4681). The low coefficient

of variation, C.V.% (2.45 < 10), suggests the reliability of the model. The regression model was further analysed by multiple correlation coefficients (R^2), including R^2, adjusted R^2 and predicted R^2 to describe how well it fits the data. The R^2 of 0.9804 reveals that only 1.2% of the total variation could not be explained by this model. The adjusted R^2 (0.9621) was close to the R^2, showing that no model reduction is required as the variables included in the equation are statistically significant. The difference between adjusted R^2 and predicted R^2 (0.9129) is less than 0.2, thus the model is suitable for predicting the *q* for the investigated parameters. Summarily, the developed model adequately represents the Pb removal by 3D GXT composite.

The significant contribution of each variable and their interactive and quadratic terms were analysed by ANOVA and the outcomes are delineated in **Table 6.4**. Likewise, the term becomes more significant with smaller *p*-value. Consequently, all the terms manifested substantial influences on the response as affirmed by their *p*-values, except the BC interactive parameter. Furthermore, the type (positive or negative) and extent of influence could be inferred from the sign and magnitude of the regression coefficient, respectively. For instance, factor B exhibited greater effect on the response as compared to factor A. Nonetheless, factor B enhances the adsorption capacity while factor A deteriorates the response

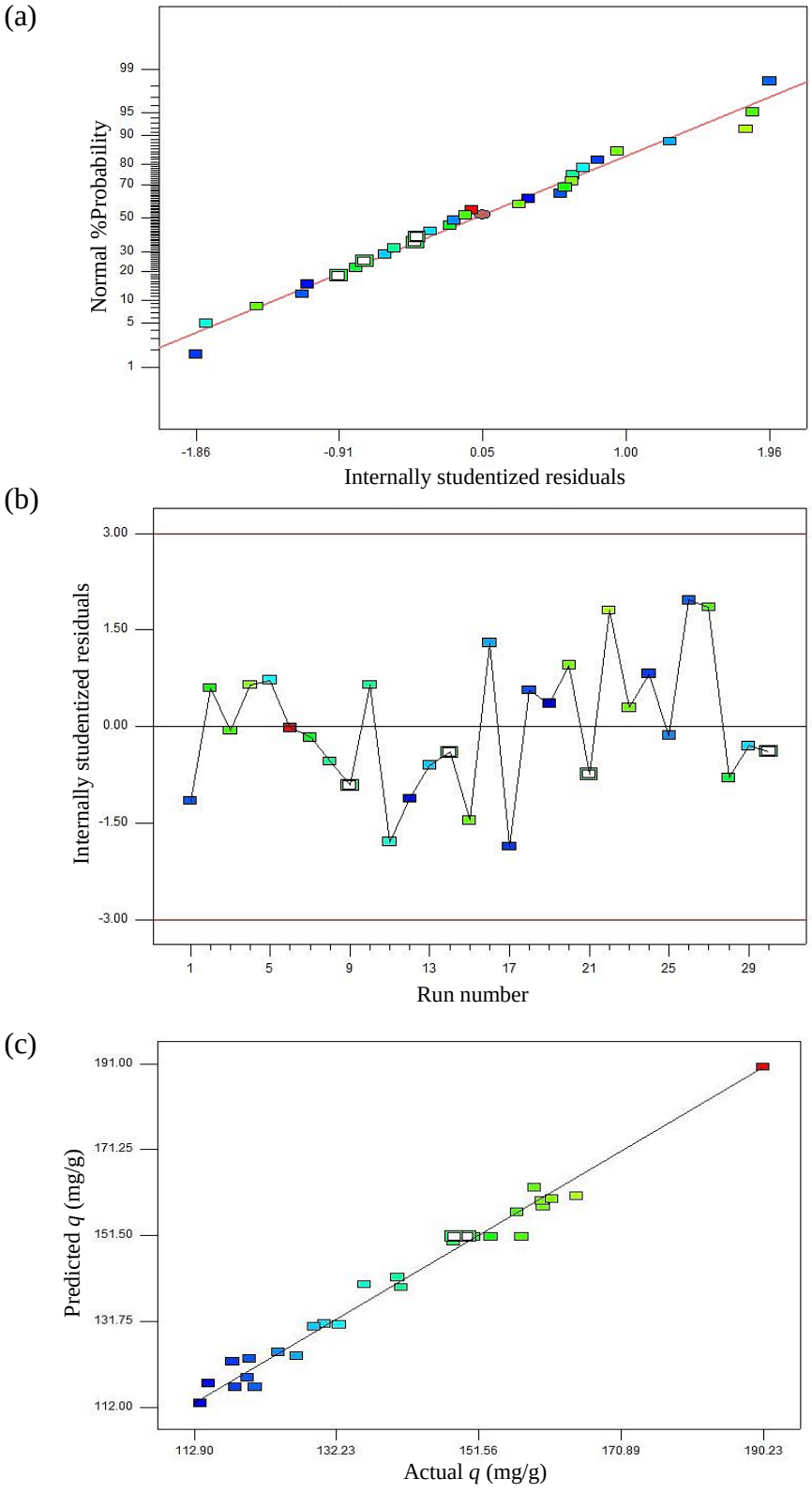


Fig. 6.11 Diagnostic plots: (a) Internally studentised residual plot, (b) internally studentised residuals vs run number plot, (c) predicted vs actual *q* plot and (d) Box-Cox plot.

(d)

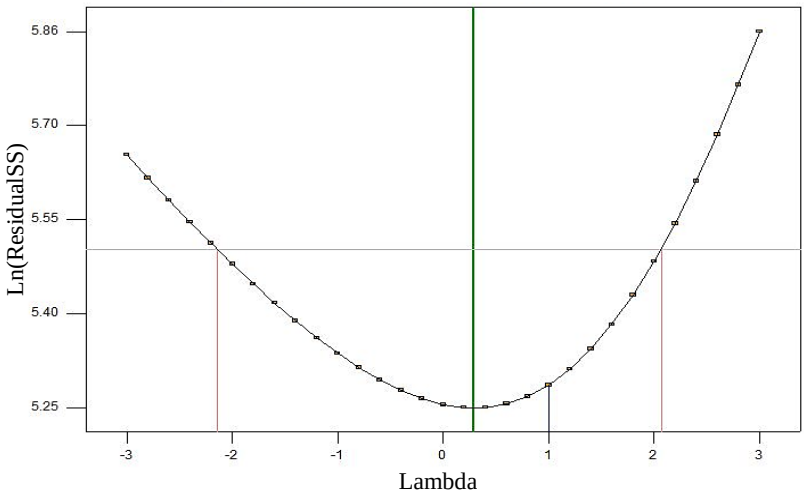


Fig. 6.11 Diagnostic plots: (a) Internally studentised residual plot, (b) internally studentised residuals vs run number plot, (c) predicted vs actual *q* plot and (d) Box-Cox plot.

Table 6.4 ANOVA results on the optimisation of Pb adsorption onto 3D GXT composite.

Source	Sum of Squares	DF	Mean Square	*F* Value	*p*-value Prob > F
Model	9887.49	14	706.25	53.62	< 0.0001
A	1031.43	1	1031.43	78.31	< 0.0001
B	3162.33	1	3162.33	240.09	< 0.0001
C	1871.77	1	1871.77	142.11	< 0.0001
D	2176.81	1	2176.81	165.27	< 0.0001
AB	165.17	1	165.17	12.54	0.0030
AC	143.82	1	143.82	10.92	0.0048
AD	109.67	1	109.67	8.33	0.0113
BC	35.76	1	35.76	2.71	0.1202
BD	131.85	1	131.85	10.01	0.0064
CD	322.34	1	322.34	24.47	0.0002
A^2	352.66	1	352.66	26.77	0.0001
B^2	234.25	1	234.25	17.79	0.0007
C^2	137.13	1	137.13	10.41	0.0056
D^2	308.84	1	308.84	23.45	0.0002
Residual	197.57	15	13.17		
Lack of Fit	137.52	10	13.75	1.14	0.4681
Pure Error	60.05	5	12.01		
Others	R^2	0.9804		Std. dev.	3.63
	Adjusted R^2	0.9621		Mean	141.56
	Predicted R^2	0.9129		C.V.%	2.56
	Adequate percision	30.132		PRESS	878.59

The variation in response following the change in variables is depicted in the 3D response surface plots (**Fig. 6.12**) whereby the presence of curvatures indicates the interaction between the variables. For each plot, two variables were altered simultaneously while the other factors were set at their centre level. The response surface plots relating the influences of adsorbent weight (A) with initial Pb concentration (B), shaking speed (C) and temperature (D) are delineated in **Fig.**

6.12 (a), **(b)** and **(c)**, respectively. Generally, the Pb adsorption capacity decreases with adsorbent mass but increases with concentration, shaking speed and temperature. The negative impact of adsorbent mass on the response could be assigned to the diminished total surface area resulting from clumping of sorption sites at high adsorbent masses. Furthermore, the increase in dosage at constant solution volume and concentration causes unsaturation of sorption sites as the availability of Pb ions in the solution is limited, and hence led to the decrease in adsorption capacity [268]. Therefore, the highest q was obtained at A < 20 mg, B > 200 mg/L, C > 150 rpm and D > 50 ^{o}C.

Fig. 6.12 (a), **(d)** and **(e)** depict the Pb adsorption capacity as a function of B and A, B and C, and B and D, respectively. It is noticeable from the plots that the initial Pb concentration exhibited a significantly positive influence on the response which is further affirmed by **Eq. (6.1)**. The increase in Pb uptake by 3D GXT composite at higher metal concentrations is a result of the stronger concentration driving force. At higher concentration, the sorption sites of the adsorbent would be surrounded by more Pb ions, minimising the mass transfer resistance to allow sufficient adsorption [273]. Thus, high q could be attained by maintaining the parameters at B > 200 mg/L, A < 20 mg, C > 150 rpm and D > 50 ^{o}C.

The effects on the interaction of agitating speed with other factors are presented in **Fig. 6.12 (b)**, **(d)** and **(f)**. In general, the Pb adsorption capacity increases with intensified shaking speed and the greatest q occurred at C > 150 rpm, A < 20 mg, B > 200 mg/L and D > 50 ^{o}C. The increase in shaking speed enhanced the mobility of the Pb ions towards the adsorbent thus promoting collision between the adsorbate and adsorbent [269].

The Pb adsorption by GXT composite was endothermic as a higher *q* was observed at higher temperature, D > 50 ^{o}C (**Fig. 6.12 (c)**, **(e)**, and **(f)**). The high Pb removal suggested that more active sites were available for adsorption at higher temperature. The solution became less viscous at high temperature and thus facilitated the transfer of adsorbate to the adsorbent surface [274].

The optimisation of Pb adsorption onto 3D GXT composite is to ensure a high adsorption capacity at low adsorbent mass, high initial Pb concentration and moderate agitating speed and temperature. The maximum *q* corresponding to the optimum experimental conditions (A = 14.95 mg, B = 300 mg/L, C = 187 rpm and D = 60 ^{o}C) was found to be 201.19 mg/g at the highest desirability of 1. The validity of the model was examined by performing the experiments at these predetermined conditions for three times. The experimental *q* was determined to be 204.76 mg/g which showed a slight discrepancy (1.78 %) with the predicted value. As a result, the established model could be employed effectively for the prediction and optimisation of Pb adsorption onto the 3D GXT composite.

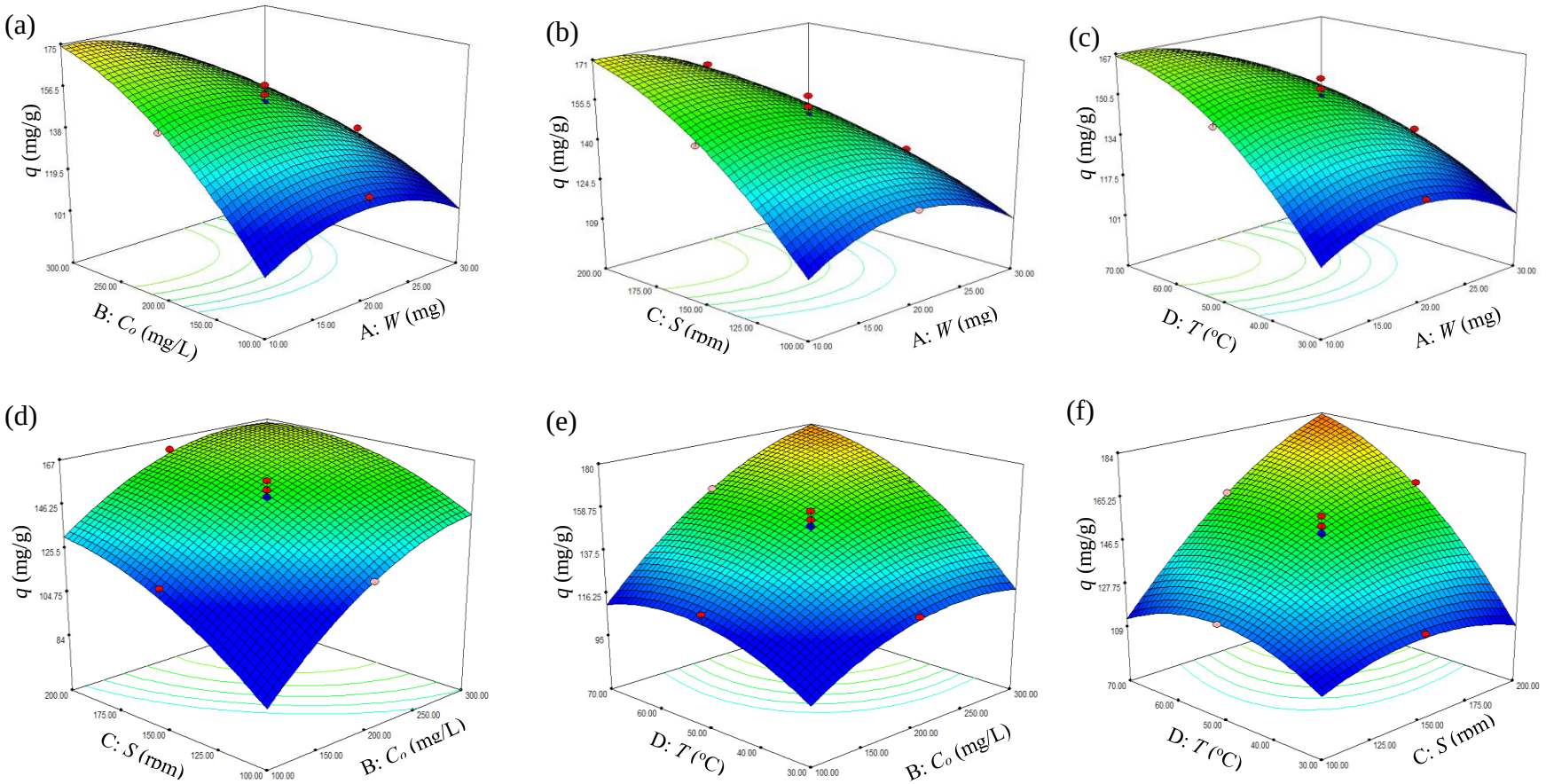


Fig. 6.12 3D surface response plots for Pb adsorption onto 3D GXT: Effects of (a) adsorbent mass and concentration, (b) adsorbent mass and shaking speed, (c) adsorbent mass and temperature, (d) concentration and shaking speed, (e) concentration and temperature, and (f) shaking speed and temperature.

6.2.3.2 Optimisation of Cd adsorption by 3D GXT composite

The adsorption of Cd onto 3D GXT composite was modelled by CCD and the experimental results are delineated in **Table 6.5**. The evaluation of these results yielded the mathematical relation between the operating variables (adsorbent mass (A), initial Cd concentration (B), pH (C) and shaking speed (D) and the response (Cd adsorption capacity, *q*). Specifically, the quadratic model equation representing the Cd adsorption onto 3D GXT composite for coded values is demonstrated by **Eq. (6.2)**.

$$q = 38.70 - 1.89A + 1.24B + 7.79C + 2.56D - 0.40AB - 0.29AC + 0.076AD + 0.66BC + 0.21BD + 0.29CD + 0.83A^2 + 0.69B^2 - 0.077C^2 + 0.30D^2 \quad \textbf{(6.2)}$$

The validity of the established model was analysed based on the ANOVA results (**Table 6.6**) and diagnostic plots (**Fig. 6.13**). As for the ANOVA, Fisher test (*F*-test) indicates the statistical significance of all terms in the developed equation at a 95 % confidence interval while a *p*-value < 0.05 signifies the statistical significance of a variable at a 95 % confidence level [272]. According to **Table 6.6**, this quadratic model was statistically significant (*F*-value = 57.11 and $p < 0.0001$) with a lack-of-fit *F*-value of 1.91 only. The high value of correlation coefficient (R^2 = 0.9816) implied that 98.16% of the variation in the response could be explained by the model. The adjusted R^2 (0.9644) approximating the R^2, indicates that all the terms in the second order polynomial equation are significant and hence model reduction was not considered. The predicted R^2 is in good agreement with the

adjusted R^2, with the discrepancy < 0.2, suggesting that the model is adequate for the predictive application. Notably, the predicted Cd adsorption capacities were found to be very close to the experimental results with residual errors varying from 0.04 to 12.19 % (**Table 6.5**), further validating the model for predicting the relationship between the independent variables and response. A coefficient of variation (C.V. %) of 3.72 (< 10) and adequate precision of 31.168 (> 4) signify the reproducibility of the model and ability of the model to navigate the design space, respectively. The developed model was further verified by the relatively small standard deviation (1.49) and PRESS (162.43).

Table 6.5 CCD design matrix for Cd adsorption onto 3D GXT composite with measured and predicted *q*, and residual error.

Run	A	B	C	D	q_{exp} (mg/g)	q_{pred} (mg/g)	Residual error (%)
1	20	150	4	125	31.93	31.29	2.05
2	30	150	4	125	29.71	28.74	3.40
3	20	250	4	125	33.54	32.83	2.17
4	30	250	4	125	29.65	28.68	3.38
5	20	150	6	125	45.41	45.55	0.31
6	30	150	6	125	42.36	41.84	1.26
7	20	250	6	125	49.35	49.73	0.76
8	30	250	6	125	44.34	44.42	0.17
9	20	150	4	175	36.28	35.26	2.90
10	30	150	4	175	34.62	33.01	4.88
11	20	250	4	175	38.36	37.64	1.92
12	30	250	4	175	34.88	33.79	3.21
13	20	150	6	175	50.93	50.68	0.50
14	30	150	6	175	47.53	47.27	0.54
15	20	250	6	175	55.67	55.70	0.04
16	30	250	6	175	51.27	50.69	1.14
17	15	200	5	150	45.50	45.80	0.66
18	35	200	5	150	36.36	38.24	4.91
19	25	100	5	150	37.50	38.98	3.80
20	25	300	5	150	43.25	43.94	1.57
21	25	200	3	150	20.03	22.81	12.19
22	25	200	7	150	54.58	53.97	1.13
23	25	200	5	100	34.25	34.78	1.52
24	25	200	5	200	43.37	45.02	3.67
25	25	200	5	150	40.43	38.70	4.48
26	25	200	5	150	37.80	38.70	2.34
27	25	200	5	150	39.90	38.70	3.11
28	25	200	5	150	37.70	38.70	2.60
29	25	200	5	150	37.82	38.70	2.26
30	25	200	5	150	37.89	38.70	2.10

Table 6.6 ANOVA results for quadratic equation describing Cd adsorption onto 3D GXT composite.

Source	Sum of Squares	DF	Mean Square	*F* Value	*p*-value Prob > F
Model	1780.74	14	127.20	57.11	< 0.0001
A	85.84	1	85.84	38.54	< 0.0001
B	36.95	1	36.95	16.59	0.0010
C	1456.89	1	1456.89	654.17	< 0.0001
D	157.46	1	157.46	70.70	< 0.0001
AB	2.60	1	2.60	1.17	0.2966
AC	1.33	1	1.33	0.60	0.4514
AD	0.09	1	0.09	0.04	0.8418
BC	6.92	1	6.92	3.11	0.0982
BD	0.71	1	0.71	0.32	0.5818
CD	1.34	1	1.34	0.60	0.4505
A^2	18.87	1	18.87	8.47	0.0108
B^2	13.07	1	13.07	5.87	0.0285
C^2	0.16	1	0.16	0.07	0.7906
D^2	2.45	1	2.45	1.10	0.3110
Residual	33.41	15	2.23		
Lack of Fit	26.46	10	2.65	1.91	0.2469
Pure Error	6.94	5	1.39		
Others	R^2	0.9816		Std. dev.	1.49
	Adjusted R^2	0.9644		Mean	40.10
	Predicted R^2	0.9105		C.V.%	3.72
	Adequate percision	31.168		PRESS	162.43

The interpretation of the diagnostic plots further evaluates the adequacy of the model. The normal probability plot of the residuals (**Fig. 6.13 (a)**) measures the normality of the data and determines whether the response transformation was needed. An S shape curve will be obtained if the data are not normally distributed as a result of incorrect model usage or response transformation was required [278]. The normal distribution of the data is confirmed as an alignment of data points

along the straight line as portrayed in **Fig. 6.13 (a)**. The plot of internally studentised residuals against the predicted Cd adsorption capacity is depicted in **Fig. 6.13 (b)**. It can be observed that the residuals are randomly scattered around zero in the plot, suggesting neither dependency of residuals on the response value nor response transformation was needed. The outlier plot for all the batch runs of Cd adsorption onto 3D GXT composite is presented in **Fig. 6.13 (c)**. A standard deviation of ±3 was used as the threshold for defining the outlier. No outlier was identified in this system as all the residuals were randomly scattered across the batch runs and within the limits. **Fig. 6.13 (d)** demonstrates the correlation plot for the predicted and experimental Cd adsorption capacities. The distribution of the data along the diagonal line shows that the actual and measured responses are close to each other, which is in agreement with the adjusted R^2 and predicted R^2. Thus, **Eq. (6.2)** is an appropriate model for describing the adsorption of Cd onto 3D GXT composite.

The influences of the four adsorption parameters on the response were also studied using the ANOVA results (**Table 6.6**). Generally, the smaller the *p*-value, the greater the contribution of the term to the response. As such, the significant model terms affecting the response are the linear terms of all the factors and quadratic terms for A and B. The contribution of these terms could be further ranked based on the *F*-test. Accordingly, C manifests the greatest contribution to the response as affirmed by its *F*-value of 654.17. The next significant variable is D (*F*-value of 70.70), followed by A (*F*-value of 38.54). It can be inferred that the solution pH played a significant role in this adsorption system.

A perturbation plot generated by deviating the four factors from their respective reference point, is employed to study the relative impact of each variable on the response (**Fig. 6.13 (e)**). It is discernible that factors C and D manifested a steeper trend while the curves for factors A and B were less steep. This indicated that the response was highly sensitive towards C and D. The positive and negative gradients of the line revealed the synergistic and antagonistic effects on the response, respectively. Moreover, the mathematical equation as expressed by **Eq. (6.2)** could also be used to determine the relative impact of each parameter on the response. The sign and numerical order of the regression coefficients in **Eq. (6.2)** decide the type and degree of influence towards the response. The negative value of A indicated that it has a negative effect on the response, while the positive values of B, C and D illustrate their synergistic effect on the response. Furthermore, the factors C and D exhibited higher impact towards the response based on their higher numerical magnitude. Therefore, the adsorption of Cd onto 3D GXT composite was highly dependent on the solution pH (C), followed by shaking speed (D), adsorbent mass (A) and initial Cd concentration (B).

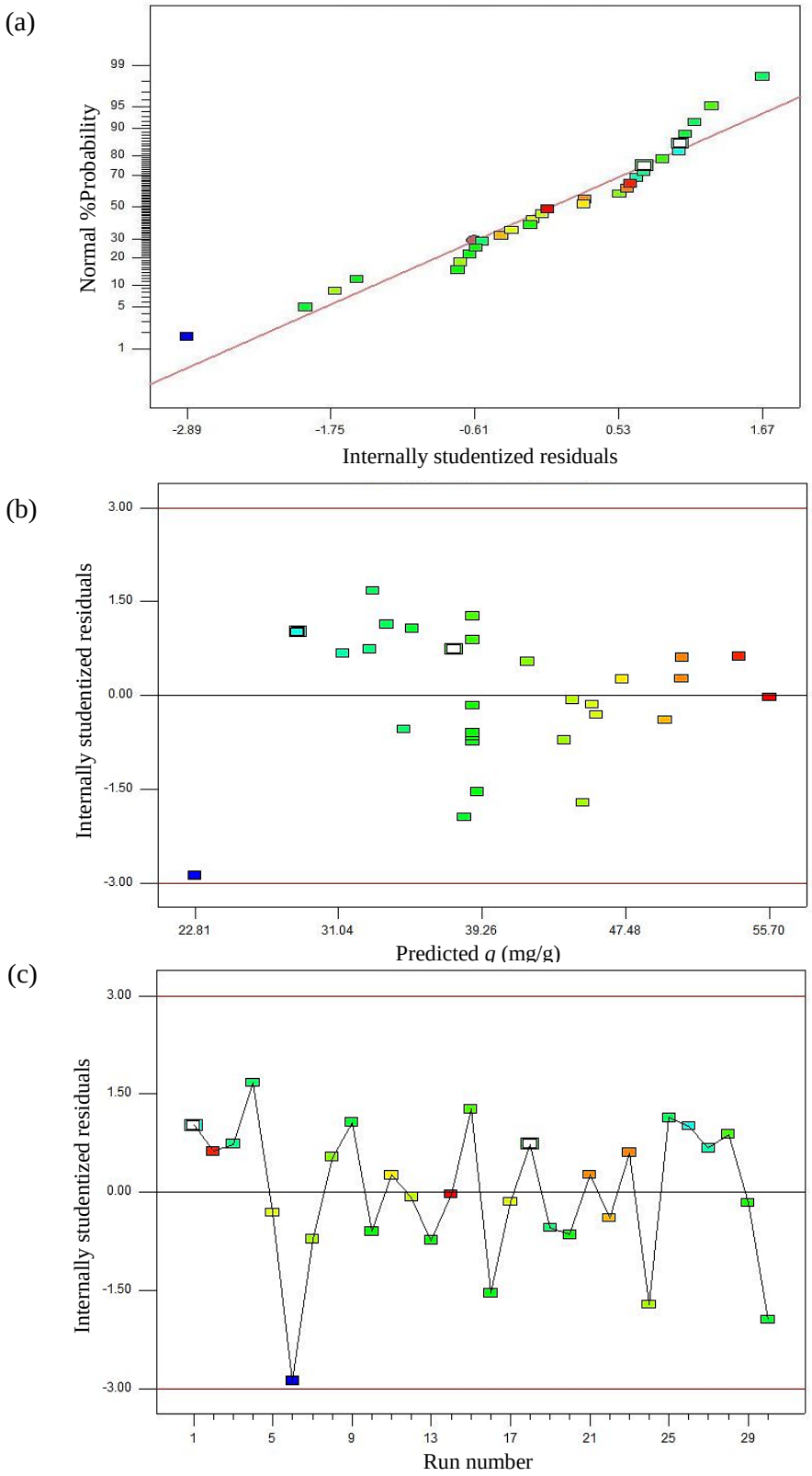
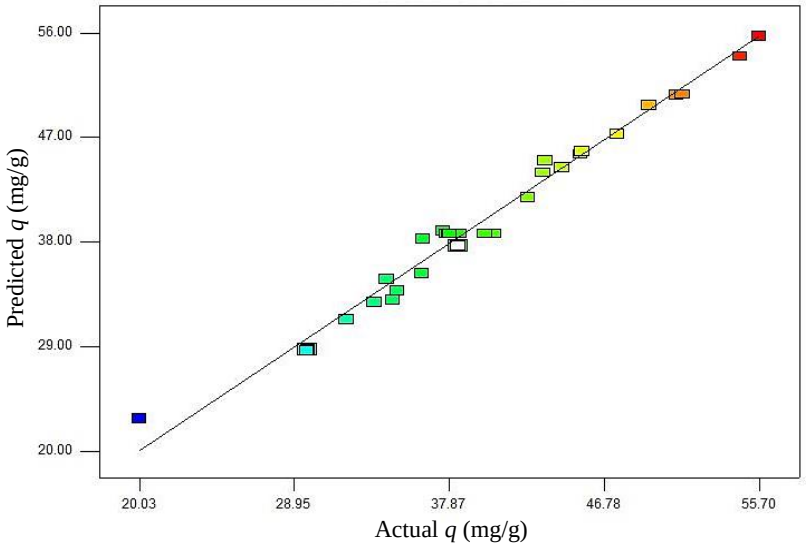


Fig. 6.13 Diagnostic plots: (a) Normal % probability plot, (b) residuals vs predicted *q* plot, (c) residuals vs run plot and (d) predicted vs actual *q* plot, and (e) perturbation plot.

(d)



(e)

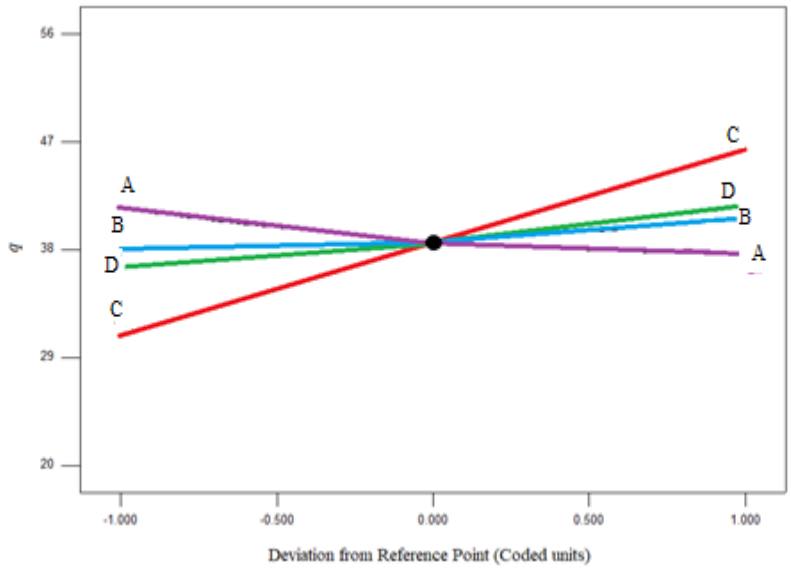


Fig. 6.13 Diagnostic plots: (a) Normal % probability plot, (b) residuals vs predicted *q* plot, (c) residuals vs run plot and (d) predicted vs actual *q* plot, and (e) perturbation plot.

The 3D response surface plots for Cd adsorption capacity of the GXT composite are depicted in **Fig. 6.14**. The response surface plots illustrate the variation in the response against two adsorption factors while other factors were fixed at their optimum values (A: 25 mg, B: 200 mg/L, C: pH 5 and D: 150 rpm). The adsorbent mass (A) was varied from 15 to 35 mg in this study while its interaction with the factors B, C and D are portrayed in **Fig. 6.14 (a)**, **(b)** and **(c)**, respectively. These figures revealed that high q was obtained at the conditions of A < 25 mg, B > 200 mg/L, C > pH 5 and D > 175 rpm. The availability of the sorption sites was governed by the adsorbent mass at a constant initial concentration. At too high adsorbent concentration, there exists a higher tendency for the adsorbent to agglomerate, thus reducing the effective surface area and elongating the diffusional pathway for adsorption. In addition, unsaturation of sorption sites might also be another factor contributing to the lower adsorption capacity [279].

The variation of initial Cd concentration (B) manifested a favourable effect on the Cd adsorption capacity as presented in **Fig. 6.14 (a)**, **(d)** and **(e)**. The initial concentration determines the driving force for overcoming the mass transfer resistance of Cd ions between the aqueous and solid phase. Hence, a higher metal concentration is beneficial for adsorption. **Fig. 6.14 (a)** illustrates that the adsorption of Cd onto 3D GXT composite had a high *q* when A < 20 mg and B > 200 mg/L. As for the interaction between initial concentration and pH, the high region of *q* occurred when B > 250 mg/L and C > pH 5 (**Fig. 6.14 (d)**). From **Fig. 6.14 (e)**, conditions as B > 250 mg/L and D > 175 rpm resulted in high *q*.

The solution pH (C) is the most prominent parameter influencing the adsorption process as it alters the metal chemistry in the solution and ionisation of the surface

functionalities of adsorbent [280]. In this study, the effect of pH on the response was studied in the range of 3 – 7 as the metal hydroxide precipitates at pH higher than 7. The interactive effects of solution pH (C) with A, B and D are shown in **Fig. 6.14 (b)**, **(d)** and **(f)**. These surface plots unveiled that higher pH enhanced the Cd adsorption capacity. At low pH (< 5), the protonation of the surface functional groups in the adsorbent had caused its surface to be positively charged. Thus, there was electrostatic repulsion between the adsorbent and metal ions which deteriorated the adsorption performance. Furthermore, there was an intensive competition between the hydrogen ions and metal ions for limited active sites due to the higher concentration of hydrogen ions at low pH condition. Conversely, the increase in pH caused the adsorbent surface to become negatively charged and hence improved the electrostatic interaction between the adsorbent and metal ions. The competition between hydrogen ions and metal ions became negligible at higher pH and thus led to higher *q*. As can be visualised from **Fig. 6.14 (b)**, **(d)** and **(f)**, the greatest *q* could be achieved by maintaining C > pH 5 with A < 25 mg, B> 250 mg/L and D > 175 rpm.

Fig. 6.14 (c), **(e)** and **(f)** depict the interactions between shaking speed (D) and A, B and C, respectively. Generally, the adsorption of Cd onto 3D GXT composite was promoted at higher agitating speed. The boundary layer encircling the adsorbent became thinner under vigorous shaking, which in turn facilitated the diffusion of metal ions into the adsorbent. In addition, the higher shaking speed also enabled constant interaction between the adsorbent and metal ions to ensure complete adsorption. As a result, the highest possible *q* could be attained at the following conditions: D > 175 rpm, A < 25 mg, B > 250 mg/L and C > pH 5.

Different results were obtained for the simultaneous interactions of the four independent variables on Cd adsorption. Therefore, identification of factor settings that will result in a desirable response is a vital part of this study. In this study, the specific goal was to maximise Cd uptake by the GXT composite. The best combination of parameter settings for achieving the specific goal was determined to be adsorbent mass (A) of 15 mg, initial Cd concentration (B) of 300 mg/L, pH (C) of 7 and shaking speed (D) of 150 rpm for the predicted q of 71.70 mg/g with the largest desirability of 1. Another three experimental runs were completed under these optimum conditions to compare the predicted q with the experimental q (67.33 mg/g). This comparison reveals that there was a slight deviation of 6.1 % from the optimised value, hence, the developed model is adequate for predicting and optimising the adsorption of Cd onto 3D GXT composite.

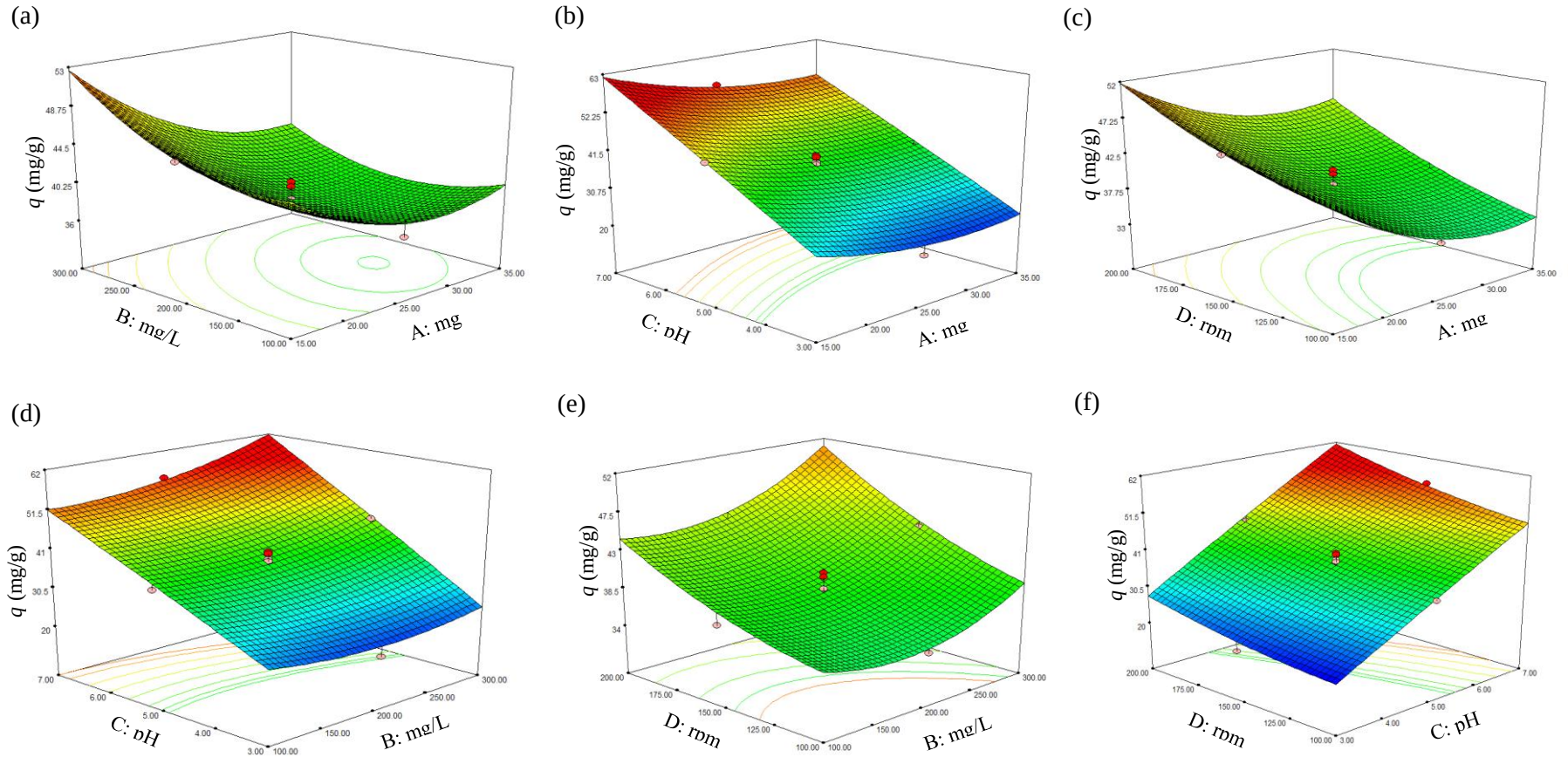


Fig. 6.14 Response surface plots: Effects of (a) adsorbent mass and concentration, (b) adsorbent mass and pH, (c) adsorbent mass and shaking speed, (d) concentration and pH, (e) concentration and shaking speed and (f) pH and shaking speed on Cd adsorption capacity.

6.2.4 Reusability of 3D GXT composite

The improper disposal of exhausted adsorbent may lead to the discharge of adsorbed pollutant into the environment. Hence, it is preferable to regenerate the spent adsorbent for minimising the overall cost and reducing the negative environmental impact [281]. Acid-base regeneration is a simple and low cost approach involving the use of an acid or alkali to recover the exhausted adsorbent [282]. The eluting agent was selected based on the efficiency, cost and environmentally friendliness. Since heavy metals adsorption is generally favoured under basic condition, desorption of the metal ions can be realised under acidic environment. Therefore, HCl (0.1 M) was employed as the desorption agent to remove the metal ions attached on the GXT composite as it is effective and low cost. During the eluting process, the presence of abundant H^+ ions could weaken the interactions between the metal ions and active sites. Meanwhile, the Cl^- ions from the HCl could interact easily with the metal ions to form complexes which were then released to the solution [281]. Washing of the eluted adsorbent with ample amount of water is imperative to recover the neutrality of adsorbent as acidic condition is not conducive for the removal of cationic heavy metals.

Fig. 6.15 (a) and **(b)** illustrate the adsorption capacities of Pb and Cd, respectively, during the 5 cycles of adsorption-regeneration. Notably, the Pb adsorption capacity of 3D GXT composite decreased from 78.68 to 66.70 mg/g after 5 continuous cycles of adsorption, maintaining 84.78 % of its adsorption performance. Moreover, the Cd adsorption capacity was reduced gradually from 27.07 to 21.86 mg/g, preserving 80.75% of its initial adsorption capacity. The decrease in the adsorption performance with increasing cycle number might be due

to the saturation of sorption sites by strongly adsorbed metal ions. Overall, the 3D GXT composite demonstrated high Pb and Cd removal with promising reusability.

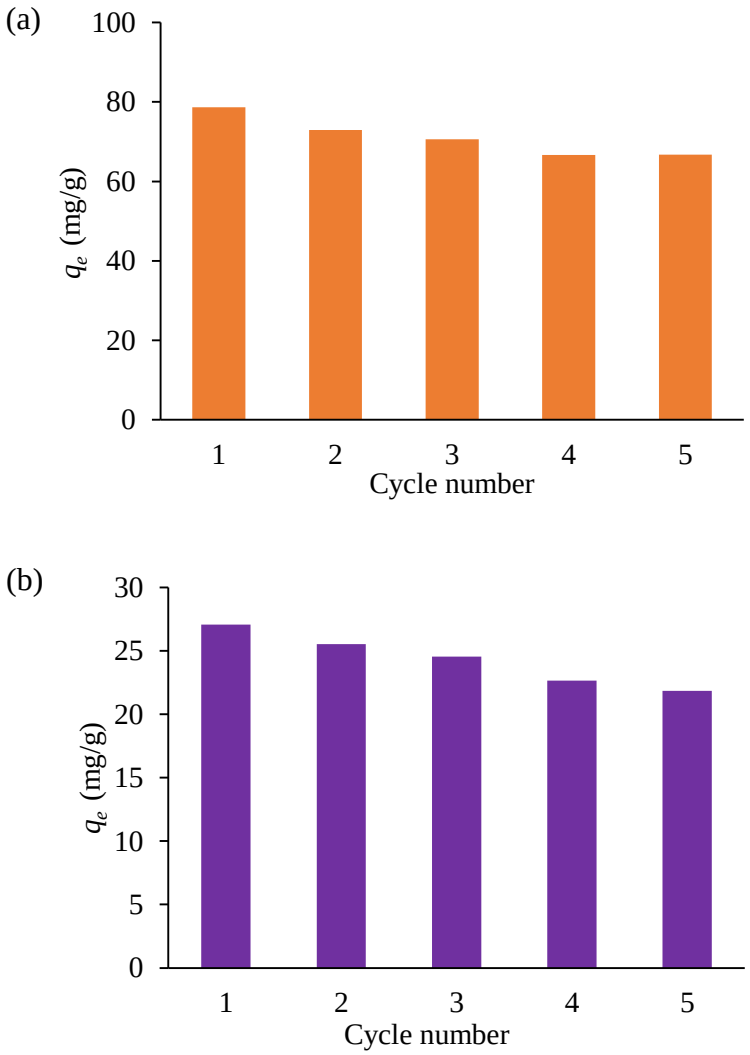


Fig. 6.15 Adsorption capacity of 3D GXT composite versus regeneration cycle for (a) Pb and (b) Cd.

6.2.5 Comparison of 3D GXT composite with other adsorbents

As depicted in **Table 6.7**, a wide variety of adsorbents were developed and utilised for the purification of Pb and Cd contaminated water which included biochar, polymer based adsorbent, metal and clay composites, etc. It is discernible that the

amount of Pb adsorbed by the 3D GXT composite was higher in comparison to other reported values (43.20 to 134.68 mg/g). Furthermore, the Cd adsorption capacity of 3D GXT composite also outperformed the reported values (19.70 to 30.78 mg/g). The comparisons suggested that the 3D GXT composite is an efficient and promising adsorbent for adsorptive sequestration of Pb and Cd ions.

Table 6.7 Comparison of Pb and Cd adsorption capacity of 3D GXT composite with other reported values.

Pb		
Adsorbent	q_e (mg/g)	Reference
Activated sludge-based biochar	49.47	[283]
Iron hydroxyphosphate composites	43.20	[284]
Poly(aniline-*co*-pyrrole) nanospheres	119.02	[285]
Methionine-montmorillonite composite	117.79	[286]
Graphene oxide/carboxymethyl chitosan aerogel	249.38	[143]
Ball-milled wheat straw biochar	134.68	[287]
3D GXT composite	**204.76**	***Present study***
Cd		
Adsorbent	q_e (mg/g)	Reference
Activated black cumin seeds	19.70	[288]
3-(trimethoxysilyl)-1-propanethiol functionalized mesoporous silica	85	[289]
Modified zeolite – zero-valent iron composites	30.78	[290]
Freshwater mussel shells biosorbent	28.61	[253]
Surface aminated biochar	23.54	[291]
3D GXT composite	**67.33**	***Present study***

6.3 Summary

This work demonstrated the 3D GXT composite as an effective adsorbent for Pb and Cd removal. The kinetic results signified the high speed adsorption of both Pb and Cd which were well correlated to the pseudo-second-order and limited by boundary layer and intraparticle diffusions. The Pb adsorption system was best described by the Langmuir isotherm and the maximum adsorption capacities from the Langmuir isotherm prediction were 132.18 - 199.22 mg/g for 30 – 70 ^{o}C. Pb was spontaneously and endothermically adsorbed to 3D GTX composite. Four adsorption parameters were optimised by RSM and the highest q (204.76 mg/g) was obtained at the following conditions: adsorbent mass of 14.95 mg, initial Pb concentration of 300 mg/L, agitation speed of 187 rpm and temperature of 60 ^{o}C. On the other hand, the Freundlich model described well the Cd adsorption system as multilayer of Cd ions occupied the heterogeneous active sites of the adsorbent. The Cd adsorption process was proven to be spontaneous and exothermic by the thermodynamic evaluation. The optimised Cd adsorption capacity was 67.33 mg/g at an adsorbent mass of 15 mg, initial Cd concentration of 300 mg/L, pH of 7 and shaking speed of 150 rpm. For both Pb and Cd removal, the 3D GXT composite was regenerable by HCl and showed adequate adsorption capacity even after 5 times of repeated adsorption-regeneration. This study advocated that the as-prepared 3D GXT composite has a great potential in purifying water polluted by heavy metals.

Chapter 7. Fixed-bed column adsorption of lead and cadmium by 3D GO/xanthan/TiO_2 composite

7.1 Introduction

The selection of suitable chemical additives for 3D GO structure synthesis was based on several criteria. The additives should assist in the formation of new 3D GO structure which is stable in water without consuming the reactive functional groups of GO extensively. It is also desirable to integrate GO with chemical additives which comprise abundant functional groups with high adsorption affinity for heavy metals. Xanthan, an anionic polysaccharide, is widely used in the preparation of multifunctional composite materials [74]. The anionic properties of xanthan endow it to be a promising candidate for attracting cationic heavy metals through coulombic attraction. Moreover, the employment of xanthan in wastewater remediation is promising as it is readily available, non-toxic, low cost and biodegradable [292].

The combination of graphene and metal/metal oxides may provide a synergistic effect to improve the adsorption performance [293]. The porous structure of the 3D GO may act as a skeletal frame for supporting the metal/metal oxides and thus exposing more active sites. Zeng et al., [136] prepared a reduced GO hydrogel integrated with manganese dioxide (MnO_2) and used it to remove Pb (356.37 mg/g). The adsorption capacity of this hydrogel outperformed the pristine reduced GO (138.40 mg/g). A 3D graphene/titanium dioxide (TiO_2) composite fabricated by Yu et al., [294] was used to adsorb uranium and it achieved an adsorption capacity of

441.3 mg/g. These studies indicated that the integration of active materials within the 3D GO structure is beneficial for adsorption.

Most of the adsorption studies on GO materials reported in the literature were investigated via batch mode. However, for practical application, a fixed-bed column should be adopted to provide more reliable data on the breakthrough time [230]. The present work focused on the adoption of 3D graphene composite integrated with xanthan and TiO_2 (3D GXT composite) for adsorptive removal of Pb and Cd via continuous mode. The effects column parameters such as bed height, inlet metal concentration and feed flowrate on the continuous adsorption of the heavy metals were investigated. The acquired data were fitted to the Thomas, Yoon-Nelson and Adams-Bohart models. Lastly, the interaction mechanisms between the heavy metals and adsorbent were evaluated based on pH study and Fourier transform infrared (FTIR) spectroscopy.

7.2 Results and discussion

7.2.1 Effects of column parameters

The fixed-bed column adsorption experiments were carried out at a Pb inlet concentration of 150 mg/L and feed flowrate of 2 mL/min, while the bed height was varied from 2 to 4 cm. The breakthrough profiles are depicted in **Fig. 7.1 (a)** while the breakthrough data are summarised in **Table 7.1**. The breakthrough (t_b) and exhaustion (t_e) times were extended from 25 to 45 min and 80 to 160 min, respectively, as the bed height was increased. Moreover, a significant increment in the volume of Pb solution treated was observed with the increase in bed height. As

more Pb ions were adsorbed at higher beds (from 12.52 mg at 2 cm to 27.31 mg at 4 cm), the bed adsorption capacity was augmented from 125.80 to 136.41 mg/g.

For Cd, the effect of bed heights (2, 3 and 4 cm) on its continuous removal was investigated using an inlet concentration of 75 mg/L and feed flowrate of 2 mL/min. The results are delineated in **Fig. 7.1 (b)** and **Table 7.1**. As observed, the increase in bed height had increased the volume of Cd solution treated, as well as the breakthrough (12.5 to 30 min) and exhaustion (85 to 170 min) times. The amount of Cd ions adsorbed increased from 5.92 mg at 2 cm to 12.84 mg at 4 cm, and hence the bed adsorption capacity was enhanced from 57.99 mg/g at 2 cm to 63.73 mg/g at 4 cm.

As shown in **Fig. 7.1 (a)** and **(b)**, the slope of the breakthrough curve is a function of bed length. Specifically, the gradient of breakthrough curve reduced with increasing bed height, resulting in broadened mass transfer zone. There were more adsorbents in larger beds, and hence larger surface area and amount of binding sites were available for adsorption of Pb and Cd ions. Furthermore, at larger bed height, the metal ions had more time to interact with the 3D GXT composite and this led to the enhanced adsorption of the metal ions [234].

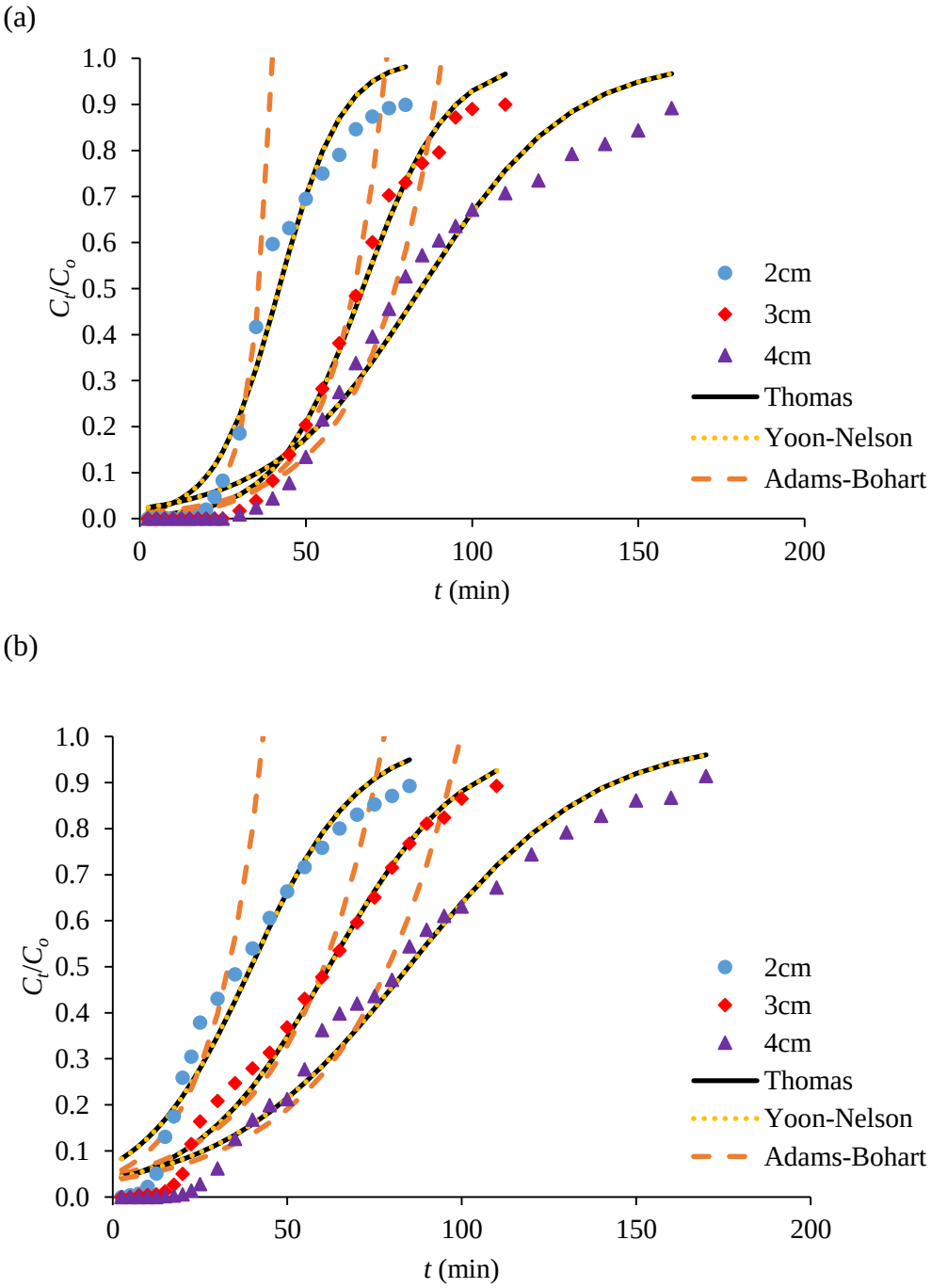


Fig. 7.1 Breakthrough curves obtained at different bed heights for (a) Pb and (b) Cd adsorption onto 3D GTX composite.

Table 7.1 Column data for 3D GTX fixed-bed column adsorption of Pb and Cd.

Pb

Z (cm)	C_o (mg/L)	Q (mL/min)	t_b (min)	t_e (min)	V_t (mL)	m_{ads} (mg)	q (mg/g)
2	150	2	25	80	160	12.52	125.80
3	150	2	35	110	220	19.81	132.05
4	150	2	45	160	320	27.31	136.41
3	100	2	40	190	380	18.64	124.77
3	200	2	22.5	100	200	20.90	139.21
3	150	1	80	260	260	21.99	146.08
3	150	3	23.33	73.33	220	19.04	127.09

Cd

Z (cm)	C_o (mg/L)	Q (mL/min)	t_b (min)	t_e (min)	V_t (mL)	m_{ads} (mg)	q (mg/g)
2	75	2	12.5	85	170	5.92	57.99
3	75	2	20	110	220	8.95	59.86
4	75	2	30	170	340	12.84	63.73
3	50	2	30	150	300	8.36	55.49
3	100	2	15	95	190	9.65	64.05
3	75	1	60	220	220	9.48	62.80
3	75	3	11.67	80	240	8.87	58.97

In order to study the influence of inlet concentration on the column performance, the inlet Pb concentration was altered from 100 to 200 mg/L while the bed height and feed flowrate were kept at 3 cm and 2 mL/min, respectively. The obtained breakthrough curves and column data are shown in **Fig 7.2 (a)** and **Table 7.1**, respectively. It is noteworthy that the breakthrough and exhaustion times were shortened from 40 to 22.5 min and 190 to 100 min, respectively, at higher inlet concentrations. Nevertheless, larger amount of Pb ions was adsorbed at higher inlet concentration (from 18.64 mg at 100 mg/L to 20.90 mg at 200 mg/L). As a

consequence, the bed adsorption capacity was increased from 124.77 to 139.21 mg/g.

The investigation on the effect of inlet concentration on column adsorption of Cd was carried out at different inlet concentrations (50 – 100 mg/L) but at fixed bed height (3 cm) and feed flowrate (2 mL/min). The results of this study are portrayed in **Fig. 7.2 (b)** and **Table 7.1**. At higher Cd concentration, the breakthrough curve became steeper and shifted towards the origin. Thus, the breakthrough and exhaustion times were shortened from 30 to 15 min and 150 to 95 min, respectively. The quantity of Cd ions adsorbed increased from 8.36 mg at 50 mg/L to 9.65 mg at 100 mg/L. Therefore, the column adsorption capacity was augmented from 55.49 to 64.05 mg/g with the increase in inlet concentrations.

At higher inlet concentration, the concentration driving force was greater, thus leading to the enhanced adsorption of Pb and Cd onto the 3D GXT column. The presence of more metal ions at higher inlet concentration facilitated the diffusion of the metal ions into the 3D GXT bed and hence boosted column adsorption performance. Nevertheless, the increase in mass transfer of the metal ions in the adsorbent bed at higher inlet concentration had contributed to the earlier saturation of the bed.

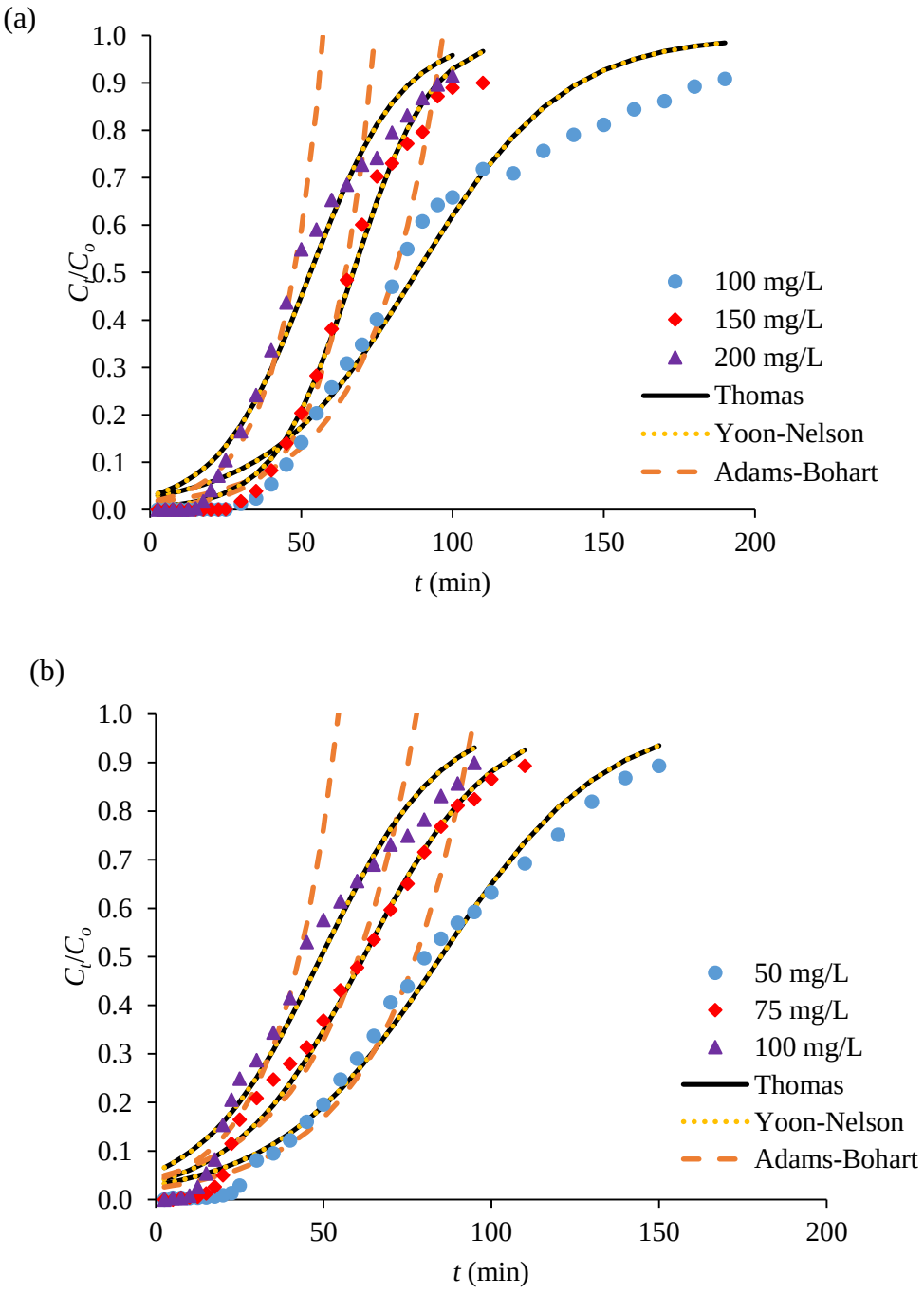


Fig. 7.2 Breakthrough curves obtained at different inlet concentrations for (a) Pb and (b) Cd adsorption onto 3D GTX composite.

The effect of feed flowrate was examined at three levels (1, 2 and 3 mL/min) while keeping the bed height (3 cm) and inlet Pb concentration (150 mg/L) constant. The breakthrough curves obtained under these conditions are depicted in **Fig. 7.3**

(a) and the adsorption data are demonstrated in **Table 7.1**. It is noticeable from **Fig. 7.3 (a)** that the shape of breakthrough curves was broader at a lower flowrate and *vice versa* at a higher flowrate. Therefore, both the breakthrough and exhaustion times were prolonged at lower flowrates. Besides, a lesser amount of Pb was adsorbed at a higher flowrate and thus the column adsorption capacity was reduced from 146.08 to 127.09 mg/g with increasing flowrate.

Fig. 7.3 (b) demonstrates the effect of feed flowrate (1 to 3 mL/min) on the column adsorption of Cd using a 3D GXT bed height and inlet concentration of 3 cm and 75 mg/L, respectively. With the increase in flowrate, the breakthrough and exhaustion times were shortened from 60 to 11.67 min and 220 to 110 min, respectively. Furthermore, the Cd uptake was less effective at higher flowrates as evident from the decreasing trend in the total mass of Cd adsorbed (from 9.48 to 8.87 mg). Similarly, a negative trend was also observed in the column adsorption capacity (from 62.80 to 58.97 mg/g) as the flowrate was increased.

The deterioration in column performance at high feed flowrate could be attributed to the inadequate residence time for the metal ions to migrate from the bulk solution into the 3D GTX composite bed. Contrarily, there was more time for the heavy metals to diffuse into the adsorbent bed at lower flowrates and hence enhanced the uptake of the metal ions.

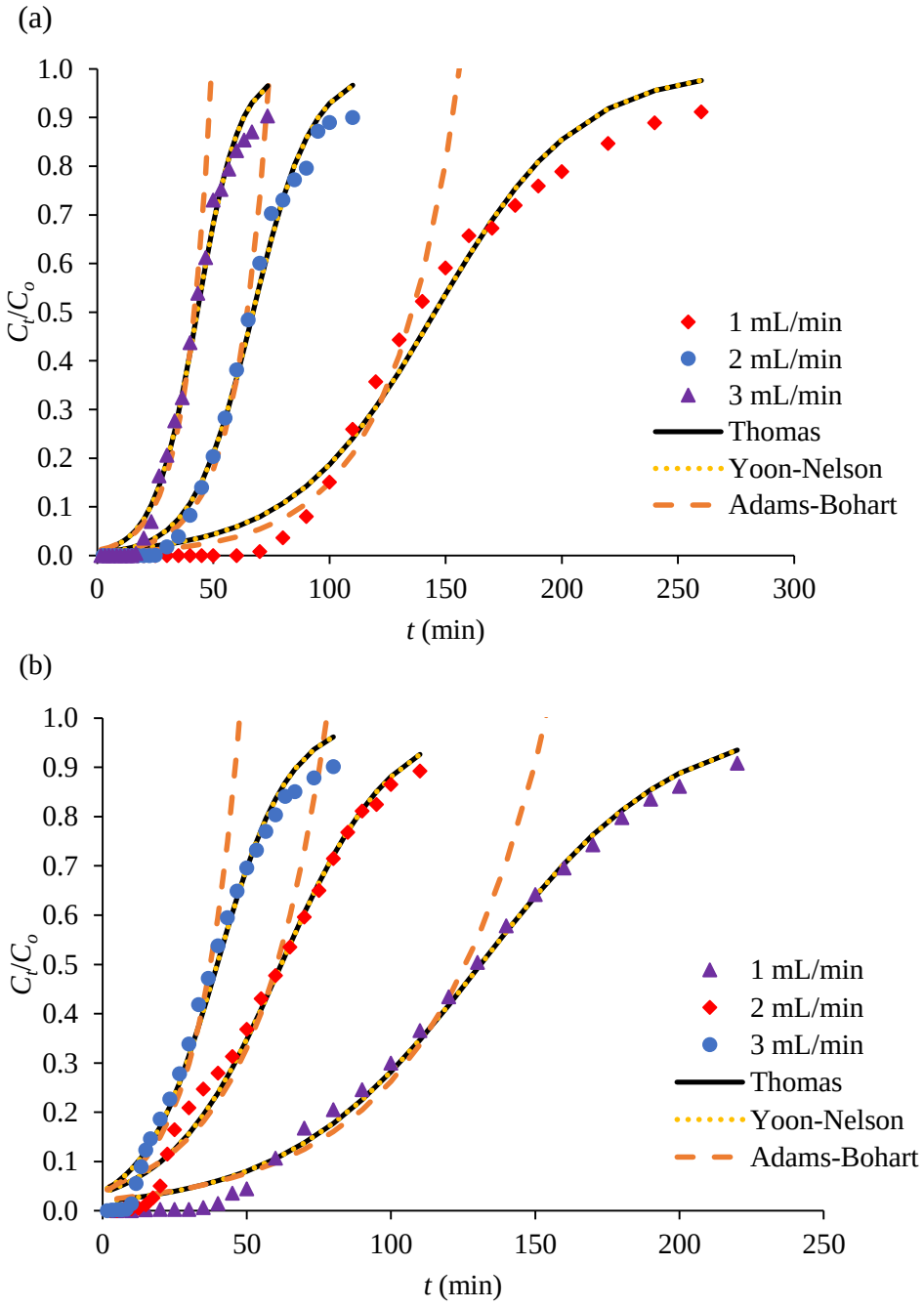


Fig. 7.3 Breakthrough curves obtained at different feed flowrates for (a) Pb and (b) Cd adsorption onto 3D GTX composite.

7.2.2 Modelling of breakthrough curve

The breakthrough curves obtained under different inlet concentrations, bed heights and feed flowrates were fitted to non-linear Thomas, Yoon-Nelson and Adams-Bohart models, as demonstrated in **Fig. 7.1** to **7.3** for each adsorption system. Their corresponding model parameters and coefficient of determination (R^2) are summarised in **Table 7.2**.

It is discernible that the Thomas model could satisfactorily express the Pb and Cd adsorption onto the 3D GXT composite column, as advocated by the high R^2 values ranging from 0.965 – 0.992 for Pb and 0.962 – 0.993 for Cd. This also indicated that the external and internal diffusion resistances were not significant for both adsorption systems. A descending trend in k_{TH} values was observed when the bed heights and inlet concentrations were increased and *vice versa* when the flowrate was increased. The higher k_{TH} values indicated a greater metal ions adsorption rate. Moreover, a higher theoretical bed capacities (q_o) were achieved at a taller bed and larger inlet concentration. The driving force for adsorption is determined by the concentration difference between the metal ions in the solution and on the adsorbent. Hence, a greater concentration difference resulted in a stronger driving force which ultimately improved the adsorption capacity [123].

The column data were also well fitted to the Yoon-Nelson model with relatively high R^2 values (0.965 – 0.992 for Pb and 0.962 – 0.993 for Cd.). The time to reach 50 % breakthrough (τ) was shortened while the rate constant (k_{YN}) was increased at higher inlet concentration and feed flowrate. The presence of more metal ions in the column had induced fast Pb and Cd adsorption, and hence led to earlier

breakthrough and exhaustion. Contradictory results were observed for greater bed height due to the longer distance of mass transfer zone.

The Adams-Bohart model could sufficiently represent the initial segment of the breakthrough curves (50% breakthrough), showing R^2 values of 0.960 – 0.995 for Pb and 0.877 – 0.961 for Cd. Generally, the larger k_{AB} values signified quicker metal ions uptake due to lower diffusion resistance, which were also reflected by the breakthrough curves with a steeper slope. The adequacy of this model suggested that the initial part of the column adsorption was governed by the external mass transfer.

Summarily, the column data adhered to the Thomas and Yoon-Nelson models. The initial part of the breakthrough curves was also well described by the Adams-Bohart model. Furthermore, a higher bed adsorption capacity could be attained at a greater bed height, lower feed flowrate and larger inlet metal concentration.

Table 7.2 Parameters of the Thomas, Yoon-Nelson and Adams-Bohart models for Pb and Cd adsorption onto 3D GTX fixed-bed column.

Pb										
***Z* (cm)**	***C_o* (mg/L)**	***Q* (mL/min)**	**Thomas**			**Yoon-Nelson**			**Adams-Bohart**		
			k_{TH}	***q_o***	***R^2***	***k_{YN}***	***τ***	***R^2***	***k_{AB}***	***N_o***	***R^2***
2	150	2	0.700	126.23	0.969	0.105	41.87	0.969	1.167	7.630	0.995
3	150	2	0.522	134.10	0.992	0.078	67.05	0.992	0.473	9.467	0.982
4	150	2	0.286	132.28	0.966	0.045	84.59	0.966	0.313	9.064	0.960
3	100	2	0.410	117.83	0.965	0.041	88.02	0.965	0.434	8.224	0.963
3	200	2	0.333	141.22	0.978	0.067	52.99	0.978	0.360	9.727	0.966
3	150	1	0.216	144.89	0.981	0.032	145.37	0.981	0.226	9.947	0.964
3	150	3	0.731	129.21	0.991	0.110	43.01	0.991	0.618	9.411	0.968
Cd										
***Z* (cm)**	***C_o* (mg/L)**	***Q* (mL/min)**	**Thomas**			**Yoon-Nelson**			**Adams-Bohart**		
			k_{TH}	***q_o***	***R^2***	***k_{YN}***	***τ***	***R^2***	***k_{AB}***	***N_o***	***R^2***
2	75	2	0.865	58.22	0.962	0.065	39.59	0.962	0.930	4.129	0.877
3	75	2	0.702	62.17	0.986	0.053	61.97	0.986	0.531	4.957	0.920
4	75	2	0.498	63.12	0.974	0.037	84.75	0.974	0.444	4.762	0.925
3	50	2	0.819	56.41	0.984	0.041	84.95	0.984	0.786	4.040	0.961
3	100	2	0.567	65.45	0.969	0.057	49.28	0.969	0.595	4.626	0.924
3	75	1	0.400	65.11	0.993	0.030	131.08	0.993	0.330	4.899	0.954
3	75	3	1.069	59.44	0.986	0.080	39.73	0.986	0.917	4.541	0.945

7.2.3 Proposed mechanisms for Pb and Cd adsorption onto 3D GXT composite

An effort was made to identify the plausible mechanism for the adsorption of Pb and Cd onto 3D GXT composite column. The PZC of the 3D GXT composite was determined to be about 4.5 (**Fig. 7.4 (a)**) signifiying that the composite surface became positively charged at pH < 4.5 and negatively charged at pH > 4.5. The target adsorbates (Pb and Cd) used in this study are cationic in nature, hence, it can be speculated that both metal ions would be electrostatically attracted to the adsorbent surface when the solution pH is greater than 4.5. Notably, a considerable amount of metal ions was adsorbed onto the adsorbent at pH < 4.5, thus, electrostatic attraction might not be the only interaction between the adsorbent and adsorbate.

In order to identify the possible sorption sites in the 3D GXT composite for Pb and Cd binding, as well as to understand the nature of Pb and Cd adsorption, FTIR spectra were recorded for the 3D GXT composite before and after adsorption. **Fig. 7.4 (b)** presents the FTIR results while the corresponding peak assignments are provided in **Table 7.3**. The FTIR results reveal that the 3D GXT composite contained a number of oxygeneous functional groups.

The significant decrease in the peak at 3306 cm^{-1} and its shift to a lower wavenumber after Pb/Cd adsorption imply that the O – H stretching was affected during the adsorption of the heavy metals. There was a negligible change in the peak at 2918 cm^{-1} even after Pb/Cd adsorption. Since the peak was ascribed to the C–H stretching, the metal ions were unlikely to be attached to the carbon atom. Other significant changes in FTIR peaks could also be seen at the following wavenumbers: 1720, 1601, 1048 and 1027 cm^{-1} which could be ascribed to C=O

stretching and C–O stretching. The adsorption of Pb/Cd seems to affect bonds with oxygen atoms, suggesting that oxygen atoms could be the primary sorption sites for Pb/Cd adsorption. Since the hydroxyl and carboxyl groups were the dominant functional groups involved in the Pb/Cd removal, the adsorption process might occur through complexation between the heavy metals and the hydroxyl and carboxyl groups of 3D GXT composite [295].

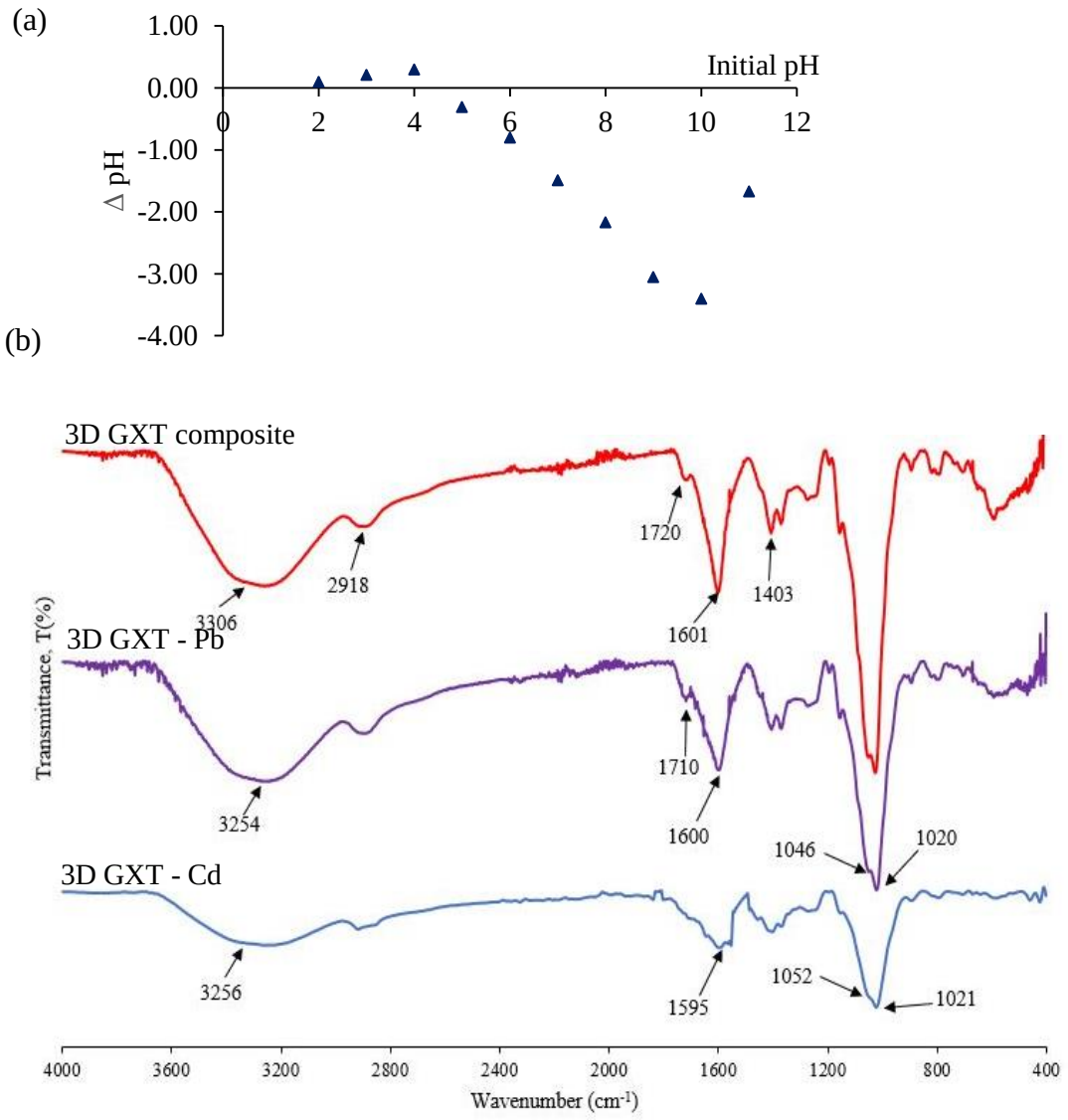


Fig 7.4 (a) PZC plot of 3D GXT composite and (b) FTIR spectra of 3D GXT composite before and after Pb and Cd adsorption.

Table 7.3 Chemical functional groups in 3D GXT composite before and, after Pb and Cd adsorption.

Wavenumber range (cm^{-1})	Functional groups	Before adsorption	After adsorption (Pb)	After adsorption (Cd)
		Wavenumber (cm^{-1})		
3600 – 3100	O – H stretch	3306	3254	3256
3000 – 2800	C – H stretch	2918	2919	2916
1750 – 1630	C = O stretch	1720	1710	-
1610 – 1550	C = O stretch	1601	1600	1595
1550 – 1300	C – H deformation	1403	1404	1402
1300 – 1000	C – O stretch	1048, 1027	1046, 1020	1052, 1021
700 – 500	Ti – O stretch	591	-	-

The 3D GXT fixed-bed exhibited higher adsorption capacity for Pb than Cd. Generally, the affinity of an adsorbent towards a metal ion is governed by its electronegativity and hydration radius. Specifically, the adsorbent would have high affinity towards the adsorbate with high electronegativity and small hydration radius. The electronegativity for Pb and Cd are 2.33 and 1.69, respectively. Besides, Pb ion has a smaller hydration radius (4.01 Å) as compared to that of Cd ion (4. 26 Å) [296].

7.2.4 Comparison of bed adsorption capacity with other adsorbents

The bed adsorption capacity of 3D GTX composite was compared with those of other fixed-beds reported in the literature and the results are shown in **Table 7.4**. It is notable that the GXT composite had a relatively high bed capacities for Pb and

Cd and hence could be considered as potential fixed-bed material for the treatment of heavy metals in wastewater.

Table 7.4 Comparison of 3D GTX fixed-bed adsorption capacities for Pb and Cd with other fixed-beds.

Adsorbent	Bed adsorption capacity, *q* (mg/g)		Reference
	Pb	Cd	
3D GXT composite	**146.08**	**64.05**	***Present study***
Modified beer lees	29.60	-	[297]
Graphite oxide coated sand	1.08	-	[298]
Polyethyleneimine on monolithic melamine sponge	85.03	-	[299]
Syzygium cumini L leaf powder	-	29.08	[300]
Magnetic graphene oxide and sand	-	9.69	[301]
Immobilized *Pleurotus ostreatus* spent substrate	-	14.40	[302]

7.3 Summary

The 3D GXT composite manifested satisfactory results in sequestrating both Pb and Cd in fixed-bed column adsorption. The continuous adsorption of the heavy metals was favourable at greater bed height, inlet concentration and lower feed flowrate. The highest bed adsorption capacities were achieved at 146.08 and 64.05 mg/g for Pb and Cd, respectively. Both the Thomas and Yoon-Nelsons models were suitable for describing the dynamic adsorption of Pb and Cd onto the 3D GXT composite. The outcomes of pH and FTIR analyses advocated that the electrostatic attraction and complexation between the metal ions and oxygenated functional groups of the adsorbent as the main adsorption mechanism for this system. This study revealed the feasibility of 3D GXT composite as an effective adsorbent for Pb and Cd elimination from aqueous effluents.

Chapter 8. Conclusions and Recommendations

8.1 Conclusions

New 3D graphene structures, namely GOCA and 3D GXT composite, were successfully synthesised through ice-templating approach and employed for the adsorptive removal of organic dyes (MY and RB5 dyes) and heavy metals (Pb and Cd), respectively. Based on the research results described in Chapters 4, 5, 6 and 7, the following conclusions can be drawn:

- The as-synthesised 3D graphene structures were structurally stable in water and could be easily retrieved from the liquid phase after the adsorption process. This eliminates the requirement for energy intensive separation methods, such as centrifugation, to recover the adsorbent at the end of adsorption.
- The FESEM images portrayed the porous structure of ice-templated 3D graphene adsorbents which are beneficial for adsorption of pollutants. The FTIR spectra indicated that the as-prepared graphene adsorbents possessed numerous chemical functional groups which could serve as active sites for the adsorbates.
- The pH study and FTIR results indicated that MY and RB5 dyes were adsorbed onto GOCA mainly through electrostatic attraction and $\pi - \pi$ stacking interaction. The mechanisms for Pb and Cd adsorption onto 3D GXT composite were related to electrostatic attraction and complexation.
- The adsorption equilibria of the GOCA-dyes systems were well represented by the Langmuir isotherm. The kinetic profiles of both dyes were in good

agreement with the pseudo-first-order and pseudo-second-order models at low and high concentration regions, respectively. The adsorption isotherms of the 3D GXT-heavy metals systems followed the Langmuir and Freundlich models, respectively. The kinetic results indicated both the Pb and Cd adsorption were well correlated to the pseudo-second-order model.

- RSM-CCD was successfully applied for the optimisation of batch adsorption systems and identification of the influential adsorption variables. The optimum adsorption capacities determined for MY dye, RB5 dye, Pb and Cd were 418.35, 656.96, 204.76 and 67.33 mg/g, respectively.
- The spent adsorbents could be easily regenerated using acids/alkalis (0.1 M HCl/0.1 M NaOH) and reused for 5 successive adsorption-desorption cycles. The elution of adsorbed pollutants was due to the intensive competition between ions of similar charge.
- The GOCA and 3D GXT composites exhibited promising results in fixed-bed column adsorption of MY and RB5 dyes, and Pb and Cd, respectively. The column data were well represented by the Thomas and Yoon-Nelson models.

8.2 Recommendations

Despite the initial objectives were achieved in this work, some other aspects were still unexplored due to limitation of time and availability of resources. Hence, recommendations for future studies are described as follows:

- In addition to single component adsorption system, the adsorption study should be carried out for binary system to establish the competitive adsorption between MY dye and RB5 dye, and Pb and Cd.
- The effect of co-existing ions on the adsorption performance of GOCA and 3D GXT adsorbent should be performed to determine how the adsorption process could be interfered by other ions.
- To fully evaluate the potential of as-prepared adsorbents as fixed-bed column materials, it is suggested to perform in situ regeneration of adsorbent under continuous mode.
- The interactive effects of column parameters on fixed-bed adsorption performance should be investigated by RSM as well as optimisation of the fixed-bed adsorption process.

References

[1] E.N. Zare, A. Motahari, M. Sillanpää, Nanoadsorbents based on conducting polymer nanocomposites with main focus on polyaniline and its derivatives for removal of heavy metal ions/dyes: A review, Environmental Research 162 (2018) 173-195.

[2] A. Mittal, V.K. Gupta, A. Malviya, J. Mittal, Process development for the batch and bulk removal and recovery of a hazardous, water-soluble azo dye (Metanil Yellow) by adsorption over waste materials (Bottom Ash and De-Oiled Soya), Journal of Hazardous Materials 151(2-3) (2008) 821-832.

[3] R. Nilsson, R. Nordlinder, U. Wass, B. Meding, L. Belin, Asthma, rhinitis, and dermatitis in workers exposed to reactive dyes, British Journal of Industrial Medicine 50(1) (1993) 65-70.

[4] B.Y.Z. Hiew, L.Y. Lee, X.J. Lee, S. Thangalazhy-Gopakumar, S. Gan, S.S. Lim, G.T. Pan, T.C.K. Yang, W.S. Chiu, P.S. Khiew, Review on synthesis of 3D graphene-based configurations and their adsorption performance for hazardous water pollutants, Process Safety and Environmental Protection 116 (2018) 262-286.

[5] F.K. Mahar, L. He, K. Wei, M. Mehdi, M. Zhu, J. Gu, K. Zhang, Z. Khatri, I. Kim, Rapid adsorption of lead ions using porous carbon nanofibers, Chemosphere 225 (2019) 360-367.

[6] Y. Chen, L. Chen, H. Bai, L. Li, Graphene oxide–chitosan composite hydrogels as broad-spectrum adsorbents for water purification, Journal of Materials Chemistry A 1(6) (2013) 1992-2001.

[7] M.M. Matlock, B.S. Howerton, D.A. Atwood, Chemical Precipitation of Lead from Lead Battery Recycling Plant Wastewater, Industrial & Engineering Chemistry Research 41(6) (2002) 1579-1582.

[8] A. Dąbrowski, Z. Hubicki, P. Podkościelny, E. Robens, Selective removal of the heavy metal ions from waters and industrial wastewaters by ion-exchange method, Chemosphere 56(2) (2004) 91-106.

[9] V. Katheresan, J. Kansedo, S.Y. Lau, Efficiency of various recent wastewater dye removal methods: A review, Journal of Environmental Chemical Engineering 6(4) (2018) 4676-4697.

[10] M. Taseidifar, F. Makavipour, R.M. Pashley, A.F.M.M. Rahman, Removal of heavy metal ions from water using ion flotation, Environmental Technology & Innovation 8 (2017) 182-190.

[11] K. Sunil, G. Karunakaran, S. Yadav, M. Padaki, V. Zadorozhnyy, R.K. Pai, Al-Ti2O6 a mixed metal oxide based composite membrane: A unique membrane for removal of heavy metals, Chemical Engineering Journal 348 (2018) 678-684.

[12] L. Yu, L. Wang, W. Xu, L. Chen, M. Fu, J. Wu, D. Ye, Adsorption of VOCs on reduced graphene oxide, Journal of Environmental Sciences 67 (2018) 171-178.

[13] J. Liu, X. Ge, X. Ye, G. Wang, H. Zhang, H. Zhou, Y. Zhang, H. Zhao, 3D graphene/δ-MnO_2 aerogels for highly efficient and reversible removal of heavy metal ions, Journal of Materials Chemistry A 4(5) (2016) 1970-1979.

[14] I.A. Aguayo-Villarreal, A. Bonilla-Petriciolet, R. Muñiz-Valencia, Preparation of activated carbons from pecan nutshell and their application in the antagonistic adsorption of heavy metal ions, Journal of Molecular Liquids 230 (2017) 686-695.

[15] S. Norouzi, M. Heidari, V. Alipour, O. Rahmanian, M. Fazlzadeh, F. Mohammadi-moghadam, H. Nourmoradi, B. Goudarzi, K. Dindarloo, Preparation, characterization and Cr(VI) adsorption evaluation of NaOH-activated carbon produced from Date Press Cake; an agro-industrial waste, Bioresource Technology 258 (2018) 48-56.

[16] I. Enniya, L. Rghioui, A. Jourani, Adsorption of hexavalent chromium in aqueous solution on activated carbon prepared from apple peels, Sustainable Chemistry and Pharmacy 7 (2018) 9-16.

[17] E. Zanin, J. Scapinello, M. de Oliveira, C.L. Rambo, F. Franscescon, L. Freitas, J.M.M. de Mello, M.A. Fiori, J.V. Oliveira, J.D. Magro, Adsorption of heavy metals from wastewater graphic industry using clinoptilolite zeolite as adsorbent, Process Safety and Environmental Protection 105 (2017) 194-200.

[18] G.V. Briã o, S.L. Jahn, E.L. Foletto, G.L. Dotto, Adsorption of crystal violet dye onto a mesoporous ZSM-5 zeolite synthetized using chitin as template, Journal of Colloid and Interface Science 508 (2017) 313-322.

[19] B. Pan, B. Pan, W. Zhang, L. Lv, Q. Zhang, S. Zheng, Development of polymeric and polymer-based hybrid adsorbents for pollutants removal from waters, Chemical Engineering Journal 151(1) (2009) 19-29.

[20] X. Li, M. Zhou, J. Jia, Q. Jia, A water-insoluble viologen-based β-cyclodextrin polymer for selective adsorption toward anionic dyes, Reactive and Functional Polymers 126 (2018) 20-26.

[21] Y.F. Lam, L.Y. Lee, S.J. Chua, S.S. Lim, S. Gan, Insights into the equilibrium, kinetic and thermodynamics of nickel removal by environmental friendly Lansium

domesticum peel biosorbent, Ecotoxicology and Environmental Safety 127 (2016) 61-70.

[22] A. Naskar, R. Majumder, Understanding the adsorption behaviour of acid yellow 99 on Aspergillus niger biomass, Journal of Molecular Liquids 242 (2017) 892-899.

[23] J.T. da Fontoura, G.S. Rolim, B. Mella, M. Farenzena, M. Gutterres, Defatted microalgal biomass as biosorbent for the removal of Acid Blue 161 dye from tannery effluent, Journal of Environmental Chemical Engineering 5(5) (2017) 5076-5084.

[24] A.Y.W. Sham, S.M. Notley, Adsorption of organic dyes from aqueous solutions using surfactant exfoliated graphene, Journal of Environmental Chemical Engineering 6(1) (2018) 495-504.

[25] F. Perreault, A. Fonseca de Faria, M. Elimelech, Environmental applications of graphene-based nanomaterials, Chemical Society Reviews 44(16) (2015) 5861-5896.

[26] B. Hayati, A. Maleki, F. Najafi, H. Daraei, F. Gharibi, G. McKay, Super high removal capacities of heavy metals (Pb^{2+} and Cu^{2+}) using CNT dendrimer, Journal of Hazardous Materials 336 (2017) 146-157.

[27] D. Vuono, E. Catizzone, A. Aloise, A. Policicchio, R.G. Agostino, M. Migliori, G. Giordano, Modelling of adsorption of textile dyes over multi-walled carbon nanotubes: Equilibrium and kinetic, Chinese Journal of Chemical Engineering 25(4) (2017) 523-532.

[28] G.M.D. Ferreira, G.M.D. Ferreira, M.C. Hespanhol, J. de Paula Rezende, A.C. dos Santos Pires, L.V.A. Gurgel, L.H.M. da Silva, Adsorption of red azo dyes on

multi-walled carbon nanotubes and activated carbon: A thermodynamic study, Colloids and Surfaces A: Physicochemical and Engineering Aspects 529 (2017) 531-540.

[29] H.W. Liang, X. Cao, W.J. Zhang, H.T. Lin, F. Zhou, L.F. Chen, S.H. Yu, Robust and highly efficient free-standing carbonaceous nanofiber membranes for water purification, Advanced Functional Materials 21(20) (2011) 3851-3858.

[30] A.E. Burakov, E.V. Galunin, I.V. Burakova, A.E. Kucherova, S. Agarwal, A.G. Tkachev, V.K. Gupta, Adsorption of heavy metals on conventional and nanostructured materials for wastewater treatment purposes: A review, Ecotoxicology and Environmental Safety 148(August 2017) (2018) 702-712.

[31] W. Gao, The chemistry of graphene oxide, Graphene Oxide: Reduction Recipes, Spectroscopy, and Applications (2015) 61-95.

[32] Y. Shen, Q. Fang, B. Chen, Environmental applications of three-dimensional graphene-based macrostructures: Adsorption, transformation, and detection, Environmental Science and Technology 49(1) (2015) 67-84.

[33] M. Rethinasabapathy, S.M. Kang, S.C. Jang, Y.S. Huh, Three-dimensional porous graphene materials for environmental applications, Carbon Letters 22(1) (2017) 1-13.

[34] Y. Guo, J. Deng, J. Zhu, X. Zhou, R. Bai, Removal of mercury(ii) and methylene blue from a wastewater environment with magnetic graphene oxide: adsorption kinetics, isotherms and mechanism, RSC Advances 6(86) (2016) 82523-82536.

[35] Z. Niu, L. Liu, L. Zhang, X. Chen, Porous graphene materials for water remediation, Small 10(17) (2014) 3434-3441.

[36] A. Shahzad, W. Miran, K. Rasool, M. Nawaz, J. Jang, S.-R. Lim, D.S. Lee, Heavy metals removal by EDTA-functionalized chitosan graphene oxide nanocomposites, RSC Advances 7(16) (2017) 9764-9771.

[37] A.I.A. Sherlala, A.A.A. Raman, M.M. Bello, A. Asghar, A review of the applications of organo-functionalized magnetic graphene oxide nanocomposites for heavy metal adsorption, Chemosphere 193 (2018) 1004-1017.

[38] B. Yu, Y. Bai, Z. Ming, H. Yang, L. Chen, X. Hu, S. Feng, S.-T. Yang, Adsorption behaviors of tetracycline on magnetic graphene oxide sponge, Materials Chemistry and Physics 198 (2017) 283-290.

[39] H. Luo, S. Zhang, X. Li, Q. Xu, J. Liu, Z. Wang, A facile route for preparation of magnetic biomass activated carbon with high performance for removal of dye pollutants, Environmental Science and Pollution Research 24(18) (2017) 15599-15608.

[40] S. Nardecchia, D. Carriazo, M.L. Ferrer, M.C. Gutiérrez, F. del Monte, Three dimensional macroporous architectures and aerogels built of carbon nanotubes and/or graphene: synthesis and applications, Chemical Society Reviews 42(2) (2013) 794-830.

[41] K. Shehzad, Y. Xu, C. Gao, X. Duan, Three-dimensional macro-structures of two-dimensional nanomaterials, Chemical Society Reviews 45(20) (2016) 5541-5588.

[42] V. Chabot, D. Higgins, A. Yu, X. Xiao, Z. Chen, J. Zhang, A review of graphene and graphene oxide sponge: material synthesis and applications to energy and the environment, Energy & Environmental Science 7(5) (2014) 1564-1564.

[43] Q. Fang, Y. Shen, B. Chen, Synthesis , decoration and properties of three-dimensional graphene-based macrostructures : A review, 264 (2015) 753-771.

[44] S. Zamani, N.S. Tabrizi, Removal of methylene blue from water by graphene oxide aerogel: Thermodynamic, kinetic, and equilibrium modeling, Research on Chemical Intermediates 41(10) (2015) 7945-7963.

[45] Y. Li, Q. Du, T. Liu, X. Peng, J. Wang, J. Sun, Y. Wang, S. Wu, Z. Wang, Y. Xia, L. Xia, Comparative study of methylene blue dye adsorption onto activated carbon, graphene oxide, and carbon nanotubes, Chemical Engineering Research and Design 91(2) (2013) 361-368.

[46] H. Yan, X. Tao, Z. Yang, K. Li, H. Yang, A. Li, R. Cheng, Effects of the oxidation degree of graphene oxide on the adsorption of methylene blue, Journal of Hazardous Materials 268 (2014) 191-198.

[47] J. Dai, T. Huang, S.q. Tian, Y.j. Xiao, J.h. Yang, N. Zhang, Y. Wang, Z.w. Zhou, High structure stability and outstanding adsorption performance of graphene oxide aerogel supported by polyvinyl alcohol for waste water treatment, Materials and Design 107 (2016) 187-197.

[48] Y. Wang, G. Xia, C. Wu, J. Sun, R. Song, W. Huang, Porous chitosan doped with graphene oxide as highly effective adsorbent for methyl orange and amido black 10B, Carbohydrate Polymers 115 (2015) 686-693.

[49] R. Yu, Y. Shi, D. Yang, Y. Liu, J. Qu, Z.Z. Yu, Graphene Oxide/Chitosan Aerogel Microspheres with Honeycomb-Cobweb and Radially Oriented Microchannel Structures for Broad-Spectrum and Rapid Adsorption of Water Contaminants, ACS Applied Materials and Interfaces 9(26) (2017) 21809-21819.

[50] K. Olszowska, J. Pang, P.S. Wrobel, L. Zhao, H.Q. Ta, Z. Liu, B. Trzebicka, A. Bachmatiuk, M.H. Rummeli, Three-dimensional nanostructured graphene: Synthesis and energy, environmental and biomedical applications, Synthetic Metals 234(October) (2017) 53-85.

[51] Y. He, N. Zhang, F. Wu, F. Xu, Y. Liu, J. Gao, Graphene oxide foams and their excellent adsorption ability for acetone gas, Materials Research Bulletin 48(9) (2013) 3553-3558.

[52] T. Ma, P.R. Chang, P. Zheng, F. Zhao, X. Ma, Fabrication of ultra-light graphene-based gels and their adsorption of methylene blue, Chemical Engineering Journal 240 (2014) 595-600.

[53] N. Zhang, H. Qiu, Y. Si, W. Wang, J. Gao, Fabrication of highly porous biodegradable monoliths strengthened by graphene oxide and their adsorption of metal ions, Carbon 49(3) (2011) 827-837.

[54] Y. Luo, S. Jiang, Q. Xiao, C. Chen, B. Li, Highly reusable and superhydrophobic spongy graphene aerogels for efficient oil/water separation, Scientific Reports 7(1) (2017) 1-10.

[55] S. Deville, Ice-Templating: Processing Routes, Architectures, and Microstructures, Springer International Publishing, Cham, 2017, pp. 171-252.

[56] M.C. Gutiérrez, M.L. Ferrer, C.R. Mateo, F. del Monte, Freeze-Drying of Aqueous Solutions of Deep Eutectic Solvents: A Suitable Approach to Deep Eutectic Suspensions of Self-Assembled Structures, Langmuir 25(10) (2009) 5509-5515.

[57] S. Deville, Freeze-casting of porous ceramics: A review of current achievements and issues, Advanced Engineering Materials 10(3) (2008) 155-169.

[58] S. Deville, The lure of ice-templating: Recent trends and opportunities for porous materials, Scripta Materialia 147 (2018) 119-124.

[59] S. Deville, Ice-templating, freeze casting: Beyond materials processing, Journal of Materials Research 28(17) (2013) 2202-2219.

[60] S. Deville, Ice-Templating and Freeze-Casting: Control of the Processes, Microstructures, and Architectures, Springer International Publishing, Cham, 2017, pp. 351-438.

[61] W.L. Li, K. Lu, J.Y. Walz, Freeze casting of porous materials: review of critical factors in microstructure evolution, International Materials Reviews 57(1) (2012) 37-60.

[62] H. Sun, Z. Xu, C. Gao, Multifunctional, ultra-flyweight, synergistically assembled carbon aerogels, Advanced Materials 25(18) (2013) 2554-2560.

[63] X. Mi, G. Huang, W. Xie, W. Wang, Y. Liu, J. Gao, Preparation of graphene oxide aerogel and its adsorption for Cu^{2+} ions, Carbon 50(13) (2012) 4856-4864.

[64] N. Lavoine, L. Bergström, Nanocellulose-based foams and aerogels: processing, properties, and applications, Journal of Materials Chemistry A 5(31) (2017) 16105-16117.

[65] S.W. Sofie, F. Dogan, Freeze Casting of Aqueous Alumina Slurries with Glycerol, Journal of the American Ceramic Society 84(7) (2001) 1459-1464.

[66] Y. Zhang, L. Hu, J. Han, Z. Jiang, Freeze casting of aqueous alumina slurries with glycerol for porous ceramics, Ceramics International 36(2) (2010) 617-621.

[67] M. Fukushima, Y.i. Yoshizawa, T. Ohji, Macroporous Ceramics by Gelation–Freezing Route Using Gelatin, Advanced Engineering Materials 16(6) (2014) 607-620.

[68] Y. Zhang, K. Zuo, Y.-P. Zeng, Effects of gelatin addition on the microstructure of freeze-cast porous hydroxyapatite ceramics, Ceramics International 35(6) (2009) 2151-2154.

[69] K.H. Zuo, Y.-P. Zeng, D. Jiang, Effect of polyvinyl alcohol additive on the pore structure and morphology of the freeze-cast hydroxyapatite ceramics, Materials Science and Engineering: C 30(2) (2010) 283-287.

[70] C.M. Pekor, P. Kisa, I. Nettleship, Effect of Polyethylene Glycol on the Microstructure of Freeze-Cast Alumina, Journal of the American Ceramic Society 91(10) (2008) 3185-3190.

[71] E. Munch, E. Saiz, A.P. Tomsia, S. Deville, Architectural Control of Freeze-Cast Ceramics Through Additives and Templating, Journal of the American Ceramic Society 92(7) (2009) 1534-1539.

[72] W. Li, K. Lu, J.Y. Walz, Formation, Structure and Properties of Freeze-Cast Kaolinite–Silica Nanocomposites, Journal of the American Ceramic Society 94(4) (2011) 1256-1264.

[73] Q. Fu, M.N. Rahaman, F. Dogan, B.S. Bal, Freeze casting of porous hydroxyapatite scaffolds. I. Processing and general microstructure, Journal of Biomedical Materials Research Part B: Applied Biomaterials 86B(1) (2008) 125-135.

[74] S. Liu, F. Yao, O. Oderinde, Z. Zhang, G. Fu, Green synthesis of oriented xanthan gum–graphene oxide hybrid aerogels for water purification, Carbohydrate Polymers 174 (2017) 392-399.

[75] A. Szepes, A. Fehér, P. Szabó-Révész, J. Ulrich, Influence of Freezing Temperature on Product Parameters of Solid Dosage Forms Prepared via the

Freeze-Casting Technique, Chemical Engineering & Technology 30(4) (2007) 511-516.

[76] R. Zhang, Y. Cao, P. Li, X. Zang, P. Sun, K. Wang, M. Zhong, J. Wei, D. Wu, F. Kang, H. Zhu, Three-dimensional porous graphene sponges assembled with the combination of surfactant and freeze-drying, Nano Research 7(10) (2014) 1477-1487.

[77] D. Koch, L. Andresen, T. Schmedders, G. Grathwohl, Evolution of porosity by freeze casting and sintering of sol-gel derived ceramics, Journal of Sol-Gel Science and Technology 26(1-3) (2003) 149-152.

[78] T.H. Tu, P.T.N. Cam, L.V.T. Huy, M.T. Phong, H.M. Nam, N.H. Hieu, Synthesis and application of graphene oxide aerogel as an adsorbent for removal of dyes from water, Materials Letters 238 (2019) 134-137.

[79] S. Jayanthi, N. KrishnaRao Eswar, S.A. Singh, K. Chatterjee, G. Madras, A.K. Sood, Macroporous three-dimensional graphene oxide foams for dye adsorption and antibacterial applications, RSC Advances 6(2) (2016) 1231-1242.

[80] S. Liao, T. Zhai, H. Xia, Highly adsorptive graphene aerogel microspheres with center-diverging microchannel structures, Journal of Materials Chemistry A 4(3) (2016) 1068-1077.

[81] Y. Long, C. Zhang, X. Wang, J. Gao, W. Wang, Y. Liu, Oxidation of SO2 to SO3 catalyzed by graphene oxide foams, Journal of Materials Chemistry 21(36) (2011) 13934-13934.

[82] E. Platero, M.E. Fernandez, P.R. Bonelli, A.L. Cukierman, Graphene oxide/alginate beads as adsorbents: Influence of the load and the drying method on

their physicochemical-mechanical properties and adsorptive performance, Journal of Colloid and Interface Science 491 (2017) 1-12.

[83] H. Bi, X. Xie, K. Yin, Y. Zhou, S. Wan, R.S. Ruoff, L. Sun, Highly enhanced performance of spongy graphene as an oil sorbent, Journal of Materials Chemistry A 2(6) (2014) 1652-1656.

[84] Y. He, Y. Liu, T. Wu, J. Ma, X. Wang, Q. Gong, W. Kong, F. Xing, Y. Liu, J. Gao, An environmentally friendly method for the fabrication of reduced graphene oxide foam with a super oil absorption capacity, Journal of Hazardous Materials 260 (2013) 796-805.

[85] Q. Yao, B. Fan, Y. Xiong, C. Jin, Q. Sun, C. Sheng, 3D assembly based on 2D structure of Cellulose Nanofibril/Graphene Oxide Hybrid Aerogel for Adsorptive Removal of Antibiotics in Water, Scientific Reports 7(April) (2017) 1-13.

[86] Y.Q. He, N.N. Zhang, X.D. Wang, Adsorption of graphene oxide/chitosan porous materials for metal ions, Chinese Chemical Letters 22(7) (2011) 859-862.

[87] M. Salzano de Luna, C. Ascione, C. Santillo, L. Verdolotti, M. Lavorgna, G.G. Buonocore, R. Castaldo, G. Filippone, H. Xia, L. Ambrosio, Optimization of dye adsorption capacity and mechanical strength of chitosan aerogels through crosslinking strategy and graphene oxide addition, Carbohydrate Polymers 211 (2019) 195-203.

[88] N.T.M. Huyen, P.T.T. Trang, N.M. Dat, N.H. Hieu, Synthesis of chitosan/graphene oxide nanocomposites for methylene blue adsorption, 020013 (2017) 020013-020013.

[89] A. Ouyang, C. Wang, S. Wu, E. Shi, W. Zhao, A. Cao, D. Wu, Highly Porous Core-Shell Structured Graphene-Chitosan Beads, ACS Applied Materials and Interfaces 7(26) (2015) 14439-14445.

[90] Y. Wang, X. Liu, H. Wang, G. Xia, W. Huang, R. Song, Microporous spongy chitosan monoliths doped with graphene oxide as highly effective adsorbent for methyl orange and copper nitrate (Cu(NO3)2) ions, Journal of Colloid and Interface Science 416 (2014) 243-251.

[91] C. Jiao, J. Xiong, J. Tao, S. Xu, D. Zhang, H. Lin, Y. Chen, Sodium alginate/graphene oxide aerogel with enhanced strength-toughness and its heavy metal adsorption study, International Journal of Biological Macromolecules 83 (2016) 133-141.

[92] Z. Ma, D. Liu, Y. Zhu, Z. Li, Z. Li, H. Tian, H. Liu, Graphene oxide/chitin nanofibril composite foams as column adsorbents for aqueous pollutants, Carbohydrate Polymers 144 (2016) 230-237.

[93] X. Fu, Y. Zhan, Y. Meng, Y. Li, C. Liao, Z. Lu, Graphene oxide/poly(vinyl alcohol) hydrogels with good tensile properties and reusable adsorption properties, Plastics, Rubber and Composites 46(2) (2017) 53-59.

[94] X. Wei, T. Huang, J.h. Yang, N. Zhang, Y. Wang, Z.w. Zhou, Green synthesis of hybrid graphene oxide/microcrystalline cellulose aerogels and their use as superabsorbents, Journal of Hazardous Materials 335 (2017) 28-38.

[95] K.C. Lai, L.Y. Lee, B.Y.Z. Hiew, S. Thangalazhy-Gopakumar, S. Gan, Facile synthesis of xanthan biopolymer integrated 3D hierarchical graphene oxide/titanium dioxide composite for adsorptive lead removal in wastewater, Bioresource Technology 309 (2020) 123296.

[96] H. Ha, K. Shanmuganathan, C.J. Ellison, Mechanically stable thermally crosslinked poly(acrylic acid)/reduced graphene oxide aerogels, ACS Appl Mater Interfaces 7(11) (2015) 6220-9.

[97] Y. Zhang, Y. Liu, X. Wang, Z. Sun, J. Ma, T. Wu, F. Xing, J. Gao, Porous graphene oxide/carboxymethyl cellulose monoliths, with high metal ion adsorption, Carbohydrate Polymers 101(1) (2014) 392-400.

[98] H. Dai, Y. Huang, H. Huang, Eco-friendly polyvinyl alcohol/carboxymethyl cellulose hydrogels reinforced with graphene oxide and bentonite for enhanced adsorption of methylene blue, Carbohydrate Polymers 185 (2018) 1-11.

[99] X. Yang, Y. Li, Q. Du, J. Sun, L. Chen, S. Hu, Z. Wang, Y. Xia, L. Xia, Highly effective removal of basic fuchsin from aqueous solutions by anionic polyacrylamide/graphene oxide aerogels, Journal of Colloid and Interface Science 453 (2015) 107-114.

[100] L. Fan, C. Luo, X. Li, F. Lu, H. Qiu, M. Sun, Fabrication of novel magnetic chitosan grafted with graphene oxide to enhance adsorption properties for methyl blue, Journal of Hazardous Materials 215-216 (2012) 272-279.

[101] I.M.N. Vold, K.M. Vårum, E. Guibal, O. Smidsrød, Binding of ions to chitosan—selectivity studies, Carbohydrate Polymers 54(4) (2003) 471-477.

[102] R. Zambare, X. Song, S. Bhuvana, J.S. Antony Prince, P. Nemade, Ultrafast Dye Removal Using Ionic Liquid-Graphene Oxide Sponge, ACS Sustainable Chemistry and Engineering 5(7) (2017) 6026-6035.

[103] S. Ye, J. Feng, Towards three-dimensional, multi-functional graphene-based nanocomposite aerogels by hydrophobicity-driven absorption, Journal of Materials Chemistry A 2(27) (2014) 10365-10365.

[104] Y. Xu, Q. Wu, Y. Sun, H. Bai, G. Shi, Three-Dimensional Self-Assembly of Graphene Oxide and DNA into Multifunctional Hydrogels, ACS Nano 4(12) (2010) 7358-7362.

[105] Q. Zhao, X. Zhu, B. Chen, Stable graphene oxide/poly(ethyleneimine) 3D aerogel with tunable surface charge for high performance selective removal of ionic dyes from water, Chemical Engineering Journal 334(August 2017) (2018) 1119-1127.

[106] M.E. Haddad, Removal of Basic Fuchsin dye from water using mussel shell biomass waste as an adsorbent: Equilibrium, kinetics, and thermodynamics, Journal of Taibah University for Science 10(5) (2016) 664-674.

[107] J. Kong, L. Huang, Q. Yue, B. Gao, Preparation of activated carbon derived from leather waste by H3PO4 activation and its application for basic fuchsin adsorption, Desalination and Water Treatment 52(13-15) (2014) 2440-2449.

[108] W. Bessashia, Y. Berredjem, Z. Hattab, M. Bououdina, Removal of Basic Fuchsin from water by using mussel powdered eggshell membrane as novel bioadsorbent: Equilibrium, kinetics, and thermodynamic studies, Environmental Research 186 (2020) 109484.

[109] Y. Guan, S. Wang, X. Wang, C. Sun, Y. Wang, L. Hu, Preparation of mesoporous Al-MCM-41 from natural palygorskite and its adsorption performance for hazardous aniline dye-basic fuchsin, Microporous and Mesoporous Materials 265 (2018) 266-274.

[110] T. Huang, J. Dai, J.h. Yang, N. Zhang, Y. Wang, Z.w. Zhou, Polydopamine coated graphene oxide aerogels and their ultrahigh adsorption ability, Diamond and Related Materials 86(January) (2018) 117-127.

[111] M. Yan, W. Huang, Z. Li, Chitosan cross-linked graphene oxide/lignosulfonate composite aerogel for enhanced adsorption of methylene blue in water, International Journal of Biological Macromolecules 136 (2019) 927-935.

[112] C. Xiang, R. Guo, J. Lan, S. Jiang, C. Wang, Z. Du, C. Cheng, Self-assembling porous 3D titanium dioxide-reduced graphene oxide aerogel for the tunable absorption of oleic acid and RhodamineB dye, Journal of Alloys and Compounds 735 (2018) 246-252.

[113] S. Tang, D. Xia, Y. Yao, T. Chen, J. Sun, Y. Yin, W. Shen, Y. Peng, Dye adsorption by self-recoverable, adjustable amphiphilic graphene aerogel, Journal of Colloid and Interface Science 554 (2019) 682-691.

[114] K.C. Lai, B.Y.Z. Hiew, L.Y. Lee, S. Gan, S. Thangalazhy-Gopakumar, W.S. Chiu, P.S. Khiew, Ice-templated graphene oxide/chitosan aerogel as an effective adsorbent for sequestration of metanil yellow dye, Bioresource Technology 274 (2019) 134-144.

[115] C.S. Cheng, J. Deng, B. Lei, A. He, X. Zhang, L. Ma, S. Li, C. Zhao, Toward 3D graphene oxide gels based adsorbents for high-efficient water treatment via the promotion of biopolymers, Journal of Hazardous Materials 263 (2013) 467-478.

[116] Y.C. Shi, A.J. Wang, X.L. Wu, J.R. Chen, J.J. Feng, Green-assembly of three-dimensional porous graphene hydrogels for efficient removal of organic dyes, Journal of Colloid and Interface Science 484 (2016) 254-262.

[117] H. Yan, H. Yang, A. Li, R. Cheng, pH-tunable surface charge of chitosan/graphene oxide composite adsorbent for efficient removal of multiple pollutants from water, Chemical Engineering Journal 284 (2016) 1397-1405.

[118] R. Nasiri, N. Arsalani, Synthesis and application of 3D graphene nanocomposite for the removal of cationic dyes from aqueous solutions : Response surface methodology design, Journal of Cleaner Production 190 (2018) 63-71.

[119] J. Wang, Z. Shi, J. Fan, Y. Ge, J. Yin, G. Hu, Self-assembly of graphene into three-dimensional structures promoted by natural phenolic acids, Journal of Materials Chemistry 22(42) (2012) 22459-22459.

[120] J. Xiao, J. Zhang, W. Lv, Y. Song, Q. Zheng, Multifunctional graphene/poly(vinyl alcohol) aerogels: In situ hydrothermal preparation and applications in broad-spectrum adsorption for dyes and oils, Carbon 123 (2017) 354-363.

[121] Y. Wang, P. Zhang, C.F. Liu, C.Z. Huang, A facile and green method to fabricate graphene-based multifunctional hydrogels for miniature-scale water purification, RSC Advances 3(24) (2013) 9240-9240.

[122] C. Liu, H. Liu, A. Xu, K. Tang, Y. Huang, C. Lu, In situ reduced and assembled three-dimensional graphene aerogel for efficient dye removal, Journal of Alloys and Compounds 714 (2017) 522-529.

[123] J. Luo, J. Lai, N. Zhang, Y. Liu, R. Liu, X. Liu, Tannic Acid Induced Self-Assembly of Three-Dimensional Graphene with Good Adsorption and Antibacterial Properties, ACS Sustainable Chemistry and Engineering 4(3) (2016) 1404-1413.

[124] L. Qiu, W. Wan, Z. Tong, R. Zhang, L. Li, Y. Zhou, Controllable and green synthesis of robust graphene aerogels with tunable surface properties for oil and dye adsorption, New Journal of Chemistry 42(2) (2018) 1003-1009.

[125] T. Jiao, H. Zhao, J. Zhou, Q. Zhang, X. Luo, J. Hu, Q. Peng, X. Yan, Self-Assembly Reduced Graphene Oxide Nanosheet Hydrogel Fabrication by Anchorage of Chitosan/Silver and Its Potential Efficient Application toward Dye Degradation for Wastewater Treatments, ACS Sustainable Chemistry and Engineering 3(12) (2015) 3130-3139.

[126] Y. Yang, S. Song, Z. Zhao, Graphene oxide (GO)/polyacrylamide (PAM) composite hydrogels as efficient cationic dye adsorbents, Colloids and Surfaces A: Physicochemical and Engineering Aspects 513 (2017) 315-324.

[127] H. Kim, S.-O. Kang, S. Park, H.S. Park, Adsorption isotherms and kinetics of cationic and anionic dyes on three-dimensional reduced graphene oxide macrostructure, Journal of Industrial and Engineering Chemistry 21 (2015) 1191-1196.

[128] K. Gupta, O.P. Khatri, Reduced graphene oxide as an effective adsorbent for removal of malachite green dye: Plausible adsorption pathways, Journal of Colloid and Interface Science 501 (2017) 11-21.

[129] L. Chen, Y. Li, Q. Du, Z. Wang, Y. Xia, E. Yedinak, J. Lou, L. Ci, High performance agar/graphene oxide composite aerogel for methylene blue removal, Carbohydrate Polymers 155 (2017) 345-353.

[130] X. Zhang, D. Liu, L. Yang, L. Zhou, T. You, Self-assembled three-dimensional graphene-based materials for dye adsorption and catalysis, Journal of Materials Chemistry A 3(18) (2015) 10031-10037.

[131] H. Gao, Y. Sun, J. Zhou, R. Xu, H. Duan, Mussel-inspired synthesis of polydopamine-functionalized graphene hydrogel as reusable adsorbents for water purification, ACS Applied Materials and Interfaces 5(2) (2013) 425-432.

[132] L. Pan, S. Liu, O. Oderinde, K. Li, F. Yao, G. Fu, Facile fabrication of graphene-based aerogel with rare earth metal oxide for water purification, Applied Surface Science 427 (2018) 779-786.

[133] S. Yang, L. Zhang, Q. Yang, Z. Zhang, B. Chen, P. Lv, W. Zhu, G. Wang, Graphene aerogel prepared by thermal evaporation of graphene oxide suspension containing sodium bicarbonate, Journal of Materials Chemistry A 3(15) (2015) 7950-7958.

[134] P. Qiu, S. Wang, C. Tian, Z. Lin, Adsorption of low-concentration mercury in water by 3D cyclodextrin/graphene composites: Synergistic effect and enhancement mechanism, Environmental Pollution 252 (2019) 1133-1141.

[135] Ihsanullah, A. Abbas, A.M. Al-Amer, T. Laoui, M.J. Al-Marri, M.S. Nasser, M. Khraisheh, M.A. Atieh, Heavy metal removal from aqueous solution by advanced carbon nanotubes: Critical review of adsorption applications, Separation and Purification Technology 157 (2016) 141-161.

[136] T. Zeng, Y. Yu, Z. Li, J. Zuo, Z. Kuai, Y. Jin, Y. Wang, A. Wu, C. Peng, 3D MnO2 nanotubes@reduced graphene oxide hydrogel as reusable adsorbent for the removal of heavy metal ions, Materials Chemistry and Physics 231 (2019) 105-108.

[137] M. Basu, A.K. Guha, L. Ray, Adsorption of Lead on Cucumber Peel, Journal of Cleaner Production 151 (2017) 603-615.

[138] Y. Zhang, B. Cao, L. Zhao, L. Sun, Y. Gao, J. Li, F. Yang, Biochar-supported reduced graphene oxide composite for adsorption and coadsorption of atrazine and lead ions, Applied Surface Science 427 (2018) 147-155.

[139] L. Largitte, T. Brudey, T. Tant, P.C. Dumesnil, P. Lodewyckx, Comparison of the adsorption of lead by activated carbons from three lignocellulosic precursors, Microporous and Mesoporous Materials 219 (2016) 265-275.

[140] S. Ben-Ali, I. Jaouali, S. Souissi-Najar, A. Ouederni, Characterization and adsorption capacity of raw pomegranate peel biosorbent for copper removal, Journal of Cleaner Production 142 (2017) 3809-3821.

[141] H. Demiral, C. Güngör, Adsorption of copper(II) from aqueous solutions on activated carbon prepared from grape bagasse, Journal of Cleaner Production 124 (2016) 103-113.

[142] Q. Fang, X. Zhou, W. Deng, Z. Liu, Hydroxyl-containing organic molecule induced self-assembly of porous graphene monoliths with high structural stability and recycle performance for heavy metal removal, Chemical Engineering Journal 308 (2017) 1001-1009.

[143] J. Luo, C. Fan, Z. Xiao, T. Sun, X. Zhou, Novel graphene oxide/carboxymethyl chitosan aerogels via vacuum-assisted self-assembly for heavy metal adsorption capacity, Colloids and Surfaces A: Physicochemical and Engineering Aspects 578 (2019) 123584.

[144] Z. Wu, W. Deng, W. Zhou, J. Luo, Novel magnetic polysaccharide/graphene oxide @Fe_3O_4 gel beads for adsorbing heavy metal ions, Carbohydrate Polymers 216 (2019) 119-128.

[145] B. Yu, J. Xu, J.H. Liu, S.T. Yang, J. Luo, Q. Zhou, J. Wan, R. Liao, H. Wang, Y. Liu, Adsorption behavior of copper ions on graphene oxide-chitosan aerogel, Journal of Environmental Chemical Engineering 1(4) (2013) 1044-1050.

[146] Z. Sui, Q. Meng, X. Zhang, R. Ma, B. Cao, Green synthesis of carbon nanotube-graphene hybrid aerogels and their use as versatile agents for water purification, Journal of Materials Chemistry 22(18) (2012) 8767-8771.

[147] M. Chen, C. Zhang, X. Li, L. Zhang, Y. Ma, L. Zhang, X. Xu, F. Xia, W. Wang, J. Gao, A one-step method for reduction and self-assembling of graphene oxide into reduced graphene oxide aerogels, Journal of Materials Chemistry A 1(8) (2013) 2869-2869.

[148] X. Feng, C. Liang, J. Yu, X. Jiang, Facile fabrication of graphene oxide-polyethylenimine composite and its application for the Cr(VI) removal, Separation Science and Technology (Philadelphia) 00(00) (2018) 1-12.

[149] Q. Liang, H. Luo, J. Geng, J. Chen, Facile one-pot preparation of nitrogen-doped ultra-light graphene oxide aerogel and its prominent adsorption performance of Cr(VI), Chemical Engineering Journal 338(December 2017) (2018) 62-71.

[150] Y. Yang, Y. Zhao, S. Sun, X. Zhang, L. Duan, X. Ge, W. Lü, Self-assembled three-dimensional graphene/Fe3O4hydrogel for efficient pollutant adsorption and electromagnetic wave absorption, Materials Research Bulletin 73 (2016) 401-408.

[151] Y. Zhuang, F. Yu, J. Ma, J. Chen, Enhanced adsorption removal of antibiotics from aqueous solutions by modified alginate/graphene double network porous hydrogel, Journal of Colloid and Interface Science 507 (2017) 250-259.

[152] H.P. Cong, X.C. Ren, P. Wang, S.H. Yu, Macroscopic multifunctional graphene-based hydrogels and aerogels by a metal ion induced self-assembly process, ACS Nano 6(3) (2012) 2693-2703.

[153] Y. Zhuang, F. Yu, H. Chen, J. Zheng, J. Ma, J. Chen, Alginate/graphene double-network nanocomposite hydrogel beads with low-swelling, enhanced

mechanical properties, and enhanced adsorption capacity, Journal of Materials Chemistry A 4(28) (2016) 10885-10892.

[154] W. Peng, H. Li, Y. Liu, S. Song, A review on heavy metal ions adsorption from water by graphene oxide and its composites, Journal of Molecular Liquids 230 (2017) 496-504.

[155] R. Sitko, E. Turek, B. Zawisza, E. Malicka, E. Talik, J. Heimann, A. Gagor, B. Feist, R. Wrzalik, Adsorption of divalent metal ions from aqueous solutions using graphene oxide, Dalton Transactions 42(16) (2013) 5682-5682.

[156] W.M. Haynes, CRC Handbook of Chemistry and Physics, 96th Edition, CRC Press2015.

[157] J.-P. Zou, H.-L. Liu, J. Luo, Q.-J. Xing, H.-M. Du, X.-H. Jiang, X.-B. Luo, S.-L. Luo, S.L. Suib, Three-Dimensional Reduced Graphene Oxide Coupled with Mn_3O_4 for Highly Efficient Removal of Sb(III) and Sb(V) from Water, ACS Applied Materials & Interfaces 8(28) (2016) 18140-18149.

[158] X. Chen, S. Zhou, L. Zhang, T. You, F. Xu, Adsorption of heavy metals by graphene oxide/cellulose hydrogel prepared from NaOH/urea aqueous solution, Materials 9(7) (2016).

[159] Z. Han, Z. Tang, S. Shen, B. Zhao, G. Zheng, J. Yang, Strengthening of Graphene Aerogels with Tunable Density and High Adsorption Capacity towards Pb^{2+}, Scientific Reports 4 (2014) 1-6.

[160] J. Teng, X. Zeng, X. Xu, J.G. Yu, Assembly of a novel porous 3D graphene oxide-starch architecture by a facile hydrothermal method and its adsorption properties toward metal ions, Materials Letters 214 (2018) 31-33.

[161] L. Liu, C. Li, C. Bao, Q. Jia, P. Xiao, X. Liu, Q. Zhang, Preparation and characterization of chitosan/graphene oxide composites for the adsorption of Au(III) and Pd(II), Talanta 93 (2012) 350-357.

[162] W.S. Hummers, R.E. Offeman, Preparation of Graphitic Oxide, Journal of the American Chemical Society 80(6) (1958) 1339-1339.

[163] X.J. Lee, L.Y. Lee, B.Y.Z. Hiew, S. Gan, S. Thangalazhy-Gopakumar, H.K. Ng, Multistage optimizations of slow pyrolysis synthesis of biochar from palm oil sludge for adsorption of lead, Bioresource Technology 245 (2017) 944-953.

[164] I. Langmuir, The adsorption of gases on plane surfaces of glass, mica and platinum, Journal of the American Chemical Society 40(9) (1918) 1361-1403.

[165] H.M.F. Freundlich, Over the Adsorption in Solution, Journal of Physical Chemistry A 57 (1906) 385-471.

[166] S. Lagergren, About the Theory of So-Called Adsorption of Soluble Substances., Kungliga Svenska Vetenskapsakademiens Handlingar 24 (1898) 1-39.

[167] Y.S. Ho, G. McKay, Sorption of dye from aqueous solution by peat, Chemical Engineering Journal 70(2) (1998) 115-124.

[168] R.-S. Juang, M.-L. Chen, Application of the Elovich Equation to the Kinetics of Metal Sorption with Solvent-Impregnated Resins, Industrial & Engineering Chemistry Research 36(3) (1997) 813-820.

[169] W.J. Weber, J.C. Morris, Kinetics of adsorption on carbon from solutions, Journal Sanitary Engeering Division Proceedings 89 (1963) 31-60.

[170] F. Raji, A. Saraeian, M. Pakizeh, F. Attarzadeh, Removal of Pb(ii) from aqueous solution by mesoporous silica MCM-41 modified by $ZnCl_2$: kinetics, thermodynamics, and isotherms, RSC Advances 5(46) (2015) 37066-37077.

[171] Y.-S. Ho, W.-T. Chiu, C.-C. Wang, Regression analysis for the sorption isotherms of basic dyes on sugarcane dust, Bioresource Technology 96(11) (2005) 1285-1291.

[172] M. Hadi, M.R. Samarghandi, G. McKay, Equilibrium two-parameter isotherms of acid dyes sorption by activated carbons: Study of residual errors, Chemical Engineering Journal 160(2) (2010) 408-416.

[173] A. Kapoor, R.T. Yang, Correlation of equilibrium adsorption data of condensible vapours on porous adsorbents, Gas Separation & Purification 3(4) (1989) 187-192.

[174] D. Marquardt, An Algorithm for Least-Squares Estimation of Nonlinear Parameters, Journal of the Society for Industrial and Applied Mathematics 11(2) (1963) 431-441.

[175] S.J.S. Chelladurai, M. K, A.P. Ray, M. Upadhyaya, V. Narasimharaj, G. S, Optimization of process parameters using response surface methodology: A review, Materials Today: Proceedings (2020).

[176] G. Derringer, R. Suich, Simultaneous Optimization of Several Response Variables, Journal of Quality Technology 12(4) (1980) 214-219.

[177] H.C. Thomas, Heterogeneous Ion Exchange in a Flowing System, Journal of the American Chemical Society 66(10) (1944) 1664-1666.

[178] Y.H. Yoon, J.H. Nelson, Application of Gas Adsorption Kinetics I. A Theoretical Model for Respirator Cartridge Service Life, American Industrial Hygiene Association Journal 45(8) (1984) 509-516.

[179] G.S. Bohart, E.Q. Adams, Some aspects of the behavior of charcoal with respect to chlorine.1, Journal of the American Chemical Society 42(3) (1920) 523-544.

[180] M.-Y. Xu, H.-L. Jiang, Z.-W. Xie, Z.-T. Li, D. Xu, F.-A. He, Highly efficient selective adsorption of anionic dyes by modified β-cyclodextrin polymers, Journal of the Taiwan Institute of Chemical Engineers 108 (2020) 114-128.

[181] O. Anjaneya, S.Y. Souche, M. Santoshkumar, T.B. Karegoudar, Decolorization of sulfonated azo dye Metanil Yellow by newly isolated bacterial strains: Bacillus sp. strain AK1 and Lysinibacillus sp. strain AK2, Journal of Hazardous Materials 190(1-3) (2011) 351-358.

[182] S.M. Sachdeva, K.V. Mani, S.K. Adaval, Y.P. Jalpota, K.C. Rasela, D.S. Chadha, Acquired toxic methaemoglobinaemia, The journal of the association of physicians of india 40(4) (1992) 239-240.

[183] S.S. Chandra, T. Nagaraja, A food poisoning outbreak with chemical dye: an investigation report, Medical Journal Armed Forces India 43(4) (1987) 291-300.

[184] B.M. Hausen, A case of allergic contact dermatitis due to metanil yellow, Contact Dermatitis 31(2) (1994) 117-118.

[185] P. Arbab, B. Ayati, M.R. Ansari, Reducing the use of nanotitanium dioxide by switching from single photocatalysis to combined photocatalysis-cavitation in dye elimination, Process Safety and Environmental Protection 121 (2019) 87-93.

[186] H. Ma, A. Kong, Y. Ji, B. He, Y. Song, J. Li, Ultrahigh adsorption capacities for anionic and cationic dyes from wastewater using only chitosan, Journal of Cleaner Production 214 (2019) 89-94.

[187] M. Hassaan, A. El Nemr, Health and Environmental Impacts of Dyes: Mini Review, 2017.

[188] L. Dai, W. Zhu, L. He, F. Tan, N. Zhu, Q. Zhou, M. He, G. Hu, Calcium-rich biochar from crab shell: An unexpected super adsorbent for dye removal, Bioresource Technology 267 (2018) 510-516.

[189] J. Ooi, L.Y. Lee, B.Y.Z. Hiew, S. Thangalazhy-Gopakumar, S.S. Lim, S. Gan, Assessment of fish scales waste as a low cost and eco-friendly adsorbent for removal of an azo dye: Equilibrium, kinetic and thermodynamic studies, Bioresource Technology 245 (2017) 656-664.

[190] C. Zheng, H. Zheng, Y. Wang, Y. Wang, W. Qu, Q. An, Y. Liu, Synthesis of novel modified magnetic chitosan particles and their adsorption performance toward Cr(VI), Bioresource Technology 267 (2018) 1-8.

[191] C. Qi, L. Zhao, Y. Lin, D. Wu, Graphene oxide/chitosan sponge as a novel filtering material for the removal of dye from water, Journal of Colloid and Interface Science 517 (2018) 18-27.

[192] A.S.K. Kumar, S.-J. Jiang, Chitosan-functionalized graphene oxide: A novel adsorbent an efficient adsorption of arsenic from aqueous solution, Journal of Environmental Chemical Engineering 4(2) (2016) 1698-1713.

[193] F.V. Ferreira, F.S. Brito, W. Franceschi, E.A.N. Simonetti, L.S. Cividanes, M. Chipara, K. Lozano, Functionalized graphene oxide as reinforcement in epoxy based nanocomposites, Surfaces and Interfaces 10 (2018) 100-109.

[194] A. Hosseinzadeh, S. Bidmeshkipour, Y. Abdi, E. Arzi, S. Mohajerzadeh, Graphene based strain sensors: A comparative study on graphene and its derivatives, Applied Surface Science 448 (2018) 71-77.

[195] B.Y.Z. Hiew, L.Y. Lee, K.C. Lai, S. Gan, S. Thangalazhy-Gopakumar, G.-T. Pan, T.C.-K. Yang, Adsorptive decontamination of diclofenac by three-dimensional graphene-based adsorbent: Response surface methodology, adsorption equilibrium, kinetic and thermodynamic studies, Environmental Research 168 (2019) 241-253.

[196] Y. Liu, S. Huang, X. Zhao, Y. Zhang, Fabrication of three-dimensional porous β-cyclodextrin/chitosan functionalized graphene oxide hydrogel for methylene blue removal from aqueous solution, Colloids and Surfaces A: Physicochemical and Engineering Aspects 539 (2018) 1-10.

[197] C. Zhang, Z. Chen, W. Guo, C. Zhu, Y. Zou, Simple fabrication of Chitosan/Graphene nanoplates composite spheres for efficient adsorption of acid dyes from aqueous solution, International Journal of Biological Macromolecules 112 (2018) 1048-1054.

[198] L. Fan, C. Luo, M. Sun, X. Li, F. Lu, H. Qiu, Preparation of novel magnetic chitosan/graphene oxide composite as effective adsorbents toward methylene blue, Bioresource Technology 114 (2012) 703-706.

[199] L.A. Kafshgari, M. Ghorbani, A. Azizi, S. Agarwal, V.K. Gupta, Modeling and optimization of Direct Red 16 adsorption from aqueous solutions using nanocomposite of MnFe2O4/MWCNTs: RSM-CCRD model, Journal of Molecular Liquids 233 (2017) 370-377.

[200] A. Zaman, J.T. Orasugh, P. Banerjee, S. Dutta, M.S. Ali, D. Das, A. Bhattacharya, D. Chattopadhyay, Facile one-pot in-situ synthesis of novel graphene oxide-cellulose nanocomposite for enhanced azo dye adsorption at optimized conditions, Carbohydrate Polymers 246 (2020) 116661.

[201] S. Omidi, A. Kakanejadifard, Eco-friendly synthesis of graphene–chitosan composite hydrogel as efficient adsorbent for Congo red, RSC Advances 8(22) (2018) 12179-12189.

[202] N.A. Travlou, G.Z. Kyzas, N.K. Lazaridis, E.A. Deliyanni, Functionalization of Graphite Oxide with Magnetic Chitosan for the Preparation of a Nanocomposite Dye Adsorbent, Langmuir 29(5) (2013) 1657-1668.

[203] M. Wang, Y. Ma, Y. Sun, S.Y. Hong, S.K. Lee, B. Yoon, L. Chen, L. Ci, J.D. Nam, X. Chen, J. Suhr, Hierarchical Porous Chitosan Sponges as Robust and Recyclable Adsorbents for Anionic Dye Adsorption, Scientific Report 7(1) (2017) 18054.

[204] X.J. Lee, L.Y. Lee, S. Gan, S. Thangalazhy-Gopakumar, H.K. Ng, Biochar potential evaluation of palm oil wastes through slow pyrolysis: Thermochemical characterization and pyrolytic kinetic studies, Bioresource Technology 236 (2017) 155-163.

[205] J. Rotta, E. Minatti, P.L.M. Barreto, Determination of structural and mechanical properties, diffractometry, and thermal analysis of chitosan and hydroxypropylmethylcellulose (HPMC) films plasticized with sorbitol, Food Science and Technology 31 (2011) 450-455.

[206] L.Y. Lee, S. Gan, M.S. Yin Tan, S.S. Lim, X.J. Lee, Y.F. Lam, Effective removal of Acid Blue 113 dye using overripe Cucumis sativus peel as an eco-friendly biosorbent from agricultural residue, Journal of Cleaner Production 113 (2016) 194-203.

[207] F. Ghorbani, S. Kamari, Core–shell magnetic nanocomposite of Fe3O4@SiO2@NH2 as an efficient and highly recyclable adsorbent of methyl red

dye from aqueous environments, Environmental Technology & Innovation 14 (2019) 100333.

[208] N. Rajamohan, M. Rajasimman, R. Rajeshkannan, V. Saravanan, Equilibrium, kinetic and thermodynamic studies on the removal of Aluminum by modified Eucalyptus camaldulensis barks, Alexandria Engineering Journal 53(2) (2014) 409-415.

[209] M. Greluk, Z. Hubicki, Kinetics, isotherm and thermodynamic studies of Reactive Black 5 removal by acid acrylic resins, Chemical Engineering Journal 162(3) (2010) 919-926.

[210] A.A. Ismaiel, M.K. Aroua, R. Yusoff, Cadmium (II)-selective electrode based on palm shell activated carbon modified with task-specific ionic liquid: kinetics and analytical applications, International Journal of Environmental Science and Technology 11(4) (2013) 1115-1126.

[211] G. Sheng, S. Zhu, S. Wang, Z. Wang, Removal of dyes by a novel fly ash–chitosan–graphene oxide composite adsorbent, RSC Advances 6(22) (2016) 17987-17994.

[212] A. Asfaram, M. Ghaedi, G.R. Ghezelbash, E.A. Dil, I. Tyagi, S. Agarwal, V.K. Gupta, Biosorption of malachite green by novel biosorbent Yarrowia lipolytica isf7: Application of response surface methodology, Journal of Molecular Liquids 214 (2016) 249-258.

[213] A. Özer, G. Gürbüz, A. Çalimli, B.K. Körbahti, Biosorption of copper(II) ions on Enteromorpha prolifera: Application of response surface methodology (RSM), Chemical Engineering Journal 146(3) (2009) 377-387.

[214] M. Roghani, S.A.A. Nakhli, M. Aghajani, M.H. Rostami, S.M. Borghei, Adsorption and oxidation study on arsenite removal from aqueous solutions by polyaniline/polyvinyl alcohol composite, Journal of Water Process Engineering 14 (2016) 101-107.

[215] Y. Deng, Y.S. Ok, D. Mohan, C.U. Pittman, X. Dou, Carbamazepine removal from water by carbon dot-modified magnetic carbon nanotubes, Environmental Research 169 (2019) 434-444.

[216] H. Sayğılı, F. Güzel, Y. Önal, Conversion of grape industrial processing waste to activated carbon sorbent and its performance in cationic and anionic dyes adsorption, Journal of Cleaner Production 93 (2015) 84-93.

[217] M.A. Moreira, K.J. Ciuffi, V. Rives, M.A. Vicente, R. Trujillano, A. Gil, S.A. Korili, E.H. de Faria, Effect of chemical modification of palygorskite and sepiolite by 3-aminopropyltriethoxisilane on adsorption of cationic and anionic dyes, Applied Clay Science 135 (2017) 394-404.

[218] H. Sayğılı, F. Güzel, High surface area mesoporous activated carbon from tomato processing solid waste by zinc chloride activation: process optimization, characterization and dyes adsorption, Journal of Cleaner Production 113 (2016) 995-1004.

[219] D. Garg, S. Kumar, K. Sharma, C.B. Majumder, Application of waste peanut shells to form activated carbon and its utilization for the removal of Acid Yellow 36 from wastewater, Groundwater for Sustainable Development 8 (2019) 512-519.

[220] H. Sayğılı, F. Güzel, Novel and sustainable precursor for high-quality activated carbon preparation by conventional pyrolysis: Optimization of produce

conditions and feasibility in adsorption studies, Advanced Powder Technology 29(3) (2018) 726-736.

[221] S. Ziane, F. Bessaha, K. Marouf-Khelifa, A. Khelifa, Single and binary adsorption of reactive black 5 and Congo red on modified dolomite: Performance and mechanism, Journal of Molecular Liquids 249 (2018) 1245-1253.

[222] S. Wong, H.H. Tumari, N. Ngadi, N.B. Mohamed, O. Hassan, R. Mat, N.A. Saidina Amin, Adsorption of anionic dyes on spent tea leaves modified with polyethyleneimine (PEI-STL), Journal of Cleaner Production 206 (2019) 394-406.

[223] J.M. Moura, D.D.R. Gründmann, T.R.S. Cadaval, G.L. Dotto, L.A.A. Pinto, Comparison of chitosan with different physical forms to remove Reactive Black 5 from aqueous solutions, Journal of Environmental Chemical Engineering 4(2) (2016) 2259-2267.

[224] M. Bhaumik, R.I. McCrindle, A. Maity, S. Agarwal, V.K. Gupta, Polyaniline nanofibers as highly effective re-usable adsorbent for removal of reactive black 5 from aqueous solutions, Journal of Colloid and Interface Science 466 (2016) 442-451.

[225] S. Chatterjee, T. Chatterjee, S.H. Woo, Influence of the polyethyleneimine grafting on the adsorption capacity of chitosan beads for Reactive Black 5 from aqueous solutions, Chemical Engineering Journal 166(1) (2011) 168-175.

[226] J. Jang, D.S. Lee, Enhanced adsorption of cesium on PVA-alginate encapsulated Prussian blue-graphene oxide hydrogel beads in a fixed-bed column system, Bioresource Technology 218 (2016) 294-300.

[227] D. Chen, J. Zhou, H. Wang, K. Yang, Batch and fixed-bed column study for p-nitrophenol, methylene blue, and U(VI) removal by polyvinyl alcohol–graphene

oxide macroporous hydrogel bead, Water Science and Technology 77(1) (2017) 91-100.

[228] D.K. Singh, V. Kumar, S. Mohan, D. Bano, S.H. Hasan, Breakthrough curve modeling of graphene oxide aerogel packed fixed bed column for the removal of Cr(VI) from water, Journal of Water Process Engineering 18 (2017) 150-158.

[229] J. Qu, T. Song, J. Liang, X. Bai, Y. Li, Y. Wei, S. Huang, L. Dong, Y. Jin, Adsorption of lead () from aqueous solution by modified Auricularia matrix waste: A fixed-bed column study, Ecotoxicology and Environmental Safety 169 (2019) 722-729.

[230] L. Yanyan, T.A. Kurniawan, M. Zhu, T. Ouyang, R. Avtar, M.H. Dzarfan Othman, B.T. Mohammad, A.B. Albadarin, Removal of acetaminophen from synthetic wastewater in a fixed-bed column adsorption using low-cost coconut shell waste pretreated with NaOH, HNO3, ozone, and/or chitosan, Journal of Environmental Management 226 (2018) 365-376.

[231] A. Ajmani, C. Patra, S. Subbiah, S. Narayanasamy, Packed bed column studies of hexavalent chromium adsorption by zinc chloride activated carbon synthesized from Phanera vahlii fruit biomass, Journal of Environmental Chemical Engineering 8(4) (2020) 103825.

[232] M. Basu, A.K. Guha, L. Ray, Adsorption of Lead on Lentil Husk in Fixed Bed Column Bioreactor, Bioresoure Technology 283 (2019) 86-95.

[233] R. R, J. T, R.K. G, S. Jacob, R. R, B.K. George, Adsorption performance of packed bed column for the removal of perchlorate using modified activated carbon, Process Safety and Environmental Protection 117 (2018) 350-362.

[234] K. Nithya, A. Sathish, P.S. Kumar, Packed bed column optimization and modeling studies for removal of chromium ions using chemically modified Lantana camara adsorbent, Journal of Water Process Engineering 33 (2020) 101069.

[235] S. Charola, R. Yadav, P. Das, S. Maiti, Fixed-bed adsorption of Reactive Orange 84 dye onto activated carbon prepared from empty cotton flower agro-waste, Sustainable Environment Research 28(6) (2018) 298-308.

[236] M. Yusuf, K. Song, L. Li, Fixed bed column and artificial neural network model to predict heavy metals adsorption dynamic on surfactant decorated graphene, Colloids and Surfaces A: Physicochemical and Engineering Aspects 585 (2020) 124076.

[237] M. Jafari, M.R. Rahimi, M. Ghaedi, H. Javadian, A. Asfaram, Fixed-bed column performances of azure-II and auramine-O adsorption by Pinus eldarica stalks activated carbon and its composite with zno nanoparticles: Optimization by response surface methodology based on central composite design, Journal of Colloid and Interface Science 507 (2017) 172-189.

[238] S. Dhakal, K. Chao, W. Schmidt, J. Qin, M. Kim, D. Chan, Evaluation of Turmeric Powder Adulterated with Metanil Yellow Using FT-Raman and FT-IR Spectroscopy, Foods 5(2) (2016).

[239] W. Ben Mbarek, E. Pineda, L. Escoda, J.J. Suñol, M. Khitouni, High efficiency decolorization of azo dye Reactive Black 5 by Ca-Al particles, Journal of Environmental Chemical Engineering 5(6) (2017) 6107-6113.

[240] S.Y. Tsang, P.S.R. Choi, C.W. Kan, C.W.M. Yuen, S.K.A. Ku, Determining Functional Groups of Commercially Available Ink-Jet Printing Reactive Dyes

Using Infrared Spectroscopy, Research Journal of Textile and Apparel 9(2) (2005) 26-38.

[241] S. Wong, N.A. Ghafar, N. Ngadi, F.A. Razmi, I.M. Inuwa, R. Mat, N.A.S. Amin, Effective removal of anionic textile dyes using adsorbent synthesized from coffee waste, Scientific Report 10(1) (2020) 2928.

[242] B.O. Isiuku, C.A. Ojike, O.U. Akakuru, F.C. Ibe, Fixed-bed adsorptive removal of metanil yellow from simulated wastewater in a fixed-bed column by nitric acid-treated-H3PO4-activated carbon (NATPAAC) from oil palm fruit mesocarpfibre, World News of Natural Sciences 17 (2018) 157-172.

[243] V.K. Gupta, Suhas, I. Tyagi, S. Agarwal, R. Singh, M. Chaudhary, A. Harit, S. Kushwaha, Column operation studies for the removal of dyes and phenols using a low cost adsorbent, Global Journal of Environmental Science and Management 2(1) (2016) 1-10.

[244] B.O. Isiuku, C.N. Nwosu, Fixed-Bed Adsorption of Metanil Yellow from Aqueous Solution on HNO_3-Treated-H_3PO_4-Activated Carbon from Gmelina Bark Asian Journal of Chemistry 29 (2017) 475-479.

[245] A.A. Ahmad, B.H. Hameed, Fixed-bed adsorption of reactive azo dye onto granular activated carbon prepared from waste, Journal of Hazardous Materials 175(1-3) (2010) 298-303.

[246] Z. Wang, S.B. Kang, W. S.W., Aqueous Solution using Polyethylenimine-Crosslinked Chitin: Batch and Fixed-bed Column Studies, Chemical Engineering Transactions 78 (2020) 97-102.

[247] Y.S. Al-Degs, M.A.M. Khraisheh, S.J. Allen, M.N. Ahmad, Adsorption characteristics of reactive dyes in columns of activated carbon, Journal of Hazardous Materials 165(1) (2009) 944-949.

[248] Y. Li, N. Tsend, T. Li, H. Liu, R. Yang, X. Gai, H. Wang, S. Shan, Microwave assisted hydrothermal preparation of rice straw hydrochars for adsorption of organics and heavy metals, Bioresource Technology 273 (2019) 136-143.

[249] M. Basu, A.K. Guha, L. Ray, Adsorption of Lead on Lentil Husk in Fixed Bed Column Bioreactor, Bioresource Technology 283 (2019) 86-95.

[250] S. Yan, Y. Cai, H. Li, S. Song, L. Xia, Enhancement of cadmium adsorption by EPS-montmorillonite composites, Environmental Pollution 252 (2019) 1509-1518.

[251] G.F. Nordberg, Historical perspectives on cadmium toxicology, Toxicology and Applied Pharmacology 238(3) (2009) 192-200.

[252] M. Basu, A.K. Guha, L. Ray, Adsorption Behavior of Cadmium on Husk of Lentil, Process Safety and Environmental Protection 106 (2017) 11-22.

[253] H.T. Van, L.H. Nguyen, V.D. Nguyen, X.H. Nguyen, T.H. Nguyen, T.V. Nguyen, S. Vigneswaran, J. Rinklebe, H.N. Tran, Characteristics and mechanisms of cadmium adsorption onto biogenic aragonite shells-derived biosorbent: Batch and column studies, Journal of Environmental Management 241 (2019) 535-548.

[254] F. Wang, Y. Pan, P. Cai, T. Guo, H. Xiao, Single and binary adsorption of heavy metal ions from aqueous solutions using sugarcane cellulose-based adsorbent, Bioresource Technology 241 (2017) 482-490.

[255] K.C. Lai, L.Y. Lee, B.Y.Z. Hiew, S. Thangalazhy-Gopakumar, S. Gan, Environmental application of three-dimensional graphene materials as adsorbents

for dyes and heavy metals: Review on ice-templating method and adsorption mechanisms, Journal of Environmental Sciences 79 (2019) 174-199.

[256] N. Yousefi, K.K.W. Wong, Z. Hosseinidoust, H.O. Sørensen, S. Bruns, Y. Zheng, N. Tufenkji, Hierarchically porous, ultra-strong reduced graphene oxide-cellulose nanocrystal sponges for exceptional adsorption of water contaminants, Nanoscale 10(15) (2018) 7171-7184.

[257] M. Zheng, F. Lian, Y. Xiong, B. Liu, Y. Zhu, S. Miao, L. Zhang, B. Zheng, The synthesis and characterization of a xanthan gum-acrylamide-trimethylolpropane triglycidyl ether hydrogel, Food Chemistry 272 (2019) 574-579.

[258] C. Tian, J. Zhao, J. Zhang, S. Chu, Z. Dang, Z. Lin, B. Xing, Enhanced removal of roxarsone by Fe_3O_4@3D graphene nanocomposites: synergistic adsorption and mechanism, Environmental Science: Nano 4(11) (2017) 2134-2143.

[259] X. Zhao, Q. Jia, N. Song, W. Zhou, Y. Li, Adsorption of Pb(II) from an Aqueous Solution by Titanium Dioxide/Carbon Nanotube Nanocomposites: Kinetics, Thermodynamics, and Isotherms, Journal of Chemical & Engineering Data 55(10) (2010) 4428-4433.

[260] H. Sharififard, m. Ghorbanpour, S. Hosseinirad, Cadmium removal from wastewater using nano-clay/TiO_2 composite: kinetics, equilibrium and thermodynamic study, Advances in environmental science and technology 4 (2018) 203-209.

[261] A. Murugesan, T. Vidhyadevi, S.S. Kalaivani, K.V. Thiruvengadaravi, L. Ravikumar, C.D. Anuradha, S. Sivanesan, Modelling of lead(II) ion adsorption onto

poly(thiourea imine) functionalized chelating resin using response surface methodology (RSM), Journal of Water Process Engineering 3 (2014) 132-143.

[262] H.H. Darzi, S.G. Larimi, G.N. Darzi, Synthesis, characterization and physical properties of a novel xanthan gum/polypyrrole nanocomposite, Synthetic Metals 162(1) (2012) 236-239.

[263] B.Y.S. Chang, N.M. Huang, M.N. An'amt, A.R. Marlinda, Y. Norazriena, M.R. Muhamad, I. Harrison, H.N. Lim, C.H. Chia, Facile hydrothermal preparation of titanium dioxide decorated reduced graphene oxide nanocomposite, International Journal of Nanomedicine 7 (2012) 3379-3387.

[264] S. Faria, C.L. de Oliveira Petkowicz, S.A.L. de Morais, M.G.H. Terrones, M.M. de Resende, F.P. de Fran ça, V.L. Cardoso, Characterization of xanthan gum produced from sugar cane broth, Carbohydrate Polymers 86(2) (2011) 469-476.

[265] W. Liu, J. Cai, Z. Ding, Z. Li, TiO_2/RGO composite aerogels with controllable and continuously tunable surface wettability for varied aqueous photocatalysis, Applied Catalysis B: Environmental 174-175 (2015) 421-426.

[266] C. Basheer, Application of Titanium Dioxide-Graphene Composite Material for Photocatalytic Degradation of Alkylphenols, Journal of Chemistry 2013 (2013) 10.

[267] G. Lui, J.-Y. Liao, A. Duan, Z. Zhang, M. Fowler, A. Yu, Graphene-wrapped hierarchical TiO_2 nanoflower composites with enhanced photocatalytic performance, Journal of Materials Chemistry A 1(39) (2013) 12255-12262.

[268] M. Nehra, N. Dilbaghi, N.K. Singhal, A.A. Hassan, K.-H. Kim, S. Kumar, Metal organic frameworks MIL-100(Fe) as an efficient adsorptive material for phosphate management, Environmental Research 169 (2019) 229-236.

[269] M.N. Zafar, Q. Dar, F. Nawaz, M.N. Zafar, M. Iqbal, M.F. Nazar, Effective adsorptive removal of azo dyes over spherical ZnO nanoparticles, Journal of Materials Research and Technology 8(1) (2019) 713-725.

[270] R. Bardestani, C. Roy, S. Kaliaguine, The effect of biochar mild air oxidation on the optimization of lead(II) adsorption from wastewater, Journal of Environmental Management 240 (2019) 404-420.

[271] F. Wang, W. Yang, P. Cheng, S. Zhang, S. Zhang, W. Jiao, Y. Sun, Adsorption characteristics of cadmium onto microplastics from aqueous solutions, Chemosphere 235 (2019) 1073-1080.

[272] M. Alimohammady, M. Jahangiri, F. Kiani, H. Tahermansouri, Highly efficient simultaneous adsorption of Cd(ii), Hg(ii) and As(iii) ions from aqueous solutions by modification of graphene oxide with 3-aminopyrazole: central composite design optimization, New Journal of Chemistry 41(17) (2017) 8905-8919.

[273] M. Gao, Z. Wang, C. Yang, J. Ning, Z. Zhou, G. Li, Novel magnetic graphene oxide decorated with persimmon tannins for efficient adsorption of malachite green from aqueous solutions, Colloids and Surfaces A: Physicochemical and Engineering Aspects 566 (2019) 48-57.

[274] L. Liu, J. Liu, L. Zhao, Z. Yang, C. Lv, J. Xue, A. Tang, Synthesis and characterization of magnetic Fe_3O_4@$CaSiO_3$ composites and evaluation of their adsorption characteristics for heavy metal ions, Environmental Science and Pollution Research 26(9) (2019) 8721-8736.

[275] C. Jiang, X. Wang, G. Wang, C. Hao, X. Li, T. Li, Adsorption performance of a polysaccharide composite hydrogel based on crosslinked glucan/chitosan for heavy metal ions, Composites Part B: Engineering 169 (2019) 45-54.

[276] S. Abolhasani, A. Ahmadpour, T. Rohani Bastami, A. Yaqubzadeh, Facile synthesis of mesoporous carbon aerogel for the removal of ibuprofen from aqueous solution by central composite experimental design (CCD), Journal of Molecular Liquids 281 (2019) 261-268.

[277] B.Y.Z. Hiew, L.Y. Lee, X.J. Lee, S. Gan, S. Thangalazhy-Gopakumar, S.S. Lim, G.-T. Pan, T.C.-K. Yang, Adsorptive removal of diclofenac by graphene oxide: Optimization, equilibrium, kinetic and thermodynamic studies, Journal of the Taiwan Institute of Chemical Engineers 98 (2019) 150-162.

[278] J. Liu, J. Wang, C. Leung, F. Gao, A Multi-Parameter Optimization Model for the Evaluation of Shale Gas Recovery Enhancement, Energies 11(3) (2018).

[279] A.C. Khorasani, S.A. Shojaosadati, Magnetic pectin-Chlorella vulgaris biosorbent for the adsorption of dyes, Journal of Environmental Chemical Engineering 7(3) (2019) 103062.

[280] R. Tabaraki, A. Nateghi, Multimetal biosorption modeling of Zn^{2+}, Cu^{2+} and Ni^{2+} by Sargassum ilicifolium, Ecological Engineering 71 (2014) 197-205.

[281] M. Vakili, S. Deng, G. Cagnetta, W. Wang, P. Meng, D. Liu, G. Yu, Regeneration of chitosan-based adsorbents used in heavy metal adsorption: A review, Separation and Purification Technology 224 (2019) 373-387.

[282] Y. Dai, N. Zhang, C. Xing, Q. Cui, Q. Sun, The adsorption, regeneration and engineering applications of biochar for removal organic pollutants: A review, Chemosphere 223 (2019) 12-27.

[283] J. Zhang, J. Shao, Q. Jin, X. Zhang, H. Yang, Y. Chen, S. Zhang, H. Chen, Effect of deashing on activation process and lead adsorption capacities of sludge-based biochar, Science of The Total Environment 716 (2020) 137016.

[284] L. Xu, C. Chen, J.-B. Huo, X. Chen, J.-C.E. Yang, M.-L. Fu, Iron hydroxyphosphate composites derived from waste lithium-ion batteries for lead adsorption and Fenton-like catalytic degradation of methylene blue, Environmental Technology & Innovation 16 (2019) 100504.

[285] J. Hosseini, E.N. Zare, D. Ajloo, Experimental and theoretical calculation investigation on effective adsorption of lead(II) onto poly(aniline-co-pyrrole) nanospheres, Journal of Molecular Liquids 296 (2019) 111789.

[286] Y. Chu, S. Zhu, M. Xia, F. Wang, W. Lei, Methionine-montmorillonite composite – A novel material for efficient adsorption of lead ions, Advanced Powder Technology (2019).

[287] Y. Cao, W. Xiao, G. Shen, G. Ji, Y. Zhang, C. Gao, L. Han, Carbonization and ball milling on the enhancement of Pb(II) adsorption by wheat straw: Competitive effects of ion exchange and precipitation, Bioresource Technology 273 (2019) 70-76.

[288] P.M. Thabede, N.D. Shooto, T. Xaba, E.B. Naidoo, Adsorption studies of toxic cadmium(II) and chromium(VI) ions from aqueous solution by activated black cumin (Nigella sativa) seeds, Journal of Environmental Chemical Engineering 8(4) (2020) 104045.

[289] S. Bagheri, M.M. Amini, M. Behbahani, G. Rabiee, Low cost thiol-functionalized mesoporous silica, KIT-6-SH, as a useful adsorbent for cadmium

ions removal: A study on the adsorption isotherms and kinetics of KIT-6-SH, Microchemical Journal 145 (2019) 460-469.

[290] S. Tasharrofi, Z. Rouzitalab, D.M. Maklavany, A. Esmaeili, M. Rabieezadeh, M. Askarieh, A. Rashidi, H. Taghdisian, Adsorption of cadmium using modified zeolite-supported nanoscale zero-valent iron composites as a reactive material for PRBs, Science of The Total Environment 736 (2020) 139570.

[291] L. Zhu, L. Tong, N. Zhao, X. Wang, X. Yang, Y. Lv, Key factors and microscopic mechanisms controlling adsorption of cadmium by surface oxidized and aminated biochars, Journal of Hazardous Materials 382 (2020) 121002.

[292] V. Badalamoole, S. Abubakar Zauro, Absorptive removal of Cu2+ and Pb2+ from aqueous solutions using xanthan gum-g-poly[(N,N′-dimethylacrylamide)-co-(2-acrylamido-2-methylpropanesulfonic acid)]–ZnO nanocomposite gel, Separation Science and Technology (2018) 1-16.

[293] A. Khan, J.E. Szulejko, P. Samaddar, K.-H. Kim, W. Eom, S.B. Ambade, T.H. Han, The effect of diverse metal oxides in graphene composites on the adsorption isotherm of gaseous benzene, Environmental Research 172 (2019) 367-374.

[294] S. Yu, D. Wei, L. Shi, Y. Ai, P. Zhang, X. Wang, Three-dimensional graphene/titanium dioxide composite for enhanced U(VI) capture: Insights from batch experiments, XPS spectroscopy and DFT calculation, Environmental Pollution 251 (2019) 975-983.

[295] M. Lu, Y. Zhang, Y. Zhou, Z. Su, B. Liu, G. Li, T. Jiang, Adsorption-desorption characteristics and mechanisms of Pb(II) on natural vanadium, titanium-

bearing magnetite-humic acid magnetic adsorbent, Powder Technology 344 (2019) 947-958.

[296] J.-H. Park, J.-H. Eom, S.-L. Lee, S.-W. Hwang, S.-H. Kim, S.-W. Kang, J.-J. Yun, J.-S. Cho, Y.-H. Lee, D.-C. Seo, Exploration of the potential capacity of fly ash and bottom ash derived from wood pellet-based thermal power plant for heavy metal removal, Science of The Total Environment 740 (2020) 140205.

[297] Y. Dong, H. Lin, Competitive adsorption of Pb(II) and Zn(II) from aqueous solution by modified beer lees in a fixed bed column, Process Safety and Environmental Protection 111 (2017) 263-269.

[298] J.-L. Gong, Y.-L. Zhang, Y. Jiang, G.-M. Zeng, Z.-H. Cui, K. Liu, C.-H. Deng, Q.-Y. Niu, J.-H. Deng, S.-Y. Huan, Continuous adsorption of Pb(II) and methylene blue by engineered graphite oxide coated sand in fixed-bed column, Applied Surface Science 330 (2015) 148-157.

[299] Y. Liu, Q. Gao, C. Li, S. Liu, K. Xia, B. Han, C. Zhou, Effective coating of crosslinked polyethyleneimine on elastic spongy monolith for highly efficient batch and continuous flow adsorption of Pb(II) and acidic red 18, Chemical Engineering Journal 391 (2020) 123610.

[300] K.S. Rao, S. Anand, P. Venkateswarlu, Modeling the kinetics of Cd(II) adsorption on Syzygium cumini L leaf powder in a fixed bed mini column, Journal of Industrial and Engineering Chemistry 17(2) (2011) 174-181.

[301] S.M. Ghasemabadi, M. Baghdadi, E. Safari, F. Ghazban, Investigation of continuous adsorption of Pb(II), As(III), Cd(II), and Cr(VI) using a mixture of magnetic graphite oxide and sand as a medium in a fixed-bed column, Journal of Environmental Chemical Engineering 6(4) (2018) 4840-4849.

[302] Y. Jin, C. Teng, S. Yu, T. Song, L. Dong, J. Liang, X. Bai, X. Liu, X. Hu, J. Qu, Batch and fixed-bed biosorption of Cd(II) from aqueous solution using immobilized Pleurotus ostreatus spent substrate, Chemosphere 191 (2018) 799-808.